H_2 Production: Formulation of Catalysts Promoting the Decomposition of Carbon-free Hydrogen Carriers

by Xiuyuan Lu

Thesis submitted for the degree of Doctor of Philosophy

School of Chemistry

Cardiff University

January 2022

Acknowledgment

Three and a half years of Ph.D. student study life passed in a flash. Looking back on the past years, I am full of gratitude. First of all, my sincere thanks to my supervisor Dr. Alberto. From the selection of the topic, the design of the research method, and the finalization of the thesis, he devoted huge efforts to it from beginning to end. I would like to thank Prof. Richard Catlow for his full support of my Ph.D. study. His generous mind and optimistic attitude will inspire me to make great efforts and innovate on the road of science. I also gratefully thank Prof. Wen-Kai Chen (Fuzhou University), Prof. Nikolaos Dimitratos (University of Bologna), Prof. Kim Daasbjerg (Aarhus University), and Dr. Andrew Logsdail for their expertise and invaluable discussions and help. I thank Prof. Alberto Villa (University of Milan) and Prof. Gang Fu (Xiamen University) gave me opportunities to visit and study at the University of Milan and Xiamen University, although some plans have not been realized because of the COVID-19. During the visiting study in Milan, I got a lot of help and fun from the lab members. I thank Ilaria, Sofia, Stefano, and Simone for giving me a wonderful memory in Milan.

I also would like to thank many lab members and school colleagues: Fabian, Julien, Cameron, Samantha, Alexandre, Rana, Kai Wang, Jia Sun, Shikai Liu, Jing Zhang, and XiaoXiao Gong, et al. It was a great pleasure working with them and I learned a lot from them. Moreover, I appreciate the colorful time spent with Nyuying Wang, Xindong Chen, Peng Yang, Ping Huang, Xiang Wang, Xiude Lin, Mei Li in Cardiff. I thank the financial support from the China Scholarship Council and Cardiff University, giving me a great opportunity to accomplish this research.

Special thanks to my grandma, she taught me to be a diligent and kind person since I was a child. I wish her all the best in heaven. Finally, I thank my family and all my friends who companying and supporting me during the tough time.

Publications

There are peer-reviewed journal papers I published during my Ph.D. study. They mainly covered research areas including hydrogen production catalysts, carbon dioxide reduction, and computational chemistry.

[1] ***Lu, X.***, Francis, S., Motta, D., Dimitratos, N., & Roldan, A. (*2020*). Mechanistic study of hydrazine decomposition on Ir (111). ***Physical Chemistry Chemical Physics***, *22*(7), 3883-3896.

[2] ***Lu, X.***; Roldan, A. (2021). Are Carbon-Based Materials Good Supports for the Catalytic Reforming of Ammonia? ***The Journal of Physical Chemistry C***, 125 (29), 15950–15958.

[3] ***Lu, X.***, Zhang, J., Chen, W. K., & Roldan, A. (2021). Kinetic and mechanistic analysis of NH_3 decomposition on Ru (0001), Ru (111) and Ir (111) surfaces. ***Nanoscale Advances***, 2021, **3**, 1624 – 1632.

[4] Li, S., Zhao, S, ***Lu, X.***, Ceccato, M., ... Daasbjerg, K. Low-Valence Znδ+ (0<δ<2) Single-Atom Material as Highly Efficient Electrocatalyst for CO_2 Reduction. (2021) ***Angewandte Chemi***, DOI: 10.1002/ange.202107550

[5] Li, S., Ceccato, M., ***Lu, X.***, Frank, S., Lock, N., Roldan, A., ... & Daasbjerg, K. (2021). Incorporation of nickel single atoms into carbon paper as self-standing electrocatalyst for CO_2 reduction. ***Journal of Materials Chemistry A***, 9(3), 1583-1592.

[6] Barlocco, I., Capelli, S., ***Lu, X.***, Tumiati, S., Dimitratos, N., Roldan, A., & Villa, A. (2020). Role of defects in carbon materials during metal-free formic acid dehydrogenation. ***Nanoscale***, 12(44), 22768-22777.

[7] Barlocco, I.; Capelli, S.; ***Lu, X.***; Bellomi, S.; Huang, X.; Wang, D.; Prati, L.; Dimitratos, N.; Roldan, A; Villa, A. (2021). Disclosing the Role of Gold on Palladium - Gold Alloyed Supported Catalysts in Formic Acid Decomposition. ***ChemCatChem***, DOI: 10.1002/cctc.202100886

Abstract

In recent years, climate change triggered by carbon dioxide (CO_2) emissions has sparked the intense concern of the entire human society. Dependable and economic hydrogen energy technology is significant to achieve the net-zero emission goal. Nitrogen-based fuels offer high hydrogen capacities and safety as a chemical hydrogen storage medium, which is expected to solve the problem of hydrogen storage and transportation. The effective nitrogen-based fuels' reforming needs high-performance and affordable catalysts, and they are critical for clean and efficient utilization. This work mainly presents computational studies of transition metals, defective and doped graphene, and single-atom catalysts in terms of their electronic structures and catalytic performances. In chapter 3, the catalytic decomposition of hydrazine, the poisoning oxidation of Ir catalyst was identified and the hydrazine decomposition mechanism leading to NH_3 and H_2 was understood. Carbon defects and doped materials as non-metal catalysts were studied to catalyze NH_3 reforming; the reaction mechanisms were resolved as a function of the defect type in chapter 4. In chapter 5, transition metal catalysts with typical catalytic performance were selected, and DFT calculations and micro-kinetic models were employed to track the surface species and product composition during the reaction process, revealing the internal relationship between the surface species, catalytic activity, and reaction conditions. Based on the above work, single-atom transition metal catalysts with specific structures were modeled, and DFT calculations and micro-kinetic models were applied to study the catalytic performance of NH_3 reforming in chapter 6. And the efficient and stable single-atom catalysts are explored to improve metal atom utilization efficiency and reduce catalyst cost. This work aims at improving the understanding of the structure and catalytic behaviors of these materials and exploring their applications in hydrogen energy, which contributes to the construction of a net-zero global society.

Preface

A part of the research discussed in chapters 3, 4, and 5 have already been accepted in peer-reviewed academic publications. The major text and supplemental information of the study in Chapter 3 were published as the mechanistic research of hydrazine decomposition mentioned in “Mechanistic study of hydrazine decomposition on Ir (111)” on *Physical Chemistry Chemical Physics*, 22(7), pp.3883-3896 and authored by Xiuyuan Lu, Samantha Francis, Davide Motta, Nikolaos Dimitratos, Alberto Roldan. This work was accomplished with the aid of Samantha Francis and Davide Motta, who provided the theoretical analysis and experiment of hydrazine decomposition on IrO_2.

The research represented in Chapter 4 was initially published as “Are carbon-based materials good supports for the catalytic reforming of ammonia? ” in *The Journal of Physical Chemistry C*, *125*(29), pp.15950-15958 and authored by Xiuyuan Lu and Alberto Roldan. The python script of the microkinetic model was finished under the guidance of my supervisor Dr. Alberto Roldan and the details of the model were listed in the supporting information.

The discussion of NH_3 decomposition on noble metals was published as “Kinetic and mechanistic analysis of NH_3 decomposition on Ru (0001), Ru (111) and Ir (111) surfaces” on *Nanoscale Advances*, *3*(6), pp.1624-1632 and authored by Xiuyuan Lu, Jing Zhang, Wenkai Chen, and Alberto Roldan. This work was accomplished with the aid of Jing Zhang who provided the modeling of NH_3 decomposition on Ru(111).

Contents

Chapter 1 Introduction

1.1 Hydrogen energy

Human activities have raised the global average temperature by around 0.87 °C since the pre-industrial period (1850–1900).[1] Associated natural catastrophes have become an urgent threat to human civilization. In recent years, climate change has sparked intense concerns in the entire human society. Syukuro Manabe, the 2021 Nobel Laureate in Physics, has proved how the increased carbon dioxide (CO_2) in the atmosphere leads to increased temperatures on the earth's surface.[2,3] The development of low carbon or carbon free energy resources to decrease greenhouse gas emissions is unquestionably vital and urgent. According to the 1.5 °C temperature limit and net-zero emissions target set by the "Paris Climate Accords ", by 2030, worldwide human-caused CO_2 emissions will have to decline by roughly 45% from 2010 levels, reaching 'net zero' around 2050. Many nations have vowed to attain emission-free objectives by the middle of this century and have suggested stronger short-term pledges in the previous two years.

The use of large-scale renewable energy and the reduction of fossil energy consumption are key strategies to achieve these targets, and molecular hydrogen is a promising technology to link renewable energies. The US Department of Energy (DOE) has announced a 160-million-dollar investment to develop technologies based on hydrogen production, transportation, storage, and application to help the country achieve net-zero emissions. Subsequently, the "Hydrogen Energy Program Development Plan" proposes a comprehensive strategic framework for hydrogen energy research, development, and demonstration in the United States over the next ten years.[4] The German Federal Ministry of Education and Research (BMBF) has committed 700 million euros to three green hydrogen flagship projects: H2Giga, H2Mare, and TransHyDE, which will solve hydrogen energy generation, storage, and transportation challenges.[5] The UK National Research and Innovation Agency (UKRI)

announced that 171 million pounds will be invested in 9 projects under the "Industrial Decarbonization Challenge" program to help the UK reach carbon neutrality by 2050. Among the selected research areas, there are six onshore carbon capture and hydrogen fuel conversion projects to implement and promote in the UK's largest industrial clusters.[6] Meanwhile, a total of £4 billion investment by 2030 is being utilized to actively encourage the development of developing low- and zero-carbon hydrogen generation, storage, and delivery systems announced by the UK government.[7] The energy sector work plan grant for 2021-2022 in the EU's "Horizon Europe" plan is roughly 200 million euros, intending to research large-scale ammonia and hydrogen fuel onboard ships and clean marine ammonia fuel engines.[8]

As a renewable energy carrier, hydrogen has become a critical option to head into a sustainable society. Hydrogen can be made from a variety of substances and used in a variety of industries including the transport sector. It also has the highest energy density (1.4×10^5 kJ kg^{-1}) of any known fuel, which is around three times that of gasoline (4.3×10^4 kJ kg^{-1}). At the same time, its utilization on energy sector such as mobile, stationary, and portable power supply only produce water environmentally. Most crucially, hydrogen can be utilized for gigawatt-hours of energy storage and as a "responsive load" on the grid to provide grid stability, allowing power producers such as nuclear and renewables to be exploited more efficiently.[9,10] Indeed, hydrogen is expected to become the central chemical feedstock and energy media in the fields of renewable energy power storage and clean energy production.

However, at present, the production cost of green hydrogen (produced from water electrolysis powered with renewables) is still high, which is nearly double the grey hydrogen (produced from fossil fuels).[11,12] Moreover, liquid hydrogen needs to be compressed at 700 atm or cooled to -253 °C to be stored and transported.[13] Alternatively, the storage of hydrogen can also be realized by hydrogen compounds (hydrides) or physical adsorption in porous materials. And the safety of hydrogen storage and transportation also needs to be considered because of its broad explosion limit (4.0% ~ 75.6% in volume concentration).[14] As a result, maintaining safe and

reliable systems is a major considerable factor in hydrogen technology development.[15] Furthermore, fuel cells and other equipment using hydrogen may need maintenance because H_2 may make the hydrogen embrittlement.[16,17]

A glance at the development trend of global low-carbon energy technology innovation by "Patents and Energy Transition: Global Trends in Clean Energy Technology Innovation", which is jointly released by the International Energy Agency (IEA) and the European Patent Office (EPO) demonstrates that substantial advancements in hydrogen energy technologies are still required.[18] The popularity of hydrogen energy technology has recently increased. Although the associated patent activity has remained stable, showing that continued research funding has ensured a consistent technological invention output, a competitive hydrogen supply market still lacks.

Geographically, Europe, Japan, and the United States are the global leaders in hydrogen energy technology. Japan is in the head position of hydrogen energy research in various fields, including fuel cells, whereas Europe is an innovator in low-carbon hydrogen supply and storage systems (including electrolyzers). Germany by itself contributes to almost half of international hydrogen energy storage patents relating to Europe. Between 2010 and 2019, the number of patent applications in the sector of hydrogen energy supply and storage rose significantly, but the technology is still very demanding, especially for fuel cells. The sustainable production of green hydrogen is inseparable from renewable energy technology. In the field of renewable energy to hydrogen, Europe ranked top one in patents related to the renewable energy sector from 2010 to 2019, accounting for 28% of the entire international patent family (only Germany contributed for 11.6%). With 25% and 20%, Japan and the United States are a close second and third position, respectively. South Korea (10%) and China (8%) have increased their patent activity in the last decade and are also leaders in low-carbon energy technology development.[18]

The major technological and economic indicators for hydrogen production and storage by 2030 have also been predicted by DOE in the "Hydrogen Energy Program

Development Plan", which is shown in Table 1-1. The development of carrier materials and catalysts for hydrogen production, storage, and transportation is the key technology research and development area. In the following, the usage of chemical hydrogen carriers on hydrogen storage and delivery will be introduced as a way to improve efficiency while lowering costs.

Table 1-1. The technological and economic indicators for hydrogen energy[4]

Indicator	Values
Electrolyzer's cost	< US $300/kW
Electrolyzer's life span	> 80,000 hours
Electrolyzer's conversion efficiency	65%
Hydrogen production cost	US$ 2/kg
Consumer terminal price	~US$ 4/kg
On-board vehicular storage cost	< US$8/kWh @ 2.2 kWh kg^{-1}
Hydrogen storage capacity	7.5 wt%

As shown in Figure 1-1, there are three main processes in hydrogen energy: (1) the production of hydrogen by renewable energy, (2) the storage and transportation depending on the needs, and (3) the conversion and application of hydrogen energy by end-use consumers.

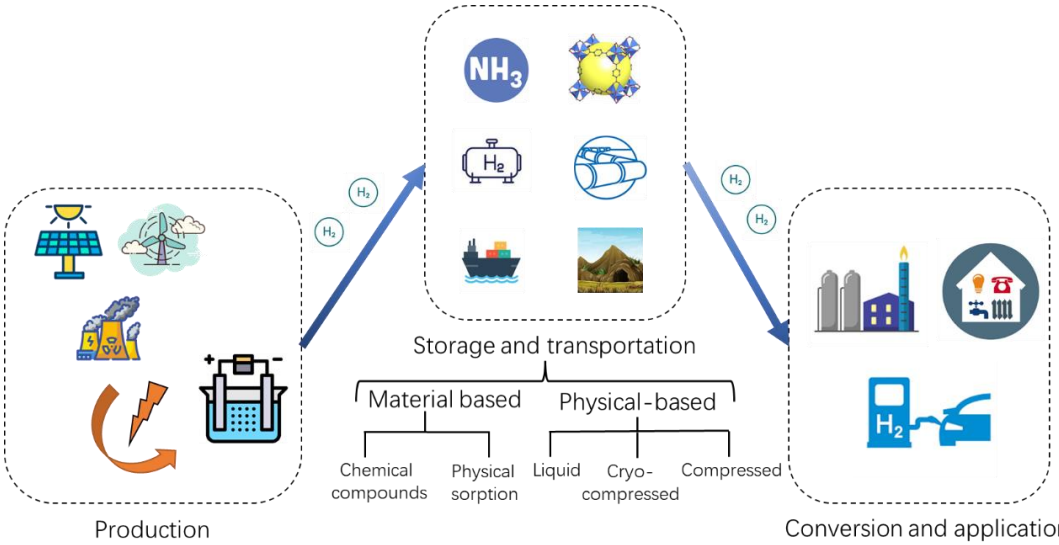

Figure 1-1. Main component and hydrogen storage technologies of the hydrogen economy

The storage and transfer of hydrogen energy serve as a link between the generation of hydrogen and its use by consumers. Hydrogen end-use applications will have various requirements putting different demands on energy-supply infrastructure,

in terms of the fueling rates, purity, and cost. Therefore, the safe, convenient, reliable, and energy-efficient hydrogen storage and transportation system are critical for the hydrogen economy, particularly when it comes to large-scale hydrogen consumption.[12]

Physical storage mainly relies on compressing and freezing the molecular gas to improve its energy density and facilitate transportation.[19,20] Compressed H_2 can be distributed by pipes, conveyed in high-pressure tanks, or transferred as a liquid via tanker truck in this manner. Hydrogen may also be carried in large quantities by rail or ship. Recently, geologic H_2 storage methods are also under development for large-scale and long-term hydrogen storage.[21,22] The advantage of physical storage methods is that the related equipment and technologies are mature. No matter for the high-pressure tanks and refrigerant systems or the tube trailers and pipelines, there is lots of experience on the operation and development, and the expenditure of infrastructures keeps reducing as a result of the rising commercial scale of the hydrogen economy.[23–26] The shortcomings are mainly on the hydrogen leakage loss (20 K boiling point) and energy input during the long- and mid-range distance transportation, as well as the concern about the safety of compressed H_2.

Hydrogen can also be densely stored and delivered at low temperatures and pressures in materials. Development of materials that incorporate high-hydrogen content as chemical compounds or by hydrogen adsorption have the potential to provide reliable and cost-effective H_2 storage with high capacities at mild temperature and pressure. Table 1-2 shows the hydrogen storage capacity of common material-based methods. Amino compounds (ammonia, ammonia borane, and hydrazine) are promising chemical carriers with their high hydrogen capacity at ambient conditions. Therefore, the development of high-efficiency synthesis/decomposition methods and catalysts of these compounds has become a crucial step for their large-scale implementation.

Table 1-2. Hydrogen storage capacities (percentage of weight wt%) and research associated with the material-based methods.

	Methods	Capacity [wt%]	References
Chemical Compounds	Ammonia	17.6	[27–29]
	Ammonia Borane	19.4	[30–32]
	Hydrazine	12.5	[33–35]
	Alanates ($LiAlH_4$)	10.5	[36,37]
	Liquid organic hydrogen carriers (Decalin)	7.3	[38–40]
	Intermetallic hydrides (Mg_2NiH_4)	3.6	[41–43]
	Formic Acid	4.4	[44–46]
Physical Materials	Hollow spheres (MOF-210)	17.6	[47–49]
	Glass capillary arrays	10.0	[50,51]
	Carbon materials (Carbon nanofiber)	6.5	[52–54]
	Metal-organic framework ($Mg_{95}Ni_5$–TiO_2/MWCNTs)	5.6	[55–58]

Once H_2 is stabilized in chemical compounds or physical adsorption, the safe transportation of hydrogen storage materials can be accomplished using conventional bulk commodities transportation methods. Although there is no need to re-develop new storage and dispensing system, these materials require temperature and pressure gradients to adsorb H_2 or catalytic reactions to transform them into H-carrier chemical compounds, which can result in considerable round-trip energy losses. Therefore, the essential requirement of hydrogen storage technologies is the development of novel methods increasing the conversion efficiency.

1.2 Non-carbon chemicals for hydrogen storage

At present, hydrogen storage technology is unable to fulfill all the requirements of practical application at the same time, *i.e.* storage density, operating temperature and pressure, reversible cycle performance, and safety. Since the construction of a hydrogen fuel transportation and injection network system requires a significant investment, and even though it has the disadvantages discussed above, research on

H-carriers is a hot topic aiming to develop high energy density fuels like methanol, formic acid, ammonia, and hydrazine. Table 1-3 lists the important properties related to the practical utilization of some carbon and nitrogen fuels. The key points of contention between carbon-based fuels and non-carbon fuels are products, health and safety, energy input, and hydrogen capacity.

Table 1-3. Comparison of common hydrogen storage compounds (IDLH: Immediately dangerous to life or Health concentration)[59,60]

Chemical Compounds	Products	IDLH (ppm)	Vapor pressure (bar at 298 K)	Explosive limits (vol% in the air)	ΔH^{θ} (kcal·mol^{-1} H_2)	Capacity (wt%)	Ignition energy (mJ)
Gasoline	C/NO_x	1100	0.42	1.4-7.6	-	-	0.14~1.35
Diesel	C/NO_x	1100	0.50	1.3-6.0	-	-	0.23
$H_2O(l)$	O_2	-	0.03	-	68.9	11.1	-
$CH_4(H_2O)$	CO_2	40000	62.7	5.0-15.0	13.9	15.4	0.4~1.3
$CH_3OH(l)$	CO	6000	0.17	5.5-44.0	20.7	12.5	~0.14
HCOOH(l)	CO_2	30	0.06	18.0-51.0	7.8	4.3	-
$NH_3(l)$	N_2	300	10.03	16.0-25.0	7.4	17.6	680
$N_2H_4(l)$	N_2	50	0.02	4.7-100.0	0.2	12.5	-

Hydrogen is commonly produced by reforming carbon-based fuels, where the CO_x production through the water-gas shift reaction is inevitable. This may poison the electrode in fuel cells, for example, the strong combination between CO and the Pt anode reduces its performance and lifespan.[61–63] As a result, the hydrogen produced from carbon-based liquid fuels reforming is usually subjected to high and low-temperature water-gas shift reactions as well as selective oxidation before the end-use. These pretreatment processes reduce the concentration of CO and make the hydrogen production process of on-board mobile steam reforming more complex and unsuitable for various application scenarios.[64,65] Only 0.2 ppm carbon oxides at 10 °C will cause a damage of Pt catalysts which is partially recoverable.[66] Compare with carbon, the tolerance of ammonia is 3~8 ppm to Pt at 70 °C and the damage is recoverable.[67] Moreover, the removal of ammonia is easier than carbon oxides in the hydrogen atmosphere. Although the explosion limits of carbon-based fuels are relatively wide, there is usually a little risk to human health. Considering the reformation

energy input and their hydrogen capacity, carbon-based fuels are not as cost-effective as nitrogen-based fuels.

Figure 1-2 shows the hydrogen production processes from N compounds and their energy flow. As a chemical hydrogen storage medium, N-based fuels have high hydrogen capacities. The hydrogen capacity of ammonia (17.6 %wt), as the most common N-based fuel, is higher than that of most carbon-based fuels. Moreover, their decomposition products are H_2 and N_2, which have no negative effect on the electrodes, giving a broad application prospect in hydrogen technologies.[27,28]

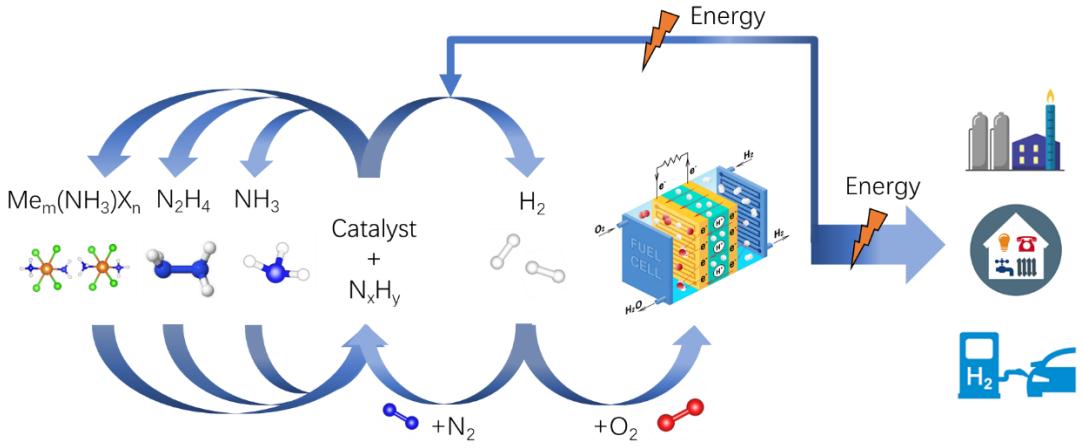

Figure 1-2. Schematic diagram of hydrogen generation from amino compounds and energy flow

One of the dark clouds hindering N-based fuels implementation is the public concern of safety and health since they are usually classified as toxic substances (Table 1-3). They, however, represent a substantially lower danger of accidental combustion or explosion than hydrogen (4.0-74.0%) and other fuel due to their high ignition energy. Legislation and exposure duration can help to restrict the health concerns associated with N-based fuels. Specifically, for ammonia, the safety limit set between 8 hours exposure time-weighted average of 25 and 50 ppm with dangerous consequences for short-term exposure to concentrations above 300 ppm.[68] To alleviate the health risk associated with N fuel leaks, solid ammonia storage technologies are also developed. For instance, suitable metal ammine salts (e.g., $Mg(NH_3)_6Cl_2$ and $Ca(NH_3)_8Cl_8$) illustrate the potential of reversible NH_3 storage with toxicity lower than

that of gasoline, moreover, the H_2 energy efficiency of the system is ~70% in the energy balance analysis.[69,70] The energy required to promote the decomposition of ammonia or hydrazine, measured per mole of hydrogen, is lower than that required for the chemical conversion of most other hydrogen-containing media. In addition, ammonia is relatively less flammable and easier to liquefy (the liquefaction pressure at 20 °C is 0.8MPa) than hydrogen. Ammonia storage which relies on the existing equipment and technology costs 0.54 \$/kg H_2 over 182 days, compared to 14.95 \$/kg H_2 for pure hydrogen storage.[71] Hydrazine hydrate ($N_2H_4 \cdot H_2O$) is stable at room temperature, which is convenient for storage and transportation. In general, as carbon-free hydrogen storage sources, N-based fuels have advantages in cost, energy density, and practical deployment. It has long-term and extensive practical experience in production and transportation, which provides a strong guarantee for the wide application as hydrogen storage media.

1.3 Hydrazine and ammonia in hydrogen energy

1.3.1 Hydrazine and its reforming

Hydrazine (N_2H_4) is made of two NH_2 groups, each with one lone pair electron on the N atom. The stable configurations of N_2H_4 are shown in Figure 1-3 that the gauche is the most favorable at DFT level.[72]

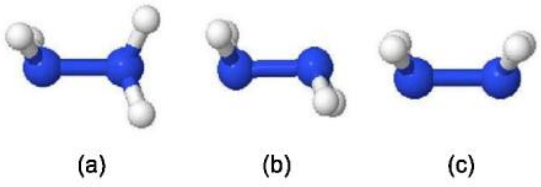

Figure 1-3. Hydrazine molecular structure in (a) gauche, (b) anti, and (c) cis configuration.

Pure hydrazine is an inorganic colorless flammable compound with an ammonia-like odor. Compared with hydrazine hydrate, hydrazine has very reactive chemical properties, *e.g.,* it is easy to explode in the air, especially in contact with metals. For this reason, it is usually handled and transported as hydrate. Hydrazine hydrate is alkaline and corrosive with boiling and flashpoints at 118 °C and 73 °C respectively.[59]

When hydrazine hydrate combines with a carbonyl group, it generates a stable solid hydrazone that can release hydrazine by reacting with warm water.[73] This method is used to deliver and dispense hydrazine safely.

At present, the large-scale industrial production of hydrazine is well understood, *i.e.*, the formation of the N-N bond is the key step. Hydrazine production processes can be grouped into three categories depending on the different formation principles of the N-N bond: (1) Chloride oxidants process; (2) Peroxide process; (3) Oxygen process. The chloride oxidants process, firstly developed by Olin Raschig in 1907, produces hydrazine from sodium hypochlorite and ammonia. This method relies on the reaction of chloramine with ammonia to create the nitrogen–nitrogen bond as well as a hydrogen chloride byproduct (*e.g.*, $NaOCl + 2NH_3 \longrightarrow H_2NNH_2 + H_2O + NaCl$);[74] Urea ($(NH_2)_2CO$) can also be reactant instead of ammonia ($(H_2N)_2CO + NaOCl + 2NaOH \longrightarrow N_2H_4 + H_2O + NaCl + Na_2CO_3$).[75] The peroxide process employs ammonia and hydrogen peroxide as the starting materials in the presence of ketone as catalysts ($2NH_3 + H_2O_2 \longrightarrow H_2NNH_2 + 2H_2O$). Compared with chloride oxidants process, the peroxide process does not produce salt as by-products.[76] The oxygen process only uses ammonia and oxygen in the air flowing through the reactor with a built-in solid catalyst, and then performs a heterogeneous catalytic reaction ($2NH_3 + 0.5O_2 \longrightarrow N_2H_4 \cdot H_2O$). The oxygen process produces high concentration hydrazine hydrate in a single step without any by-product, which has great development potential and application prospects.[77]

Hydrazine is an important raw material in the manufacturing of fine chemicals. It is commonly utilized in the production of commercial chemical goods including medications, pesticides, and water treatment agents.[78–80] In addition, it was used as rocket propulsion fuel as early as during World War II, and now, it has been used as an alternative to hydrogen in fuel cells experimentally.[81,82] To synthesize metal powder materials from solution, hydrazine can be employed as a reducing agent producing high purity and consistent scale metal crystals.[83–85]

1.3.2 N_2H_4 catalysts

N_2H_4 contains 12.5 wt% of hydrogen but its total decomposition is only achieved in the presence of catalysts. The catalysts' transformation from monometal to alloy and the employment of alkaline materials as catalysts' support are two important strategies to promote catalytic hydrazine decomposition.

Initially, monometallic nanoparticles (NPs) catalysts are the main research objects. Cho *et al.* synthesized an Ir(9-35 wt%)/γ-Al_2O_3 catalyst with the average particle size of 2 nm by the multi-step impregnation method.[86] They found that, although it can catalyze hydrazine into hydrogen-rich gas at room temperature, the yield of H_2 at low temperature (< 573K) is not satisfied. To investigate the catalytic performance of monometallic nanoparticles on the hydrazine decomposition, Xu *et al.* carried out a series of research work and prepared metal nanoparticle catalysts by chemical reduction method, including Rh, Ru, Ir, Pd, Pt, Co, Ni, and Fe.[33,87] However, the catalytic activity and H_2 selectivity of these monometallic catalysts are poor. The Rh NPs with a size of 16 nm had the highest hydrogen selectivity (43.8%) in the catalytic decomposition of hydrous hydrazine, whereas the Co, Ru, and Ir NPs only had a 7% selectivity and Cu, Ni, Fe, Pt, and Pd, were found to be inactive. Meanwhile, the investigation of the catalytic decomposition in the gas phase demonstrates that the presence of H_2O has a significant impact on the activity and selectivity due to the hydrogen bonds between H_2O and N_2H_4 molecules.[88]

Except for the composition of the catalysts, the reaction temperature is also crucial for the activity and selectivity in the hydrazine catalytic decomposition. The catalytic activity will be enhanced by an increase in temperature, however, the effect on H_2 selectivity will differ depending on the metal, *e.g.*, the catalytic hydrous hydrazine decomposition does not happen on Ni NPs at room temperature and showed catalytic activity with an H_2 selectivity of 33% at 323 K, while with the temperature increase from room temperature to 343K, the selectivity of H_2 on Rh NPs decreases from 43.8 % to 34 %.[89,90]

Alloy nanoparticle systems usually outperform monometallic materials in terms of catalytic activity and selectivity due to their unique surface electronic states and geometric arrangements. To find a better catalyst for hydrazine decomposition and further reduce the catalysts' cost, a variety of bimetallic and trimetallic NP catalysts have been developed so far. Table 1-4 compares the hydrous hydrazine catalytic decomposition activity of alloy catalysts with different compositions.

Liu *et al.* discovered that the hydrogen selectivity of small alloyed nanocages was equal to that of the large ones (67 %), showing that the bimetallic catalyst's surface structure influenced catalytic selectivity more than the surface area.[91] In the study of Rh-Ni catalyst at room temperature, Sanjay and Qiang Xu found that, although Ni itself was inactive to the decomposition of hydrous hydrazine and Rh itself had a low hydrogen selectivity, the alloy of Ni–Rh was able to drastically enhance the hydrogen selectivity reaching 100% at Ni/Rh = 1:4 composition. However, as the amount of Rh in the system was raised, hydrogen selectivity dropped and finally stayed at 43%.[92] It is found that even a very low content of Ir in the Ni–Ir bimetallic nano-catalyst gives an excellent catalytic performance.[93,94] Similarly, although Ni and Pt are inactive for hydrous hydrazine decomposition, Ni–Pt bimetallic catalysts have good catalytic activity and hydrogen selectivity in general. As a result, a Ni–Pt bimetallic NP catalyst is a unique catalyst that combines two inactive components for high catalytic activity.[95] Due to the coexistence of two metals on the surface and the presence of intermetallic Ni–Pd bonds, Ni–Pd bimetallic NP catalysts demonstrated significantly improved catalytic performance. The catalytic performance of $Ni_{0.60}Pd_{0.40}$ had the maximum hydrogen selectivity of 82%.[96,97] Co-noble metals, Fe-noble metals, and Cu-based nano-catalysts also have been investigated; however, the H_2 selectivity on these catalytic systems at room temperature is lower than 30%.[33] In terms of noble metal-free catalysts, Singh *et al.* demonstrated that $Ni_{0.50}Fe_{0.50}$ exhibited 81% hydrogen selectivity without NaOH at 343 K and when NaOH (0.5 M) was added to the reaction, the hydrogen selectivity improved to 100%.[98] With and without NaOH, the hydrogen selectivity of the Ni_2B catalytic system was 90.0 % and 72.0 %, respectively.[99]

Several trimetallic catalysts also have been investigated for hydrogen production by hydrazine decomposition. Wang *et al.* found that Mo acted as an electron donor for Ni and Fe atoms, which transformed Ni–Fe–Mo NP catalyst to endow itself with high catalytic activity for hydrogen generation from hydrous hydrazine decomposition.[100] Bhattacharjee *et al.* carried out a detailed investigation on the unsupported Ni-Fe-Pd system. The results show that at 298 K, the hydrogen selectivity of $Ni_{30}Fe_{30}Pd_{40}$, $Ni_{35}Fe_{35}Pd_{30}$, and $Ni_{40}Fe_{40}Pd_{20}$ was 100% and the $Ni_{30}Fe_{30}Pd_{40}$ performed the best reaction rate among these three catalysts at 318 K. $Cu@Fe_5Ni_5$ NPs at 8.5 nm had 100% hydrogen selectivity, outstanding activity, and stability for the breakdown of hydrous hydrazine, according to the work by Zhang and colleagues.[101] In the literature experiments, the metallic composition, temperature and the size of the particles are main parameters influence the H_2 selectivity. Although not all the experimental conditions are totally same in the Table 1-4, such as the addition regent, it shows the research potential of alloy systems for hydrous hydrazine catalytic decomposition by comparing and discussing their performance.

Table 1-4. The catalytic activity of bimetallic and trimetallic NP catalysts for the decomposition of hydrous hydrazine.

Bimetallic	Temperature/K	Size/nm	H_2 selectivity/%	Ref.
Pd-Ir(nanocage, octopods)	298	14-25	67	[91]
Rh-Ni ($Rh_{0.80}Ni_{0.20}$)	298	3	100	[92]
Ir-Ni ($Ir_{0.05}Ni_{0.95}$)	298	5	100	[93,94]
Pt-Ni ($Pt_{0.07}$ $Ni_{0.93}$)	298	5	100	[95]
Pd-Ni ($Pd_{0.40}Ni_{0.60}$)	323	5	82	[96,97]
Ni-Fe ($Ni_{0.50}Fe_{0.50}$)	343	10	81	[98]
Ni-B (Ni_2B)	298	-	72	[99]
Trimetallic				
Ni–Fe–Mo (NiFeMo)	323	<5	100	[100]
Ni–Fe–Pd ($Ni_{0.4}Fe_{0.4}Pd_{0.2}$)	298	2-3nm	100	[102]
$Cu@Fe_5Ni_5$	298	8.5	100	[101]

Immobilizing nanoparticles on a support surface is used, in practice, to prevent the aggregation and agglomeration of the nanoparticles during catalysis cycles, which reduces the surface area and active sites. In addition, for the catalyst of hydrazine decomposition system, the introduction of alkaline supports can also offer a basic

chemical environment to significantly promote hydrogen selectivity.

Table 1-5. The catalytic activity of SiO_2, Al_2O_3, and CeO_2 supported catalysts for the decomposition of hydrazine.

	Temperature/K	Conversion/%	H_2 selectivity/%	Ref.
SiO_2 support				
Ru (8.0 wt%)	673	100	~100	[88]
Rh (8.0 wt%)	723	100	100	[88]
Ir (8.0 wt%)	773	100	~100	[88]
Ni (12.0 wt%)	303	40	>90	[88]
Pd (12.0 wt%)	303	<10	>90	[88]
Pt (12.0 wt%)	353	~100	>90	[88]
Al_2O_3 support				
Ir (9-35wt%)	298	100	6	[86]
Ni (38.3 wt%)	303	-	93	[103]
$NiIr_{0.016}$ (Ir: 2.0 wt%)	303	-	99	[103]
CeO_2 support				
Ni (6.0 wt%)	387	~100	~100	[106]
$Ni_{0.6}Pt_{0.4}$ (Pt: 2.4 wt%)	303	~100	~100	[105]

As shown in Table 1-5, Zheng *et al.* studied several supported group VIII (8,9,10) metal catalysts and discovered that, while Ni, Pd, and Pt nanoparticles performed poorly in hydrazine decomposition, Ni/SiO_2, Pd/SiO_2, and Pt/SiO_2 all catalyzed hydrazine reforming with good H_2 selectivity at low temperatures. Similarly, at high temperatures, hydrazine decomposes rapidly into H_2 and N_2 over SiO_2 supported Ru, Co, Rh, and Ir catalysts.[88] Al_2O_3 is an amphoteric support for catalysts as well. Compared to Ni/Al_2O_3, $NiIr_x/Al_2O_3$ catalysts displayed a 6-fold improvement and the H_2 selectivity over 99%.[103] He *et al.* also employed extended X-ray absorption fine structure measurements to investigate Ni/Al_2O_3 catalysts modified by Pt and Au. The results showed that, compared with Au, Ir and Pt were more easily alloyed with Ni on Al_2O_3 since the coordination numbers of Ir-Ni and Pt-Ni were larger. [103] He *et al.* prepared Ni/Al_2O_3 and Ni-Al hydrotalcite catalysts using the precipitation and impregnation methods and determined the relationship between the basic site and the catalyst's performance. They concluded that the strong metal-support interaction can promote the fracture of the N-H bond, thereby improving the catalyst's hydrogen production selectivity.[104] Jiang *et al.* reported a $Ni_{0.6}Pt_{0.4}/CeO_2$ bimetallic catalyst

synthesized by the one-pot evaporation-induced self-assembly method. The conversion of hydrazine and H_2 selectivity reached 100% at room temperature.[105]

The catalytic decomposition of hydrazine is affected by several factors, such as catalyst type, reaction temperature, and additives, which will result in the change of hydrogen production selectivity and reaction rate. The decomposition reaction involves several steps and several reaction intermediates. The mechanism still needs to be fully understood from both experiment and atomic views.

There are two hydrazine catalytic decomposition mechanisms on metal catalysts depending on the types of bonds broken at the first step. These are the incomplete decomposition mechanism (N-N breaking) and the complete decomposition (N-H breaking), as shown in Figure 1-4. From the bond cleavage energy (286 kJ mol^{-1} for N–N bond cleavage and 360 kJ mol^{-1} for N–H bond cleavage), it is thought that the N–N bond scission is more accessible than N–H bond cleavage.[33] However, the metal-H interaction on the catalyst's surface may decrease the N–H cleavage energy barrier.[88]

When N_2H_4 is adsorbed on a bridge site of the metal catalyst's surface, *e.g.*, Fe, Ni, Cu, and Ir, the breaking of the N-N bond to produce NH_2 are more favorable thermodynamically and kinetically.[107,108] Then the NH_2 group will interact and promote the N_2H_4 dehydrogenation to produce NH_3, and eventually, the N^* will recombine into N_2.

In the complete decomposition route, the metal–H bond is favored over the metal–N, and the N–H cleavage energy barrier becomes lower than that of N–N cleavage, *e.g.*, on Pt.[109] When the N–H bond cleavage is completed, H* recombine into H_2 and desorbed from the surface together with N_2.

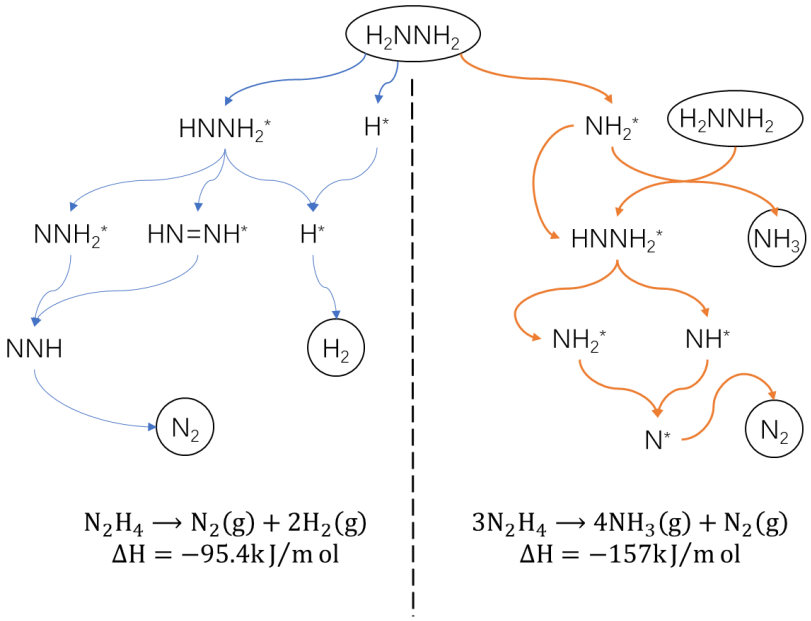

Figure 1-4. Schematic illustration of the two hydrazine catalytic decomposition mechanisms.

1.3.3 Ammonia and its reforming

Ammonia (NH_3) is a compound containing only nitrogen and hydrogen with a molecular mass is 17.03 Da. It is colorless at normal temperature and pressure with a strong pungent smell. It turns into liquid ammonia with a density of 0.682 $g \cdot m^{-3}$ when the pressure is 1 atm and the temperature is 240 K (boiling point). A pressure of 1000 kPa is required to liquefy it at 298 K. The nitrogen atom in the ammonia molecule presents as sp^3 orbital hybridization, with five valence electrons (two lone pair electrons and three unpaired electrons). The three unpair electrons of the nitrogen atom combine with the valence electrons of the three hydrogen atoms to generate the ammonia molecule. The three N-H bonds are not in the same plane due to the repulsive effect of lone electron pairs, but at an angle of 107 ° 13', and the molecular space structure is triangular cone type with high polarity (C_{3v}).

Haber Bosch needs a large amount of hydrogen and nitrogen and do not produce CO_2 in the process. However, today, large part of hydrogen is produced by natural gas reforming and water gas shift, which result serious CO_2 emissions. The Haber–Bosch method for commercial ammonia synthesis generates more than 146 million tons of ammonia per

year and consumes 1–2 % of world energy.[110] Over a Fe-based catalyst, the Haber–Bosch process produces NH_3 by molecular hydrogen and nitrogen at 650-750 K and 50-200 bar ($N_2 + 3H_2 \longrightarrow 2NH_3, \Delta H^{\Theta} = -91.8kJ\ mol^{-1}$).[111,112] The industrial process, however, has some drawbacks, including the high cost of hydrogen, severe reaction conditions, significant energy consumption, and a considerable CO_2 emission. The intensive consumption of fossil energy and the serious impact on the ecological environment urge human beings on developing sustainable green ammonia synthesis processes. Therefore, researchers are committed to developing several methods, such as the biochemical, photocatalytic, plasma chemical and electrochemical method.

The biochemical method employs nitrogenase enzymes to fix nitrogen and generate NH_3 under mild conditions.[113] High-performance photocatalysts for the nitrogen reduction reaction (NRR) employ light to push e^- into the N_2 antibonding.[114,115] By producing very powerful electrons, plasma-based techniques can activate N_2 without the need for a catalyst to generate NH_3.[116,117] In addition, electrocatalytic ammonia synthesis can be carried out at room temperature by electrocatalytic reduction of N_2 molecule and has a wide range of energy (wind energy, solar energy, etc.) and reactants (N_2 and H_2O) sources.[118–121] These novel synthesis methods are not only promising for sustainable green NH_3 generation, but they are also instructive for catalysis studies of other chemical reactions.

Ammonia is an essential bulk chemical commodity for social development as an agricultural fertilizer, industrial raw material, and energy source. Specifically, the main application of ammonia is for fertilization, e.g., around 88 % of ammonia was utilized as fertilizer in the United States annually.[122] It also can be applied as the precursor to nitrogenous compounds, i.e., HNO_3, hydrazine, phenol, acrylonitrile, and others. Furthermore, its high H_2 capacity triggers the comprehensive investigations of ammonia fuel cells and ammonia combustion engines.[28,123–126]

The utilization of ammonia catalytic decomposition involves three scenarios, environmental protection, protective gas, and fuel cell hydrogen supply. In the chemical industry, most of the nitrogen in biomass, coal, and petroleum is converted into NH_3 in

the process of gasification and refining. The by-product NH_3 needs to be decomposed, otherwise, it will poison the catalysts of other reaction processes, corrode the equipment and pollute the air. Meanwhile, ammonia as a protective gas can be used in steel, nonferrous metal heat treatment, and float glass manufacture.[127,128] Most importantly, for hydrogen fuel cells or ammonia fuel cells, ammonia catalytic decomposition supplies a carbon-free fuel.

The reversible reaction of ammonia synthesis and decomposition is one of the most well-studied catalytic reactions. Normally, it is speculated the best synthesis catalyst can also become the best decomposition catalyst. However, Boisen *et al.* pointed out that due to the different reaction environments and rate-determining elementary steps between synthesis and decomposition of ammonia, the above speculation is not fully applicable.[129]

1.3.4 NH_3 catalysts

Decomposition catalyst. In the past two decades, the research of ammonia decomposition catalysts has attracted extensive attention. Next, I will introduce mono-metal, alloys, single-atom, and transition metal nitride catalysts for catalytic ammonia decomposition.

Table 1-6 summarised the catalytic activity of monometallic NP catalysts for the decomposition of ammonia on different support materials. Ganley *et al.* studied the turn-over frequency (TOF) of 13 different monometallic catalysts supported on Al_2O_3 and found the catalytic activity is in the sequence of Ru > Ni > Rh > Co > Ir > Fe ≫ Pt > Cr > Pd > Cu.[130] The investigation of monometallic catalysts supported on carbon nanotubes (CNTs) shows the activity order as Ru > Rh ≫ Ni > Pt ≫ Pd > Fe.[131] And when it comes to $MgAl_2O_4$ support, the catalysts' performance is as Ru > Co > Ni > Fe > Cu.[129] Although the catalytic sequence is varied due to the reaction condition and support materials, it is clear that Ru is the best noble metal for the ammonia decomposition, followed by Fe, Ni, Co.

Table 1-6. The catalytic activity of monometallic NP catalysts for the decomposition of ammonia on different support materials.

Al_2O_3 support	Temperature(K)	TOF(s^{-1})	Rate of reaction (mmol min^{-1} g_{cat}^{-1})	Ref.
Ru (0.5 wt%)	853	6.85		[130]
Ni (1.0 wt%)	853	4.21		[130]
Rh (0.5 wt%)	853	2.26		[130]
Ir (1.0 wt%)	853	1.33		[130]
Fe (1.0 wt%)	853	7.86×10^{-1}		[130]
Pt (1.0 wt%)	853	3.27×10^{-1}		[130]
Cr (1.0 wt%)	853	2.20×10^{-2}		[130]
Pd (0.5 wt%)	853	2.57×10^{-2}		[130]
Cu (1.0 wt%)	853	1.90×10^{-2}		[130]
CNTs				
Ru (0.5 wt%)	673	1.5	2.0×10^{-3}	[131]
Ni (0.5 wt%)	673	1.5×10^{-1}	1.2×10^{-4}	[131]
Rh (0.5 wt%)	673	1.5×10^{-1}	2.1×10^{-4}	[131]
Pd (0.5 wt%)	673	3.3×10^{-2}	5.6×10^{-5}	[131]
Fe (0.5 wt%)	673	2.2×10^{-2}		[131]
Pt (0.5 wt%)	673	4.1×10^{-2}	7.3×10^{-5}	[131]
SiO_2 support				
Ir (10 wt%)	973		30.6	[136]
Ni (10 wt%)	923		21.1	[136]
Ru (10 wt%)	923		30.9	[136]
$MgAl_2O_5$				
Co (5.2 wt%)	773		1.7×10^{-1}	[129]
Cu (5.4 wt%)	773		1.1×10^{-1}	[129]
Fe (4.6 wt%)	773		1.0×10^{-1}	[129]
Ni (5.0 wt%)	773		1.2×10^{-1}	[129]
Ru (8.0 wt%)	773		3.7×10^{-1}	[129]

On Ru nanoparticles, the maximum probability for the low-coordinated surface atom involve edge between NPs' facets is found for particles of 1.8-2.5 nm, and for particles larger than that, the probability for such sites monotonically decreases. This behavior explains why Ru catalytic activity first increases and lately decreases with the average particle size for the NH_3 reforming.[132] The surface acidity, conductivity, and metal-support interaction also have a significant impact on the ammonia decomposition performance of the supported Ru catalyst. It was found that the stronger the basicity and conductivity of the support, the easier the N_2 desorption from the

surface, and the higher the ammonia decomposition activity of the Ru catalyst.[131] Adding suitable additives to Ru-based catalysts is another typical technique to boost their activity. Kowalczyk *et al.* investigated the effect of K, Cs, and Ba on the Ru catalyzed ammonia decomposition and found that electrons transferred from the additives to the Ru surface, which promoted the desorption of binding N atoms on the surface and improved the ammonia decomposition rate of Ru based catalyst.[115,133] In addition, nano Ru catalysts with core-shell structure (Ru@SiO_2 and Ru@Ni) have also been developed to deal with the agglomeration phenomenon caused by high temperature during ammonia decomposition.[134,135]

The high cost of Ru catalyst makes it unsuitable for large-scale industrialization. Fe-based catalysts are attractive alternatives that are widely used in industrial ammonia synthesis. Kowalczyk *et al.* investigated the effect of potassium additives on the catalytic activity of Fe-based catalysts and found that N is the dominant species on the catalysts. Potassium additives promote the activity of ammonia decomposition on Fe.[137,138] Ohtsuka *et al.* studied the thermal catalytic mechanism of ammonia decomposition on Fe and demonstrated that NH_3 and Fe form Fe_4N, Fe_3N at the beginning, and the desorption of N_2 molecule happened at above 350 °C.[139,140] Fe_2O_3 (12 wt%) supported on mesoporous materials (CMK-5 and C/SBA-15) showed an ammonia conversion of ~100 % at 700 °C. Core-shell structures Fe@SiO_2 showed high ammonia decomposition activity and high-temperature stability.[141,142]

Ni and Co are also transition metals with the potential to be commercial ammonia decomposition catalysts. Zhang *et al.* demonstrated that only Ni^0 particles with an average size of less than 2.9 nm exhibited significant activity, with 2.3 nm being the optimal size.[143] Despite this, a negligible amount of ammonia converts to H_2 on the carbon-supported Ni catalysts at 500 °C, whereas mesoporous SBA-15 and Al_2O_3 support for Ni can achieve 578 and 496 mol_{H2} mol_{Ni}^{-1} h^{-1} at the same temperature, respectively.[144,145] Adding K additives had no obvious effect on the NH_3 decomposition catalytic activity of Ni/SiO_2.[146] Co has weaker nitrogen binding than Fe, hence cobalt-based catalysts have higher catalyst activity of NH_3 decomposition, especially at low

reaction temperatures.[147] A study reported that 5 wt% Co incorporated on silicate has an ammonia conversion of 73% at 600 °C.[148] Co supported on multi-walled carbon nanotubes (MWCNTs) has higher activity than Fe and Ni catalysts. At 500 °C, Co converts 60% ammonia, whereas Fe and Ni convert 14.8% and 25.4%, respectively.[149] K will promote the performance of Co-based catalysts while Cr and Mn resulted in decreased activity.[150]

Similar to the hydrazine decomposition, bimetallic catalysts' activity to ammonia decomposition varies from the synergistic effects of the components. Table 1-7 shows the catalytic activity of CNTs, Al_2O_3 and SiO_2 supported bimetallic catalysts for ammonia decomposition. Zhang and co-workers synthesized a Fe-Co alloy nanoparticle supported on CNTs and discovered that at 873 K, it exhibits a reaction rate comparable to Ru/CNTs.[151] In addition, bimetallic Fe-Mo, Fe-Ni, and Co-Mo supported on Al_2O_3 have shown good performance, *e.g.* the conversion of NH_3 reaches 100% at 773 K on Fe_4Ni/Al_2O_3.[152–154] The catalytic activity of Co-Mo catalyst supported on SiO_2 is not as good as that supported on Al_2O_3 with an NH_3 conversion 14% at 773 K.[155]

Table 1-7. The catalytic activity of CNTs, Al_2O_3, and SiO_2 supported bimetallic catalysts for the decomposition of ammonia.

	Temperature (K)	Conversion (%)	Rate of reaction ($mmol_{H2}$ min^{-1} g_{cat}^{-1})	Ref.
$Fe_5Co/CNTs$ (Co: 0.83 wt%)	873	49	3.0×10^{-3}	[151]
$FeMo/Al_2O_3$ (Mo: 5 wt%)	873	78	9.8×10^{-3}	[152]
Fe_4Ni/Al_2O_3 (Ni: 2 wt%)	773	100	9.5×10^{-4}	[153]
$CoMo_{1.6}/Al_2O_3$ (Co: 1.85 wt%)	773	56	4.5×10^{-3}	[154]
$Co_{2.3}Mo/SiO_2$ (Co: 3.47 wt%)	773	14	2.8×10^{-4}	[155]

Aside from traditional metallic catalysts, single-atom catalysts (SACs), in which the active metal species reside as isolated single atoms anchored on the support, have emerged as a new frontier in catalytic ammonia decomposition in the last decade

(Table 1-8). With unique structures, SACs not only exhibit a high level of activity and selectivity, but they have the maximum catalyst-atom efficiency, as they use all the atoms forming the site. In other words, its appearance signifies a new approach to balancing catalyst cost and efficiency. So far, there is little research on ammonia decomposition by SACs, however, their activities for ammonia decomposition could be deducted by the catalytic effect on the ammonia synthesis reaction. Noticeably, Wang *et al.* identified N-coordinated Fe atoms on nitrogen-doped carbon support (Fe/NC) as high-selective catalysts with a faradaic efficiency of over 56.55 % for nitrogen reduction reaction (N2RR). Molecular dynamic simulations illustrated that the great selectivity of the N2RR over the hydrogen evolution reaction (HER) was ascribed to the low energy barrier of N_2 splitting toward Fe/NC.[156] This also shed light on the catalytic decomposition of ammonia by SACs with tunable electronic configuration.

It is generally believed that catalytic ammonia decomposition reaction on metals mainly includes the following steps: 1) Chemical adsorption of NH_3 on metallic active sites; 2) Ammonia (NH_3^*) step by step dehydrogenation to form N^* and H^*; 3) adsorbed N^* and H^* recombination and desorption.[157–162] Depending on the rate-determining steps, two mechanisms have been proposed.

Table 1-8. The catalytic activity of SACs for the ammonia electrochemical synthesis.

Catalysts	Electrolytes	Yield rate	Faradaic efficiency (%)	Ref.
Au/C_3N_4 (0.15 wt%)	5 mM H_2SO_4	1305 $\mu g \cdot h^{-1} mg_{Au}^{-1}$	11.1	[163]
Ru/NC (0.18 wt%)	50 mM H_2SO_4	120.9 $\mu g \cdot h^{-1} mg_{cat}^{-1}$	29.6	[164]
Fe/NC (1.2 wt%)	0.1 M NaOH	7.48 $\mu g \cdot h^{-1} mg_{cat}^{-1}$	56.55	[156]
Co/NPS (1.4 wt%)	0.05 M Na_2SO_4	14.62 $\mu g \cdot h^{-1} cm^{-2}$	10.5	[165]
Cu/NC (5.31 wt%)	0.1 M NaOH/HCl	53.3/49.3 $\mu g \cdot h^{-1} mg_{cat}^{-1}$	13.8/11.7	[166]

For the noble metals, Ru, Rh, Ir, etc., if T > 750 K the rate-determining step is splitting the N-H bond. Tsai and Weinberg found that the rate-determining step of NH_3 decomposition on Ru(0001) is temperature-dependent; when temperatures are above 750 K, the cleavage of the N−H bond in ammonia becomes the slowest step.[167] Ganley *et al.* calculated the desorption rate of nitrogen using the nitrogen bond energies of

several metals and found that, on Rh, Pt, Ir, Cu, Pd surfaces, the TOF decreases with the increase of activation energy of N-H bond breaking.[130] Bradford *et al.* proposed that the NH bond cleavage and recombinative nitrogen desorption are the slowest kinetic processes based on their research of ammonia decomposition on C and Al_2O_3 supported Ru particles.[168]

For the non-noble metals, Fe, Co, Ni, *etc.*, the recombinative desorption of N_2 determines the rate of the reaction. Chellappa *et al.* studied ammonia decomposition kinetics over Ni-Pt/Al_2O_3 at temperatures ranging from 520 to 690 °C and concluded that recombinative nitrogen desorption limits the rate of ammonia breakdown.[169] Duan *et al.* studied the decomposition mechanism of ammonia on Fe(110), Co(111), and Ni(111) by DFT. They found that, after ammonia dehydrogenation, the N* atom exists in the hollow site of the catalyst, and the size of the energy barrier of N* atom recombination desorption plays a decisive role in the reaction rate. Compared with Ni and Co catalysts, the desorption barrier of Fe is larger, resulting in higher N* coverage and blocking the catalytic sites of Fe.[160]

1.4 Research contents

Through the previous literature review on hydrogen energy, it can be found that the decomposition of nitrogen-based fuel as hydrogen storing media is a key technology for hydrogen energy implementation. Hence, the discovery of catalysts with great catalytic performance and affordable price is critical for applying nitrogen-based fuel to hydrogen generation. However, catalysts for nitrogen-based fuel reforming, the investigation of the design, microstructure, and mechanism of such catalysts still lack breakthroughs. To improve the related theoretical research, the main research work in this study is summarized as follows:

This research work was mainly carried out in the following aspects：

1. In the study of the catalytic decomposition of hydrazine, the poisoning oxidation of Ir catalyst was identified and the hydrazine decomposition mechanism leading to NH_3 and H_2 was understood.

2. Carbon defects and doped materials as non-metal catalysts were studied to catalyze NH_3 reforming; the reaction mechanisms were resolved as a function of the defect type.

3. Transition metal catalysts with typical catalytic performance were selected and DFT calculations and micro-kinetic models were employed to track the surface species and product composition during the reaction process, revealing the internal relationship between the surface species, catalytic activity, and reaction conditions.

4. Based on the above work, single-atom transition metal catalysts with specific structures were modeled, and DFT calculations and micro-kinetic models were applied to study the catalytic performance of NH_3 reforming. And the efficient and stable single-atom catalysts are explored to improve metal atom utilization efficiency and reduce catalyst cost.

1.5 Reference

(1) Shukla, P. R.; Skea, J.; Calvo Buendia, E.; Masson-Delmotte, V.; Pörtner, H. O.; Roberts, D. C.; Zhai, P.; Slade, R.; Connors, S.; Van Diemen, R. IPCC, 2019: Climate Change and Land: An IPCC Special Report on Climate Change, Desertification, Land Degradation, Sustainable Land Management, Food Security, and Greenhouse Gas Fluxes in Terrestrial Ecosystems. **2019**.

(2) Manabe, S. Role of Greenhouse Gas in Climate Change. *Tellus A: Dynamic Meteorology and Oceanography* **2019**, *71* (1), 1620078.

(3) Manabe, S.; Stouffer, R. J. Simulation of Abrupt Climate Change Induced by Freshwater Input to the North Atlantic Ocean. *Nature* **1995**, *378* (6553), 165–167.

(4) McQueen, S.; Stanford, J.; Satyapal, S.; Miller, E.; Stetson, N.; Papageorgopoulos, D.; Rustagi, N.; Arjona, V.; Adams, J.; Randolph, K.; Peterson, D.; Hill, L.; Koleva, M.; Reinhardt, T.; Frye, E.; Schrecengost, R.; Kokkinos, A.; Litynski, J.; Conrad, R.; Soloveichik, G.; Tew, D.; Litzelman, S.; Vetrano, J.; Onuschak, R.; Hahn, A.; Hsieh, E.; Costa, R. *Department of Energy Hydrogen Program Plan*; DOE/EE-2128; US Department of Energy (USDOE), Washington DC (United States), 2020. https://doi.org/10.2172/1721803.

(5) Green Hydrogen for a sustainable future – pilot action within the European Research Area (ERA) - BMBF https://www.bmbf.de/bmbf/shareddocs/kurzmeldungen/en/green-hydrogen-for-a-sustainable-future.html (accessed 2021 -10 -24).

(6) UKRI awards £171m in UK decarbonisation to nine projects

https://www.ukri.org/news/ukri-awards-171m-in-uk-decarbonisation-to-nine-projects/ (accessed 2021 -10 -24).
(7) UK government launches plan for a world-leading hydrogen economy https://www.gov.uk/government/news/uk-government-launches-plan-for-a-world-leading-hydrogen-economy (accessed 2021 -10 -24).
(8) Commission to invest €14.7 billion from Horizon Europe https://ec.europa.eu/commission/presscorner/detail/en/IP_21_2993 (accessed 2021 -10 -24).
(9) Schell, L. S.; Reed, J. G.; Zhao, L.; Brouwer, J.; Samuelsen, S. Comparing the Levelized Cost of Returned Energy (LCORE) Values for Hydrogen-Based Conversion Pathways and Batteries. *ECS Transactions* **2020**, *96* (1), 43.
(10) Schoenung, S. M.; Keller, J. O. Commercial Potential for Renewable Hydrogen in California. *International Journal of Hydrogen Energy* **2017**, *42* (19), 13321–13328.
(11) Kumar, S. S.; Himabindu, V. Hydrogen Production by PEM Water Electrolysis–A Review. *Materials Science for Energy Technologies* **2019**, *2* (3), 442–454.
(12) Abdalla, A. M.; Hossain, S.; Nisfindy, O. B.; Azad, A. T.; Dawood, M.; Azad, A. K. Hydrogen Production, Storage, Transportation and Key Challenges with Applications: A Review. *Energy conversion and management* **2018**, *165*, 602–627.
(13) Rossini, F. D. A Report on the International Practical Temperature Scale of 1968. *Pure and Applied Chemistry* **1970**, *22* (3–4), 555–570.
(14) Abohamzeh, E.; Salehi, F.; Sheikholeslami, M.; Abbassi, R.; Khan, F. Review of Hydrogen Safety during Storage, Transmission, and Applications Processes. *Journal of Loss Prevention in the Process Industries* **2021**, 104569.
(15) Moradi, R.; Groth, K. M. Hydrogen Storage and Delivery: Review of the State of the Art Technologies and Risk and Reliability Analysis. *International Journal of Hydrogen Energy* **2019**, *44* (23), 12254–12269.
(16) Chen, L.; Xiong, X.; Tao, X.; Su, Y.; Qiao, L. Effect of Dislocation Cell Walls on Hydrogen Adsorption, Hydrogen Trapping and Hydrogen Embrittlement Resistance. *Corrosion Science* **2020**, *166*, 108428.
(17) Chen, Y.; Zhao, S.; Ma, H.; Wang, H.; Hua, L.; Fu, S. Analysis of Hydrogen Embrittlement on Aluminum Alloys for Vehicle-Mounted Hydrogen Storage Tanks: A Review. *Metals* **2021**, *11* (8), 1303.
(18) Patents and the Energy Transition – Analysis https://www.iea.org/reports/patents-and-the-energy-transition (accessed 2021 -10 -24).
(19) Nagpal, M.; Kakkar, R. An Evolving Energy Solution: Intermediate Hydrogen Storage. *International Journal of Hydrogen Energy* **2018**, *43* (27), 12168–12188.
(20) Hassan, I. A.; Ramadan, H. S.; Saleh, M. A.; Hissel, D. Hydrogen Storage Technologies for Stationary and Mobile Applications: Review, Analysis and Perspectives. *Renewable and Sustainable Energy Reviews* **2021**, *149*, 111311.
(21) Zivar, D.; Kumar, S.; Foroozesh, J. Underground Hydrogen Storage: A Comprehensive Review. *International Journal of Hydrogen Energy* **2021**, *46* (45), 23436–23462.
(22) Tarkowski, R. Underground Hydrogen Storage: Characteristics and Prospects. *Renewable and Sustainable Energy Reviews* **2019**, *105*, 86–94.

(23) Elgowainy, A.; Reddi, K.; Sutherland, E.; Joseck, F. Tube-Trailer Consolidation Strategy for Reducing Hydrogen Refueling Station Costs. *International Journal of Hydrogen Energy* **2014**, *39* (35), 20197–20206. https://doi.org/10.1016/j.ijhydene.2014.10.030.
(24) Cardella, U.; Decker, L.; Klein, H. Roadmap to Economically Viable Hydrogen Liquefaction. *International Journal of Hydrogen Energy* **2017**, *42* (19), 13329–13338. https://doi.org/10.1016/j.ijhydene.2017.01.068.
(25) Baldwin, D. *FINAL REPORT - Development of High Pressure Hydrogen Storage Tank for Storage and Gaseous Truck Delivery*; DOE-HEXAGON-GO18062; Hexagon Lincoln LLC, Lincoln, NE (United States), 2017. https://doi.org/10.2172/1373926.
(26) Cardella, U.; Decker, L.; Sundberg, J.; Klein, H. Process Optimization for Large-Scale Hydrogen Liquefaction. *International Journal of Hydrogen Energy* **2017**, *42* (17), 12339–12354. https://doi.org/10.1016/j.ijhydene.2017.03.167.
(27) Valera-Medina, A.; Xiao, H.; Owen-Jones, M.; David, W. I.; Bowen, P. J. Ammonia for Power. *Progress in Energy and Combustion Science* **2018**, *69*, 63–102.
(28) Lamb, K. E.; Dolan, M. D.; Kennedy, D. F. Ammonia for Hydrogen Storage; A Review of Catalytic Ammonia Decomposition and Hydrogen Separation and Purification. *International Journal of Hydrogen Energy* **2019**, *44* (7), 3580–3593.
(29) Wijayanta, A. T.; Oda, T.; Purnomo, C. W.; Kashiwagi, T.; Aziz, M. Liquid Hydrogen, Methylcyclohexane, and Ammonia as Potential Hydrogen Storage: Comparison Review. *International Journal of Hydrogen Energy* **2019**, *44* (29), 15026–15044.
(30) Alpaydın, C. Y.; Gülbay, S. K.; Colpan, C. O. A Review on the Catalysts Used for Hydrogen Production from Ammonia Borane. *International Journal of Hydrogen Energy* **2020**, *45* (5), 3414–3434.
(31) Mboyi, C. D.; Poinsot, D.; Roger, J.; Fajerwerg, K.; Kahn, M. L.; Hierso, J.-C. The Hydrogen-Storage Challenge: Nanoparticles for Metal-Catalyzed Ammonia Borane Dehydrogenation. *Small* **2021**, 2102759.
(32) Wang, C.; Zhao, J.; Du, X.; Sun, S.; Yu, X.; Zhang, X.; Lu, Z.; Li, L.; Yang, X. Hydrogen Production from Ammonia Borane Hydrolysis Catalyzed by Non-Noble Metal-Based Materials: A Review. *Journal of Materials Science* **2021**, *56* (4), 2856–2878.
(33) Cheng, Y.; Wu, X.; Xu, H. Catalytic Decomposition of Hydrous Hydrazine for Hydrogen Production. *Sustainable Energy & Fuels* **2019**, *3* (2), 343–365.
(34) He, L.; Liang, B.; Huang, Y.; Zhang, T. Design Strategies of Highly Selective Nickel Catalysts for H2 Production via Hydrous Hydrazine Decomposition: A Review. *National Science Review* **2018**, *5* (3), 356–364.
(35) Rees, N. V.; Compton, R. G. Carbon-Free Energy: A Review of Ammonia-and Hydrazine-Based Electrochemical Fuel Cells. *Energy & Environmental Science* **2011**, *4* (4), 1255–1260.
(36) Milanese, C.; Garroni, S.; Gennari, F.; Marini, A.; Klassen, T.; Dornheim, M.; Pistidda, C. Solid State Hydrogen Storage in Alanates and Alanate-Based Compounds: A Review. *Metals* **2018**, *8* (8), 567.
(37) Suárez-Alcántara, K.; Tena-Garcia, J. R.; Guerrero-Ortiz, R. Alanates, a Comprehensive Review. *Materials* **2019**, *12* (17), 2724.
(38) Aakko-Saksa, P. T.; Cook, C.; Kiviaho, J.; Repo, T. Liquid Organic Hydrogen Carriers

for Transportation and Storing of Renewable Energy–Review and Discussion. *Journal of Power Sources* **2018**, *396*, 803–823.

(39) Modisha, P. M.; Ouma, C. N.; Garidzirai, R.; Wasserscheid, P.; Bessarabov, D. The Prospect of Hydrogen Storage Using Liquid Organic Hydrogen Carriers. *Energy & fuels* **2019**, *33* (4), 2778–2796.

(40) Niermann, M.; Drünert, S.; Kaltschmitt, M.; Bonhoff, K. Liquid Organic Hydrogen Carriers (LOHCs)–Techno-Economic Analysis of LOHCs in a Defined Process Chain. *Energy & Environmental Science* **2019**, *12* (1), 290–307.

(41) Kim, K. C. A Review on Design Strategies for Metal Hydrides with Enhanced Reaction Thermodynamics for Hydrogen Storage Applications. *International Journal of Energy Research* **2018**, *42* (4), 1455–1468.

(42) Rusman, N. A. A.; Dahari, M. A Review on the Current Progress of Metal Hydrides Material for Solid-State Hydrogen Storage Applications. *International Journal of Hydrogen Energy* **2016**, *41* (28), 12108–12126.

(43) Schneemann, A.; White, J. L.; Kang, S.; Jeong, S.; Wan, L. F.; Cho, E. S.; Heo, T. W.; Prendergast, D.; Urban, J. J.; Wood, B. C. Nanostructured Metal Hydrides for Hydrogen Storage. *Chemical reviews* **2018**, *118* (22), 10775–10839.

(44) Müller, K.; Brooks, K.; Autrey, T. Hydrogen Storage in Formic Acid: A Comparison of Process Options. *Energy & Fuels* **2017**, *31* (11), 12603–12611.

(45) Sordakis, K.; Tang, C.; Vogt, L. K.; Junge, H.; Dyson, P. J.; Beller, M.; Laurenczy, G. Homogeneous Catalysis for Sustainable Hydrogen Storage in Formic Acid and Alcohols. *Chemical reviews* **2018**, *118* (2), 372–433.

(46) Onishi, N.; Iguchi, M.; Yang, X.; Kanega, R.; Kawanami, H.; Xu, Q.; Himeda, Y. Development of Effective Catalysts for Hydrogen Storage Technology Using Formic Acid. *Advanced Energy Materials* **2019**, *9* (23), 1801275.

(47) Dalai, S.; Savithri, V.; Sharma, P. Investigating the Effect of Cobalt Loading on Thermal Conductivity and Hydrogen Storage Capacity of Hollow Glass Microspheres (HGMs). *Materials Today: Proceedings* **2017**, *4* (11), 11608–11616.

(48) Mehrizi, M. Z.; Abdi, J.; Rezakazemi, M.; Salehi, E. A Review on Recent Advances in Hollow Spheres for Hydrogen Storage. *International Journal of Hydrogen Energy* **2020**, *45* (35), 17583–17604.

(49) Schmid, G. H.; Bauer, J.; Eder, A.; Eisenmenger-Sittner, C. A Hybrid Hydrolytic Hydrogen Storage System Based on Catalyst-Coated Hollow Glass Microspheres. *International Journal of Energy Research* **2017**, *41* (2), 297–314.

(50) Prewitz, M.; Gaber, M.; Müller, R.; Marotztke, C.; Holtappels, K. Polymer Coated Glass Capillaries and Structures for High-Pressure Hydrogen Storage: Permeability and Hydrogen Tightness. *International Journal of Hydrogen Energy* **2018**, *43* (11), 5637–5644. https://doi.org/10.1016/j.ijhydene.2017.12.092.

(51) Zhevago, N. K.; Chabak, A. F.; Denisov, E. I.; Glebov, V. I.; Korobtsev, S. V. Storage of Cryo-Compressed Hydrogen in Flexible Glass Capillaries. *International Journal of Hydrogen Energy* **2013**, *38* (16), 6694–6703. https://doi.org/10.1016/j.ijhydene.2013.03.107.

(52) Mohan, M.; Sharma, V. K.; Kumar, E. A.; Gayathri, V. Hydrogen Storage in Carbon Materials—A Review. *Energy Storage* **2019**, *1* (2), e35.

(53) Xia, Y.; Yang, Z.; Zhu, Y. Porous Carbon-Based Materials for Hydrogen Storage: Advancement and Challenges. *Journal of Materials Chemistry A* **2013**, *1* (33), 9365–9381.
(54) Sdanghi, G.; Maranzana, G.; Celzard, A.; Fierro, V. Hydrogen Adsorption on Nanotextured Carbon Materials. *Hydrogen Storage Technologies; Wiley-Blackwell: Hoboken, NJ, USA* **2018**, 263–320.
(55) Ren, J.; Langmi, H. W.; North, B. C.; Mathe, M. Review on Processing of Metal–Organic Framework (MOF) Materials towards System Integration for Hydrogen Storage. *International Journal of Energy Research* **2015**, *39* (5), 607–620.
(56) Langmi, H. W.; Ren, J.; North, B.; Mathe, M.; Bessarabov, D. Hydrogen Storage in Metal-Organic Frameworks: A Review. *Electrochimica Acta* **2014**, *128*, 368–392.
(57) Lim, K. L.; Kazemian, H.; Yaakob, Z.; Daud, W. W. Solid-State Materials and Methods for Hydrogen Storage: A Critical Review. *Chemical Engineering & Technology: Industrial Chemistry-Plant Equipment-Process Engineering-Biotechnology* **2010**, *33* (2), 213–226.
(58) Gangu, K. K.; Maddila, S.; Mukkamala, S. B.; Jonnalagadda, S. B. Characteristics of MOF, MWCNT and Graphene Containing Materials for Hydrogen Storage: A Review. *Journal of Energy Chemistry* **2019**, *30*, 132–144. https://doi.org/10.1016/j.jechem.2018.04.012.
(59) Lide, D. R. *CRC Handbook of Chemistry and Physics*; CRC press, 2004; Vol. 85.
(60) Immediately Dangerous to Life or Health | NIOSH | CDC https://www.cdc.gov/niosh/idlh/default.html (accessed 2021 -12 -06).
(61) Valdés-López, V. F.; Mason, T.; Shearing, P. R.; Brett, D. J. Carbon Monoxide Poisoning and Mitigation Strategies for Polymer Electrolyte Membrane Fuel Cells–A Review. *Progress in Energy and Combustion Science* **2020**, *79*, 100842.
(62) Shabani, B.; Hafttananian, M.; Khamani, S.; Ramiar, A.; Ranjbar, A. A. Poisoning of Proton Exchange Membrane Fuel Cells by Contaminants and Impurities: Review of Mechanisms, Effects, and Mitigation Strategies. *Journal of Power Sources* **2019**, *427*, 21–48.
(63) Devrim, Y.; Albostan, A.; Devrim, H. Experimental Investigation of CO Tolerance in High Temperature PEM Fuel Cells. *International Journal of Hydrogen Energy* **2018**, *43* (40), 18672–18681.
(64) Schmittinger, W.; Vahidi, A. A Review of the Main Parameters Influencing Long-Term Performance and Durability of PEM Fuel Cells. *Journal of power sources* **2008**, *180* (1), 1–14.
(65) Wang, Y.; Diaz, D. F. R.; Chen, K. S.; Wang, Z.; Adroher, X. C. Materials, Technological Status, and Fundamentals of PEM Fuel Cells–a Review. *Materials Today* **2020**, *32*, 178–203.
(66) Shabani, B.; Hafttananian, M.; Khamani, Sh.; Ramiar, A.; Ranjbar, A. A. Poisoning of Proton Exchange Membrane Fuel Cells by Contaminants and Impurities: Review of Mechanisms, Effects, and Mitigation Strategies. *Journal of Power Sources* **2019**, *427*, 21–48. https://doi.org/10.1016/j.jpowsour.2019.03.097.
(67) Misz, U.; Talke, A.; Heinzel, A.; Konrad, G. Sensitivity Analyses on the Impact of Air Contaminants on Automotive Fuel Cells. *Fuel Cells* **2016**, *16* (4), 444–462.

(68) EH40, H. Workplace Exposure Limits. *London: Health and Safety Executive* **2011**.
(69) Klerke, A.; Hviid Christensen, C.; K. Nørskov, J.; Vegge, T. Ammonia for Hydrogen Storage: Challenges and Opportunities. *Journal of Materials Chemistry* **2008**, *18* (20), 2304–2310. https://doi.org/10.1039/B720020J.
(70) Christensen, C. H.; Sørensen, R. Z.; Johannessen, T.; Quaade, U. J.; Honkala, K.; Elmøe, T. D.; Køhler, R.; Nørskov, J. K. Metal Ammine Complexes for Hydrogen Storage. *Journal of Materials Chemistry* **2005**, *15* (38), 4106–4108.
(71) Kojima, Y. A Green Ammonia Economy. In *10th annual NH 10th annual NH3 fuel conference*; 2013.
(72) Tafreshi, S. S.; Roldan, A.; de Leeuw, N. H. Density Functional Theory Calculations of the Hydrazine Decomposition Mechanism on the Planar and Stepped Cu (111) Surfaces. *Physical Chemistry Chemical Physics* **2015**, *17* (33), 21533–21546.
(73) Asazawa, K.; Yamada, K.; Tanaka, H.; Oka, A.; Taniguchi, M.; Kobayashi, T. A Platinum-Free Zero-Carbon-Emission Easy Fuelling Direct Hydrazine Fuel Cell for Vehicles. *Angewandte Chemie* **2007**, *119* (42), 8170–8173.
(74) Colton, E. *Studies on the Synthesis of Hydrazine*; University of Illinois at Urbana-Champaign, 1954.
(75) Troyan, J. E. Properties, Production, and Uses of Hydrazine. *Industrial & Engineering Chemistry* **1953**, *45* (12), 2608–2612.
(76) Kent, J. A. *Riegel's Handbook of Industrial Chemistry*; Springer Science & Business Media, 2012.
(77) 潘伟雄; 郭建行. Ammonia Air Oxidation Process One-Step Synthesis Hydrazine Hydrate or Carbodiimide. CN106995388A, August 1, 2017.
(78) Vogel, M.; Büldt, A.; Karst, U. Hydrazine Reagents as Derivatizing Agents in Environmental Analysis–a Critical Review. *Fresenius' journal of analytical chemistry* **2000**, *366* (8), 781–791.
(79) Nguyen, K. H.; Hao, Y.; Chen, W.; Zhang, Y.; Xu, M.; Yang, M.; Liu, Y.-N. Recent Progress in the Development of Fluorescent Probes for Hydrazine. *Luminescence* **2018**, *33* (5), 816–836.
(80) Nguyen MC USAF, H. N.; Chenoweth, J. A.; Bebarta MC USAF, V. S.; Albertson, T. E.; Nowadly MC USAF, C. D. The Toxicity, Pathophysiology, and Treatment of Acute Hydrazine Propellant Exposure: A Systematic Review. *Military medicine* **2021**, *186* (3–4), e319–e326.
(81) Pakdehi, S. G.; Salimi, M.; Rasoolzadeh, M. A Review on Decomposition of Hydrazine and Its Kinetics as a Novel Approach for COFree H_2 Production. *Researches and Applications in Mechanical Engineering* **2014**, *3*, 21–25.
(82) Serov, A.; Kwak, C. Direct Hydrazine Fuel Cells: A Review. *Applied Catalysis B: Environmental* **2010**, *98* (1–2), 1–9.
(83) Wang, Y.; Shi, Y.-F.; Chen, Y.-B.; Wu, L.-M. Hydrazine Reduction of Metal Ions to Porous Submicro-Structures of Ag, Pd, Cu, Ni, and Bi. *Journal of Solid State Chemistry* **2012**, *191*, 19–26.
(84) Littrell, D. M.; Bowers, D. H.; Tatarchuk, B. J. Hydrazine Reduction of Transition-Metal Oxides. *Journal of the Chemical Society, Faraday Transactions 1: Physical Chemistry in Condensed Phases* **1987**, *83* (11), 3271–3282.

(85) Gui, Z.; Fan, R.; Mo, W.; Chen, X.; Yang, L.; Hu, Y. Synthesis and Characterization of Reduced Transition Metal Oxides and Nanophase Metals with Hydrazine in Aqueous Solution. *Materials research bulletin* **2003**, *38* (1), 169–176.
(86) Cho, S. J.; Lee, J.; Lee, Y. S.; Kim, D. P. Characterization of Iridium Catalyst for Decomposition of Hydrazine Hydrate for Hydrogen Generation. *Catalysis letters* **2006**, *109* (3), 181–186.
(87) Singh, S. K.; Zhang, X.-B.; Xu, Q. Room-Temperature Hydrogen Generation from Hydrous Hydrazine for Chemical Hydrogen Storage. *Journal of the American Chemical Society* **2009**, *131* (29), 9894–9895.
(88) Zheng, M.; Cheng, R.; Chen, X.; Li, N.; Li, L.; Wang, X.; Zhang, T. A Novel Approach for CO-Free H2 Production via Catalytic Decomposition of Hydrazine. *International journal of hydrogen energy* **2005**, *30* (10), 1081–1089.
(89) Singh, S. K.; Lu, Z.-H.; Xu, Q. Temperature-Induced Enhancement of Catalytic Performance in Selective Hydrogen Generation from Hydrous Hydrazine with Ni-Based Nanocatalysts for Chemical Hydrogen Storage, 2011.
(90) Singh, A. K.; Yadav, M.; Aranishi, K.; Xu, Q. Temperature-Induced Selectivity Enhancement in Hydrogen Generation from Rh–Ni Nanoparticle-Catalyzed Decomposition of Hydrous Hydrazine. *International journal of hydrogen energy* **2012**, *37* (24), 18915–18919.
(91) Liu, M.; Zheng, Y.; Xie, S.; Li, N.; Lu, N.; Wang, J.; Kim, M. J.; Guo, L.; Xia, Y. Facile Synthesis of Pd–Ir Bimetallic Octapods and Nanocages through Galvanic Replacement and Co-Reduction, and Their Use for Hydrazine Decomposition. *Physical Chemistry Chemical Physics* **2013**, *15* (28), 11822–11829.
(92) Singh, S. K.; Xu, Q. Complete Conversion of Hydrous Hydrazine to Hydrogen at Room Temperature for Chemical Hydrogen Storage. *Journal of the American Chemical Society* **2009**, *131* (50), 18032–18033.
(93) Zhao, P.; Cao, N.; Su, J.; Luo, W.; Cheng, G. NiIr Nanoparticles Immobilized on the Pores of MIL-101 as Highly Efficient Catalyst toward Hydrogen Generation from Hydrous Hydrazine. *Acs Sustainable Chemistry & Engineering* **2015**, *3* (6), 1086–1093.
(94) Singh, S. K.; Xu, Q. Bimetallic Nickel-Iridium Nanocatalysts for Hydrogen Generation by Decomposition of Hydrous Hydrazine. *Chemical communications* **2010**, *46* (35), 6545–6547.
(95) Singh, S. K.; Xu, Q. Bimetallic Ni- Pt Nanocatalysts for Selective Decomposition of Hydrazine in Aqueous Solution to Hydrogen at Room Temperature for Chemical Hydrogen Storage. *Inorganic chemistry* **2010**, *49* (13), 6148–6152.
(96) Bhattacharjee, D.; Mandal, K.; Dasgupta, S. High Performance Nickel–Palladium Nanocatalyst for Hydrogen Generation from Alkaline Hydrous Hydrazine at Room Temperature. *Journal of Power Sources* **2015**, *287*, 96–99.
(97) Singh, S. K.; Iizuka, Y.; Xu, Q. Nickel-Palladium Nanoparticle Catalyzed Hydrogen Generation from Hydrous Hydrazine for Chemical Hydrogen Storage. *International journal of hydrogen energy* **2011**, *36* (18), 11794–11801.
(98) Singh, S. K.; Singh, A. K.; Aranishi, K.; Xu, Q. Noble-Metal-Free Bimetallic Nanoparticle-Catalyzed Selective Hydrogen Generation from Hydrous Hydrazine for

Chemical Hydrogen Storage. *Journal of the American Chemical Society* **2011**, *133* (49), 19638–19641.

(99) Deng, M.; Fu, S. Y.; Yang, F.; Wu, P.; Tong, D. G. Urchin-like Amorphous Ni2B Alloys: Efficient Antibacterial Materials and Catalysts for Hydrous Hydrazine Decomposition to Produce H2. *Journal of nanoscience and nanotechnology* **2016**, *16* (3), 2394–2400.

(100) Wang, H.-L.; Yan, J.-M.; Li, S.-J.; Zhang, X.-W.; Jiang, Q. Noble-Metal-Free NiFeMo Nanocatalyst for Hydrogen Generation from the Decomposition of Hydrous Hydrazine. *Journal of Materials Chemistry A* **2014**, *3* (1), 121–124.

(101) Wang, J.; Li, Y.; Zhang, Y. Precious-Metal-Free Nanocatalysts for Highly Efficient Hydrogen Production from Hydrous Hydrazine. *Advanced Functional Materials* **2014**, *24* (45), 7073–7077.

(102) Bhattacharjee, D.; Dasgupta, S. Trimetallic NiFePd Nanoalloy Catalysed Hydrogen Generation from Alkaline Hydrous Hydrazine and Sodium Borohydride at Room Temperature. *Journal of Materials Chemistry A* **2015**, *3* (48), 24371–24378.

(103) He, L.; Huang, Y.; Liu, X. Y.; Li, L.; Wang, A.; Wang, X.; Mou, C.-Y.; Zhang, T. Structural and Catalytic Properties of Supported Ni–Ir Alloy Catalysts for H2 Generation via Hydrous Hydrazine Decomposition. *Applied Catalysis B: Environmental* **2014**, *147*, 779–788.

(104) He, L.; Huang, Y.; Wang, A.; Wang, X.; Chen, X.; Delgado, J. J.; Zhang, T. A Noble-Metal-Free Catalyst Derived from Ni-Al Hydrotalcite for Hydrogen Generation from N2H4 · H2O Decomposition. *Angewandte Chemie* **2012**, *124* (25), 6295–6298. https://doi.org/10.1002/ange.201201737.

(105) Jiang, Y.-Y.; Dai, H.-B.; Zhong, Y.-J.; Chen, D.-M.; Wang, P. Complete and Rapid Conversion of Hydrazine Monohydrate to Hydrogen over Supported Ni–Pt Nanoparticles on Mesoporous Ceria for Chemical Hydrogen Storage. *Chemistry–A European Journal* **2015**, *21* (43), 15439–15445.

(106) Kang, W.; Varma, A. Hydrogen Generation from Hydrous Hydrazine over Ni/CeO2 Catalysts Prepared by Solution Combustion Synthesis. *Applied Catalysis B: Environmental* **2018**, *220*, 409–416.

(107) Dai, H.; Dai, H.-B.; Zhong, Y.-J.; Kang, Q.; Sun, L.-X.; Wang, P. Kinetics of Catalytic Decomposition of Hydrous Hydrazine over CeO2-Supported Bimetallic Ni–Pt Nanocatalysts. *International Journal of Hydrogen Energy* **2017**, *42* (9), 5684–5693.

(108) Al-Haydari, Y. K.; Saleh, J. M.; Matloob, M. H. Adsorption and Decomposition of Hydrazine on Metal Films of Iron, Nickel, and Copper. *The Journal of Physical Chemistry* **1985**, *89* (15), 3286–3290.

(109) Alberas, D. J.; Kiss, J.; Liu, Z.-M.; White, J. M. Surface Chemistry of Hydrazine on Pt (111). *Surface science* **1992**, *278* (1–2), 51–61.

(110) Nørskov, J.; Chen, J.; Miranda, R.; Fitzsimmons, T.; Stack, R. *Sustainable Ammonia Synthesis–Exploring the Scientific Challenges Associated with Discovering Alternative, Sustainable Processes for Ammonia Production*; US DOE Office of Science, 2016.

(111) Jennings, J. R. *Catalytic Ammonia Synthesis: Fundamentals and Practice*; Springer Science & Business Media, 1991.

(112) Schlögl, R. Catalytic Synthesis of Ammonia—A “Never-Ending Story”?

Angewandte Chemie International Edition **2003**, *42* (18), 2004–2008.

(113) Ortiz-Medina, J. F.; Grunden, A. M.; Hyman, M. R.; Call, D. F. Nitrogen Gas Fixation and Conversion to Ammonium Using Microbial Electrolysis Cells. *ACS Sustainable Chemistry & Engineering* **2019**, *7* (3), 3511–3519.

(114) Zhang, S.; Zhao, Y.; Shi, R.; Zhou, C.; Waterhouse, G. I.; Wu, L.-Z.; Tung, C.-H.; Zhang, T. Efficient Photocatalytic Nitrogen Fixation over Cuδ+-Modified Defective ZnAl-Layered Double Hydroxide Nanosheets. *Advanced Energy Materials* **2020**, *10* (8), 1901973.

(115) Wang, W.; Zhang, H.; Zhang, S.; Liu, Y.; Wang, G.; Sun, C.; Zhao, H. Potassium-Ion-Assisted Regeneration of Active Cyano Groups in Carbon Nitride Nanoribbons: Visible-Light-Driven Photocatalytic Nitrogen Reduction. *Angewandte Chemie International Edition* **2019**, *58* (46), 16644–16650.

(116) Hawtof, R.; Ghosh, S.; Guarr, E.; Xu, C.; Mohan Sankaran, R.; Renner, J. N. Catalyst-Free, Highly Selective Synthesis of Ammonia from Nitrogen and Water by a Plasma Electrolytic System. *Science Advances 5* (1), eaat5778. https://doi.org/10.1126/sciadv.aat5778.

(117) Kumari, S.; Pishgar, S.; E. Schwarting, M.; F. Paxton, W.; M. Spurgeon, J. Synergistic Plasma-Assisted Electrochemical Reduction of Nitrogen to Ammonia. *Chemical Communications* **2018**, *54* (95), 13347–13350. https://doi.org/10.1039/C8CC07869F.

(118) Patil, S. B.; Wang, D.-Y. Exploration and Investigation of Periodic Elements for Electrocatalytic Nitrogen Reduction. *Small* **2020**, *16* (45), 2002885.

(119) Hochman, G.; Goldman, A.; Felder, F. A.; Mayer, J.; Miller, A.; Holland, P. L.; Goldman, L.; Manocha, P.; Song, Z.; Aleti, S. The Potential Economic Feasibility of Direct Electrochemical Nitrogen Reduction as a Route to Ammonia. **2019**.

(120) Ripepi, D.; Zaffaroni, R.; Schreuders, H.; Boshuizen, B.; Mulder, F. M. Ammonia Synthesis at Ambient Conditions via Electrochemical Atomic Hydrogen Permeation. *ACS Energy Letters* **2021**, *6*, 3817–3823.

(121) Guo, Y.; Wang, G.; Shen, S.; Wei, G.; Xia, G.; Zhang, J. On Scaling Relations of Single Atom Catalysts for Electrochemical Ammonia Synthesis. *Applied Surface Science* **2021**, *550*, 149283.

(122) *Mineral Commodity Summaries*; 2021.

(123) Zhao, Y.; Setzler, B. P.; Wang, J.; Nash, J.; Wang, T.; Xu, B.; Yan, Y. An Efficient Direct Ammonia Fuel Cell for Affordable Carbon-Neutral Transportation. *Joule* **2019**, *3* (10), 2472–2484.

(124) Siddiqui, O.; Dincer, I. A Review and Comparative Assessment of Direct Ammonia Fuel Cells. *Thermal Science and Engineering Progress* **2018**, *5*, 568–578.

(125) Zincir, B. A Short Review of Ammonia as an Alternative Marine Fuel for Decarbonised Maritime Transportation. In *International Conference on Energy, Environment and Storage of Energy*; 2020; pp 373–380.

(126) Dimitriou, P.; Javaid, R. A Review of Ammonia as a Compression Ignition Engine Fuel. *International Journal of Hydrogen Energy* **2020**, *45* (11), 7098–7118.

(127) de Foy, M. P. Feasibility Study of Low-Carbon Ammonia and Steel Production in Europe. *Separation and Purification*.

(128) Valera-Medina, A.; Roldan, A. Ammonia from Steelworks. In *Sustainable Ammonia Production*; Inamuddin, Boddula, R., Asiri, A. M., Eds.; Green Energy and Technology; Springer International Publishing: Cham, 2020; pp 69–80. https://doi.org/10.1007/978-3-030-35106-9_4.

(129) Boisen, A.; Dahl, S.; Nørskov, J. K.; Christensen, C. H. Why the Optimal Ammonia Synthesis Catalyst Is Not the Optimal Ammonia Decomposition Catalyst. *Journal of Catalysis* **2005**, *230* (2), 309–312.

(130) Ganley, J. C.; Thomas, F. S.; Seebauer, E. G.; Masel, R. I. A Priori Catalytic Activity Correlations: The Difficult Case of Hydrogen Production from Ammonia. *Catalysis Letters* **2004**, *96* (3), 117–122. https://doi.org/10.1023/B:CATL.0000030108.50691.d4.

(131) Yin, S.-F.; Zhang, Q.-H.; Xu, B.-Q.; Zhu, W.-X.; Ng, C.-F.; Au, C.-T. Investigation on the Catalysis of COx-Free Hydrogen Generation from Ammonia. *Journal of Catalysis* **2004**, *224* (2), 384–396.

(132) Jacobsen, C. J. H.; Dahl, S.; Hansen, P. L.; Törnqvist, E.; Jensen, L.; Topsøe, H.; Prip, D. V.; Møenshaug, P. B.; Chorkendorff, I. Structure Sensitivity of Supported Ruthenium Catalysts for Ammonia Synthesis. *Journal of Molecular Catalysis A: Chemical* **2000**, *163* (1), 19–26. https://doi.org/10.1016/S1381-1169(00)00396-4.

(133) Raróg-Pilecka, W.; Szmigiel, D.; Kowalczyk, Z.; Jodzis, S.; Zielinski, J. Ammonia Decomposition over the Carbon-Based Ruthenium Catalyst Promoted with Barium or Cesium. *Journal of Catalysis* **2003**, *218* (2), 465–469. https://doi.org/10.1016/S0021-9517(03)00058-7.

(134) Li, Y.; Yao, L.; Song, Y.; Liu, S.; Zhao, J.; Ji, W.; Au, C.-T. Core–Shell Structured Microcapsular-like Ru@ SiO 2 Reactor for Efficient Generation of CO x-Free Hydrogen through Ammonia Decomposition. *Chemical communications* **2010**, *46* (29), 5298–5300.

(135) Cao, N.; Su, J.; Luo, W.; Cheng, G. Hydrolytic Dehydrogenation of Ammonia Borane and Methylamine Borane Catalyzed by Graphene Supported Ru@ Ni Core–Shell Nanoparticles. *International journal of hydrogen energy* **2014**, *39* (1), 426–435.

(136) Choudhary, T. V.; Sivadinarayana, C.; Goodman, D. W. Catalytic Ammonia Decomposition: COx-Free Hydrogen Production for Fuel Cell Applications. *Catalysis Letters* **2001**, *72* (3), 197–201.

(137) Kowalczyk, Z.; Sentek, J.; Jodzis, S.; Muhler, M.; Hinrichsen, O. Effect of Potassium on the Kinetics of Ammonia Synthesis and Decomposition over Fused Iron Catalyst at Atmospheric Pressure. *Journal of Catalysis* **1997**, *169* (2), 407–414.

(138) Jedynak, A.; Kowalczyk, Z.; Szmigiel, D.; Raróg, W.; Zieliński, J. Ammonia Decomposition over the Carbon-Based Iron Catalyst Promoted with Potassium. *Applied Catalysis A: General* **2002**, *237* (1–2), 223–226.

(139) Ohtsuka, Y.; Xu, C.; Kong, D.; Tsubouchi, N. Decomposition of Ammonia with Iron and Calcium Catalysts Supported on Coal Chars. *Fuel* **2004**, *83* (6), 685–692.

(140) Zhang, J.; Comotti, M.; Schüth, F.; Schlögl, R.; Su, D. S. Commercial Fe-or Co-Containing Carbon Nanotubes as Catalysts for NH 3 Decomposition. *Chemical communications* **2007**, No. 19, 1916–1918.

(141) Lu, A.-H.; Nitz, J.-J.; Comotti, M.; Weidenthaler, C.; Schlichte, K.; Lehmann, C.

W.; Terasaki, O.; Schuth, F. Spatially and Size Selective Synthesis of Fe-Based Nanoparticles on Ordered Mesoporous Supports as Highly Active and Stable Catalysts for Ammonia Decomposition. *Journal of the American Chemical Society* **2010**, *132* (40), 14152–14162.

(142) Feyen, M.; Weidenthaler, C.; Güttel, R.; Schlichte, K.; Holle, U.; Lu, A.-H.; Schüth, F. High-Temperature Stable, Iron-Based Core-Shell Catalysts for Ammonia Decomposition. *Chem. Eur. J* **2011**, *17* (2), 598–605.

(143) Zhang, J.; Xu, H.; Li, W. Kinetic Study of NH3 Decomposition over Ni Nanoparticles: The Role of La Promoter, Structure Sensitivity and Compensation Effect. *Applied Catalysis A: General* **2005**, *296* (2), 257–267. https://doi.org/10.1016/j.apcata.2005.08.046.

(144) Zheng, W.; Zhang, J.; Ge, Q.; Xu, H.; Li, W. Effects of CeO2 Addition on Ni/Al2O3 Catalysts for the Reaction of Ammonia Decomposition to Hydrogen. *Applied Catalysis B: Environmental* **2008**, *80* (1), 98–105. https://doi.org/10.1016/j.apcatb.2007.11.008.

(145) Liu, H.; Wang, H.; Shen, J.; Sun, Y.; Liu, Z. Preparation, Characterization and Activities of the Nano-Sized Ni/SBA-15 Catalyst for Producing COx-Free Hydrogen from Ammonia. *Applied Catalysis A: General* **2008**, *337* (2), 138–147. https://doi.org/10.1016/j.apcata.2007.12.006.

(146) Li, X.-K.; Ji, W.-J.; Zhao, J.; Wang, S.-J.; Au, C.-T. Ammonia Decomposition over Ru and Ni Catalysts Supported on Fumed SiO2, MCM-41, and SBA-15. *Journal of Catalysis* **2005**, *236* (2), 181–189. https://doi.org/10.1016/j.jcat.2005.09.030.

(147) Bell, T. E.; Torrente-Murciano, L. H2 Production via Ammonia Decomposition Using Non-Noble Metal Catalysts: A Review. *Top Catal* **2016**, *59* (15), 1438–1457. https://doi.org/10.1007/s11244-016-0653-4.

(148) Varisli, D.; Kaykac, N. G. COx Free Hydrogen Production over Cobalt Incorporated Silicate Structured Mesoporous Catalysts. *Applied Catalysis B: Environmental* **2012**, *127*, 389–398. https://doi.org/10.1016/j.apcatb.2012.08.042.

(149) Zhang, H.; Alhamed, Y. A.; Al-Zahrani, A.; Daous, M.; Inokawa, H.; Kojima, Y.; Petrov, L. A. Tuning Catalytic Performances of Cobalt Catalysts for Clean Hydrogen Generation via Variation of the Type of Carbon Support and Catalyst Post-Treatment Temperature. *International Journal of Hydrogen Energy* **2014**, *39* (31), 17573–17582. https://doi.org/10.1016/j.ijhydene.2014.07.183.

(150) Lendzion-Bielun, Z.; Narkiewicz, U.; Arabczyk, W. Cobalt-Based Catalysts for Ammonia Decomposition. *Materials* **2013**, *6* (6), 2400–2409. https://doi.org/10.3390/ma6062400.

(151) Zhang, J.; Müller, J.-O.; Zheng, W.; Wang, D.; Su, D.; Schlögl, R. Individual Fe−Co Alloy Nanoparticles on Carbon Nanotubes: Structural and Catalytic Properties. *Nano Lett.* **2008**, *8* (9), 2738–2743. https://doi.org/10.1021/nl8011984.

(152) Lorenzut, B.; Montini, T.; Bevilacqua, M.; Fornasiero, P. FeMo-Based Catalysts for H2 Production by NH3 Decomposition. *Applied Catalysis B: Environmental* **2012**, *125*, 409–417. https://doi.org/10.1016/j.apcatb.2012.06.011.

(153) Simonsen, S. B.; Chakraborty, D.; Chorkendorff, I.; Dahl, S. Alloyed Ni-Fe Nanoparticles as Catalysts for NH3 Decomposition. *Applied Catalysis A: General*

2012, *447–448*, 22–31. https://doi.org/10.1016/j.apcata.2012.08.045.

(154) Ji, J.; Duan, X.; Qian, G.; Zhou, X.; Tong, G.; Yuan, W. Towards an Efficient CoMo/γ-Al2O3 Catalyst Using Metal Amine Metallate as an Active Phase Precursor: Enhanced Hydrogen Production by Ammonia Decomposition. *International Journal of Hydrogen Energy* **2014**, *39* (24), 12490–12498. https://doi.org/10.1016/j.ijhydene.2014.06.081.

(155) Duan, X.; Qian, G.; Zhou, X.; Chen, D.; Yuan, W. MCM-41 Supported CoMo Bimetallic Catalysts for Enhanced Hydrogen Production by Ammonia Decomposition. *Chemical Engineering Journal* **2012**, *207–208*, 103–108. https://doi.org/10.1016/j.cej.2012.05.100.

(156) Wang, M.; Liu, S.; Qian, T.; Liu, J.; Zhou, J.; Ji, H.; Xiong, J.; Zhong, J.; Yan, C. Over 56.55% Faradaic Efficiency of Ambient Ammonia Synthesis Enabled by Positively Shifting the Reaction Potential. *Nature communications* **2019**, *10* (1), 1–8.

(157) Jiang, Z.; Qin, P.; Fang, T. Mechanism of Ammonia Decomposition on Clean and Oxygen-Covered Cu (1 1 1) Surface: A Dft Study. *Chemical Physics* **2014**, *445*, 59–67.

(158) He, C.; Wang, H.; Huai, L.; Liu, J. Mechanism of Ammonia Decomposition and Oxidation on Ir (100): A First-Principles Study. *The Journal of Physical Chemistry C* **2012**, *116* (45), 24035–24045.

(159) Zhao, J.; Cui, C.; Wang, H.; Han, J.; Zhu, X.; Ge, Q. Insights into the Mechanism of Ammonia Decomposition on Molybdenum Nitrides Based on DFT Studies. *The Journal of Physical Chemistry C* **2018**, *123* (1), 554–564.

(160) Duan, X.; Ji, J.; Qian, G.; Fan, C.; Zhu, Y.; Zhou, X.; Chen, D.; Yuan, W. Ammonia Decomposition on Fe (1 1 0), Co (1 1 1) and Ni (1 1 1) Surfaces: A Density Functional Theory Study. *Journal of Molecular Catalysis A: Chemical* **2012**, *357*, 81–86.

(161) Duan, X.; Qian, G.; Fan, C.; Zhu, Y.; Zhou, X.; Chen, D.; Yuan, W. First-Principles Calculations of Ammonia Decomposition on Ni (110) Surface. *Surface science* **2012**, *606* (3–4), 549–553.

(162) Yeo, S. C.; Han, S. S.; Lee, H. M. Mechanistic Investigation of the Catalytic Decomposition of Ammonia (NH3) on an Fe (100) Surface: A DFT Study. *The Journal of Physical Chemistry C* **2014**, *118* (10), 5309–5316.

(163) Qin, Q.; Heil, T.; Antonietti, M.; Oschatz, M. Single-Site Gold Catalysts on Hierarchical N-Doped Porous Noble Carbon for Enhanced Electrochemical Reduction of Nitrogen. *Small Methods* **2018**, *2* (12), 1800202.

(164) Geng, Z.; Liu, Y.; Kong, X.; Li, P.; Li, K.; Liu, Z.; Du, J.; Shu, M.; Si, R.; Zeng, J. Achieving a Record-High Yield Rate of 120.9 for N2 Electrochemical Reduction over Ru Single-Atom Catalysts. *Advanced Materials* **2018**, *30* (40), 1803498.

(165) Liu, Y.; Xu, Q.; Fan, X.; Quan, X.; Su, Y.; Chen, S.; Yu, H.; Cai, Z. Electrochemical Reduction of N 2 to Ammonia on Co Single Atom Embedded N-Doped Porous Carbon under Ambient Conditions. *Journal of Materials Chemistry A* **2019**, *7* (46), 26358–26363.

(166) Zang, W.; Yang, T.; Zou, H.; Xi, S.; Zhang, H.; Liu, X.; Kou, Z.; Du, Y.; Feng, Y. P.; Shen, L. Copper Single Atoms Anchored in Porous Nitrogen-Doped Carbon as Efficient PH-Universal Catalysts for the Nitrogen Reduction Reaction. *ACS Catalysis*

2019, *9* (11), 10166–10173.

(167) Tsai, W.; Weinberg, W. H. Steady-State Decomposition of Ammonia on the Ruthenium (001) Surface. *Journal of Physical Chemistry* **1987**, *91* (20), 5302–5307.

(168) Bradford, M. C.; Fanning, P. E.; Vannice, M. A. Kinetics of NH3Decomposition over Well Dispersed Ru. *Journal of Catalysis* **1997**, *172* (2), 479–484.

(169) Chellappa, A. S.; Fischer, C. M.; Thomson, W. J. Ammonia Decomposition Kinetics over Ni-Pt/Al2O3 for PEM Fuel Cell Applications. *Applied Catalysis A: General* **2002**, *227* (1–2), 231–240.

Chapter 2 Theory and Methodology

2.1 Solving the Schrödinger equation

Quantum mechanics is applied to obtain a mathematical model of the electron behaviors in accurate *ab initio* approaches. Computational chemists are using this method to analyze the geometry, electronic structure, and reactivity of chemicals leading to novel materials. The primary goal of *ab initio* methods is to achieve an iterative approximate solution to the time-independent Schrödinger equation. The time-independent Schrödinger equation, represented in Eq. 2-1, occupies a central place in computer modeling, materials development, and chemical reactions.[1]

$$\hat{\mathrm{H}}|\psi\rangle = E|\psi\rangle \qquad \text{Eq. 2-1}$$

Where $\hat{\mathrm{H}}$ is the Hamiltonian operator and ψ is eigenstates of the Hamiltonian. ψ contains all the information of the system and each of these solutions (wave functions), ψ_{n}, has an associated eigenvalue (state energy), $E = \langle\psi|\hat{\mathrm{H}}|\psi\rangle$, a real number that satisfies the eigenvalue equation. The multi-terms equation, Eq. 2-2, can be used to describe the Hamiltonian:

$$\hat{\mathrm{H}} = -\frac{\hbar^2}{2}\sum_{\mathrm{i}=1}^{\mathrm{N}}\frac{\nabla^2}{m_i} + \sum_{\mathrm{i}=1}^{\mathrm{N}}\mathrm{V}(\mathrm{r_i}) + \sum_{\mathrm{i}=1}^{\mathrm{N}}\sum_{\mathrm{j}<\mathrm{i}}\mathrm{U}(\mathrm{r_i},\mathrm{r_j}) \qquad \text{Eq. 2-2}$$

Where $\mathrm{m_i}$ is the mass of the i^{th} particle, h is Planck's constant and ∇ is a vector differential operator. Moreover, $\mathrm{r_i}$ represents the position of the i^{th} particle. The three components in the right of the equation represent the following energies in sequence: (1) each particle's kinetic energy, (2) the potential energy of the electrons and the nuclei, and (3) the interaction energy between the particles. Essentially, it shows the way how the nuclei and electron behaviors have been considered in quantum mechanics.

Additionally, the eigenstates (wavefunctions) in the Schrödinger equation can be estimated. The Hartree product (Eq. 2-3) combines the wavefunctions of individual particles to give us a kind of representation for the wavefunction of a many-particle

system.[2,3] By considering the individual particle is in a single average effect generated by all the other individuals, it is the unsymmetrized form of the Slater determinant in the Hartree–Fock method (an *ab initio* quantum method to solve the Schrödinger equation) and is intrinsically mean-field, implying that the particles are independent.[4]

$$\psi = \psi_1(\mathrm{r}_1)\psi_2(\mathrm{r}_2) \ldots \psi_\mathrm{n}(\mathrm{r}_\mathrm{n}) \qquad \text{Eq. 2-3}$$

By solving the Schrödinger equation, the electron-nuclei system (without the relativistic effect) can be specified, and all physical and chemical properties of materials can be obtained. However, precisely describing the interaction energy between different electrons is difficult.

The self-consistent field methods (SCF) are implemented to solve the Schrödinger equation accompanying the appearance of computers. The different methods (e.g., Hartree-Fock method or density functional theory) estimating wave functions or electron density can be applied to solve the Schrödinger equation and obtain an improved accurate result in a shorter computational time. Normally, when the iteration reaches convergence, the relative accurate numerical solution of the Schrödinger equation is obtained. These approaches have offered insights into the investigation of materials and chemical processes for scientists, even though they are still time-consuming and costly.

2.2 Density functional theory

In this thesis, the Vienna *ab initio* Simulation Package (VASP) based on the density functional theory (DFT) is employed to optimize and simulate the materials and reactions.[5,6] Therefore, the DFT will be mainly introduced in the following.

Kohn and Hohenberg developed two basic mathematical theorems that underpin the entire methodology of DFT.[7] The first theorem is: The Schrödinger equation's ground-state energy is a unique functional of the electron density. According to this theorem, the ground-state electron density determines all the ground state's characteristics, including its energy and wave function. It means that the computational complexity can be reduced from 3N (3 dimensions of N electrons) to 3, which

significantly decreases the difficulty of the Schrödinger equation solving. Then, the second Hohenberg-Kohn theorem established an essential feature of the electron density functional: the real electron density, to the Schrödinger equation solution, is the one that minimizes the overall functional's energy. This points the direction to find the solution of the Schrödinger equation.

In 1965, based on the Born–Oppenheimer approximation (decoupling electronic and ionic movements) and non-relativistic approximation, Kohn and Sham represented the system's charge density using the single electron wave function and subsequently solved the multi-electron system's ground state problem.[8,9] The Kohn-Sham equations are written as follows, Eq. 2-4:

$$-\frac{\mathrm{h}^2}{2\mathrm{m}}\nabla^2 + \mathrm{V_{E-N}}(\mathrm{r_i}) + \mathrm{V_H}(\mathrm{r_i}) + \mathrm{V_{XC}}(\mathrm{r_i})\psi_\mathrm{i}(\mathrm{r_i}) = \epsilon_\mathrm{i}\psi_\mathrm{i}(\mathrm{r_i}) \qquad \text{Eq. 2-4}$$

The terms on the left represent, in order, $-\frac{\mathrm{h}^2}{2\mathrm{m}}\nabla^2$ the kinetic energy of the electrons, $\mathrm{V_{E-N}}(\mathrm{r_i})$ the interaction between an electron and the collection of atomic nuclei, $\mathrm{V_H}(\mathrm{r_i})$ the Hartree potential which describes the electron Coulomb repulsion, and $\mathrm{V_{XC}}(\mathrm{r_i})$ the correction for all the quantum mechanical effects that are not included in the "known" terms.

And when I introduce the electron density ($\rho(r)$) based on the first Hohenberg-Kohn theorem, the variation of the multi-particle system energy ($E[\rho(r)]$) to the electron density can be converted into the variation to a single electronic wave function ($\varphi_j(r)$). Compared with the Schrödinger equations (Eq. 2-1 and Eq. 2-2), the solution of the Kohn-Sham equations is the single-electron wave function that depends on only three spatial variables, $\psi_i(r_i)$. The energy eigenvalue is used as a Lagrange multiplier in the process of varying the system energy. The following equation, Eq. 2-5, can be derived after simplification:

$$\{-\frac{1}{2}\nabla^2 + V_{KS}[\rho(r)]\}\varphi_j(r) = E_j\varphi_j(r) \qquad \text{Eq. 2-5}$$

Where $V_{KS}[\rho(r)]$ is a contraction term, considering the action of external potential field ($v(r)$), Coulomb exclusion potential ($V_c[\rho(r)]$) and exchange-correlation potential ($V_{xc}[\rho(r)]$), as shown in Eq. 2-6.

$$V_{KS}[\rho(r)] = v(r) + V_c[\rho(r)] + V_{xc}[\rho(r)]$$
$$= v(r) + \int \frac{\rho(r')}{|r - r'|} dr' + \frac{\delta V_{xc}[\rho(r)]}{\delta \rho(r)} \quad \text{Eq. 2-6}$$

The consideration of the interaction between the electron's exchange and correlation in DFT equations implies that, theoretically, the accurate solution of the Schrödinger equation can be achieved using a known $V_{xc}[\rho(r)]$. Meanwhile, the description of the exchange-correlation energy has a significant impact on the precision of the solution. To maintain the balance between accuracy and computing cost, an appropriate exchange-correlation component should be introduced.

2.3 The exchange and correlation functional

Currently, there are two approximation methods to evaluate the exchange and correlation potential in the DFT simulation: local density approximation (LDA) and generalized gradient approximation (GGA).[10–13] LDA was initially applied to the evaluation of exchange-correlation energy ($V_{xc}[\rho(r)]$) with a homogeneous electron gas model.[14] This method only works well on the physical properties for the systems with relatively constant electron density, e.g., metal surface. To obtain more accurate results, GGA was developed. It is a more efficient method than LDA in terms of chemistry research, with a lower computational cost but higher accuracy. By introducing the charge density gradients to electron exchange energy, the exchange-correlation potential not only depends on a value of the point density (see in Eq. 2-7), also on its distribution, which is favorable for the simulation of the heterogeneous electron density.

$$V_{xc}^{GGA}[\rho(r)] = \frac{\delta E_{xc}^{GGA}}{\delta \rho(r)} - \nabla \frac{\delta E_{xc}^{GGA}}{\delta\left(\nabla \rho(r)\right)} \quad \text{Eq. 2-7}$$

Many approximations on the electron density gradient have been implemented on the DFT calculation, such as Perdew-Wang 86 (PW86), Beccke-Perdew (BP), Lee-Yang-Parr (LYP), Perdew-Wang 91 (PW91), Perdew-Burke-Enzerhof (PBE), Revised Perdew-Burke-Enzerhof (rPBE).[15–19] The results are consistent with the experimental data in most cases for geometries, vibrational frequencies, and charge densities.

Furthermore, hybrid functionals (such as B3LYP, PBE0, and HSE, etc.) which mixed the Hartree-Fock exchange term with exchange and correlation functionals, are proposed to describe some physical and chemical characters more accurately, e.g., the bandgap in semiconductors.[20–22] While the more precise the resolution, the higher the processing cost. Considering accuracy-cost balance, in this thesis, the GGA is mainly processed in rPBE functional form. The rPBE method is a convinced non-empirical functional, which means that its functional form and construction parameters are based on physical constraints rather than fitting across a collection of known systems.

2.4 Plane-wave and Pseudopotentials

Considering the influence of the delocalization of electrons and nuclei's periodic potential on the electronic structure of ideal solid materials, the computational cost for solving the Schrödinger equation is very high, even with the DFT. The most efficient way to tackle this challenge is to create a repeated unit cell expanding with a periodic model. Blöch theorem indicates that, in a periodic system, wave function takes the form of a plane-wave ($e^{ik\cdot r}$) modulated by a periodic function, as shown in *Eq. 2- 8*, providing a theoretical basis for the above method.

$$\psi_k(r) = e^{ik\cdot r}\, u_k(r) \qquad \textit{Eq. 2- 8}$$

Where ψ_k is the wave function of the crystal, k is the crystal momentum vector, u_k is a periodic function with the same periodicity of the momentum vector, and r is the coordinates.

This theorem proved that it is possible to solve the Schrödinger equation for each value of k independently. The vector space r is called real space, and the vector space k is called reciprocal space (or simply k space). Bravais lattice uses an infinite array of discrete points to define a crystalline arrangement and it can be divided up into Brillouin zones in the k space. The settlement of k space plays an important role in plane-wave DFT calculations because the integrals (*Eq. 2- 9*) in the Brillouin zone defined by k space (representing the primitive cell) take a substantial amount of the

computational resources. The solution given by Monkhort and Pack, which needs the specification of the number of k points in each direction in reciprocal space, is commonly utilized.[23]

$$\rho(r) = \int |\psi_{\mathrm{k}}(\mathrm{r})|^2 \mathrm{d}^3\mathrm{k} \approx \sum_{\mathrm{k}} |\psi_{\mathrm{k}}(\mathrm{r})|^2 \qquad \textit{Eq. 2- 9}$$

An infinite number of wavevectors (plane-waves) could be used to describe the wavefunctions. Normally, the more functions included in the basis set, the higher accurate results obtained. However, the high-energy plane-wave functions will only promote a little accuracy of the description. To make the calculation feasible, suitable cut-off energy of the plane-wave functions should be set corresponding to the relation of $E_{cutoff} = \frac{\hbar}{2m}|k|^2$.

The discussion above points to the fact that large energy cut-offs must be used to include plane-waves that oscillate on short-length scales in real space. This is problematic because the wave functions of tightly bound core electrons in atoms are associated with this kind of oscillation. However, core electrons are not especially important in defining chemical bonding and other physical characteristics of materials; these properties are dominated by the less tightly bound valence electrons. The most important approach to reducing the computational burden due to core electrons is to use pseudopotentials. This method is based on separating core and valence electrons and substituting the nuclear and core electrons potential with a suitable pseudopotential, which has the same effect on valence electrons. Ideally, a pseudopotential is developed by considering an isolated atom of one element, but the formed pseudopotential can then be used reliably for calculations that place this atom in any chemical environment without further adjustment of the pseudopotential. While this approach limits the accuracy of the model, it allows the efficient use of a plane-wave basis set to describe the valence electrons wavefunction. This approach has been further optimized, especially for first-row elements and 3d transition metals with the projector augmented wave method (PAW).[5] Therefore, VASP calculations with PAW were performed in the research.

In Figure 2- 1 (a) and (b), the energy differences of graphene and Ni bulk are

converged at 500 eV and 400 eV, respectively. To unify the cut-off energy in the following study, kinetic energy cutoff of 500 eV is applied to the studies. The product, ka, between the number of k-points, k, in any direction, and the length of the basis vector in this direction, a, is applied to help choose the initial k-point sampling, that is: ka ~30 Å, for metals; ka ~ 20 Å, for semiconductors; ka ~ 15 Å, for insulators. This is checked by the k-points convergence study for Ni bulk in Figure 2- 1 (c).

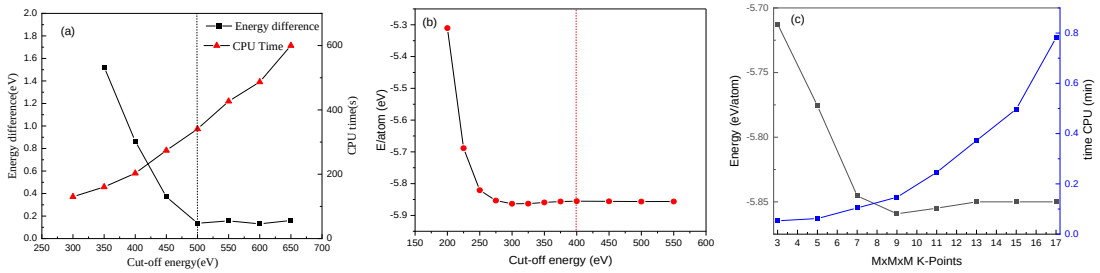

Figure 2- 1. Cut-off energy convergence test for (a) graphene and (b) Ni bulk, and (c) k-points convergence study for Ni bulk.

2.5 Exploring the potential energy surface

There are still many things that need to be considered when simulating a reaction model, such as long-range dispersion interactions, geometry optimization, and transition state searching. In this section, I will discuss how the potential energy surface (PES) of a model can be efficiently explored to obtain accurate structures and apply it to several chemical problems.

2.5.1 Correction of dispersion interactions

Because only local characteristics are employed to compute the exchange-correlation energy, the functionals like LDA and GGA fail to estimate electron dispersion forces (long-range electron correlations). However, dispersion interactions play a crucial role in some situations, especially for the surface reactivity involving the large system of polarizable atoms. In this work, a commonly used method, DFT-D3, is applied to correct the dispersion interaction in the DFT calculations.[24] The dispersion

correction energy term (E_{disp}) is computed as the total contributions from all atomic pairs in the system within a certain cutoff radius, see in Eq. 2-10:

$$E_{disp} = -\sum_{A,B} \frac{C_{AB}^6}{r_{AB}^6} \quad \text{Eq. 2-10}$$

Where r_{AB} is the distance between atom A and B, and C_{AB} is the dispersion coefficient, which varies based on the element and immediate chemical environment of each atom. With an acceptable computational burden by adding the dispersion energy to computed DFT energy, DFT-D3 has been proved to describe dispersion forces effectively in DFT calculation.

2.5.2 Geometry optimization

The nuclei and electrons can be treated separately in the geometry optimization according to the Born-Oppenheimer approximation. So, iterations of ionic (the outer layer loop) and electronic loops (the inner layer loop) are processed in the geometry optimization computations. The nuclei's coordinates can be adjusted along with the PES by the classical mechanics' law. To derive the forces on the ionic coordinates, the outer layer loop will use the converged results of the inner layer loop, which guides the atomic coordinates optimizing the pathway to the ground-state configuration. And the configuration will be modified until fulfilling the user-defined threshold for energy and inter-atomic forces. In other words, the previously described iteration works aim to search for the local minima of the PES around the input geometry. And several optimization algorithms have been developed, such as the quasi-Newton (RMM-DIIS) and the conjugate gradient algorithm.[25,26] The selection of the optimization algorithm should be combined with a certain model and tested by comparing the convergence time.

2.5.3 Transition state search and NEB methods

The transition state theory (TST) believes that the reactant molecules do not only

directly form products through simple collision but must go through a transition state with activation energy. TST is applied to calculate rate constants for elementary reactions/steps which have intrinsic reaction barriers, which can be depicted in Figure 2-2. Within the TST framework, the rate constant has the general form Eq. 2-11:

$$k_{TST} = \frac{k_B T}{h} \frac{q_{TS}^0}{q_R^0} e^{\left(-\frac{\Delta E_{TS}}{k_B T}\right)} \quad \text{Eq. 2-11}$$

Where q_{TS}^0 and q_R^0 are the partition functions for the transition states (TS) and reactants concerning their ground states. ΔE_{TS} is the barrier energy which equals the energy difference between the transition state and the reactant or product. k_B and h is the Boltzmann constant and Planck constant, respectively.

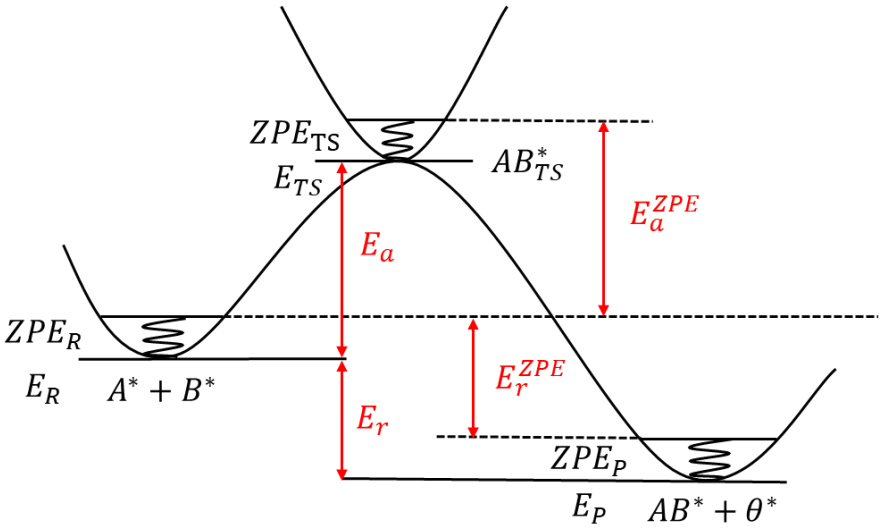

Figure 2-2. Schematic energy diagram for a surface reaction. A^*, B^* and AB^* are the adsorbed species, θ^* represents an active site, and the transition state is AB_{TS}^*. ZPE is the zero-point energy. E_r is the reaction energy and E_a is the activation energy.

The transition state of a chemical reaction has the highest potential energy along the reaction coordinate corresponding to the highest saddle point on the minimum energy path of the reaction. Specifically, saddle points are identified as points in which PES's first derivative of the energy is zero and the second derivative is positive in all but one direction. In mathematical terms, this is expressed as Eq. 2-12:

$$\frac{\partial E}{\partial x_i} = 0; \frac{\partial^2 E}{\partial x_i^2} > 0; \frac{\partial^2 E}{\partial x_\tau^2};\ i \neq \tau \quad \text{Eq. 2-12}$$

The climbing image nudged elastic band (cNEB) and improved dimer methods were employed to find saddle points and minimum energy paths in this work. Along the reaction pathway, the nudged elastic band (NEB) method optimizes a series of

intermediate configurations created by linear coordinates interpolation of the reactant and product. In each configuration optimization, the algorithm seeks the lowest energy while remaining equal spacing to its neighbors. Furthermore, it generates the spring force connecting each pair of configurations and the energy of structures is optimized under such forces to obtain a more accurate minimum energy path. The cNEB method is a little tweak to the NEB method in which the picture with the highest energy is located to the saddle point. In some simple systems, the reaction end-points can be guessed, and the nudged elastic band can be used to find reaction pathways.[27,28] Reaction endpoints may be predicted in some simple systems, then the NEB method can be used to discover reaction pathways. However, it has been demonstrated that, in complex systems, reactions frequently occur through unanticipated pathways. The dimer approach addresses this issue by looking for saddle points that correlate to more complex and uncertain reaction processes.

2.6 Challenges for DFT

Currently, DFT has been employed widely in the investigation of materials and chemistry,[29–31] however, the exchange-correlation functional is responsible for both DFT's successes and challenges. Despite recent improvements, there are still difficulties in using density functional theory to properly describe several problems:

(1) DFT describes different spin multiplicity by exchange-correlation functional, different way that HF theory that describes it by the exchange integral on the occupied orbital, therefore, relative energy of states is often poorly described.

(2) The improved accuracy by the hybrid DFT functionals take a tremendous computational cost, especially for the large multi-electron complex. Despite hybrid methods with a suitable parametrized amount of exact exchange that may derive better results, there are still difficulties in accurately simulating band gaps and ferromagnetism properties.

(3) DFT’s description of excited-state properties has been mainly improved in recent work by optimizing functionals with simultaneous good performance for valence

excitations and charge-transfer excitations. However, the development of the time-dependent-DFT methods with higher accuracy to treat molecular spectra and band gaps still needs more works.

To tackle these problems, a uniform functional with the accurate treatment of electron's correlation need to be developed.

2.7 Data analysis

2.7.1 Electronic structure analysis

Bader charge analysis. Bader's atoms-in-molecule analysis is employed to analyze the atomic electron charge distribution in a system. This approach defines an atom based on zero flux surfaces, which is a 2D surface with the minimum perpendicular charge density to it.[32,33] The charge contained within the Bader volume is a reasonable estimate of the total atomic charge. Moreover, it can also be applied to determine multipole moments of interacting atoms and the hardness of atoms.

The density of states (DOS) and work function (WF). DOS stands for the density of energy levels available to electrons and is used to characterize the electronic state of a material. As shown in Eq. 2-13, the electronic DOS can be calculated in VASP by integrating the corresponding electron density in the k space.

$$\rho(E)dE = number\ of\ electron\ states\ with\ energies\ in\ interval\ (E, E+dE) \qquad \text{Eq. 2-13}$$

In general, topological features of the system, such as band structure, have a significant influence on the density of states attributes. The continuous density of states means that the increase in electron energy makes more states available for occupation. There are no states available for electrons to occupy inside the band-gap of a material with a discontinuous density of states. The WF is the minimum thermodynamic energy required to remove an electron from a solid's valence band to a point in the vacuum immediately outside the solid surface. It is calculated by *Eq. 2- 14*:

$$\Phi = \mathrm{E}_{\mathrm{vacuum}} - \mathrm{E}_{valence} \qquad \textit{Eq. 2- 14}$$

in which $\mathrm{E}_{\mathrm{vacuum}}$ is the average potential of the unit cell and $\mathrm{E}_{valence}$ is the

highest energy band occupied by an electron on the surface.

The d-band theory is effective in determining the bond formation and reactivity trends in transition metals.[34,35] It describes the interaction between adsorbate valence states and the *s* and *d* states of a transition-metal surface. The filling of the antibonding states determines the bond strength, however, unlike gas-phase chemistry, where it is dictated by the number of electrons in the system, the filling of the antibonding states relative to the Fermi level determines the interaction with extended materials like metal surfaces. Hence, the energy of the d-band center relative to the Fermi level is an excellent initial indicator of bond strength since the antibonding states are always above the Fermi level, which is calculated by the following equation Eq. 2-15:

$$\epsilon_{\mathrm{d}} = \frac{\int_{-\infty}^{+\infty} \mathrm{n_d}(\epsilon)\epsilon \mathrm{d}\epsilon}{\int_{-\infty}^{+\infty} \mathrm{n_d}(\epsilon)\mathrm{d}\epsilon} \qquad \text{Eq. 2-15}$$

where ϵ represents the energy of the states and $n_d(\epsilon)$ is the electron density of d states. The greater the d states' energy or the higher the antibonding states' energy compared to the Fermi level, the stronger the bond.

2.7.2 Frequency calculations and the zero-point energy

The first derivative of PES is the force field of the atom and the derivative of the force field is the Hessian matrix (as shown in Eq. 2-16). The Hessian matrix ($|\mathrm{H}$) can be used to determine the vibrational modes of a system or group of atoms, in which r are the coordinates of atoms. The displacements and energy associated with each vibrational mode are represented by the eigenvectors and eigenvalues of the Hessian matrix.

$$|H_{ij} = \frac{\partial^2 E}{\partial r_i \partial r_j}; force_i = \frac{\partial E}{\partial r_i} \qquad \text{Eq. 2-16}$$

The zero-point energy (ZPE) is the lowest possible energy that a quantum mechanical system may have. Unlike in classical mechanics, quantum systems constantly fluctuate in their lowest energy state as described by the Heisenberg uncertainty principle. The harmonic approximation is employed to estimate the effects of the quantum mechanical harmonic oscillator. The minimum energy corrected by the

zero-point energy can be achieved by Eq. 2-17.

$$E = E_0 + \sum_i \frac{hv_i}{2} \qquad \text{Eq. 2-17}$$

in which, E_0 is the ground energy derived from a DFT calculation and v_i are the normal frequency modes.

2.7.3 Thermodynamic calculation

Calculation of thermodynamic properties (entropy, enthalpy, and free energy) at a certain temperature is the first step to investigate the reaction's thermodynamics and the preparation for microkinetic models. We coded Python scripts to achieve the calculation of partition functions and thermodynamic properties as described in the flow diagram Figure 2-3. Furthermore, the properties at high temperatures were extrapolated from the optimized data at 0K and neglected any electronic excitation. To improve the accuracy of the energy, ZPE is employed to correct the static DFT electronic energy.

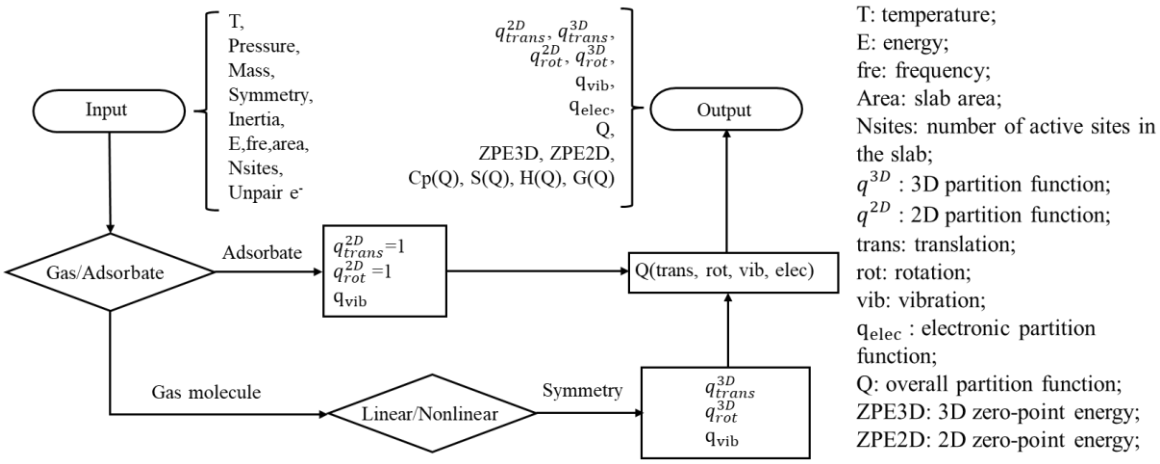

Figure 2-3. Coded flow diagram for finding thermodynamic properties.

```
matlab.engine
pandas

Input=(pressure,Mass,symmetry,inertia,areaS,Nsites,mag,fre)
if geometry == 'linear':
        eng.thermal_linear_molecule(Input)
if geometry == 'nonlinear':
        eng.thermal_nonlinear_molecule(Input)
if geometry == 'surface':
        eng.thermal_surface(Input)
if geometry == 'adsorbate':
        eng.thermal_adsorbate(Input)
```

Figure 2-4. The pseudo-code of thermodynamic calculations.

The temperature effect on adsorption energy (E_{ads}), reaction energy (E_r), activation energy (E_a) is taken into account to obtain more accurate results. The global partition function, Q, is used to depict the energy as a function of temperature for the intermediates on the surface or in the gas phase, and the basic thermodynamic characters such as entropy (S, Eq. 2-18), specific heat at constant pressure (C_p, Eq. 2-19) and enthalpy (H, Eq. 2-20) can be derived by the global partition function (Q); k_B is the Boltzmann constant, T is the temperature. Q is calculated as Eq. 2-22, where the translational, rotational, vibrational, electronic, and nuclear contributions are considered.

$$S = k_B \ln Q + k_B T \left(\frac{\partial \ln Q}{\partial T}\right)_V \quad \text{Eq. 2-18}$$

$$C_p = T \left(\frac{\partial S}{\partial T}\right)_P \quad \text{Eq. 2-19}$$

$$H = E_{DFT} + E_{(S=0,T=0,ZPE)} + \int_0^T C_p \, \partial T \quad \text{Eq. 2-20}$$

$$G = H - TS \quad \text{Eq. 2-21}$$

$$Q = q_{trans} \times q_{rot} \times q_{vib} \times q_{elec} \times q_{nuclear} \quad \text{Eq. 2-22}$$

The electronic partition function is approximated to the ground state multiplicity, e.g., $q_{elec}^{NH_3} = 1$, and the nuclear partition functions are unity, i.e., $q_{nuclear} = 1$. The vibrational partition function of a system is obtained via Eq. 2-23.

$$q_{vib} = \prod_{i=1}^{N} \frac{1}{1 - e^{-h\nu_i / k_B T}} \quad \text{Eq. 2-23}$$

Where ν_i is a specific vibrational mode and N is the number of modes. The

vibrational partition function in the gas phase, q_{vib}^{gas}, is also calculated using the equation above for $3N_i$-6 and $3N_i$-5 vibrational degrees of freedom of a non-linear and linear molecule in the gas phase, respectively, where N_i is the number of atoms in the molecule. The 2D vibrational partition function includes all modes for the surface adsorbates. The 2D-translational partition function for an adsorbate molecule is derived by the Eq. 2-24, where A_{cat} is the average area of one active site on the surface.

$$q_{trans}^{2D}(A,T) = \left(\frac{2\pi m k_B T}{h^2}\right) A_{cat} \quad \text{Eq. 2-24}$$

The 3D-translational partition function for a molecule is calculated by Eq. 2-25, where $V_{(P,T)}$ is derived by $V_{(P,T)} = k_B T/p$, p is the pressure of the gas phase.

$$q_{trans}^{3D} = V_{(P,T)} \times \frac{(2\pi m k_B T)^{3/2}}{h^3} \quad \text{Eq. 2-25}$$

The rotational partition function for a free molecule is calculated by Eq. 2-26 and Eq. 2-27, depending on its symmetry and linear type.

$$q_{rot}^{linear} = \frac{\pi^{1/2}}{\sigma h}(I_z)^{1/2}(8\pi^2 k_B T)^{1/2} \quad \text{Eq. 2-26}$$

$$q_{rot}^{nonlinear} = \frac{1}{\sigma}\left(\frac{8\pi^2 k_B T}{h^2}\right)^{3/2}\sqrt{\pi I_x I_y I_z} \quad \text{Eq. 2-27}$$

Where σ is the symmetry factor and I is the moment of inertia defined as Eq. 2-28, in which the sum is over the atoms in the molecule, m_i is the mass of atom and r_i is its distance from the rotation axis. I_x, I_y and I_z is the moment of inertia about the x-, y- and z-axis that passes through the center of mass of the species, respectively.

$$I = \sum_i m_i r_i^2 \quad \text{Eq. 2-28}$$

2.7.4 Reaction constants calculation

I coded another script to calculate the reaction rate constants of all elementary steps. Figure 2-5 shows the process of the script. The detailed information of the equations used in the script is introduced in the following.

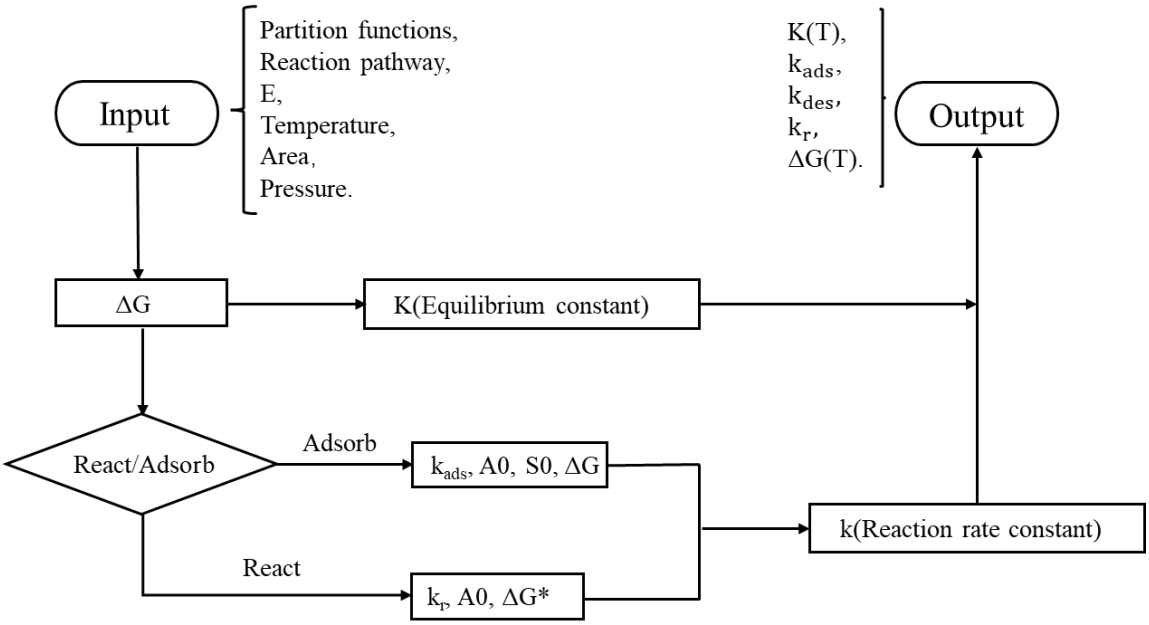

Figure 2-5. The flow diagram of reaction rate constant and equilibrium constant calculation

The adsorption transition state energy, barrier energy of adsorption and desorption processes are calculated by Eq. 2-29, Eq. 2-30 and Eq. 2-31, respectively:

$$\mathrm{E_{ts}} = \mathrm{E_{gas}} + \mathrm{E_{surf}} + \left(\mathrm{ZPE_{2D}^{gas}} - \mathrm{ZPE_{3D}^{gas}}\right) \quad \text{Eq. 2-29}$$

$$\mathrm{E_a^{ads}} = \mathrm{E_{ts}} - \mathrm{E_{gas}} - \mathrm{E_{surf}} \quad \text{Eq. 2-30}$$

$$\mathrm{E_a^{des}} = \mathrm{E_{ts}} - \mathrm{E_{adsorbate}} \quad \text{Eq. 2-31}$$

The adsorption energy is calculated by Eq. 2-32:

$$\mathrm{E_{ads}} = \mathrm{E_{gas}} + \mathrm{E_{surf}} - \mathrm{E_{adsorbate}} \quad \text{Eq. 2-32}$$

In the above formulas, E_{surf}, $\mathrm{E_{gas}}$, $\mathrm{E_{adsorbate}}$ and $\mathrm{E_{ts}}$ are the energies of the clean surface, isolate gas molecule, adsorbate system, and transition states, respectively. The difference between the 2- (ZPE_{2D}^{gas}) and 3-dimensional (ZPE_{3D}^{gas}) zero-point energy is applied to describe the adsorption transition state energy.

The classical Hertz-Knudsen equation was employed to estimate the rate of adsorption, as following Eq. 2-33 to Eq. 2-40.

$$\mathrm{Q_{reactants}} = \left(\mathrm{q_{trans2D}^{ads}} \times \mathrm{Q_{notrans3D}^{gas}}\right)^{(\mathrm{stoichio_{ads}})} \times \mathrm{Q_{surf}^{(stoichio_{surf})}} \quad \text{Eq. 2-33}$$

$$Q_{ts}^{2D} = \left(q_{vib2D}^{ads}\right)^{(stoichio_{ads})} \times Q_{surf}^{(stoichio_{surf})} \quad \text{Eq. 2-34}$$

$$Q_{reactants} = \left(Q_{3D}^{ads}\right)^{stoichio_{ads}} \quad \text{Eq. 2-35}$$

$$Sticky_{ads} = \frac{Q_{ts}^{2D}}{Q_{reactants}} \times e^{-\frac{E_a^{ads}}{k_B T}} \quad \text{Eq. 2-36}$$

$$Sticky_{des} = \frac{Q_{ts}^{2D}}{Q_{products}} \times e^{-\frac{E_a^{des}}{k_B T}} \quad \text{Eq. 2-37}$$

$$A_0 = areaS \times \frac{1}{(2\pi m k_B T)^{0.5}} \quad \text{Eq. 2-38}$$

$$k_{ads} = A_0 \times Sticky_{ads} \quad \text{Eq. 2-39}$$

$$k_{des} = A_0 \times Sticky_{des} \quad \text{Eq. 2-40}$$

where A_0 is the pre-exponential factor, $areaS$ is the average surface of an active site and m is the mass of the adsorbates. The sticking coefficients, $Sticky_{ads}$ and $Sticky_{des}$, are measures of the fraction of incident molecules that adsorb upon the surface, according to the collision theory, and are calculated via Eq. 2-36 and Eq. 2-37. [36]

As for the surface reactions in the heterogeneous catalytic system, which is considered in our research, the constant rate (k) of each surface elementary step is commonly computed using the transition state theory (TST) approximation of Eyring and Evans and Polanyi, as follows (Eq. 2-41):[37]

$$k_r = A_0 e^{-\frac{\Delta G^*}{k_B T}} = \frac{k_B T}{h} \frac{Q_{TS}}{Q_{IS}} e^{-\frac{\Delta G^*}{k_B T}} \quad \text{Eq. 2-41}$$

where h is the Plank constant, k_B is the Boltzmann constant, T is the temperature, A_0 is the pre-exponential factor, ΔG* is the reaction activation energy, and Q_{TS} and Q_{IS} are the partition functions of transition states and reactants, respectively. The translations and rotations of the adsorbed species are frustrating, and therefore, I considered only vibrational modes.

I have considered an active site where the reactants and products in every elementary step occupy only one site on the surface. Consequently, the coverage of free sites, $\theta_*(t)$, is defined by Eq. 2-42, where the $\theta_i(t)$ represents the coverage of the intermediates present in the reaction system.

$$\theta_*(\mathrm{t}) = 1 - \sum_{\mathrm{i}}^{\mathrm{n}} \theta_{\mathrm{i}}(\mathrm{t}) \qquad \text{Eq. 2-42}$$

2.7.5 Adsorption/desorption and reaction simulation

The dehydrogenation and adsorption/desorption elementary steps during the ammonia decomposition and their rate equations are listed below (Table 2-1). There are three kinds of elementary steps in the ammonia decomposition: 'A' and 'D' represent the adsorption and desorption processes, respectively, and 'R' is the surface reaction.

Table 2-1. Elementary steps in the ammonia decomposition

No.	Reaction	Rate equation
A1	$\mathrm{NH_3} + * \longrightarrow \mathrm{NH_3^*}$	$\mathrm{r_{a1}} = \mathrm{k_{a1}} Y_{\mathrm{NH_3}}(\mathrm{t})\theta_*(\mathrm{t})$
D1	$\mathrm{NH_3^*} \longrightarrow \mathrm{NH_3} + *$	$r_{d1} = k_{d1}\theta_{NH_3}(t)$
R1	$\mathrm{NH_3^*} + * \longrightarrow \mathrm{NH_2^*} + \mathrm{H^*}$	$r_{r1} = k_{r1}\theta_{NH_3}(t)\theta_*(\mathrm{t})$
R2	$\mathrm{NH_2^*} + \mathrm{H^*} \longrightarrow \mathrm{NH_3^*} + *$	$r_{\mathrm{r2}} = k_{\mathrm{r2}}\theta_{NH_2}(t)\theta_{\mathrm{H}}(t)$
R3	$\mathrm{NH_2^*} + * \longrightarrow \mathrm{NH^*} + \mathrm{H^*}$	$r_{\mathrm{r3}} = k_{\mathrm{r3}}\theta_{NH_2}(t)\theta_*(\mathrm{t})$
R4	$\mathrm{NH^*} + \mathrm{H^*} \longrightarrow \mathrm{NH_2^*} + *$	$r_{\mathrm{r4}} = k_{\mathrm{r4}}\theta_{\mathrm{NH}}(t)\theta_H(t)$
R5	$\mathrm{NH^*} + * \longrightarrow \mathrm{N^*} + \mathrm{H^*}$	$r_{\mathrm{r5}} = k_{\mathrm{r5}}\theta_{NH}(t)\theta_*(\mathrm{t})$
R6	$\mathrm{N^*} + \mathrm{H^*} \longrightarrow \mathrm{NH^*} + *$	$r_{r6} = k_{r6}\theta_N(t)\theta_H(t)$
R7	$2\mathrm{N^*} \longrightarrow N_2^* + *$	$r_{r7} = k_{r7}\theta_N^2(t)$
R8	$N_2^* + * \longrightarrow 2\mathrm{N^*}$	$r_{r8} = k_{r8}\theta_{N_2}(t)\theta_*(\mathrm{t})$
D2	$N_2^* \longrightarrow N_2 + *$	$r_{d2} = k_{d2}\theta_{N_2}(t)$
A2	$N_2 + * \longrightarrow N_2^*$	$\mathrm{r_{a2}} = \mathrm{k_{a2}} Y_{\mathrm{N_2}}(\mathrm{t})\theta_*(\mathrm{t})$
R9	$2\mathrm{H^*} \longrightarrow H_2^* + *$	$r_{r9} = k_{r9}\theta_H^2(t)$
R10	$H_2^* + * \longrightarrow 2\mathrm{H^*}$	$r_{r10} = k_{r10}\theta_{H_2}(t)\theta_*(\mathrm{t})$
D3	$H_2^* \longrightarrow \mathrm{H_2} + *$	$r_{d3} = k_{d3}\theta_{H_2}(t)$
A3	$\mathrm{H_2} + * \longrightarrow H_2^*$	$\mathrm{r_{a3}} = \mathrm{k_{a3}} Y_{H_2}(\mathrm{t})\theta_*(\mathrm{t})$

* $Y_{molecule}(t)$ is the time-dependent ratio between the molecule's partial pressure and the total number of active sites on the catalyst.

In heterogeneous catalysis, the temperature-programmed desorption (TPD) technique is a powerful tool to study the mechanisms of molecular adsorption/desorption and surface reactions since it allows researchers to study the interaction of gas species with catalysts surfaces and at which temperature (i.e., energy) events take place. In my simulated process, the temperature-programmed

reaction model starts from the pre-adsorbed molecule, e.g., N_2 and H_2, the temperature increases at a different rate from 200 to 1000 K while any gas was extracted to avoid the re-adsorption of gases. It is also applied to examine the adsorption properties of any molecular species over different surfaces in this research. And the derivatives of species in the model can be derived by the rate equations in Table 2-1 as follows:

$$\frac{\mathrm{dY_{N_2}}}{\mathrm{dt}} = \mathrm{r}_{d2} \quad \text{Eq. 2-43}$$

$$\frac{\mathrm{dY_{H_2}}}{\mathrm{dt}} = \mathrm{r_{d3}} \quad \text{Eq. 2-44}$$

$$\frac{\mathrm{d\theta_N}}{\mathrm{dt}} = \mathrm{r_{r5}} - \mathrm{r_{r6}} - 2 \times r_{r7} + 2 \times r_{r8} \quad \text{Eq. 2-45}$$

$$\frac{\mathrm{d\theta_H}}{\mathrm{dt}} = \mathrm{r_{r1}} - \mathrm{r_{r2}} + \mathrm{r_{r3}} - \mathrm{r_{r4}} + \mathrm{r_{r5}} - \mathrm{r_{r6}} - 2 \times r_9 - 2 \times r_{10} \quad \text{Eq. 2-46}$$

$$\frac{\mathrm{d\theta_*}}{\mathrm{dt}} = -\left(\frac{\mathrm{d\theta_N}}{\mathrm{dt}} + \frac{\mathrm{d\theta_H}}{\mathrm{dt}}\right) \quad \text{Eq. 2-47}$$

The batch reactor is the most common reactor vessel in industrial operations.[38,39] The batch reactor simulations shed a light on the design of the catalyst and provide detailed reaction process information. The batch reactor models under a variety of conditions is employed here to investigate the catalytic properties when the catalytic surface is in contact with a given amount of NH_3. And the derivatives of species in the model can be derived by the rate equations in Table 2-1 as follows:

$$\frac{\mathrm{dY_{NH_3}}}{\mathrm{dt}} = -\mathrm{r_{a1}} + \mathrm{r_{d2}} \quad \text{Eq. 2-48}$$

$$\frac{\mathrm{dY_{N_2}}}{\mathrm{dt}} = -\mathrm{r_{a2}} + \mathrm{r}_{d2} \quad \text{Eq. 2-49}$$

$$\frac{\mathrm{dY_{H_2}}}{\mathrm{dt}} = -\mathrm{r_{a3}} + \mathrm{r_{d3}} \quad \text{Eq. 2-50}$$

$$\frac{\mathrm{d\theta_{NH_3}}}{\mathrm{dt}} = r_{\mathrm{a1}} - r_{\mathrm{d1}} - r_{\mathrm{r1}} + r_{\mathrm{r2}} \quad \text{Eq. 2-51}$$

$$\frac{\mathrm{d\theta_{NH_2}}}{\mathrm{dt}} = r_{\mathrm{r1}} - r_{\mathrm{r2}} - r_{\mathrm{r3}} + r_{\mathrm{r4}} \quad \text{Eq. 2-52}$$

$$\frac{\mathrm{d\theta}_{NH}}{\mathrm{dt}} = \mathrm{r_{r3}} - \mathrm{R_{r4}} - \mathrm{R_{r5}} + \mathrm{R_{r6}} \quad \text{Eq. 2-53}$$

$$\frac{\mathrm{d\theta_N}}{\mathrm{dt}} = \mathrm{r_{r5}} - \mathrm{r_{r6}} - 2 \times \mathrm{r_{r7}} + 2 \times r_{r8} \quad \text{Eq. 2-54}$$

$$\frac{\mathrm{d\theta_H}}{\mathrm{dt}} = \mathrm{r_{r1}} - \mathrm{r_{r2}} + \mathrm{r_{r3}} - \mathrm{r_{r4}} + \mathrm{r_{r5}} - \mathrm{r_{r6}} - 2 \times r_9 - 2 \times r_{10} \quad \text{Eq. 2-55}$$

$$\frac{\mathrm{d}\theta_{\mathrm{N_2}}}{\mathrm{dt}} = \mathrm{r_{r7}} - r_{r8} - r_{d2} + \mathrm{r_{a2}} \quad \text{Eq. 2-56}$$

$$\frac{\mathrm{d}\theta_{\mathrm{H_2}}}{\mathrm{dt}} = \mathrm{r_{r9}} - r_{r10} - r_{d3} + \mathrm{r_{a3}} \quad \text{Eq. 2-57}$$

$$\frac{\mathrm{d}\theta_{*}}{\mathrm{dt}} = -\left(\frac{\mathrm{d}\theta_{\mathrm{NH_3}}}{\mathrm{dt}} + \frac{\mathrm{d}\theta_{\mathrm{NH_2}}}{\mathrm{dt}} + \frac{\mathrm{d}\theta_{NH}}{\mathrm{dt}} + \frac{\mathrm{d}\theta_{\mathrm{N}}}{\mathrm{dt}} + \frac{\mathrm{d}\theta_{\mathrm{H}}}{\mathrm{dt}} + \frac{\mathrm{d}\theta_{\mathrm{N_2}}}{\mathrm{dt}} + \frac{\mathrm{d}\theta_{\mathrm{H_2}}}{\mathrm{dt}}\right) \quad \text{Eq. 2-58}$$

2.8 Computational resources

VASP calculations were performed on CPU resources provided by the Supercomputing Wales (Hawk) and the Materials Chemistry Consortium (Thomas and Young). The details of each computing cluster are summarised in Table 2-2.

Table 2-2. The details of supercomputing employed in the research

Cluster name	CPU Type	Cores/node	Core frequency	# of nodes
Hawk	Intel Xeon Gold	20	2.40GHz	216
	AMD Epyc	32	2.50GHz	64
Thomas	Intel Xeon E5	24	2.20GHz	705
Young	Intel Xeon Gold	40	2.50GHz	576

A node is a physical self-contained computer unit in a distributed supercomputing cluster. It has its processors (CPU or GPU), memory, I/O, and storage. And cores are single computing processors in nodes. Each node can have multiple processors and each processor can have multiple cores. The cores/node in Table 2-2 stands for the number of cores per node. These cores share a memory, I/O, and storage. We can see that, in terms of cores/node, Young has a bigger size compared with Hawk and Thomas, which means it performs better in the heavily parallel calculations. Aside from the hardware, the job management system is responsible for the fulfillment of computation work. There are two Linux job management systems used in the research: the portable Batch System (PBS) on Thomas and Young; and the simple Linux utility for resource management (SLURM) on Hawk. They are highly accessible and fault-tolerant systems that organize and schedule all computing jobs in a large cluster depending on the available computing resources and submitted jobs.

2.9 Reference

(1) Schrödinger, E. An Undulatory Theory of the Mechanics of Atoms and Molecules. *Phys. Rev.* **1926**, *28* (6), 1049–1070. https://doi.org/10.1103/PhysRev.28.1049.

(2) Lindsay, R. B. On the Atomic Models of the Alkali Metals. *Journal of Mathematics and Physics* **1924**, *3* (4), 191–236. https://doi.org/10.1002/sapm192434191.

(3) Hartree, D. R. The Wave Mechanics of an Atom with a Non-Coulomb Central Field. Part I. Theory and Methods. *Mathematical Proceedings of the Cambridge Philosophical Society* **1928**, *24* (1), 89–110. https://doi.org/10.1017/S0305004100011919.

(4) Froese Fischer, C. General Hartree-Fock Program. *Computer Physics Communications* **1987**, *43* (3), 355–365. https://doi.org/10.1016/0010-4655(87)90053-1.

(5) Kresse, G.; Joubert, D. From Ultrasoft Pseudopotentials to the Projector Augmented-Wave Method. *Physical review b* **1999**, *59* (3), 1758.

(6) Kresse, G.; Hafner, J. Ab Initio Molecular Dynamics for Liquid Metals. *Phys. Rev. B* **1993**, *47* (1), 558–561. https://doi.org/10.1103/PhysRevB.47.558.

(7) Hohenberg, P.; Kohn, W. Density Functional Theory (DFT). *Phys. Rev* **1964**, *136*, B864.

(8) Born, M.; Oppenheimer, R. Zur Quantentheorie Der Molekeln. *Annalen der Physik* **1927**, *389* (20), 457–484. https://doi.org/10.1002/andp.19273892002.

(9) Kohn, W.; Sham, L. J. Self-Consistent Equations Including Exchange and Correlation Effects. *Physical review* **1965**, *140* (4A), A1133.

(10) Perdew, J. P.; Chevary, J. A.; Vosko, S. H.; Jackson, K. A.; Pederson, M. R.; Singh, D. J.; Fiolhais, C. Atoms, Molecules, Solids, and Surfaces: Applications of the Generalized Gradient Approximation for Exchange and Correlation. *Phys. Rev. B* **1992**, *46* (11), 6671–6687. https://doi.org/10.1103/PhysRevB.46.6671.

(11) Langreth, D. C.; Mehl, M. J. Beyond the Local-Density Approximation in Calculations of Ground-State Electronic Properties. *Phys. Rev. B* **1983**, *28* (4), 1809–1834. https://doi.org/10.1103/PhysRevB.28.1809.

(12) Barth, U. von; Hedin, L. A Local Exchange-Correlation Potential for the Spin Polarized Case. i. *J. Phys. C: Solid State Phys.* **1972**, *5* (13), 1629–1642. https://doi.org/10.1088/0022-3719/5/13/012.

(13) Oliver, G. L.; Perdew, J. P. Spin-Density Gradient Expansion for the Kinetic Energy. *Phys. Rev. A* **1979**, *20* (2), 397–403. https://doi.org/10.1103/PhysRevA.20.397.

(14) Kohn, W.; Sham, L. J. Quantum Density Oscillations in an Inhomogeneous Electron Gas. *Physical Review* **1965**, *137* (6A), A1697.

(15) Perdew, J. P.; Yue, W. Accurate and Simple Density Functional for the Electronic Exchange Energy: Generalized Gradient Approximation. *Phys. Rev. B* **1986**, *33* (12), 8800–8802. https://doi.org/10.1103/PhysRevB.33.8800.

(16) Perdew, J. P.; Burke, K.; Wang, Y. Generalized Gradient Approximation for the Exchange-Correlation Hole of a Many-Electron System. *Physical review B* **1996**, *54* (23), 16533.

(17) Ernzerhof, M.; Scuseria, G. E. Assessment of the Perdew–Burke–Ernzerhof Exchange-Correlation Functional. *The Journal of chemical physics* **1999**, *110* (11), 5029–5036.
(18) Hammer, B.; Hansen, L. B.; Nørskov, J. K. Improved Adsorption Energetics within Density-Functional Theory Using Revised Perdew-Burke-Ernzerhof Functionals. *Physical review B* **1999**, *59* (11), 7413.
(19) Parr, R. G.; Yang, W. Density Functional Approach to the Frontier-Electron Theory of Chemical Reactivity. *Journal of the American Chemical Society* **1984**, *106* (14), 4049–4050.
(20) Becke, A. D. Density‐functional Thermochemistry. III. The Role of Exact Exchange. *J. Chem. Phys.* **1993**, *98* (7), 5648–5652. https://doi.org/10.1063/1.464913.
(21) Perdew, J. P.; Ernzerhof, M.; Burke, K. Rationale for Mixing Exact Exchange with Density Functional Approximations. *J. Chem. Phys.* **1996**, *105* (22), 9982–9985. https://doi.org/10.1063/1.472933.
(22) Heyd, J.; Scuseria, G. E.; Ernzerhof, M. Hybrid Functionals Based on a Screened Coulomb Potential. *The Journal of chemical physics* **2003**, *118* (18), 8207–8215.
(23) Monkhorst, H. J.; Pack, J. D. Special Points for Brillouin-Zone Integrations. *Physical review B* **1976**, *13* (12), 5188.
(24) Grimme, S.; Antony, J.; Ehrlich, S.; Krieg, H. A Consistent and Accurate Ab Initio Parametrization of Density Functional Dispersion Correction (DFT-D) for the 94 Elements H-Pu. *J. Chem. Phys.* **2010**, *132* (15), 154104. https://doi.org/10.1063/1.3382344.
(25) Press, W. H.; Vetterling, W. T.; Teukolsky, S. A.; Flannery, B. P. *Numerical Recipes*; Cambridge university press Cambridge, 1986; Vol. 818.
(26) Pulay, P. Convergence Acceleration of Iterative Sequences. The Case of SCF Iteration. *Chemical Physics Letters* **1980**, *73* (2), 393–398.
(27) Henkelman, G.; Uberuaga, B. P.; Jónsson, H. A Climbing Image Nudged Elastic Band Method for Finding Saddle Points and Minimum Energy Paths. *J. Chem. Phys.* **2000**, *113* (22), 9901–9904. https://doi.org/10.1063/1.1329672.
(28) Henkelman, G.; Jónsson, H. Improved Tangent Estimate in the Nudged Elastic Band Method for Finding Minimum Energy Paths and Saddle Points. *J. Chem. Phys.* **2000**, *113* (22), 9978–9985. https://doi.org/10.1063/1.1323224.
(29) He, Q.; Yu, B.; Li, Z.; Zhao, Y. Density Functional Theory for Battery Materials. *Energy & Environmental Materials* **2019**, *2* (4), 264–279.
(30) Cui, X.; Tang, C.; Zhang, Q. A Review of Electrocatalytic Reduction of Dinitrogen to Ammonia under Ambient Conditions. *Advanced Energy Materials* **2018**, *8* (22), 1800369.
(31) Shet, S. P.; Priya, S. S.; Sudhakar, K.; Tahir, M. A Review on Current Trends in Potential Use of Metal-Organic Framework for Hydrogen Storage. *International Journal of Hydrogen Energy* **2021**.
(32) Tang, W.; Sanville, E.; Henkelman, G. A Grid-Based Bader Analysis Algorithm without Lattice Bias. *J. Phys.: Condens. Matter* **2009**, *21* (8), 084204. https://doi.org/10.1088/0953-8984/21/8/084204.
(33) Yu, M.; Trinkle, D. R. Accurate and Efficient Algorithm for Bader Charge Integration.

J. Chem. Phys. **2011**, *134* (6), 064111. https://doi.org/10.1063/1.3553716.
(34) Norsko, J. K. Chemisorption on Metal Surfaces. *Reports on Progress in Physics* **1990**, *53* (10), 1253.
(35) Nørskov, J. K. Electronic Factors in Catalysis. *Progress in surface science* **1991**, *38* (2), 103–144.
(36) Goldberger, M. L.; Watson, K. M. *Collision Theory*; Courier Corporation, 2004.
(37) Chorkendorff, I.; Niemantsverdriet, J. W. *Concepts of Modern Catalysis and Kinetics*; John Wiley & Sons, 2017.
(38) Fernández, L.; Gamallo, M.; González-Gómez, M. A.; Vázquez-Vázquez, C.; Rivas, J.; Pintado, M.; Moreira, M. T. Insight into Antibiotics Removal: Exploring the Photocatalytic Performance of a Fe3O4/ZnO Nanocomposite in a Novel Magnetic Sequential Batch Reactor. *Journal of environmental management* **2019**, *237*, 595–608.
(39) Okolie, J. A.; Rana, R.; Nanda, S.; Dalai, A. K.; Kozinski, J. A. Supercritical Water Gasification of Biomass: A State-of-the-Art Review of Process Parameters, Reaction Mechanisms and Catalysis. *Sustainable energy & fuels* **2019**, *3* (3), 578–598.

Chapter 3 Hydrazine reforming on Ir(111)

Hydrogen transport and storage technology remain one of the critical challenges of the hydrogen economy. Hydrazine (N_2H_4) is a carbon-free hydrogen carrier that has been widely used as fuel in the field of space exploration. I have combined experiments and computer simulations to gain a better understanding of the N_2H_4 decomposition on Ir catalyst, the most efficient catalyst for hydrazine decomposition up to date. We have identified metallic Ir rather than IrO_2 as the active phase for hydrazine decomposition and carried out density functional theory (DFT) calculations to systematically investigate the changes in the electronic structure along with the catalytic decomposition mechanisms. Three catalytic mechanisms to hydrazine decomposition over Ir(111) have been found: (i) intramolecular reaction between hydrazine molecules, (ii) intramolecular reaction between co-adsorbed amino groups, and (iii) hydrazine dehydrogenation assisted by co-adsorbed amino groups. These mechanisms follow five different pathways for which transition states and intermediates have been identified. The results show that hydrazine decomposition on Ir(111) starts preferentially with an initial N-N bond scission followed by hydrazine dehydrogenation assisted by the amino produced, eventually leading to ammonia and nitrogen production. The preference for N-N scission mechanisms was rationalized by analyzing the electronic structure. This analysis showed that upon hydrazine adsorption, the π bond between nitrogen atoms becomes weaker.

3.1 Introduction

In recent years, air pollution, global warming, and new legislation are increasing the demand for low-carbon energy. Hydrogen has been recognized as a clean fuel with high power density, which, in combination with efficient fuel cells, could supply enough power to minimize the current environmental pressure.[1] However, hydrogen transport and storage technology remain one of the critical challenges of the hydrogen economy.

At present, it is very difficult to find novel materials with a high hydrogen storage capacity, and attention is being paid to molecular storage systems such as alcohols, formic acid, ammonia, and hydrazine.

Hydrazine (N_2H_4) is a carbon-free hydrogen carrier with 12.5 wt% hydrogen content, it remains liquid between 2 and 114 °C and is stable in aqueous solutions. As early as 1970, Raschig developed the first commercial process to produce hydrazine, and now, there are many mature processes to produce it, e.g., from urea, Bayer Ketazine, and peroxide processes.[2,3] Especially, recent research has demonstrated the promise of producing hydrazine via microbial conversion of biomass.[4] N_2H_4 is widely used in the manufacturing of agrochemicals, rubber production, and space exploration-related industries. In the latest case, N_2H_4 is used as a propellant fuel for space vehicles and satellites due to the highly exothermic decomposition reactions (*Path* 1 and *Path* 2) generating gaseous products, i.e. N_2, H_2, and NH_3.[5]

$$N_2H_4 \rightarrow N_2 + 2H_2 \qquad \Delta G(273K) = -1.46\ eV \qquad \text{Path 1}$$

$$N_2H_4 \rightarrow 4/3NH_3 + 1/3N_2 \qquad \Delta G(273K) = -1.72\ eV \qquad \text{Path 2}$$

The decomposition process does not strictly follow stoichiometric paths as it is affected by many factors including the nature of the catalyst and the reaction temperature.[6] Since the catalyst strongly determines the activity and selectivity of the process, there have been several studies to develop efficient catalysts for hydrazine decomposition. The earliest commercialized catalyst for hydrazine dissociation consisted of supported Ir particles on γ-alumina (Ir/γ-Al_2O_3). This catalyst was used in spacecraft control thrusters for spontaneous ignition and stability.[7] Cho *et al*. prepared high loading Ir/γ-Al_2O_3 catalysts with multiple impregnation methods and investigated the decomposition of hydrous hydrazine. They found that the catalysts were able to show high hydrogen selectivity only under reaction temperatures above 200 °C.[8] Aika *et al*. investigated the decomposition mechanism on Ir by a micro-catalytic gas chromatographic technique at ~150 °C and showed that the products were only NH_3 and N_2.[5] With the aims to make the catalyst more affordable and widening its applications, Xu *et al*. synthesized a series of mono- and bimetallic nanoparticles (Rh,

Co, Ru, Ir, Fe, Cu, Ni, Pt, Pd) and tested their catalytic activity for hydrazine decomposition.[9–11] The synergistic effect and electron transfer between metals in the alloys improved the H_2 selectivity and activity of the decomposition reaction. And adding NaOH to solution is an effective way to suppress the NH_3 formation, sicne the low protonation of the hydrous hydrazine. Manukyan *et al*. prepared Cu nanoparticles covered by a FeNi alloy, for which hydrogen selectivity reached 100% at 70 °C.[12] Maurel *et al.* studied ^{15}N-labeled hydrazine decomposition on transition metals and found that N_2 is always formed from a single hydrazine molecule without any N-N bond breakage or N scrambling under the range of temperature 60 – 300 °C.[13] Although these precedent works bring insights to the possible reaction pathway, a complete understanding of the catalytic process is still ambiguous and controversial. Computational simulations can provide an atomistic approach to identify the role of the metal active sites along the reaction pathways.

Computational studies have described the full network of reaction pathways in the N_2H_4 decomposition process on metal catalysts. Electronic structure calculations showed that the N_2H_4 dehydrogenation process on terraced and stepped Cu(111) surface and on Rh(111) takes place between co-adsorbed NH_2 resulting from N–N scissions and adsorbed N_2H_x (x = 1-4) dehydrogenation.[14,15]

Thus far, the Ir-based catalysts remain the standard for the decomposition of hydrazine although systematic mechanistic information on the decomposition mechanism over Ir is scarce.[16] For this reason, we have performed accurate simulations including dispersion corrections following three different catalytic mechanisms: (i) intramolecular reaction between hydrazine, (ii) intramolecular reaction between co-adsorbed NH_2, and (iii) hydrazine dehydrogenation assisted by co-adsorbed NH_2 groups.[17] We also provide a comprehensive rationalization of the decomposition process on Ir(111) on its electronic structure, which agrees with our experiment results.

3.2 Computational methods

All calculations have been carried out by the Vienna Ab-initio Simulation Package (VASP) utilizing spin-polarized density functional theory (DFT).[18,19] The exchange-correlation energy was calculated using the Perdew-Burke-Ernzerhof (PBE)[20] form of the generalized gradient approximation (GGA),[21] and the effect of inner cores, including non-spherical contributions to the gradient corrections, were represented by the projector augmented wave (PAW).[21,22] To improve the description of the long-range interaction, we employed the zero damping DFT-D3 method of Grimme,[23] which has been proven to be an upgrade on several systems.[24–26] We used plane-wave basis sets with a kinetic energy cutoff of 500 eV. Optimized structures were converged within a threshold of internal forces smaller than 0.02 eV/Å with the conjugate gradient algorithm and an electronic relaxation threshold of 10^{-5} eV.

The calculated lattice parameter for iridium is 3.843 Å, which is in good agreement with the experimental value of 3.839 Å.[27] The surface was represented by a p(4x4) supercell slab model with 5 atomic layers, where the top three were fully relaxed and the bottom fixed at the bulk lattice. Different slab thicknesses for Ir and IrO_2 were tested until convergence was achieved within 1 meV per atom. The Brillouin zone was sampled by a Γ-centered 3×3×1 Monkhorst-Pack grid with Methfessel-Paxton smearing broadening of σ = 0.2 eV to acquire an accurate description of the total energy. A vacuum of 15 Å was added perpendicular to the surface to avoid spurious interaction with periodic images. Upon molecular interaction, dipole correction along the z-direction was applied to enhance the energy convergence.

There are three main conformations of hydrazine in the gas phase, i.e. gauche, trans, and eclipsed. The energy of trans and eclipsed conformations are 0.13 and 0.36 eV higher than the gauche conformation, respectively.[14] Hence, we used the energy of the gauche conformation as the gas-phase N_2H_4 energy to calculate its adsorption energy and the relative values of intermediates along with the energy profiles according to Eq 3-1.

$$E_{N_yH_x}^{ads} = \left(E_{N_yH_x}^{surf} + (4-x)E_H^{surf} + (2-y)E_N^{surf}\right) - \left(\left((4-x)+(2-y)+1\right)E^{surf} + E_{N_2H_4}^{gas}\right) \quad \text{Eq 3-1}$$

Where E_{NyHx}^{surf} denotes the total energy of the adsorbed N_yH_x on a surface, E_H^{surf} and E_N^{surf} are, respectively, the energies of an adsorbed atom of hydrogen and nitrogen on the surface. Additionally, E^{surf} and E_{N2H4}^{gas} represent the energy of the naked surface and an isolated hydrazine molecule in the gas phase.

We combined the climb-image nudged elastic band (ci-NEB)[28,29] and the improved dimer method (IDM)[30] to find the saddle point of the transition states (TS), making sure that there is a unique imaginary frequency along with the reaction coordinate. The reaction energy (E_r) is given by the difference between the final state (FS) energy and the initial state (IS) energy (Eq 3-2). Thus, a negative value means an exothermic step. We defined the forward and reverse activation barriers (E_a) as the energy difference represented by Eq 3-3 and Eq 3-4.

$$E_r = E_{FS} - E_{IS} \quad \text{Eq 3-2}$$

$$E_a(\text{forward}) = E_{TS} - E_{IS} \quad \text{Eq 3-3}$$

$$E_a(\text{reverse}) = E_{TS} - E_{FS} \quad \text{Eq 3-4}$$

3.3 Experimental methods

Materials. There are six primary reagents used in the experiment. Hydrazine monohydrate (reagent grade, 98%, cat. 207942) is obtained from Sigma-Aldrich, sodium hydroxide (pellets, cat. 30620-1KG) from Fluka, hydrochloric acid (conc. 37%, cat. 258148) from Sigma-Aldrich, iridium chloride (99.95%, cat. 12184.06) from Alfa aesar, cerium oxide nano-powder (particles size <25nm, cat. 544841) from Sigma-Aldrich and urea (powder, Bioreagent, cat. U5378).

Catalyst preparation. The deposition precipitation method has been employed to prepare the monometallic Ir catalyst. The metal precursor $IrCl_4 \cdot H_2O$ was dissolved to 400 mL solution to ensure 10 mg of iridium on the final catalyst. Then, 10.06 g urea was added in solution to keep a pH of 4.10, and 0.990 g of CeO_2 were dispersed in the

solution as support. This solution was warm up to 80 °C and left till the pH remained constant at around 7 for 4 hours. The synthesized catalyst was filtrated and dried in an oven at 110 °C; part of the catalyst was then kept for catalytic studies. Afterwards, the remaining catalysts were heat-treated in air at 400 °C for 3 hours and later treated in 10% H_2/Ar mixture at 600 °C for 6 hours.

Catalytic tests. The performances of the catalytic materials were studied using a volumetric gas displacement system, which consisted of a tightly sealed round bottom flask connected to an acid trap and a gas burette to measure the volume of produced gas. 8 mL of 0.5M NaOH solution was brought at 50 °C with 76.2 mg of 1 wt.% Ir/CeO_2 under stirring. After that, 0.3 mL of 3.3M hydrazine solution was added, and the system was purged with N_2 without stirring. Finally, stirring was started to prompt the reaction.

The gases produced by the reaction passed through a solution of HCl to trap any gaseous ammonia present in the stream. The moles of gas produced were then calculated and used to quantify the final yield of H_2 production reaction, Eq 3-5. Blank comparisons were performed to prove the stability of the hydrazine solution in absence of catalysts and quantify the gases produced by the mixed reactants.

$$\mathrm{H\ Yield} = \frac{3 * \frac{\mathrm{nH_2} + \mathrm{nN_2}}{\mathrm{nN_2H_{4\ initial}}} - 1}{8} * 100 \qquad \text{Eq 3-5}$$

Where H yield is in percentage, nH_2 + nN_2 are total moles of gas produced, nN_2H_4 initial are the moles of hydrazine at the beginning of the reaction.

The experimental tests were performed at least three times in the same conditions in order to validate the data obtained.

Characterization. (Figure 3-1 to Figure 3-3 were obtained by Davide Motta.) Scanning electron microscope (SEM) was performed to study the morphology and content of iridium on the sample. The images were taken on Hitachi TM3030PLUS (Tokyo, Japan) equipped with Quantax70 Energy-Dispersive X-ray spectroscopy (EDX).

SEM-EDX allowed the quantification of the Ir element on the samples (0.98 ± 0.05 wt.%), which is close to the theoretical loading value of 1 wt.%. Figure 3-1 obtained by

Davide Motta displays the distribution of the active metal on the support that appears to be homogeneous among the surface.

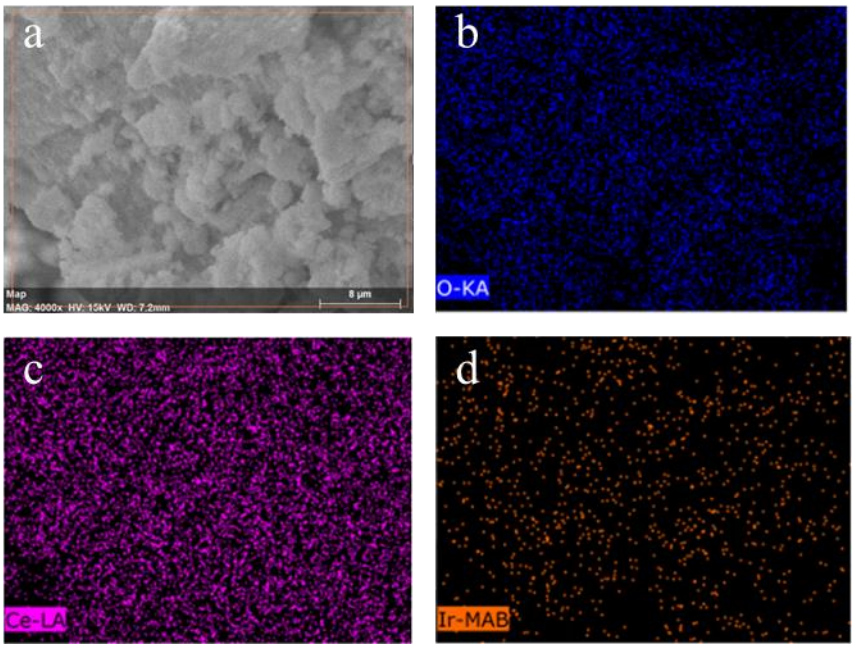

Figure 3-1. a) SEM image of Ir/CeO_2, b-d) the EDS mapping of its surface for the main element present in the catalyst.

X-Ray diffraction (XRD) analyses were performed with PANanalytical X'PertPRO X-ray diffractometer (Almelo, The Netherlands) using Cu K radiation and worked at 40 kV and 30 mA. The diffraction patterns were recorded between 10 °– 80 ° 2θ at a step size of 0.017 °.

For metallic iridium, the diffraction peaks at 2θ of 40.8 °, 47.2 °, 69.1 ° and 83.6 ° correspond to the (111), (200), (220) and (311) planes respectively, which are the most stable forms for Ir. While the X-ray diffract at 2θ of 28.1 °, 35.0 °, 39.8 ° and 55.3 ° correspond to IrO_2 surface of (110), (101), (200) and (211) respectively. Figure 3-2 does not exhibit any these peaks but only the CeO_2 pattern, 2θ = 29.3 °, 33.1 °, 47.5 ° and 57.6 ° for (111), (200), (220) and (311) planes respectively.

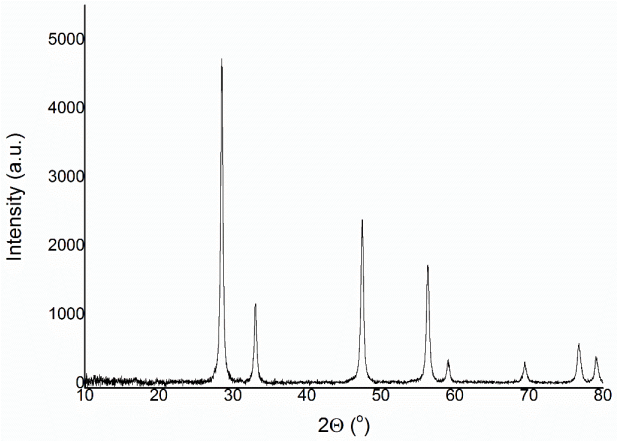

Figure 3-2. X-Ray diffraction pattern for Ir/CeO_2

X-ray photoelectron spectroscopy (XPS) was performed on a Kratos axis ultra- equipped with a delay line detector photoelectron spectrometer using monochromatic AlKα radiation (12 mA, 12 kV). The signal was averaged from a surface area of approximately 700×300 μm. Compensation of the charges on the insulated samples was achieved using the Kratos immersion lens and then setting the C 1s peak at 284.8 eV. The analysis of the data was done by CasaXPS (v2.3.17, Teignmouth, UK).

XPS (Figure 3-3) was performed to analyze the dried Ir/CeO_2 and reduced Ir/CeO_2 samples followed by H_2/Ar flow at 600 °C allowing us to confirm the oxidation state of the active metal on the surface. The 4f region in Figure 3-3 shows that two patterns are convoluted in two pair of peaks. One pattern is for the metallic iridium, $4f_{7/2}$ BE of 61.0 eV, while the other stands for Ir^{4+} and $4f_{7/2}$ BE of 62.0 eV, in agreement with previous reports.[31] The deconvolution of the spectrum reveals that the metallic iridium constitutes 70.6% of all superficial iridium in the reduced catalyst, whereas it constitutes only 8.6% of the total iridium on the surface without the reduction heat treatment.

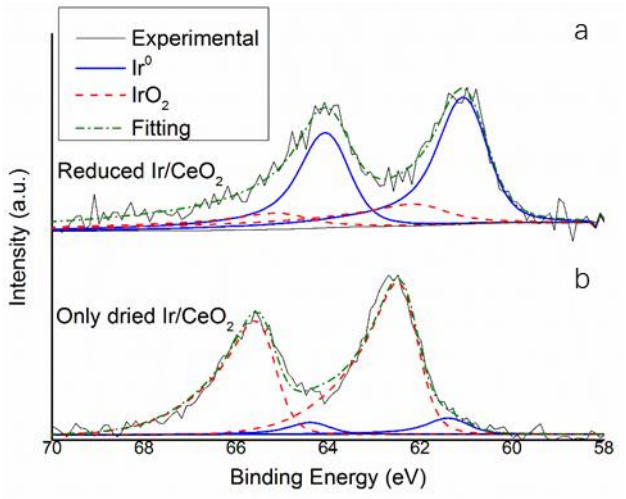

Figure 3-3. XPS spectrum of Ir 4f region for Ir/CeO_2 with deconvolution for metallic Ir and iridium oxide, a) after and b) before the heat treatment.

3.4 Results and Discussion

Of the three major conformations of isolated hydrazine, gauche has presented as the most stable. Upon optimization, the molecule presented bond lengths of 1.450 Å for N–N and an average N–H bond of 1.020 Å. We studied its adsorption on IrO_2 surfaces and Ir(111) owing to the possible presence of an IrO_2 surface under typical reaction conditions.

3.4.1 Adsorption on the IrO_2 surface

We optimized the IrO_2 low Miller index surfaces (001), (100), (110) (101) and (111) and calculated their surface energies using the equation (Eq 3-6). The theoretical analysis of hydrazine decomposition on IrO_2 was carried out by Samantha Francis.

$$\gamma_{hkl} = \frac{E_{slab,hkl}^{relaxed} - E_{bulk}}{A_{hkl}} - \frac{E_{slab,hkl}^{unrelaxed} - E_{bulk}}{2A_{hkl}} \qquad \text{Eq 3-6}$$

Where γ_{hkl} is the surface energy of the slab, E_{bulk} is the total energy of the bulk, N is the number of bulk units in the slab, and finally, A_{hkl} is the (hkl) surface area. It was determined that the stability of IrO_2 surfaces follows the order (101) > (110) > (100) > (001) > (111), which is in agreement with previous studies, see appendix Figure S3-

3.[32] Once the most stable (101, 110 and 100) slabs were optimized, we adsorbed the molecules of N_2H_4, NH_3 and the atoms N and H on non-equivalent sites. The most stable geometries are represented in Figure S*3-3*. Adsorption energies are calculated using Eq 3-7 and are shown in Table 3-1.

$$E_{ads} = E_{mol+surf} - (E_{surf} + E_{mol}) \quad \text{Eq 3-7}$$

Where E_{ads} is the energy of adsorption, $E_{mol+surf}$ is the energy of the molecule/atom adsorbed on the surface, E_{surf} is the energy of the naked surface and E_{mol} is the energy of the molecule in the gas phase. The references for N and H adsorptions are half energies of gas-phase nitrogen and hydrogen molecule respectively.

Table 3-1. The calculated adsorption energies of N_2H_4, NH_3, N and H on the most stable sites of IrO_2((101), (110) and (100)).

Adsorbate	E_{ads} (eV)		
	(101)	(110)	(100)
N	-3.16	-3.65	-3.92
H	-3.13	-3.57	-3.46
NH_3	-2.02	-2.46	-2.69
N_2H_4	-2.35	-3.24	-2.81

The adsorption energies in Table 3-1 indicate that any of the three surfaces considered will adsorb N_2H_4 very strongly. The relative adsorption energies between N_2H_4 and atomic N and H show that on the (101) surface, and to a lower extent on the (110), hydrazine decomposition into N and H is thermodynamically favorable. Nevertheless, the strong adsorption of these species will irreversibly occupy the adsorption site. To verify the IrO_2 caused deactivation, a decomposition test of hydrazine over the Ir/CeO_2 sample was performed. The reaction was followed at 50 °C by the volume of the gas collected in a gas burette. The yield was calculated from the produced gaseous species according to Eq 3-5 and was represented in Figure 3-4. The catalyst without reduction heat treatment (mainly IrO_2) exhibits negligible catalytic activity to the hydrazine decomposition. These results are also in line with previous experimental results, the efficacy of an Ir catalyst toward hydrazine decomposition

diminished upon its oxidation.[33] This result validates our DFT calculations made for the IrO_2 surface, which means only metallic iridium plays a role in the hydrazine decomposition over Ir catalyst.

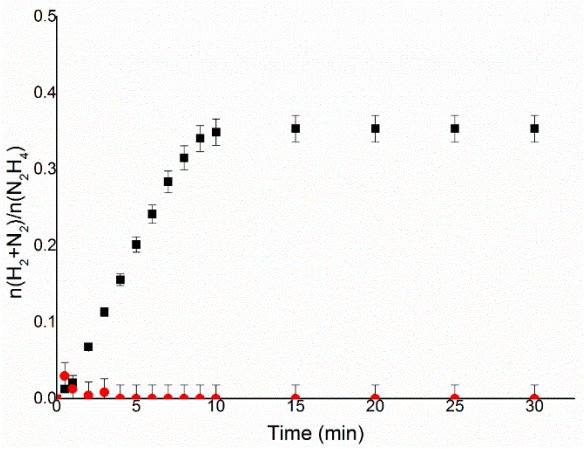

Figure 3-4. $n(H_2+N_2)/n(N_2H_2)$ versus time for hydrous hydrazine decomposition over Ir/CeO_2 using 0.3mL of 3.3M hydrazine monohydrate in 8mL 0.5M of NaOH solution, at 50 °C and 76.2 mg of catalyst, for a substrate/metal ratio of 250, with a stirring rate of 1050 rpm. Black squared measurements correspond to reduced samples, while red circles indicate the non-reduced sample.

Figure 3-4 also includes information regarding stoichiometry at the equilibrium reaction. For the hydrazine decomposition over Ir/CeO_2, the $n(H_2+N_2)/n(N_2H_4)$ increased to about 1/3 after equilibrium, and only a small fraction of hydrogen was obtained in the reaction product. This result shows that the hydrazine decomposition on Ir follows Path 2 under our experimental conditions. Based on these results, we analyzed the structures and energies of all the species on the Ir(111) to elaborate on the different reaction pathways.

3.4.2 Species on Ir(111) surface

The most stable *fcc* Ir surface is the close-packed (111) in which atoms are arranged in a hexagonal lattice with a separation of 2.692 Å. We investigated several adsorption geometries on the surface for the different species along with the three reaction mechanisms and described the most stable below.

N_2H_4. We approached the hydrazine gauche conformation to four non-equivalent

sites, i.e. top, bridge, and fcc and hcp hollows, with parallel and perpendicular orientations on the clean Ir(111) surface to identify the most stable adsorption geometry, see *Figure 3-5a*. The molecule binds through both nitrogen atoms almost parallel to the flat surface in a bridge site with an Ir-N average distance of 2.137 Å. Exothermic adsorption of 2.70 eV (shown in Table 3-2) elongates the N–N bond to 1.472 Å from 1.450 Å in the gauche conformation, while the distance of N–H bonds shorten to 0.977 Å from the original 1.024 Å. Similar results were found by Agusta *et al*. investigated N_2H_4 adsorption on Ni(111) and suggested the anti-conformation as the most stable configuration during the hydrazine adsorption but the cis-conformation as a transition state for the decomposition reaction.[34]

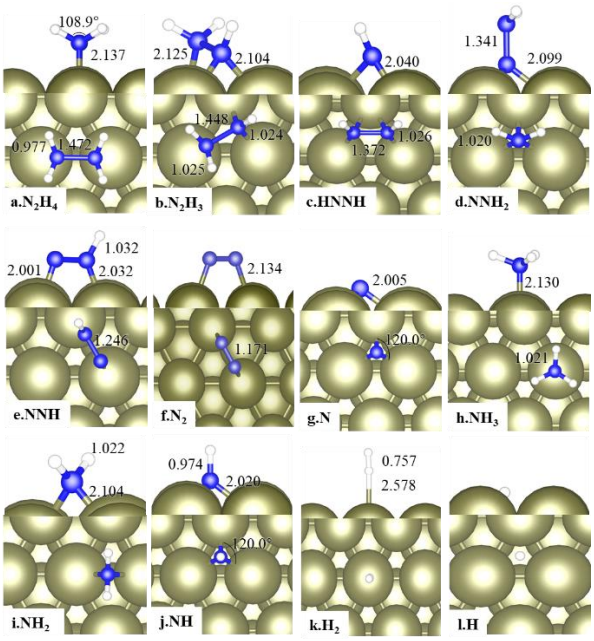

Figure 3-5. Side and Top view of adsorbed N_2H_x (x = 0-4), NH_x (x = 0-3) and H species on the Ir(111) surface (side view and top view). All distances inset are in Å. Blue spheres represent N atoms, white is hydrogen, and Ir is the large green sphere.

Table 3-2. Adsorption energies (E_{ads}) and average bond lengths (d), including coordination (η), of the adsorbed species on the Ir(111). We added the isolated hydrazine molecule in the gas phase for comparison.

Adsorbate	E_{ads} (eV)	d(Ir–N^1) (Å)	d(Ir–N^2) (Å)	d(N^1–N^2) (Å)	d(N^1–H) (Å)	d(N^2–H) (Å)
N_2H_4 gas	--	--	--	1.450	η (2); 1.020	η (2); 1.020
N_2H_4	-2.70	2.137	2.137	1.472	η (2); 0.977	η (2); 0.977
N_2H_3	-2.97	2.125	η (2); 2.104	1.448	η (2); 1.025	1.024
HNNH	-2.47	η (2); 2.040	η (2); 2.040	1.372	1.026	1.026
NNH_2	-2.79	η (3); 2.099	-	1.341	-	η (2); 1.020
NNH	-3.06	2.032	2.011	1.246	1.032	-
NH_3	-1.95	2.130	-	-	η (3); 1.021	-
NH_2	-3.72	2.104	-	-	η (2); 1.022	-
NH	-4.31	η (3); 2.020	-	-	0.974	-
N_2	-1.14	2.134	2.134	1.171	-	-
H_2	-0.53	-	-	-	-	-
N	-0.56	η (3); 2.005				
H	-0.86	-	-	-	-	-

We have carried out an analysis of the electron density arrangement to characterize the bonding between the hydrazine and the Ir(111) surface. Figure 3-6 shows the charge density flux calculated as the difference between the charge density of the total adsorbate system and the sum of the charge densities of the molecule and the clean surface in the same geometry (Eq 3-8). Upon N_2H_4 adsorption, the charge density accumulates between N–Ir bonds leading to sp^3 hybridization of the N orbitals and the weakening of the N–N bond, which is in line with its elongation from the gas phase geometry. This electronic rearrangement breaks the planarity of the molecule, as noticed in Figure 3-5a.

$$\rho_{transfer} = \rho_{surf+molecule} - (\rho_{surf} + \rho_{molecule}) \qquad \text{Eq 3-8}$$

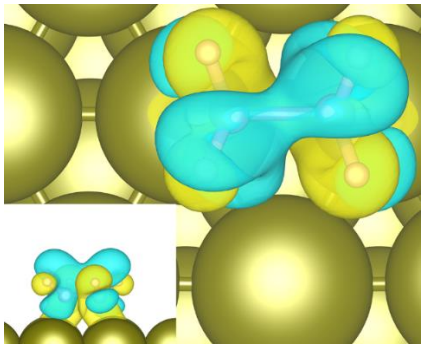

Figure 3-6. Top and side view (inset) of the partial charge density flow upon N_2H_4

adsorption. Yellow and blue iso-surfaces (0.01 e/Å^3) denote gain and depletion of electron density, respectively. Blue spheres represent N atoms, white is hydrogen, and Ir is the large green sphere.

We also employed the density of states (DOS) and the Bader charge analysis to characterize the N–Ir interaction. Their analysis showed that one N_2H_4 molecule donates 0.6 e^- to the Ir(111) surface during the adsorption process, see Table S3-1 for atomic charges. Moreover, the DOS shows how the electronic structure is affected by the interactions between the surface and adsorbate. Figure 3-7 helps to compare the DOS of the naked surface and isolated molecule with the adsorbed system. It shows a clear shift to lower energies of the N_2H_4 orbitals. In particular, the antibonding orbital (π^*) associated with lone pairs moves below the Fermi energy, which decreases the N–N bond order agreeing with the bond elongation previously observed. Initially, one may think that it contradicts the charge transfer, i.e. from the molecule to the surface, even though, this is a common case where the electron rearrangement leads to back-donation into the antibonding orbital.[35]

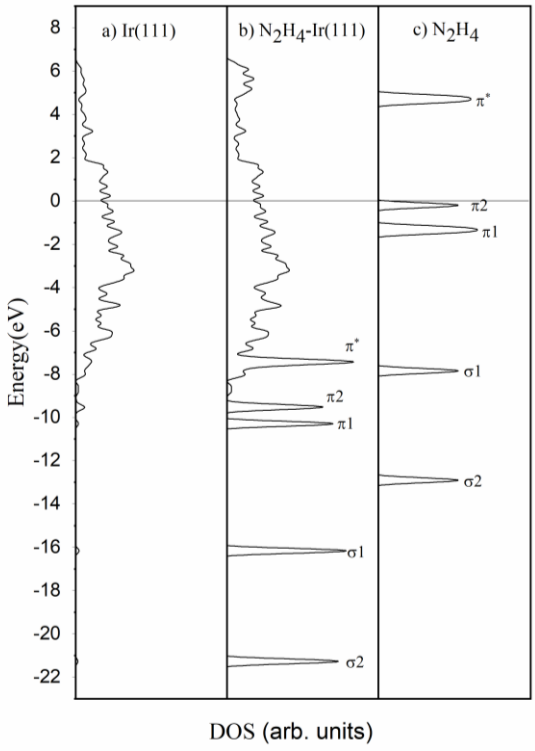

Figure 3-7. The total density of states of a) bare Ir(111), b)N_2H_4/Ir(111) and c) isolated gauche N_2H_4. The horizontal line across diagrams represents the common Fermi

energy.

Once N_2H_4 is adsorbed, we explored the adsorption sites and geometry of the different intermediates.

N_2H_3. The N_2H_3 intermediate is a product of N_2H_4 dehydrogenation. This species prefers to sit on fcc hollow site with an adsorption energy of -2.97 eV. It lies with the NH part bridging two surface atoms, i.e. η (2), with an Ir–N bond length of 2.104 Å. The NH_2 part has an Ir–N bond length of 2.125 Å and N-N bond elongate to 1.448 Å (Figure 3-5*b*). These results are similar to those on Rh(111) and Cu(111) surfaces.[14,15]

N_2H_2 has two isomers depending on the reaction pathway: HNNH and NNH_2 (Figure 3-5c and d). The binding of the HNNH structure on Ir(111) occurs through both nitrogen atoms positioned on hcp sites almost parallel to the surface and releases 2.47 eV. The NNH_2 intermediate adsorbs perpendicularly to the surface through a single N on an fcc hollow site (E_{ads} = -2.79 eV). The adsorption and molecular geometries are related to the N orbitals, which are also characterized by the N–N bond lengths, 1.341 and 1.372 Å for NNH_2 and HNNH respectively. These distances compare very well with previous benchmarks, i.e. 1.345 and 1.359 Å on Cu(111), and 1.429 and 1.367 Å on Rh(111) surface.[14,15]

N_2H. Further dehydrogenation leads to N_2H intermediate, which preferentially adsorbs on a bridge site, Figure 3-5e. This intermediate is firmly bound to the surface, E_{ads}= -3.06 eV, and the distance between the two nitrogen atoms is much shorter than in previous cases, 1.246 Å, showing an increment to the bond order although N–N is still longer than the same species in the gas phase (1.150 Å).[36]

N_2. The adsorption of molecular nitrogen was studied at different sites on the Ir(111) surface. The most stable configuration is N_2 parallel to the surface on a bridge site at 2.134 Å (Figure 3-5f). The adsorption process releases 1.14 eV relative to gas-phase N_2. Moreover, the length of the N–N bond increased to 1.171 Å from 1.098 Å in the gas phase, which compares well with a reported experimental value of 1.098 Å.[37]

N adatoms adsorb preferably on fcc hollow sites releasing the energy of 0.56 eV relative to gas-phase N_2. The average distance between the three Ir atoms and N is

2.005 Å.

NH_3, as shown in Figure 3-5h, prefers to adsorb on the top sites at 2.130 Å from neighboring Ir atoms. Exothermic adsorption of 1.95 eV (compared to isolated NH_3) results from the interaction of the NH_3 lone pair electrons with Ir 3d electrons.

NH_2. The bridge site is the most stable adsorption mode for NH_2, releasing 3.72 eV; this is larger than the other intermediates containing two nitrogen atoms (e.g. NNH_2, HNNH). The average Ir–N bond length is 2.104 Å. The N–H bond length (1.022 Å) is close to the experimentally reported distance in the gas phase (1.024 Å).[38]

NH. The most stable adsorption site of imide is the hollow fcc (η = 3) perpendicular to the surface. This intermediate is largely stabilized by the surface (E_{ads}= -4.31 eV) for which the Ir–N bond length is 2.020 Å. It shows that the adsorption energy is negatively correlated with the distance between N atom and Ir atoms on the surface.

H_2. Hydrogen molecules prefer to be physisorbed perpendicularly to the surface, releasing 0.53 eV due to long-range interactions. The result is close to the former theoretical studies (E_{ads}= -0.46 eV).[39] The distance to the surface Ir atoms is 2.578 Å for the top site.

H adatoms prefer to adsorb on the fcc sites of the Ir(111) surface (Figure 3-5l). H lies at a distance of 1.900 Å to Ir with an adsorption energy of 0.86 eV in comparison to isolated H_2 molecules. This results in stronger adsorption compared with a previous study (E_{ads}= -0.41 eV) as we considered dispersion corrections.[40]

3.4.3 N_2H_4 decomposition pathways on Ir(111)

In the following section, we have discussed the elementary reaction steps for each mechanism of the catalytic decomposition of N_2H_4 on Ir(111). Forward and backward energy reactions and activation energies are summarized in Table 3-3. We have listed the frequencies related to the reaction coordinate of all the reactions across the different mechanisms in Table S3-2. Nearly all imaginary vibrations modes are stretching except the dehydrogenation of NNH*, which is an N-H bending.

Dehydrogenation. Starting with N_2H_4, the process of breaking an N–H bond and

placing H on the most stable surface site is endothermic (E_r= 0.18 eV) with an energy barrier (activation energy) of 1.08 eV. The process is schematically represented in Figure 3-8a. This first step leads to N_2H_3 (see the energy profile Figure 3-13), which following dehydrogenation derives into symmetrical or asymmetrical species. The asymmetric path (Figure 3-8b) is endothermic by 0.57 eV with an activation energy of 1.02 eV, making it highly improbable. The symmetric step (Figure 3-8c) is also endothermic (0.54 eV) and leads to HNNH and an H ad-atom upon overtaking a significant barrier of 2.05 eV.

HNNH is the symmetric product of the N_2H_3 dehydrogenation, and the following dehydrogenation step leads to N_2H, which lies 0.19 eV below reactants after overtaking a barrier of 0.70 eV (Figure 3-8e). It is the most feasible intramolecular dehydrogenation reaction of any intermediate on the Ir(111) surface. The asymmetric intermediate (NNH_2) requires overtaking an energy barrier of 0.83 eV to produce N_2H, see Figure 3-8d. The decomposition of N_2H_2 on Ir(111) is more favorable than on Cu(111),[14] which has higher barrier energies of 1.35 eV for NNH_2 and 1.68 eV for N_2H. Its subsequent dehydrogenation (Figure 3-8f) towards N_2 and H has a high energy barrier of 1.31 eV and the products lie only 0.02 eV below, making the process energetically unfavorable.

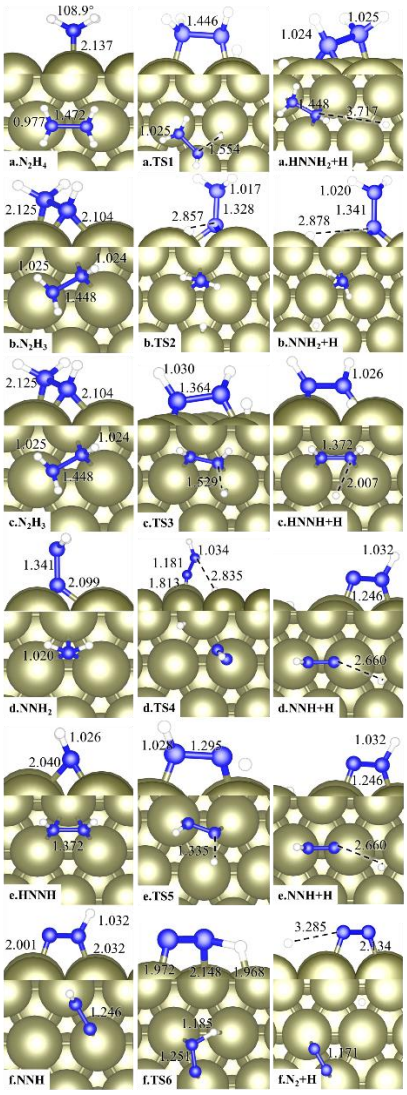

Figure 3-8. Top and side views of the initial, transition and final states for the dehydrogenation pathways: a) N_2H_4 dehydrogenation, b) N_2H_3 dehydrogenation to NNH_2, c) N_2H_3 dehydrogenation to HNNH, d) NNH_2 dehydrogenation, e) HNNH dehydrogenation, f) NNH dehydrogenation. All inset distances are in Å. Blue spheres represent N atoms, white is hydrogen, and Ir is the large green sphere.

N–N dissociation. The exothermic breaking of the hydrazine N–N bond (E_r= -0.52 eV) leads to the formation of amino species (NH_2) with an energy barrier of 0.71 eV, see Figure 3-9a. In comparison with the dehydrogenation pathway, the dissociation is more energetically favorable in agreement with previous studies.[13] Nevertheless, the results are not as favorable as previously reported (E_a= 0.52 eV and E_r= -0.93 eV)[16] due to the dispersion corrections included. It has been largely proven that including

dispersion corrections, even by semi-empirical methods, leads to a more accurate description of molecular interactions since effects like dipoles, e.g. in absorbed hydrazine and NH_2, are not otherwise considered.

Resulting from an initial dehydrogenation, N_2H_3 breaks the N–N bond (Figure 3-9b) through an energy barrier of 0.78 eV leading to NH and NH_2 species on the surface. These species lie at 0.71 eV below the energy value of the initial state. Again, the N-dissociation path is energetically more favorable than the dehydrogenations steps. Similarly, the scission of N–N on the asymmetric N_2H_2 requires 0.73 eV to overtake the energy barrier leading to NH_2 species and N on the surface 0.53 eV below the initial state (Figure 3-9c). The N-dissociation of the symmetric N_2H_2 (Figure 3-9d) is thermodynamically more favorable than the asymmetric by 0.96 eV with the same E_a= 0.73 eV. The dissociation to N and NH intermediates from N_2H (Figure 3-9e) is driven by the formation of products (E_r= -1.21 eV) but prevented by a high energy barrier of 1.43 eV.

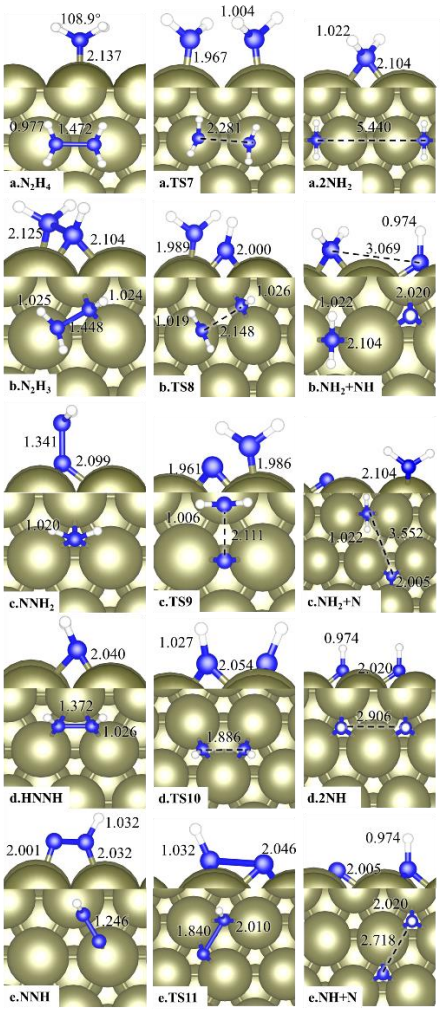

Figure 3-9. Top and side views of the initial, transition and final states for the dissociation pathway of (a) N_2H_4, (b) N_2H_3, (c) NNH_2, (d) HNNH and (e) NNH. All inset distances are in Å. Blue spheres represent N atoms, white is hydrogen, and Ir is the large green sphere.

Intermolecular dehydrogenation. Upon dissociation of N–N intermediates, the NH_x (x= 1-3) species may assist the dehydrogenation process of co-adsorbed species, i.e. having higher nucleophilicity to drive the proton transfer. Indeed, previously we showed the N-dissociation to be energetically favorable over dehydrogenation, and consequently, the produced NH_2 can withdraw H from co-adsorbed N_2H_x (x= 1-4) intermediates forming NH_3, see Figure 3-10.

The co-adsorption of NH_2 at a distance of 3.674 Å from N_2H_4 destabilizes the system by 0.13 eV compared with isolated species. The intermolecular dehydrogenation proceeds through a barrier of only 0.20 eV with an energy gain of E_r=

-0.47 eV. Similarly, the co-adsorption of other species is destabilized by around 0.2 eV. Assisted dehydrogenation processes have energy barriers smaller than 0.55 eV, except for asymmetric N_2H_2 (E_a= 1.02 eV). This mechanism is driven by the formation of NH_3 and the most likely to take place once NH_2 is present on the surface (see Table 3-3 and Figure 3-15).

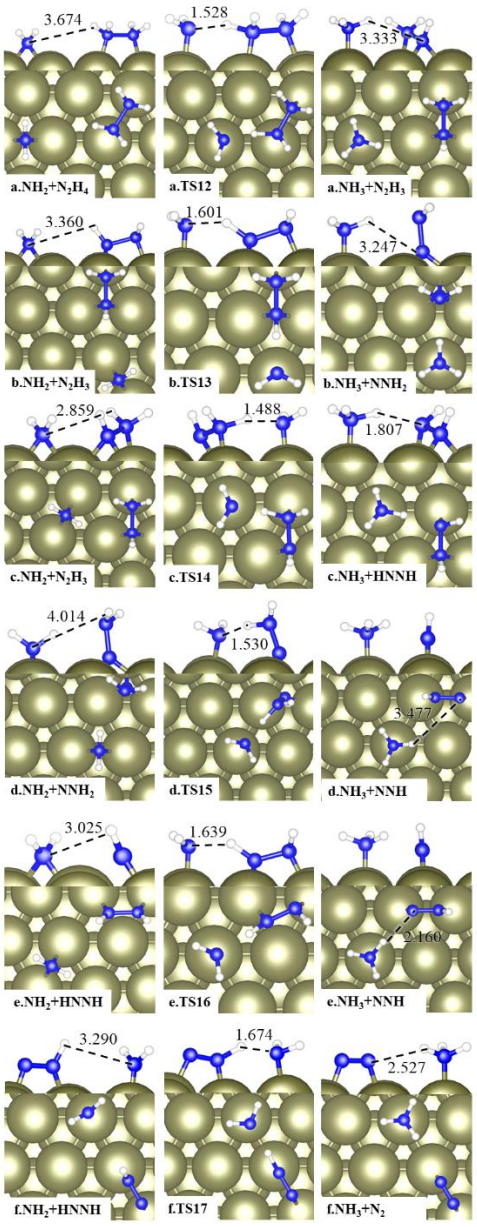

Figure 3-10**.** Top and side views of the initial, transition, and final states for N2Hx (x= 1-4) attacked by NH_2. (a) N_2H_4 to N_2H_3, (b) N_2H_3 to NNH_2, (c) N_2H_3 to HNNH, (d) NNH_2 to NNH, (e) HNNH to NNH and (e) NNH to N_2. All inset distances are in Å. Blue spheres represent N atoms, white is hydrogen, and Ir is the large green sphere.

We have also studied the NH_2 assisted dehydrogenation of NH_2 and NH_x (x= 1-2) species leading to NH_3, see Figure 3-11. The process between two NH_2 has a driving energy of -0.59 eV upon overtaking a small energy barrier of 0.34 eV. The barrier of the interaction between NH_2 and NH is kinetically limiting (E_a= 0.98 eV) with the reaction energy of -0.91 eV. As the barrier energy of the reaction between NH_2 is relatively higher than with N_2H_4, by 0.14 eV, NH_2 prefers reacting with N_2H_4 instead of NH_2.

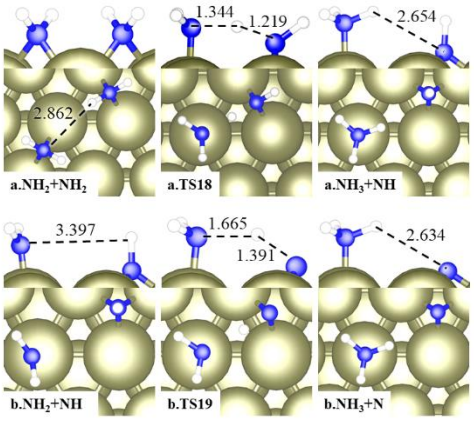

Figure 3-11. The top and side view of the initial, transition, and final states for the interaction of NH_2 molecules. (a) NH_2 and (b) NH. All inset distances are in Å. Blue spheres represent N atoms, white is hydrogen, and Ir is the large green sphere.

NH_x dehydrogenation. Several steps lead to the formation of NH_x (x = 1-3) species. These species may undertake further dehydrogenations leading to a complete decomposition into N_2 and H_2, see Figure 3-12. Starting with NH_3, its first N–H bond scission needs to overcome barrier energy of 1.79 eV to produce co-adsorbed NH_2 and H at 0.76 eV above the initial state. In the cases of NH_2 and NH, the dehydrogenation steps are also unlikely due to their high barrier energies of 1.96 eV and 1.18 eV, respectively. While these barriers are relatively small compared to the ones found on Cu(111),[24] Rh(111),[15] Pt(111),[41] Ir(100).[42] In line with previous benchmarks, hydrogen ad-atoms easily combine with NH_2 that eventually yields NH_3 molecules.

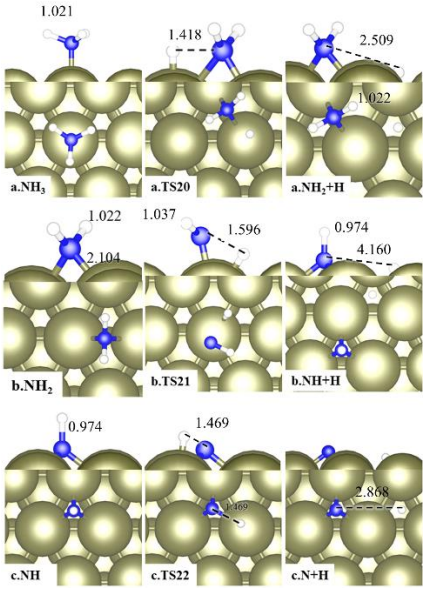

Figure 3-12. Top and side views of the initial, transition, and final states for NH_3 dehydrogenation, (a) NH_3 decomposition, (b) NH_2 decomposition (c) NH decomposition. All inset distances are in Å. Blue spheres represent N atoms, white is hydrogen, and Ir is the large green sphere.

Table 3-3. Reaction (E_r) and barrier (E_a) energies for the forward and reverse reaction steps. * denotes the adsorbed state, E_r values of the adsorption and desorption processes are equal to the E_{ads} values (i.e. relative to the gas-phase), and υ is the imaginary frequencies of the transition states.

Reactions		Ir (111)			
		E_r (eV)	E_a forward (eV)	E_a reverse (eV)	υ (cm^{-1})
Adsorption-desorption					
R1	$N_2H_4 \leftrightarrow N_2H_4$*	-2.7			
R2	NH_3* $\leftrightarrow NH_3$	1.90			
R3	N_2* $\leftrightarrow N_2$	1.14			
R4	H_2* $\leftrightarrow H_2$	1.37			
Dehydrogenation					
R5	N_2H_4* $\leftrightarrow N_2H_3$*+H*	0.18	1.08	0.91	956.9
R6	N_2H_3* $\leftrightarrow NNH_2$*+H*	0.57	1.02	0.45	482.8
R7	N_2H_3* $\leftrightarrow$ HNNH*+H*	0.54	2.05	1.51	1126.8
R8	HNNH* $\leftrightarrow$ NNH* + H*	-0.19	0.70	0.89	1115.8

R9	NNH_2*↔NNH* + H*	0.11	0.83	0.72	386.1
R10	NNH*↔ N_2* + H*	-0.02	1.31	1.33	910.2
N-N dissociation					
R11	N_2H_4*↔2NH_2*	-0.52	0.71	1.23	154.3
R12	N_2H_3*↔NH_2*+NH*	-0.71	0.78	1.48	356.9
R13	NNH_2*↔NH_2* + N*	-0.53	0.73	1.26	398.7
R14	NHNH*↔ 2NH*	-1.49	0.73	2.22	549.7
R15	NNH*↔ NH* + N*	-1.21	1.43	2.64	571.9
Intermolecular dehydrogenation					
R16	N_2H_4* + NH_2* ↔ N_2H_3* + NH_3*	-0.47	0.20	0.67	335.8
R17	N_2H_3* + NH_2* ↔ HNNH* + NH_3*	-0.13	0.23	0.36	268.3
R18	HNNH* + NH_2* ↔ NNH* + NH_3*	-1.03	0.19	1.22	322.9
R19	N_2H_3* + NH_2* ↔ NNH_2* +NH_3*	-0.28	0.37	0.64	252.5
R20	NNH_2* + NH_2* ↔ NNH* +NH_3*	-0.49	1.02	1.5	654.9
R21	NNH* + NH_2* ↔ N_2* + NH_3*	-1.35	0.55	1.89	1291.0
NH_x (x = 1,2,3) dehydrogenation					
R22	NH_3* ↔ NH_2* + H*	0.76	1.79	1.03	1229.5
R23	NH_2* ↔ NH* + H*	1.66	1.96	0.30	1274.3
R24	NH* ↔ N* + H*	0.07	1.18	1.12	1154.5
Interaction of NH_2 intermediates					
R25	2NH_2* ↔ NH* + NH_3*	-0.59	0.34	0.93	124.1
R26	NH* + NH_2* ↔ N* + NH_3*	-0.91	0.98	1.89	213.9
N_2 generation					
R27	2N* ↔ N_2*	-0.59	2.02	2.61	568.3
H_2 generation					
R28	2H* ↔ H_2*	0.31	0.51	0.20	271.1

From the analysis of the previous reaction pathways, we conclude that the primary mechanism for the N_2H_4 decomposition on Ir(111) is the intermolecular dehydrogenation once NH_2 is on the surface. It implies that the N–N scission also takes place. These two mechanisms yield N_2 and NH_3 from a single N_2H_4 molecule under mild conditions, in line with the experiments.[43]

3.4.4 Desorption of products

Previously, we described the favorable formation of NH_3 *via* N–N scission and dehydrogenation pathways. These mechanisms may also generate N and H ad-atoms on the surface, which recombination yields N_2 and H_2 molecules. The formation of an N_2 molecule is exothermic by 0.59 eV but has an energy barrier of 2.02 eV. On the other hand, the formation of H_2 is endothermic by 0.31 eV with an accessible barrier of 0.51 eV. These simple thermodynamic analyses agree with previous results in which NH_3 was observed at temperatures as low as 150 °C, temperatures above 200 °C were necessary to observe H_2.[5,8]

3.4.5 Energy profiles

We summarized the energy profiles of the three reaction mechanisms in Figure 3-13, Figure 3-14, and Figure 3-15. The first figure contains the two different pathways for intramolecular dehydrogenation; the second is the analysis of the intermolecular dehydrogenation pathway between NH_2 and N_2H_4, and the last one depicts the dehydrogenation reactions between NH_2 from N–N scission.

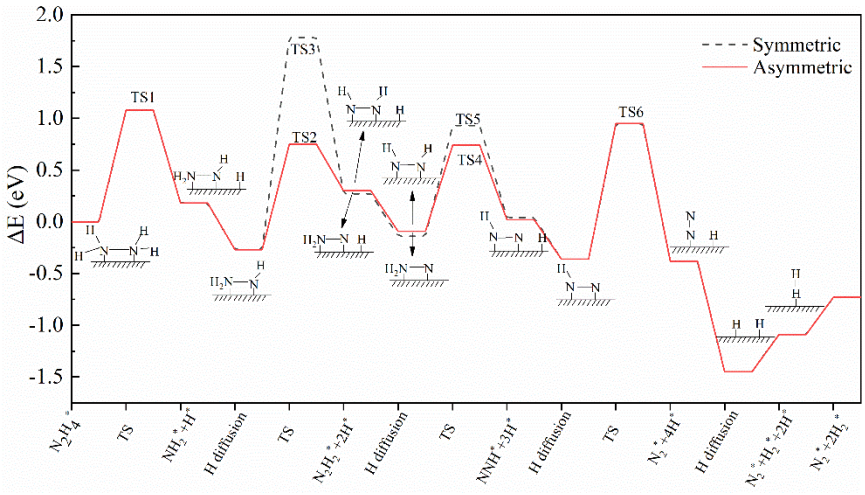

Figure 3-13. Intramolecular dehydrogenation pathways of N_2H_4 dissociation over the Ir(111) surface. TS indicates the energy of the transition energies.

According to Table 3-3 and Figure 3-13, the reaction R7 (N_2H_3*↔HNNH*+H is the dominant reaction barrier (TS3) for the intramolecular symmetry dehydrogenation

pathway with an energy of 2.05 eV. The only step to generate N_2, R10, has a limiting barrier (TS6) of 1.31 eV, whereas hydrogen desorption energy is 1.37 eV. These energy requirements are higher than those found in the NH_2 assisted dehydrogenation pathway.

According to the DOS and thermodynamics analyses (Table 3-3, Figure 3-6 and Figure 3-15), N-N bond breakage is the prevailing pathway through the whole decomposition process and produces NH_2, NH, and N fragments (R11, R12, R13, and R14) with relatively low reaction energies and barriers, which may assist the dehydrogenation process on co-adsorbed N_2H_4. And the large barrier energy of TS21 in Figure 3-15, 1.96 eV, stabilizes the existence of NH_2 on the surface.

The intermolecular NH_2 assisted dehydrogenation (R16-21) of N_2H_4 (Figure 3-14) may produce large amounts of NH_3 as its dehydrogenation (R22) is largely endothermic (E_r= 0.76 eV). Indeed, an assisted symmetric dehydrogenation step is thermodynamically favorable with energy barriers (TS12-15) no more than 0.55 eV. The assisted dehydrogenation will yield N_2 from undissociated N_2H_4 molecules in agreement with isotopic data.[43]

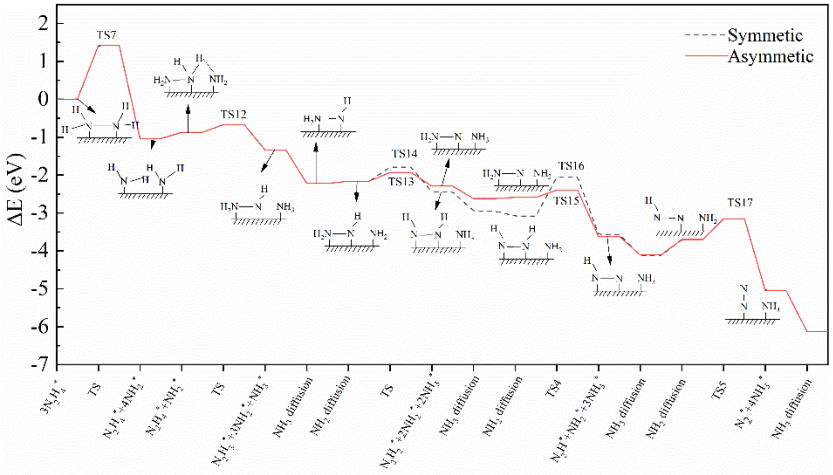

Figure 3-14. Intermolecular dehydrogenation of hydrazine via NH_2 attack pathways over the Ir(111) surface. TS indicates the energy of the transition energies.

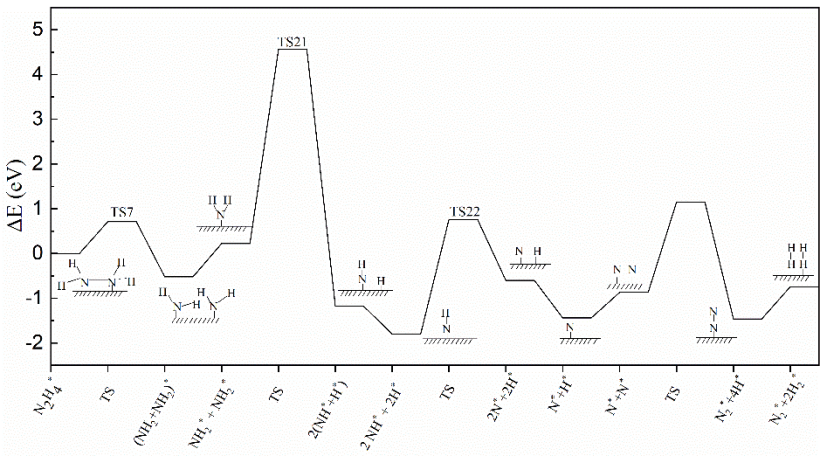

Figure 3-15. N-N bond breaking and subsequent dehydrogenation pathways of N_2H_4 dissociation over the Ir(111) surface. TS indicates the energy of the transition energies.

In summary, N_2H_4 tends to split into NH_2 early in the decomposition process. These intermediates assist the dehydrogenation of co-adsorbed N_2H_x (x = 1-4) species yielding NH_3 and N_2 molecules. The crucial role of NH_2 in the selectivity control agrees with the mechanism on Ir(100),[42] Cu(111),[14] Rh(111),[15] Pt(111).[41] At higher temperatures, the competitive intramolecular dehydrogenation pathway generates molecular hydrogen, consistent with experimental studies.[44] While at low temperature, reduced Ir/CeO_2 exhibits a yield toward hydrogen formation of 0.73% ± 0.12% in our experiment.

3.4.6 Infrared spectra

Infrared spectroscopy (IR) plays an important role in the characterization of the catalytic process, due to its ability to identify intermediate species along with the reaction mechanisms. We derived the spectra of the different adsorbed species present during the dehydrogenation of hydrazine. Figure 3-16a shows that the strength of the hydrogen vibrations decreases with the dehydrogenation, and the peak associated with the N-N vibration has an obvious red-shift in the spectrum.[45–47] This shift indicates that the dehydrogenation process will make the N-N bond stronger, increasing the bond order, in agreement with the dissociation energies R11 – R15. Figure 3-16b shows the spectra derived from the species with a single nitrogen atom, i.e. NH_3, NH_2, NH, and N. The distinctive stretching of ammonia is at 1010.8 cm^{-1},[47,48]

which shift to lower wavenumbers with the dehydrogenation species becoming IR-active at 750 cm^{-1} for NH intermediate.

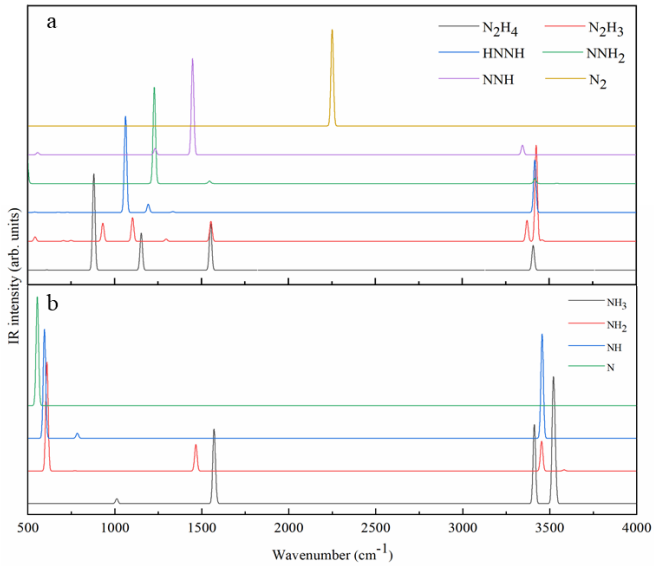

Figure 3-16. a) Infrared spectra for adsorbate N_2H_4, N_2H_3, HNNH, NNH_2, NNH, and N_2); b) Infrared spectra for adsorbate NH_3, NH_2, NH, and N

3.5 Conclusions

We have combined computational and experimental techniques to compare the adsorption process of hydrazine and products of its decomposition on Ir(111) and IrO_2 surfaces. We found that the strong molecular adsorptions on IrO_2 block the catalytic site. We followed the catalytic pathways and decomposition mechanisms of N_2H_4 decomposition on Ir(111) using density functional theory (DFT) calculations. We have studied the electron density and density of states (DOS) of the hydrazine adsorbate system and explained the N-N bond scission by the molecular orbital theory. Furthermore, we analyze the vibrations of hydrazine, NH_3, and their intermediates to support the experimental findings from infrared spectra. Intermediate adsorptions were followed by the analysis of three catalytic mechanisms (intramolecular reaction between hydrazine, the intramolecular reaction between NH_2, and NH_2 assisted dehydrogenation). The results show that hydrazine decomposition prefers to start with an initial N-N bond scission toward an NH_2 intermediate, which facilitates the subsequent dehydrogenation from N_2H_x (x = 1-4) to produce N_2 and NH_3. It is

challenging to produce hydrogen ad-atoms by N-H bond breaking and perform recombination of hydrogen molecules at moderate temperatures because of the high activation barriers and reaction energies. Therefore, it can be understood from our calculations that at ambient conditions, the main products are NH_3 and N_2, as supported by experimental work, and that controlling the antibonding molecular orbital (π*) occupation may lead to a more selective decomposition towards molecular hydrogen.

3.6 References

(1) Smith, M. J.; Alabi, O.; Hughes, N.; Dodds, P. E.; Turner, K.; Irvine, J. T. The Economic Impact of Hydrogen and Fuel Cells in the UK. *H2FC Supergen, London, UK* **2017**.

(2) Hayashi, H. Hydrazine Synthesis: Commercial Routes, Catalysis and Intermediates. *Research on chemical intermediates* **1998**, *24* (2), 183–196.

(3) Schirmann, J.-P. Method for Preparing Hydrazine Hydrate, February 2003.

(4) Qiao, S.; Yin, X.; Tian, T.; Jin, R.; Zhou, J. Hydrazine Production by Anammox Biomass with NO Reversible Inhibition Effects. *Green Chemistry* **2016**, *18* (18), 4908–4915.

(5) Aika, K.; Ohhata, T.; Ozaki, A. Hydrogenolysis of Hydrazine over Metals. *Journal of Catalysis* **1970**, *19* (2), 140–143.

(6) Rehse, K.; Shahrouri, T. Hydrazine Derivatives. *Archiv der Pharmazie: An International Journal Pharmaceutical and Medicinal Chemistry* **1998**, *331* (10), 308–312.

(7) Schulz-Ekloff, G.; Hoppe, R. Electron Diffraction Determination of an Orientation-Relationship for Iridium-on-η-Alumina. *Catal Lett* **1990**, *6* (3), 383–387. https://doi.org/10.1007/BF00764005.

(8) Cho, S. J.; Lee, J.; Lee, Y. S.; Kim, D. P. Characterization of Iridium Catalyst for Decomposition of Hydrazine Hydrate for Hydrogen Generation. *Catalysis letters* **2006**, *109* (3–4), 181–186.

(9) Singh, S. K.; Xu, Q. Complete Conversion of Hydrous Hydrazine to Hydrogen at Room Temperature for Chemical Hydrogen Storage. *Journal of the American Chemical Society* **2009**, *131* (50), 18032–18033.

(10) Singh, S. K.; Zhang, X.-B.; Xu, Q. Room-Temperature Hydrogen Generation from Hydrous Hydrazine for Chemical Hydrogen Storage. *Journal of the American Chemical Society* **2009**, *131* (29), 9894–9895.

(11) Singh, S. K.; Iizuka, Y.; Xu, Q. Nickel-Palladium Nanoparticle Catalyzed Hydrogen Generation from Hydrous Hydrazine for Chemical Hydrogen Storage. *International Journal of Hydrogen Energy* **2011**, *36* (18), 11794–11801.

(12) Manukyan, K. V.; Cross, A.; Rouvimov, S.; Miller, J.; Mukasyan, A. S.; Wolf, E. E. Low Temperature Decomposition of Hydrous Hydrazine over FeNi/Cu Nanoparticles.

Applied Catalysis A: General **2014**, *476*, 47–53.
(13) Block, J.; Schulz-Ekloff, G. The Catalytic Decomposition of Nitrogen-15-Labeled Hydrazine on MgO-Supported Iron. *Journal of Catalysis* **1973**, *30* (2), 327–329.
(14) Tafreshi, S. S.; Roldan, A.; de Leeuw, N. H. Density Functional Theory Calculations of the Hydrazine Decomposition Mechanism on the Planar and Stepped Cu(111) Surfaces. *Phys. Chem. Chem. Phys.* **2015**, *17* (33), 21533–21546. https://doi.org/10.1039/C5CP03204K.
(15) Deng, Z.; Lu, X.; Wen, Z.; Wei, S.; Liu, Y.; Fu, D.; Zhao, L.; Guo, W. Mechanistic Insight into the Hydrazine Decomposition on Rh (111): Effect of Reaction Intermediate on Catalytic Activity. *Physical Chemistry Chemical Physics* **2013**, *15* (38), 16172–16182.
(16) Zhang, P.-X.; Wang, Y.-G.; Huang, Y.-Q.; Zhang, T.; Wu, G.-S.; Li, J. Density Functional Theory Investigations on the Catalytic Mechanisms of Hydrazine Decompositions on Ir(111). *Catalysis Today* **2011**, *165* (1), 80–88. https://doi.org/10.1016/j.cattod.2011.01.012.
(17) Grimme, S.; Antony, J.; Ehrlich, S.; Krieg, H. A Consistent and Accurate Ab Initio Parametrization of Density Functional Dispersion Correction (DFT-D) for the 94 Elements H-Pu. *The Journal of chemical physics* **2010**, *132* (15), 154104.
(18) Kresse, G.; Furthmüller, J. Efficiency of Ab-Initio Total Energy Calculations for Metals and Semiconductors Using a Plane-Wave Basis Set. *Computational materials science* **1996**, *6* (1), 15–50.
(19) Bucko, T.; Hafner, J.; Lebegue, S.; Angyán, J. G. Improved Description of the Structure of Molecular and Layered Crystals: Ab Initio DFT Calculations with van Der Waals Corrections. *The Journal of Physical Chemistry A* **2010**, *114* (43), 11814–11824.
(20) Perdew, J. P.; Burke, K.; Ernzerhof, M. Generalized Gradient Approximation Made Simple. *Physical review letters* **1996**, *77* (18), 3865.
(21) Perdew, J. P.; Ruzsinszky, A.; Csonka, G. I.; Vydrov, O. A.; Scuseria, G. E.; Constantin, L. A.; Zhou, X.; Burke, K. Restoring the Density-Gradient Expansion for Exchange in Solids and Surfaces. *Physical review letters* **2008**, *100* (13), 136406.
(22) Kresse, G.; Joubert, D. From Ultrasoft Pseudopotentials to the Projector Augmented-Wave Method. *Physical review b* **1999**, *59* (3), 1758.
(23) Grimme, S.; Ehrlich, S.; Goerigk, L. Effect of the Damping Function in Dispersion Corrected Density Functional Theory. *Journal of computational chemistry* **2011**, *32* (7), 1456–1465.
(24) Tafreshi, S. S.; Roldan, A.; Dzade, N. Y.; de Leeuw, N. H. Adsorption of Hydrazine on the Perfect and Defective Copper (111) Surface: A Dispersion-Corrected DFT Study. *Surface Science* **2014**, *622*, 1–8.
(25) Dzade, N.; Roldan, A.; de Leeuw, N. A Density Functional Theory Study of the Adsorption of Benzene on Hematite (α-Fe2O3) Surfaces. *Minerals* **2014**, *4* (1), 89–115.
(26) Roldan, A.; de Leeuw, N. H. A Kinetic Model of Water Adsorption, Clustering and Dissociation on the Fe3S4{001} Surface. *Physical Chemistry Chemical Physics* **2017**, *19* (19), 12045–12055.
(27) Singh, H. P. Determination of Thermal Expansion of Germanium, Rhodium and Iridium by X-Rays. *Acta Crystallographica Section A: Crystal Physics, Diffraction, Theoretical and General Crystallography* **1968**, *24* (4), 469–471.

(28) Mills, G.; Jónsson, H. Quantum and Thermal Effects in H 2 Dissociative Adsorption: Evaluation of Free Energy Barriers in Multidimensional Quantum Systems. *Physical review letters* **1994**, *72* (7), 1124.
(29) Mills, G.; Jónsson, H.; Schenter, G. K. Reversible Work Transition State Theory: Application to Dissociative Adsorption of Hydrogen. *Surface Science* **1995**, *324* (2–3), 305–337.
(30) Heyden, A.; Bell, A. T.; Keil, F. J. Efficient Methods for Finding Transition States in Chemical Reactions: Comparison of Improved Dimer Method and Partitioned Rational Function Optimization Method. *The Journal of chemical physics* **2005**, *123* (22), 224101.
(31) Freakley, S. J.; Ruiz‐Esquius, J.; Morgan, D. J. The X-Ray Photoelectron Spectra of Ir, IrO2 and IrCl3 Revisited. *Surface and Interface Analysis* **2017**, *49* (8), 794–799. https://doi.org/10.1002/sia.6225.
(32) Matz, O.; Calatayud, M. Periodic DFT Study of Rutile IrO2: Surface Reactivity and Catechol Adsorption. *The Journal of Physical Chemistry C* **2017**, *121* (24), 13135–13143.
(33) Schmidt, E.; W, E. Oxidation Resistance of Hydrazine Decomposition Catalysts, Part I: Alumina-Supported Iridium Catalyst. *Oxidation of Metals* **1975**.
(34) Agusta, M. K.; Kasai, H. First Principles Investigations of Hydrazine Adsorption Conformations on Ni(111) Surface. *Surface Science* **2012**, *606* (7), 766–771. https://doi.org/10.1016/j.susc.2012.01.009.
(35) Hoffmann, R. A Chemical and Theoretical Way to Look at Bonding on Surfaces. *Rev. Mod. Phys.* **1988**, *60* (3), 601–628. https://doi.org/10.1103/RevModPhys.60.601.
(36) Pople, J. A.; Curtiss, L. A. The Energy of N2H2 and Related Compounds. *J. Chem. Phys.* **1991**, *95* (6), 4385–4388. https://doi.org/10.1063/1.461762.
(37) Huber, K. *Molecular Spectra and Molecular Structure: IV. Constants of Diatomic Molecules*; Springer US, 1979. https://doi.org/10.1007/978-1-4757-0961-2.
(38) Haynes, W. M. *CRC Handbook of Chemistry and Physics*; CRC Press, 2014.
(39) Ferrin, P. A.; Kandoi, S.; Zhang, J.; Adzic, R.; Mavrikakis, M. Molecular and Atomic Hydrogen Interactions with Au−Ir Near-Surface Alloys. *J. Phys. Chem. C* **2009**, *113* (4), 1411–1417. https://doi.org/10.1021/jp804758y.
(40) Liu, C.; Zhu, L.; Wen, X.; Yang, Y.; Li, Y.-W.; Jiao, H. Hydrogen Adsorption on Ir(111), Ir(100) and Ir(110)—Surface and Coverage Dependence. *Surface Science* **2020**, *692*, 121514. https://doi.org/10.1016/j.susc.2019.121514.
(41) Rosca, V.; Koper, M. T. M. Electrocatalytic Oxidation of Ammonia on Pt(111) and Pt(100) Surfaces. *Phys. Chem. Chem. Phys.* **2006**, *8* (21), 2513–2524. https://doi.org/10.1039/B601306F.
(42) Huang, W.; Lai, W.; Xie, D. First-Principles Study of Decomposition of NH3 on Ir(100). *Surface Science* **2008**, *602* (6), 1288–1294. https://doi.org/10.1016/j.susc.2008.01.029.
(43) Maurel, R.; Menezo, J. C. Catalytic Decomposition of 15N-Labeled Hydrazine on Alumina-Supported Metals. *Journal of Catalysis* **1978**, *51* (2), 293–295. https://doi.org/10.1016/0021-9517(78)90304-4.
(44) Al-Haydari, Y. K.; Saleh, J. M.; Matloob, M. H. Adsorption and Decomposition of Hydrazine on Metal Films of Iron, Nickel, and Copper. *The Journal of Physical Chemistry* **1985**, *89* (15), 3286–3290.

(45) Гурвич, Л. В.; Вейц, И. В.; Alcock, C. B.; Институт высоких температур (Академия наук СССР); Государственный институт прикладной химии (Soviet Union). *Thermodynamic Properties of Individual Substances*; 1989.
(46) Durig, J. R.; Griffin, M. G.; Macnamee, R. W. Raman Spectra of Gases. XV: Hydrazine and Hydrazine-D4. *Journal of Raman Spectroscopy* **1975**, *3* (2–3), 133–141. https://doi.org/10.1002/jrs.1250030204.
(47) Yamaguchi, A.; Ichishima, I.; Shimanouchi, T.; Mizushima, S.-I. Far Infra-Red Spectrum of Hydrazine. *Spectrochimica Acta* **1960**, *16* (11–12), 1471–1485.
(48) Koops, Th.; Visser, T.; Smit, W. M. A. Measurement and Interpretation of the Absolute Infrared Intensities of NH3 and ND3. *Journal of Molecular Structure* **1983**, *96* (3), 203–218. https://doi.org/10.1016/0022-2860(83)90049-2.

Chapter 4 Ammonia reforming on carbon materials

Carbon-based materials are commonly used in catalysis as metal-free catalysts and as support for metal particles. We investigated a series of graphene point defects on the NH_3 reforming process using the density functional theory and shed light on their role in the catalytic reforming of ammonia. The adsorption of molecules and intermediates on carbon vacancies, lattice reconstructions, partial oxidations and dopants was analyzed to provide details on the most favorable interactions. Thermochemical investigations revealed the structures active for NH_3 adsorption and dehydrogenation. However, these defects are ineffective to desorb the reaction products, i.e., N_2 and H_2. Based on transition state theory, we implemented microkinetic simulations and found that the rate-determining step is either the NH_3 activation or the desorption of reformed molecules, depending on the defect type. Batch reaction simulations within a wide temperature and time range indicated that, although the NH_3 dehydrogenation may occur, the active sites become poisoned by the H or N anchored atoms; therefore, in the long term, carbon-based materials are inert towards the NH_3 reforming.

4.1 Introduction

The development of reliable and economic hydrogen energy technologies is one of the most prominent research topics in current times. The direct industrial implementation of hydrogen energy is inhibited by high risks and costs associated with its transport and storage.[1,2] Compared with other molecular energy vectors, such as methanol, ethanol, formic acid, and methane, ammonia (NH_3) is a suitable carbon-free hydrogen energy carrier with high hydrogen capacity (17.64 wt%) and stable properties under mild conditions.[3–6] Catalysts promoting the NH_3 reforming process are not trivial, and usually, the catalysts' supports play a crucial role in the reaction efficiency.[7] Indeed, the catalyst's support should have a large area with inert or synergistic properties to the aimed reaction.

Carbon-based materials have long been deemed suitable catalyst supports because of their high surface area, chemical resistance, low cost, and good recycling properties.[8]

Carbon-based supports have shown catalytic activity by themselves. Pereira and co-workers used carbon nanotubes as catalysts for the oxidative dehydrogenation of ethylbenzene to styrene with a conversion of 19.6% catalyzed by the untreated carbon material.[9] Qu *et al.* found N-doped graphene to be a metal-free electrode with three-times higher electrocatalytic activity than platinum for the oxygen reduction reaction (ORR).[10] Furthermore, Zhang *et al.* investigated the mechanism of ORR on point defects in graphene clusters for fuel cell applications using density functional theory (DFT) methods.[11] Su *et al.* studied the impact of defects in graphene oxide on the catalytic activities for the oxidative coupling of amines to imines. The results suggest that the enhanced catalytic activity can be linked to the unpaired electrons in the system.[12] Although there is plenty of research focusing on applying carbon-based supports and carbon catalysts, the mechanism of NH_3 reforming on defective graphene remains unclear.[13,14]

Point defects (including vacancies and lattice heteroatoms) are the most fundamental defects on graphene surfaces, which can be detected under advanced microscopic technologies. These point defects modify the local electronic structure and the properties of carbon-based materials.[15–18] The literature on defective graphene suggests that single vacancies and mixed defects show a strong combination with hydrogen, providing a compelling advantage to retain it over pristine graphene.[19] Therefore, these point defects have the potential to be active sites for NH_3 reforming. However, the short life span of intermediates and complex micro-structures concerning the reaction processes at the atomic level thwart the investigations of carbocatalysis on point defects.

For this reason, we performed DFT and microkinetic analyses on defective graphene to provide accurate information on their role in the NH_3 reforming process. This paper discusses the reaction pathway of NH_3 reforming on the different point defects, the results on batch and temperature-programmed desorption simulations on promising candidates. We rationalized the results observed using accurate electronic structure calculations and shed light on carbon-based materials for NH_3 reforming and H_2 storage.

4.2 Methodology

The Vienna Ab-initio Simulation Package (VASP) was employed to simulate the NH_3 reforming reaction on defective and doped graphene within the DFT frameworks.[20,21] The spin-polarized revised Perdew-Burke-Ernzerhof (rPBE) method of the generalized gradient approximation (GGA) was adopted to describe the exchange-correlation with a plane-wave kinetic cutoff energy of 500 eV.[22] The projector augmented wave (PAW) includes non-spherical contributions from the core to the gradient corrections.[23–25] The long-range interactions were characterized by the DFT-D3 method of Grimme with zero dampings.[26] The optimized convergence thresholds of internal forces and electronic relaxation were set to 0.02 eV/Å and 10^{-5} eV, respectively. A 3×3×1 k-spacing Monkhorst-Pack grid sampled the Brillouin zone with a smearing broadening of 0.2 eV.

The optimized lattice parameter of pristine graphene is 2.469 Å, which is in agreement with the benchmark value, 2.460 Å.[27] All surfaces were represented by a supercell slab model (vacancies and Stone-Wales defects: *p(6×6)*; doped: *p(4×4)*) to avoid the interaction between defects. We added 15 Å of vacuum perpendicular to the slab to prevent any spurious interaction with periodic images. Dipole correction perpendicular to the surface was applied upon the molecular adsorption.

The molecular adsorption energy (E_{ads}) is defined by Eq 4-1, and the relative energy (ΔE) is calculated by Eq 4-2:

$$E_{ads} = E_{system} - E_{surface} - E_{molecule} \quad \text{Eq 4-1}$$

$$\Delta E = E_{system} + \frac{n}{2} * E_{H_2} - E_{surface} - E_{NH_3} \quad \text{Eq 4-2}$$

Where E_{system} is the total energy of the adsorbed system, $E_{surface}$ denotes the energy of the clean surface, including pristine graphene and the defects, E_{NH_3} and E_{H_2} are the energies of NH_3 and H_2 isolated molecules. The half energy of the hydrogen molecule refers to the energy of one H atom, and n is the number of H dissociated from NH_3 in the particular stage defining ΔE. The formation energy of defective graphene surfaces is represented by Eq 4-3.

$$\mathrm{E_{formation}} = \mathrm{E}_{defects} - \mathrm{n} * \mathrm{E_{graphene}} \quad \text{Eq 4-3}$$

Where $E_{defects}$ is the energy of the defective surface, n is the number of atoms in the slab, and $E_{graphene}$ is the energy of pristine graphene per atom. The energy of the transition states (TS) between intermediates along the reaction profiles was determined by the climbing image nudged elastic band (ci-NEB) combined with the improved dimer method (IDM), ensuring a unique imaginary frequency along the reaction coordinate.[28–30] We defined the activation barriers (E_a) as the energy difference between the TS and the initial states (IS). The reaction energies (E_r) are given by the difference between the final states (FS) and the IS energies. A negative value indicates an exothermic reaction step (Eq 4-4).

$$E_a = E_{TS} - E_{IS} \quad \text{Eq 4-4}$$

$$E_r = E_{FS} - E_{IS} \quad \text{Eq 4-5}$$

We implemented the thermodynamic and kinetic outcomes obtained from DFT into NH_3 reforming microkinetic simulations grounded on the transition state theory (TST).[31–33] The thermochemistry and kinetic models are detailed in the Supporting Information (SI).

4.3 Results and discussion

4.3.1 Surface models

Vacancy surfaces models

We considered two kinds of vacancy defects on pristine graphene, i.e., single vacancy (SV) and double vacancy (DV), and three types of stone-wales defects, i.e., Stone-Wales (SW), vacancy Stone-Wales arrangement-1 (VSW-1), and vacancy Stone-Wales arrangement-2 (VSW-2). The optimized structures are shown in Figure 4-1 and Figure 4-2. The formation energies of defective graphene with respect to pristine graphene (Figure 4-1a) are in Table 4-1, which are in excellent agreement with previous benchmarks.

Simple vacancy defects. SV is the most basic defect in graphene and can be observed using transmission electron (TEM) and scanning tunneling (STM)

microscopies.[15,16] Upon the local Jahn-Teller distortion, there is only one carbon atom with a dangling bond at a distance of 1.395 Å to the closest neighbor, much shorter than in pristine graphene, 1.426 Å (Figure 4-1b). Ugeda *et al.* found an increase in the local density of states on SV's dangling bond, triggering a protrusion in the STM images.[34] The SV formation energy is 7.64 eV, which is in agreement with the previous literature. [35-36] The DV is created by removing two neighboring atoms, see Figure 4-1c. The fully relaxed DV presents no dangling bonds and features two pentagons and one octagon instead of four hexagons in the perfect graphene. The formation energy of a DV is 7.49 eV, also in agreement with benchmark values.[37,38]

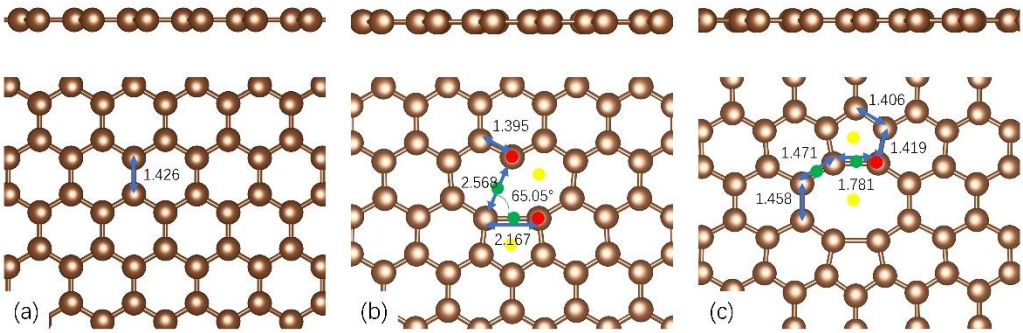

Figure 4-1. Structure representations of (a) pristine graphene, (b) single vacancy, and (c) double vacancy on graphene. Khaki spheres represent carbon atoms. Red, yellow, and green dots indicate top, hollow, and bridge adsorption sites. Distances are given in Å.

Stone-Wales defects are generated by reconstructing the graphitic lattice, i.e., switching between pentagons, hexagons, and heptagons. These are regular in carbon material with sp2 hybridization. As seen in Figure 4-2a, four hexagons are transformed into two pentagons and two heptagons in the Stone-Wales defect (SW) by rotating one of the C-C bonds by 90°. SW has a formation energy of 4.76 eV. The rotation of one bond in the DV's octagon transforms the defect into a vacancy Stone-Wales defect arrangement-1 (VSW-1) with three pentagons and three heptagons, see Figure 4-2.[21] The total formation energy of this defect is 6.15 eV, which is 1.34 eV lower than that of DV, implying a thermodynamically favorable reconstruction. Rotating one more edge C-C bond in the heptagons transforms VSW-1 to VSW-2, see Figure 4-2c. This defect's formation energy is 7.14 eV, higher than the VSW-1 by 1 eV and in agreement with the former

investigations.[18] These last VSW types of defects are frequently observed in electron microscopy experiments.[17] Among these three Stone-Wales defects, the bond rotation only creates the surface fluctuation on SW with the shortest C-C bond.

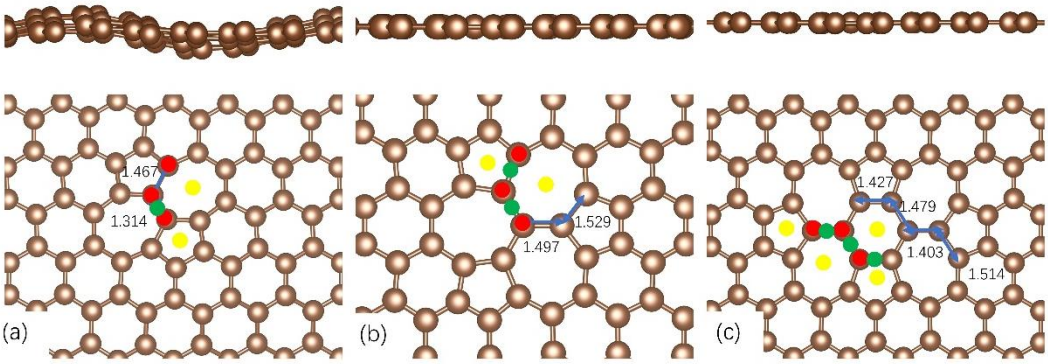

Figure 4-2. Structure of the reconstructed graphene defects (a) Stone-Wales, (b) vacancy Stone-Wales-1, and (c) vacancy Stone-Wales-2. Khaki spheres represent carbon atoms. Red, yellow, and green dots indicate top, hollow, and bridge adsorption sites. Distances are given in Å.

Table 4-1. Formation energies of defective graphene structures with respect to pristine graphene.

Surface	This work (eV)	Reference (eV)
SV	7.64	7.78 (LDA),[35] 7.80 (PW91),[39] 7.0±0.5(Exp.)[36]
DV	7.49	8.7 (Exp.)[37], 7.6 (LDA)[38]
SW	4.76	5.2 (LDA),[40] 4.8 (PW91),[40] 4.82 (PBE)[41]
VSW-1	6.15	-
VSW-2	7.14	-

Doped surface models

The charge and spin density distribution of graphene could be modified by dopants, an effective method to tune graphite surface properties.[42] We considered the substitution of one graphitic (from pristine lattice) or pyridinic carbon (from a vacancy) by a heteroatom, e.g., O, N, B, and S. Besides, we have also included the carboxyl and hydroxyl groups as local defects.

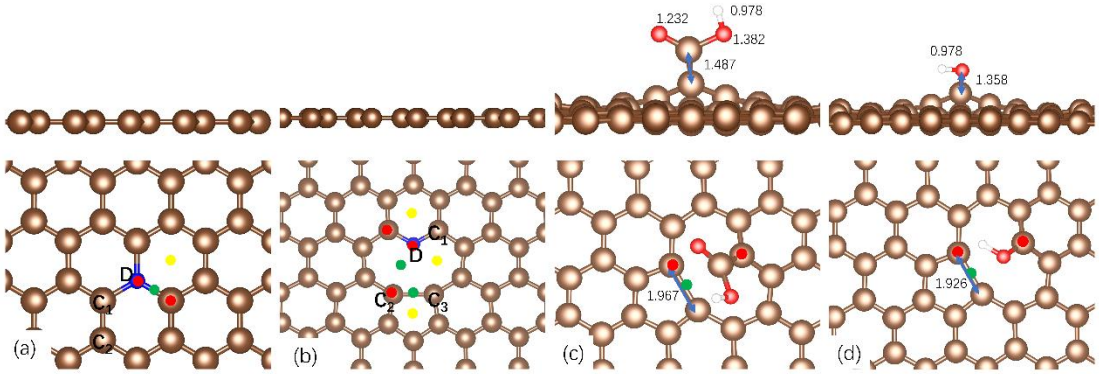

Figure 4-3. Representation of doped structures: (a) graphitic, (b) pyridinic, (c) carboxyl, and (d) hydroxyl group. The blue and khaki spheres represent the dopant and carbon atoms, respectively. Red, yellow and green buttons represent top, hollow, and bridge sites. In c and d, red and white spheres represent oxygen and hydrogen.

Table 4 - 2. Structural parameters of graphitic and pyridinic doped graphene structures. Pristine graphene, SV, COOH, and OH values are included for the comparison. Labels D, C_1, DC_2, C_3 are depicted in Figure 4-3.

	Graphitic dopant		Pyridinic dopant			
	DC_1(Å)	$\angle DC_1C_2$(°)	DC_1(Å)	DC_2(Å)	C_2C_3(Å)	$\angle DC_2C_3$(°)
Graphene	1.426	120.0	1.395	-	-	-
SV	-	-	-	2.568	2.167	65.1
O	1.489	117.5	1.370	2.559	1.971	67.4
N	1.415	120.1	1.336	2.545	1.910	68.0
B	1.484	118.7	1.535	2.272	2.565	55.6
S	1.627	116.7	1.634	2.393	2.158	63.2

As shown in Figure 4-3, among the graphitic dopant, only graphitic N dopants (GN) shorten the lattice length from 1.426 Å in pristine graphene to 1.415 Å. The pyridinic nitrogen-doped system (PN) presents the closest bond length between the heteroatom and the lattice-carbon atoms (DC_1 label in Figure 4-3). The graphitic sulfur-doped (GS) structure has the most severe lattice expansion as S has the biggest atomic radius of the dopants considered. Due to the atomic radius's size relative to the carbon atom, PO and PN increase the angles $\angle DC_2C_3$ compared with the angle of 65.1° in SV, while PB and PS decrease it. Especially in PB, with a small atomic radius and electronegativity, the boron atom moves closer to the defect center. The presence of a carboxyl and hydroxyl group pulls up the dangling carbon, shortening the C-C distance

compared with SV.

4.3.2 NH_3 adsorption and reforming

We have investigated all the non-equivalent adsorptions and configurations of the species along the NH_3 reforming process to derive the relative energies between them as a function of the local surface defects.

Table 4-3. Molecule adsorption and relative energies of surface species (eV) on the defective graphene surfaces.

Surface	NH_3*	NH_2*	NH*	N*	H*	N_2*	H_2*
Pristine	-0.11	2.47	4.29	4.33	1.46	-0.11	-0.07
SV	-1.28	-1.55	-4.07	-6.65	-2.17	-2.31	-2.54
DV	-0.15	-0.63	-2.07	-1.98	0.00	-0.12	-0.03
SW	-0.14	1.21	1.64	2.20	0.40	-0.11	-0.06
VSW-1	-0.10	0.77	2.24	2.98	-0.24	-0.09	-0.04
VSW-2	-0.12	1.12	2.37	2.00	0.22	-0.09	-0.05
GO	-0.02	-0.88	-0.43	0.54	-1.39	0.07	-0.06
PO	-0.11	0.24	-1.78	-1.69	-0.77	0.13	-0.04
GN	-0.67	0.60	2.75	2.96	0.25	-0.67	-0.37
PN	-0.16	-0.26	-1.97	-2.15	-1.08	0.40	-0.01
GB	-0.66	0.61	1.82	2.71	0.13	-0.67	-0.36
PB	-0.97	-1.56	-3.46	-6.57	-1.88	-0.28	-0.21
GS	-0.17	0.20	0.97	1.93	-0.27	-0.09	-0.06
PS	-0.69	-1.05	-2.98	-2.92	-1.47	-2.00	-0.36
COOH	-0.48	0.37	-1.37	-4.19	-0.74	-0.14	-2.77
OH	-0.55	0.58	-1.56	-4.40	-0.61	-0.13	-0.08

Table 4-3 summarizes the adsorption and relative energies of the most favorable configurations of NH_x (x = 1 - 3) and atomic and molecular hydrogen and nitrogen. The adsorption modes on SV and DV are represented in appendix Figure S4-1 of the supplementary information (SI) and on PO, GO, and PN in Figure S4-2 as selected doped examples.

According to Sabatier's principle, the optimal interaction of reactive species with the catalysts should be neither too weak nor too strong. Due to the inactive π system in pristine graphene, SW, VSW-1, VSW-2, GN, GB, and GS (as shown in Figure S4-3), their interaction with NH_2 and NH are very weak or unfavorable, and hence, these are not

considered further for the mechanistic study. On the other hand, the weakening of the conjugated π system in SV, DV, GO, PO, PN, PB, and PS creates the active region for the reactants to interact, making these defects promising candidates to catalyze the ammonia reforming. The low electron density at the pz orbital of dangling carbon connected to COOH and OH is not enough to stabilize the NH_2 upon the first hydrogenation inhibiting the process (Table 4-3).

SV can adsorb the NH_3 molecule effectively with an N-C distance of 1.475 Å. However, upon NH_3 complete dehydrogenation, the N atom incorporates into the carbon lattice with a rather exothermic step. This process could be used as a method for N-dope graphene materials. The DV interaction with reaction intermediates depends on the number of hydrogens attached to N, which finally is incorporated in the carbon lattice. In the case of doped C-structures, the introduction of oxygen and nitrogen in the lattice rearranges the electronic structure and, since the electronegativity sequence is O > N > C and the ammonia molecule has an unpair electron, the preferrable ammonia adsorption is the nearby unpopulated C-orbitals, i.e., next to the dopant or opposite to the pyridinic heteroatom. The electron density localized at the PO and PN difficult the adsorption of NH_3 but not the electron-deficient NH_X ($x \leq 2$). Other heteroatoms like B and S in pyridinic positions are reactive and dehydrogenate NH_3 spontaneously, leaving N and H atoms firmly bound to the surface. Interestingly, the presence of COOH and OH species behaves similarly to PB and PS, except that the first dehydrogenation is endothermic.

4.3.3 Thermochemistry

The calculated energy profiles for NH_3 reforming on local defects, i.e., vacancies and doped graphene surfaces, are shown in the Figure 4-4 and Figure 4-5. The energy differences of SW, VSW-1, VSW-2, GN, GB, and GS during the dehydrogenation are endothermic, similar to pristine graphene. The only carbon-defective system with a moderate NH_3 reforming pathway is DV ($|\Delta E_{max}| < 2.07$ eV), which seems a suitable candidate as a non-metallic catalyst.

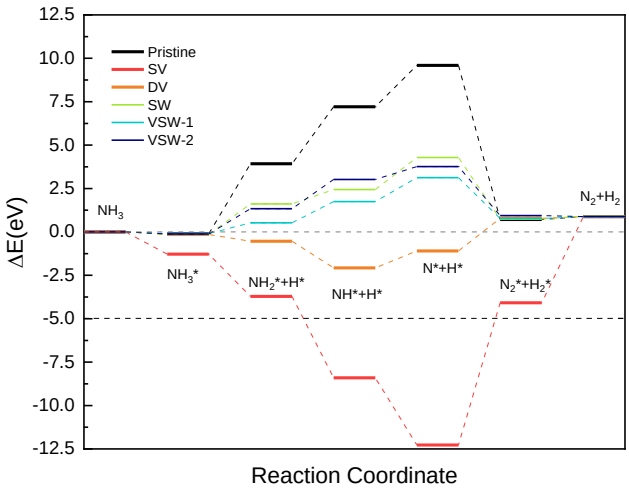

Figure 4-4. Thermodynamic energy profile of NH_3 reforming on defective graphene. Pristine graphene is also represented for comparison. The asterisk (*) denotes surface species. The dashed line at -5 eV indicates an arbitrary limit set to guide the eye.

The complete NH_3 dehydrogenation is thermodynamically favorable on PN, PB, GO, PO, PS, OH, and COOH surfaces (Figure 4-5). However, severe surface deformation and high energy differences between elementary steps, e.g., the recombination of N_2 and H_2 on PB, suppress the overall reaction possibility on PB, PS, OH, and COOH. Considering that the reaction energies along the pathway should be moderate, we will investigate every elementary reaction on PO, GO, and PN.

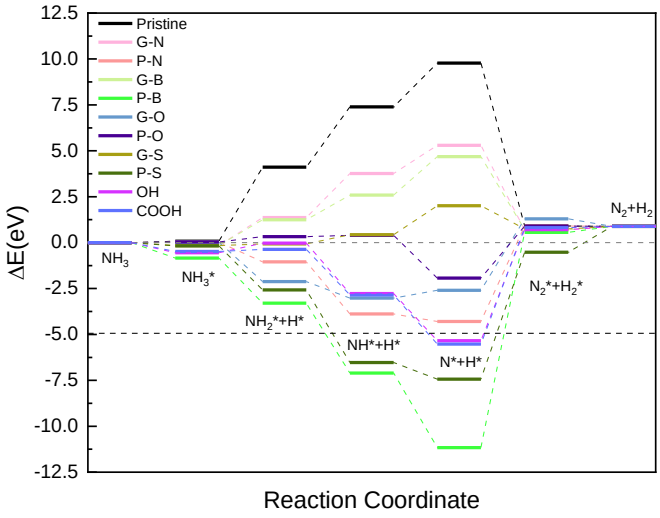

Figure 4-5. Thermodynamic energy profiles of NH_3 reforming on doped graphene. Pristine graphene is also represented for comparison. The asterisk (*) denotes surface species. The dashed line at -5 eV indicates an arbitrary limit set to guide the eye.

The electron transfer between the N in NH_3 and the C-dangling bonds plays a

crucial role in activating the N-H bond required for triggering the first dehydrogenation step. Therefore, SV, DV, PO, GO, and PN surfaces are selected from the defects above for further thermodynamic and kinetic investigations. We computed the free reaction and barrier energies of ammonia reforming according to the reaction mechanism in Table 4-4. We plotted them as a function of the temperature in Figure 4-6 and Figure S4-4, where the 'R + odd numbers' are the direct reactions and 'R + even numbers' are the reverse reactions, respectively.

Table 4-4. Elementary steps in NH_3 reforming process—asterisk (*) denotes a free surface site and surface species.

No.	Dehydrogenation/recombination	No.	Adsorption/Desorption
R1	$\mathrm{NH_3^* + * \longrightarrow NH_2^* + H^*}$	A1	$\mathrm{NH_3 + * \longrightarrow NH_3^*}$
R2	$\mathrm{NH_2^* + H^* \longrightarrow NH_3^* + *}$	D1	$\mathrm{NH_3^* \longrightarrow NH_3 + *}$
R3	$\mathrm{NH_2^* + * \longrightarrow NH^* + H^*}$	A2	$\mathrm{H_2 + * \longrightarrow H_2^*}$
R4	$\mathrm{NH^* + H^* \longrightarrow NH_2^* + *}$	D2	$\mathrm{H_2^* \longrightarrow H_2 + *}$
R5	$\mathrm{NH^* + * \longrightarrow N^* + H^*}$	A3	$\mathrm{N_2 + * \longrightarrow N_2^*}$
R6	$\mathrm{N^* + H^* \longrightarrow NH^* + *}$	D3	$\mathrm{N_2^* \longrightarrow N_2 + *}$
R7	$\mathrm{2N^* \longrightarrow N_2^* + *}$		
R8	$\mathrm{N_2^* + * \longrightarrow 2N^*}$		
R9	$\mathrm{2H^* \longrightarrow H_2^* + *}$		
R10	$\mathrm{H_2^* + * \longrightarrow 2H^*}$		

The ammonia's N-H bond activation in R1 represents the molecule's stability on the surfaces and its dehydrogenation likelihood. Hence, the high active barrier of R1 on DV, PO, and PN inhibits the dehydrogenation process. Further investigations on the use of synergistic carbon-catalyst may help overtake the first NH_3 dehydrogenation (on DV and PN) or facilitate the H_2 desorption, explaining the improvement of activity in the oxidative coupling of amines to imines when creating defects over graphene.[12] Compared with defective graphene, H adatoms associative recombination (R9) is the rate-determining step on the three doped surfaces (PO, GO, and PN). It has a significant activation energy (~4 eV) and is highly endothermic. Therefore, PO, GO, and PN catalysts will be deactivated quickly by hydrogen poisoning.

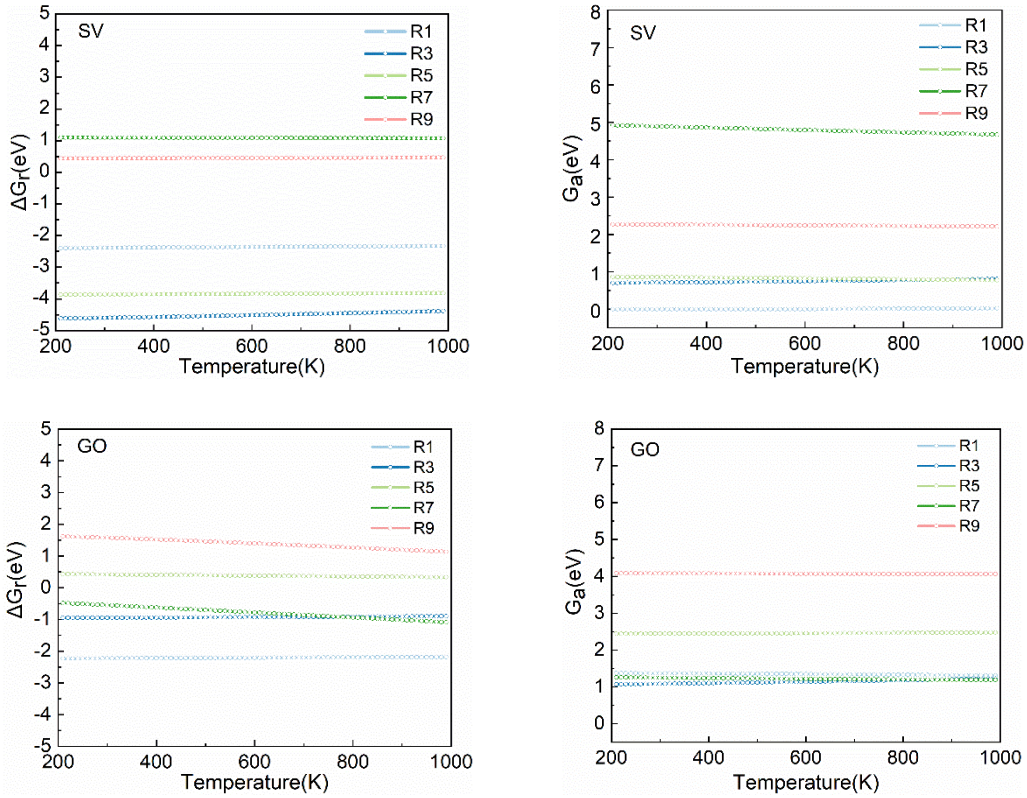

Figure 4-6. Free reaction (ΔG_r) and barrier (G_a) energies of the elementary steps in the ammonia dehydrogenation (R1, R3, R5) and molecular N_2 and H_2 formations (R7 and R9) on SV and GO as a function of the temperature.

4.3.4 Microkinetics

All elementary step's reaction rate constants were calculated based on the DFT outcomes and summarized in Table S4-1 and Table S4-2 in the SI. Some reactions have negligible reaction rates, e.g., R7 on SV, R5 and R9 on GO. However, to describe the reaction as accurately as possible, all the elementary steps were included in the microkinetic modelling.

Temperature programmed desorption (TPD)

We simulated the individual desorption of N_2 and H_2 from the considered surfaces as a crucial step to complete the catalytic cycle. Figure 4-7 shows that the N_2 molecule cannot desorb easily from SV and DV due to the strong interaction between the N atom and the carbon's dangling bond, *i.e.*, the N atom fills the C-vacancy, decreasing the

surface's free energy dramatically (Figure 4-4). On the other hand, N_2 desorption from GO and PO occurs at accessible although very different temperatures (400 K and 640 K at 0.15 ML, respectively) again due to the N's strong interaction with C-dangling bonds. Such interaction is weaker in PN's presence because of the electronic structure difference between N (one lone pair of electrons) and O atom (two lone pair of electrons). Since the dopant (O, N) participates in the conjugated π system, the interaction between H and C-dangling bonds on the dopant system is more favorable than on vacancy surfaces. The desorption temperature of H_2 is mild (460 K at 0.15 ML) on DV because of the recovery of the pentagon structure after the desorption. As seen in the thermochemistry section, H_2 evolution from PN, PO, and GO is very unfavorable and occurs at temperatures higher than 1000K. Generally, with the rise of N and H coverage on the investigated surfaces, the TPD patterns of both molecules have a ~25 K shift to lower temperatures.

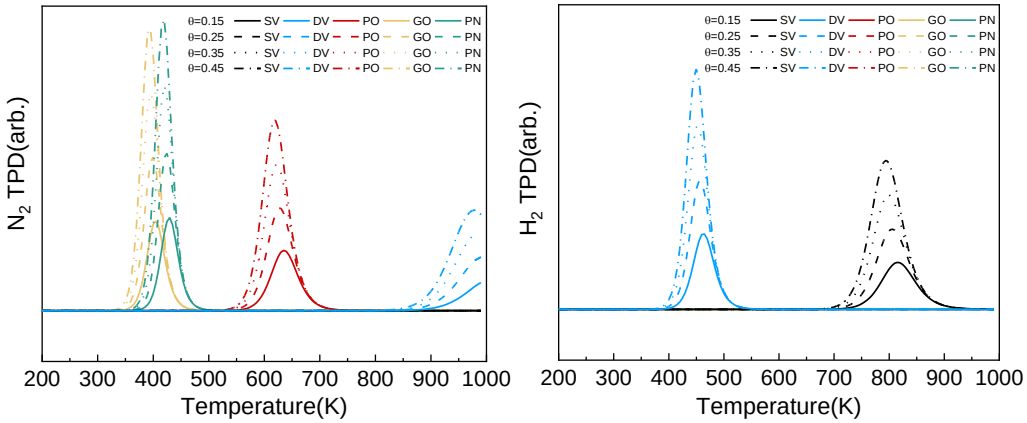

Figure 4-7. Simulated N_2 (left) and H_2 (right) TPD patterns on different graphene local defects at various initial coverages (θ in ML) and with a heating rate of 1 K/min. The temperature and time step of the numerical integration is 10K and 1s, respectively.

Batch reactor simulations

Batch reactor simulations were employed to analyze the NH_3 reforming process on the selected surfaces. Considering the high barrier energy of NH_3 dehydrogenation on DV, PO, and PN, these surfaces will present negligible changes in NH_3 concentration in batch reactor simulations. Contrarily, SV and GO structures showed considerable intake of molecular NH_3 depending on the temperature and exposure

time, Figure S4-11. The NH_3 contents on SV and GO reached the steady-state after ~600 s.

In terms of SV (Figure 4-8), the small energy barrier (0.11 eV) of the first dehydrogenation (R1) leads to NH_2 and H adsorbed on the surface. From 300 K, the consecutive dehydrogenation of NH_x species leads to a rapid increase of N and H coverages. As the temperature rises, NH_x and H adatoms recombine, forming NH_3*, which desorbs from the surface establishing an equilibrium between $NH_3 \rightleftharpoons NH_x^* + (3-x)H^*$. Beyond 700 K, the equilibrium is shifted as H_2 desorbs from the active sites. At this stage, N adatoms accumulate on the surfaces breaking the former plateau of ~0.25 ML. These results also revealed the crucial role of high temperature in the synthesis of N-doping graphene/graphite by thermal treatment with NH_3.[43,44]

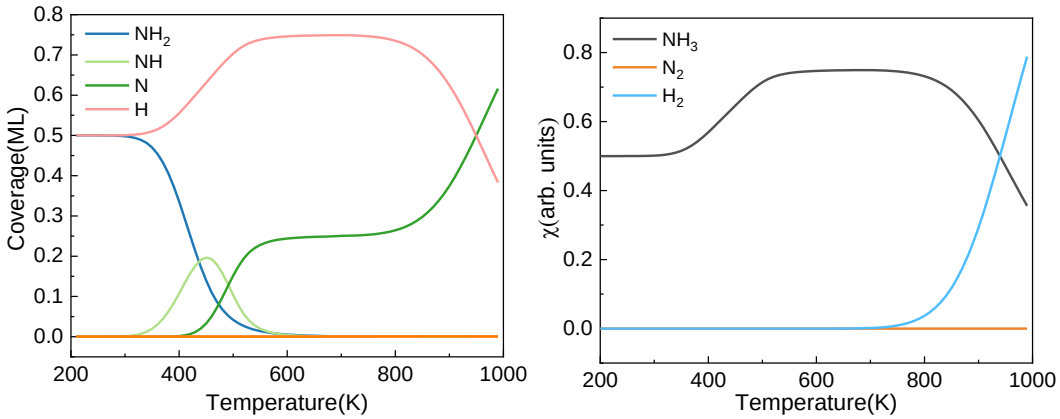

Figure 4-8. The steady-state of surface species distribution (left) on SV surface and the ratio (χ) of gaseous species (right) as functions of temperature in the batch reactor simulations. The initial ratio of NH_3: surface sites is 1:1, and the reaction time is 600s. The temperature and time step of the numerical integration is 10K and 1s, respectively.

Opposite to R1 on SV, the NH_3 dehydrogenation requires a temperature as high as 700 K on GO to proceed, as shown in Figure 4-9. R1 is driven by the desorption of N_2 but inhibited by an increase in H coverage, which eventually poisons the active sites. Note that the limited H_2 evolution opens the scope for designing high-Faraday efficient electrocatalysts based on GO structures. Contrary to carbon vacancies, the GO structure is not favorable as a precursor for the synthesis of N-doping graphene/graphite as confirmed in previous research.[45,46] And during the synthesis of

GO, impurities are difficult to remove. The activity in catalytic reactions may therefore be presented by heteroatoms.

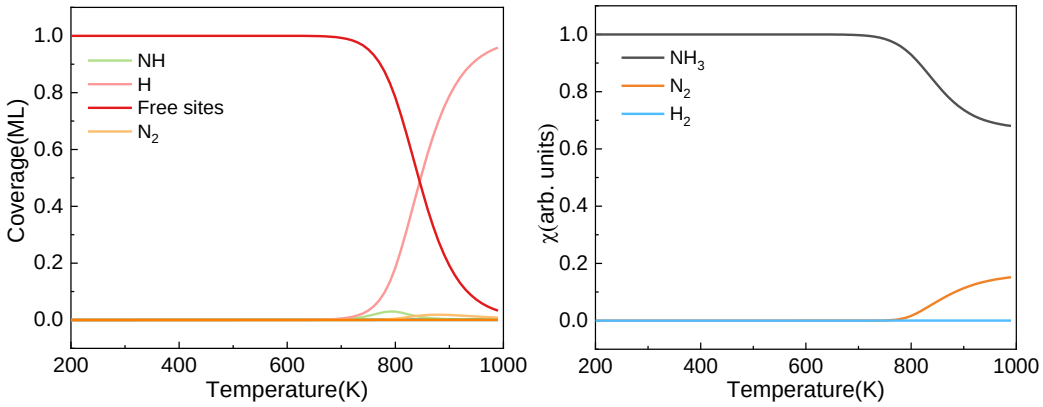

Figure 4-9. The steady-state of surface species distribution (left) on GO surface and the ratio (χ) of gaseous species (right) as functions of temperature in the batch reactor simulations. The initial ratio of NH_3: surface sites is 1:1, and the reaction time is 600s. The temperature and time step of the numerical integration is 10K and 1s, respectively.

4.3.5 Why do SV defects activate NH_3 molecules?

We analyzed the electronic structure of the isolated and NH_3-adsorbed systems using the density of states (DOS) and the Bader atoms-in-molecule methods to characterize SV's N-C interaction. Bader analysis showed that a charge transfer of 0.37 e- from NH_3 to the SV surface site upon adsorption drives a charge depletion from all the N-H bonds (0.34 e-), weakening it and promoting its scission in agreement with the mentioned bond elongation results (Figure 4-10(a)). Moreover, the DOS projection on the H orbitals (Figure 4-10(b)) shows the electronic structure rearrangement upon NH_3 adsorption on the SV site. The increase in H-states above the Fermi energy further indicates the activation of the N-H bond.

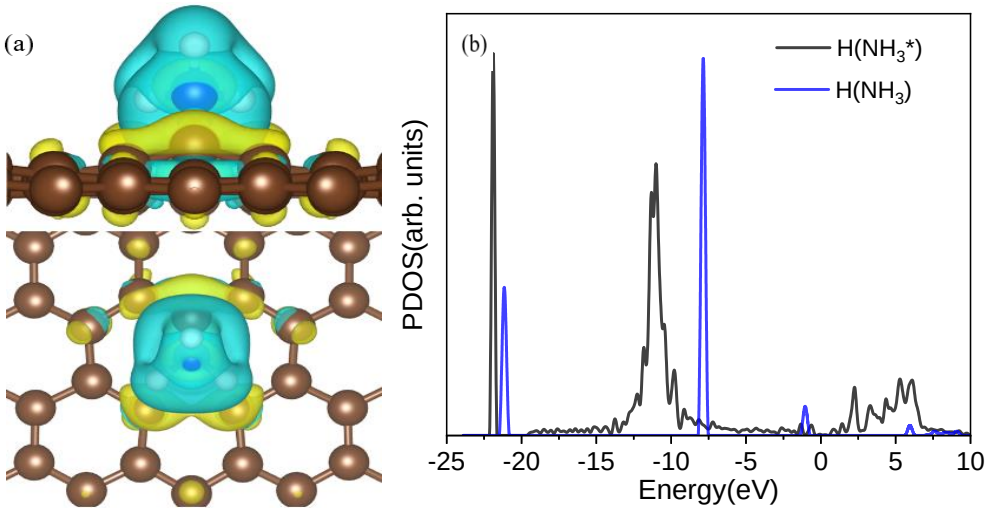

Figure 4-10. (a) Partial charge density flow upon NH_3 adsorption (top view and side view). Yellow and blue iso-surfaces denote gain and depletion of electron density with an iso-surface value of 0.01 e/Å^3. The blue sphere represents N; white is H, and khaki is C. (b) DOS diagram of isolate and adsorbate NH_3 on SV projected on the hydrogen atoms in the molecule.

4.4 Conclusions

The catalytic activity of carbon materials was investigated by analyzing the NH_3 reforming mechanism on pristine and a series of point defects graphene (C-vacancy and dopants). We modeled the surfaces and compared our results with previous benchmarks. We explored the different adsorption sites and conformation of the species involved in the NH_3 reforming, i.e., NH_x (x = 1-3), H and N, and H_2 and N_2. We identified vacancies (SV and DV) and doped (PN, PO, and GO) structures to be potential catalysts by comparing the thermodynamic reaction pathways. We found the reforming rate-determining steps to be the NH_3 activation and first dehydrogenation and the N and H recombination and molecular desorption. These results imply that co-catalysts may be able to accelerate and tune the graphite catalytic activity, e.g., for high-efficient electrocatalysts. Batch reaction simulations described the reaction processes along the temperature and time. They indicated that although SV and GO can dehydrogenate NH_3, these sites will be poisoned respectively by N and H adatoms' strong interactions. We rationalized the NH_3 activation

on carbon dangling bonds based on electronic analysis, which indicated a charge transfer of 0.37 e^- from the N-H bond to the SV, triggering the NH_3 first dehydrogenation. The simulation in this study is under gaseous reaction conditions. When it comes to solution reaction, the adsorption modelling of competitive species and implicit solvent models can be applied to consider the solvent effect. The study demonstrated that the carbon-based materials are long-term inert supports for the catalytic NH_3 reforming even in the presence of defects.

4.5 Reference

(1) Abe, J. O.; Popoola, A. P. I.; Ajenifuja, E.; Popoola, O. M. Hydrogen Energy, Economy and Storage: Review and Recommendation. *International Journal of Hydrogen Energy* **2019**, *44* (29), 15072–15086.

(2) Dincer, I.; Acar, C. Review and Evaluation of Hydrogen Production Methods for Better Sustainability. *International journal of hydrogen energy* **2015**, *40* (34), 11094–11111.

(3) Bell, T. E.; Ménard, H.; González Carballo, J.-M.; Tooze, R.; Torrente-Murciano, L. Hydrogen Production from Ammonia Decomposition Using Co/γ-Al2O3 Catalysts – Insights into the Effect of Synthetic Method. *International Journal of Hydrogen Energy* **2020**. https://doi.org/10.1016/j.ijhydene.2020.07.090.

(4) Bell, T. E.; Torrente-Murciano, L. H 2 Production via Ammonia Decomposition Using Non-Noble Metal Catalysts: A Review. *Topics in Catalysis* **2016**, *59* (15–16), 1438–1457.

(5) Mah, A. X. Y.; Ho, W. S.; Bong, C. P. C.; Hassim, M. H.; Liew, P. Y.; Asli, U. A.; Kamaruddin, M. J.; Chemmangattuvalappil, N. G. Review of Hydrogen Economy in Malaysia and Its Way Forward. *International Journal of Hydrogen Energy* **2019**, *44* (12), 5661–5675.

(6) Lamb, K. E.; Dolan, M. D.; Kennedy, D. F. Ammonia for Hydrogen Storage; A Review of Catalytic Ammonia Decomposition and Hydrogen Separation and Purification. *International Journal of Hydrogen Energy* **2019**, *44* (7), 3580–3593.

(7) Smith, C.; Hill, A. K.; Torrente-Murciano, L. Current and Future Role of Haber–Bosch Ammonia in a Carbon-Free Energy Landscape. *Energy & Environmental Science* **2020**, *13* (2), 331–344.

(8) Yürüm, Y.; Taralp, A.; Veziroglu, T. N. Storage of Hydrogen in Nanostructured Carbon Materials. *International journal of hydrogen energy* **2009**, *34* (9), 3784–3798.

(9) Pereira, M. F. R.; Figueiredo, J. L.; Órfão, J. J.; Serp, P.; Kalck, P.; Kihn, Y. Catalytic Activity of Carbon Nanotubes in the Oxidative Dehydrogenation of Ethylbenzene. *Carbon* **2004**, *42* (14), 2807–2813.

(10) Qu, L.; Liu, Y.; Baek, J.-B.; Dai, L. Nitrogen-Doped Graphene as Efficient Metal-Free Electrocatalyst for Oxygen Reduction in Fuel Cells. *ACS nano* **2010**, *4* (3), 1321–

1326.
(11) Zhang, L.; Xu, Q.; Niu, J.; Xia, Z. Role of Lattice Defects in Catalytic Activities of Graphene Clusters for Fuel Cells. *Physical Chemistry Chemical Physics* **2015**, *17* (26), 16733–16743.
(12) Su, C.; Acik, M.; Takai, K.; Lu, J.; Hao, S.; Zheng, Y.; Wu, P.; Bao, Q.; Enoki, T.; Chabal, Y. J. Probing the Catalytic Activity of Porous Graphene Oxide and the Origin of This Behaviour. *Nature communications* **2012**, *3* (1), 1–9.
(13) Navalon, S.; Dhakshinamoorthy, A.; Alvaro, M.; Garcia, H. Carbocatalysis by Graphene-Based Materials. *Chemical reviews* **2014**, *114* (12), 6179–6212.
(14) Su, D. S.; Perathoner, S.; Centi, G. Nanocarbons for the Development of Advanced Catalysts. *Chemical reviews* **2013**, *113* (8), 5782–5816.
(15) Anton, R.; Schneidereit, I. In Situ TEM Investigations of Dendritic Growth of Au Particles on HOPG. *Physical Review B* **1998**, *58* (20), 13874.
(16) Rodríguez-Manzo, J. A.; Cretu, O.; Banhart, F. Trapping of Metal Atoms in Vacancies of Carbon Nanotubes and Graphene. *ACS nano* **2010**, *4* (6), 3422–3428.
(17) Lee, G.-D.; Wang, C. Z.; Yoon, E.; Hwang, N.-M.; Kim, D.-Y.; Ho, K. M. Diffusion, Coalescence, and Reconstruction of Vacancy Defects in Graphene Layers. *Physical review letters* **2005**, *95* (20), 205501.
(18) Banhart, F.; Kotakoski, J.; Krasheninnikov, A. V. Structural Defects in Graphene. *ACS nano* **2011**, *5* (1), 26–41.
(19) Yadav, S.; Zhu, Z.; Singh, C. V. Defect Engineering of Graphene for Effective Hydrogen Storage. *International journal of hydrogen energy* **2014**, *39* (10), 4981–4995.
(20) Kresse, G.; Furthmüller, J. Efficiency of Ab-Initio Total Energy Calculations for Metals and Semiconductors Using a Plane-Wave Basis Set. *Computational materials science* **1996**, *6* (1), 15–50.
(21) Bucko, T.; Hafner, J.; Lebegue, S.; Angyán, J. G. Improved Description of the Structure of Molecular and Layered Crystals: Ab Initio DFT Calculations with van Der Waals Corrections. *The Journal of Physical Chemistry A* **2010**, *114* (43), 11814–11824.
(22) Hammer, B.; Hansen, L. B.; Nørskov, J. K. Improved Adsorption Energetics within Density-Functional Theory Using Revised Perdew-Burke-Ernzerhof Functionals. *Physical review B* **1999**, *59* (11), 7413.
(23) Perdew, J. P.; Burke, K.; Ernzerhof, M. Generalized Gradient Approximation Made Simple. *Physical review letters* **1996**, *77* (18), 3865.
(24) Kresse, G.; Joubert, D. From Ultrasoft Pseudopotentials to the Projector Augmented-Wave Method. *Physical review b* **1999**, *59* (3), 1758.
(25) Blöchl, P. E.; Jepsen, O.; Andersen, O. K. Improved Tetrahedron Method for Brillouin-Zone Integrations. *Physical Review B* **1994**, *49* (23), 16223.
(26) Grimme, S.; Ehrlich, S.; Goerigk, L. Effect of the Damping Function in Dispersion Corrected Density Functional Theory. *Journal of computational chemistry* **2011**, *32* (7), 1456–1465.
(27) Geim, A. K. Graphene: Status and Prospects. *science* **2009**, *324* (5934), 1530–1534.
(28) Sheppard, D.; Xiao, P.; Chemelewski, W.; Johnson, D. D.; Henkelman, G. A

Generalized Solid-State Nudged Elastic Band Method. *The Journal of chemical physics* **2012**, *136* (7), 074103.
(29) Ghasemi, A.; Xiao, P.; Gao, W. Nudged Elastic Band Method for Solid-Solid Transition under Finite Deformation. *The Journal of Chemical Physics* **2019**, *151* (5), 054110.
(30) Xiao, P.; Sheppard, D.; Rogal, J.; Henkelman, G. Solid-State Dimer Method for Calculating Solid-Solid Phase Transitions. *The Journal of Chemical Physics* **2014**, *140* (17), 174104.
(31) Evans, M. G.; Polanyi, M. Some Applications of the Transition State Method to the Calculation of Reaction Velocities, Especially in Solution. *Transactions of the Faraday Society* **1935**, *31*, 875–894.
(32) Eyring, H. The Activated Complex and the Absolute Rate of Chemical Reactions. *Chemical Reviews* **1935**, *17* (1), 65–77.
(33) Eyring, H. The Activated Complex in Chemical Reactions. *The Journal of Chemical Physics* **1935**, *3* (2), 107–115.
(34) Ugeda, M. M.; Brihuega, I.; Guinea, F.; Gómez-Rodríguez, J. M. Missing Atom as a Source of Carbon Magnetism. *Physical Review Letters* **2010**, *104* (9), 096804.
(35) Wang, Z.; Zhou, Y. G.; Bang, J.; Prange, M. P.; Zhang, S. B.; Gao, F. Modification of Defect Structures in Graphene by Electron Irradiation: Ab Initio Molecular Dynamics Simulations. *The Journal of Physical Chemistry C* **2012**, *116* (30), 16070–16079.
(36) Thrower, P. A.; Mayer, R. M. Point Defects and Self-Diffusion in Graphite. *Physica Status Solidi. A, Applied Research* **1978**, *47* (1), 11–37.
(37) El-Barbary, A. A.; Telling, R. H.; Ewels, C. P.; Heggie, M. I.; Briddon, P. R. Structure and Energetics of the Vacancy in Graphite. *Physical Review B* **2003**, *68* (14), 144107.
(38) Kaxiras, E.; Pandey, K. C. Energetics of Defects and Diffusion Mechanisms in Graphite. *Physical review letters* **1988**, *61* (23), 2693.
(39) Singh, R.; Kroll, P. Magnetism in Graphene Due to Single-Atom Defects: Dependence on the Concentration and Packing Geometry of Defects. *Journal of Physics: Condensed Matter* **2009**, *21* (19), 196002.
(40) Li, L.; Reich, S.; Robertson, J. Defect Energies of Graphite: Density-Functional Calculations. *Physical Review B* **2005**, *72* (18), 184109.
(41) Ma, J.; Alfe, D.; Michaelides, A.; Wang, E. Stone-Wales Defects in Graphene and Other Planar s p 2-Bonded Materials. *Physical Review B* **2009**, *80* (3), 033407.
(42) Wang, H.; Maiyalagan, T.; Wang, X. Review on Recent Progress in Nitrogen-Doped Graphene: Synthesis, Characterization, and Its Potential Applications. *Acs Catalysis* **2012**, *2* (5), 781–794.
(43) Wang, X.; Li, X.; Zhang, L.; Yoon, Y.; Weber, P. K.; Wang, H.; Guo, J.; Dai, H. N-Doping of Graphene through Electrothermal Reactions with Ammonia. *science* **2009**, *324* (5928), 768–771.
(44) Lin, Y.-C.; Lin, C.-Y.; Chiu, P.-W. Controllable Graphene N-Doping with Ammonia Plasma. *Applied Physics Letters* **2010**, *96* (13), 133110.
(45) Li, X.; Wang, H.; Robinson, J. T.; Sanchez, H.; Diankov, G.; Dai, H. Simultaneous Nitrogen Doping and Reduction of Graphene Oxide. *Journal of the American Chemical Society* **2009**, *131* (43), 15939–15944.
(46) Geng, D.; Chen, Y.; Chen, Y.; Li, Y.; Li, R.; Sun, X.; Ye, S.; Knights, S. High Oxygen-

Reduction Activity and Durability of Nitrogen-Doped Graphene. *Energy & Environmental Science* **2011**, *4* (3), 760–764.

Chapter 5 Ammonia reforming on transition metals

5.1 NH_3 reforming on noble metals

Current environmental concerns are drawing the attention of all communities to exploit resources with low or even zero carbon emissions.[1] Molecular hydrogen is recognized as an energy vector to drive sustainable growth; nevertheless, it presents high risks and costs associated with its transport and storage.[2] Alternatively, ammonia (NH_3) is a suitable carbon-free molecule to store H_2, which decomposition produces only H_2 and N_2.[3,4] It is easy to transport and store as it is liquid at room temperature under low pressure. Each year, around 150 million tons of NH_3 is synthesized and traded around the world.[5] Indeed, the high hydrogen content of NH_3 (17.64 wt%) makes it more attractive than bulk commodities such as methanol (12.50 wt%), ethanol (13.04 wt%), formic acid (4.35 wt%), and acetic acid (6.66 wt%). Although the decomposition of NH_3 is an endothermic process, the oxidation of produced H_2 (as fuels) is highly exothermic, making this reaction worthwhile.[6] The presence of a catalyst can facilitate NH_3 decomposition, and therefore, detailed investigations on mechanisms and their limitations are of paramount importance to develop selective and efficient catalysts.

Extensive studies have shed light on the ammonia decomposition mechanisms on various metals, such as Fe,[7–9] Ni,[10–13] Co,[14,15] Cu (111),[16] Pd (111),[17] Pt,[18] Rh (111),[19] Ru (0001)[20–27] and Ir.[28–32] Boisen employed a model describing the catalytic trends over transition metal catalysts and found Ru to be the most active metal for this reaction.[33] Egawa *et al.* investigated the desorption and kinetic process of NH_3 decomposition on Ru surfaces using electron spectroscopy and diffraction techniques.[34] They observed that the reaction takes place from 400 K reaching an equilibrium with H_2 and NH_3 in the gas phase at around 500 K, while the formation rate of N_2 peaks at 570 K according to the thermal-desorption spectra. Mortensen *et al.* applied supersonic molecular beam

techniques to study the dissociation of ammonia also on the Ru(0001) surface and proposed a mechanism dominated by the diffusion of intermediates species.[35]

Although Ru shows good activity for catalyzing this process, its scarcity makes its large-scale implementation prohibitive unless it is used as dispersed fine nanoparticles. On the other hand, the price of Ir is relatively low, and it is currently employed to decompose similar molecules (*e.g.* N_2H_4) as fuel in spaceships.[36] George *et al.* reported that Ir catalysts have several orders of magnitude higher activity to decompose NH_3 than other transition metals such as Pd, Pt, and Rh at 750 K.[37] Santra *et al.* carried out a temperature-programmed reaction study on Ir(100) and found that the associative nitrogen desorption is the crucial step for continuous and efficient ammonia decomposition.[29] Huang *et al.* arrived at the same conclusion using computational methods on Ir(111) and Ir(110).[31] They also suggested that the competition between desorption and dissociation can be tuned via the control of pressure and temperature during the reaction.

To develop more efficient catalysts, many experimental studies of ammonia decomposition on Ru and Ir catalysts focused on the relationship between the composition and atomicity of catalysts and products yields. Temporal analysis of products (TAP)[38,39] and steady-state isotopic transient kinetic analysis (SSITKA)[40–42] can both be applied to study the characteristics of the active sites and provide information on the adsorptions and reactions. García *et al.* carried out multi-pulse TAP experiments to understand the main mechanistic features involved in the catalytic decomposition of NH_3 over carbon-supported Ru and Ir catalysts.[32] The results suggested that the surface life-time of N species on the Ir surface is shorter than on the Ru surface, leading to faster N_2 desorption. John and co-workers found that NH_x species are the primary surface intermediates from 623 K to 673 K (204 kPa) and adsorbate N is the most abundant intermediates during 623K to 773 K using SSITKA.[41] To date, a systematic and detailed comparison of the exact mechanism and microkinetic model for the NH_3 decomposition on Ru and Ir supported nanoparticles is scarce in the literature, especially including the model describing Ru fcc surface, which

is observed in the Ru nanoparticles size range of 2.0-5.5 nm.[43]

Due to the complexity and difficulty to observe the adsorbed reaction intermediates, many aspects concerning the reaction processes at the atomic level remain unclear. For this reason, we have performed a density functional theory (DFT) investigation providing accurate information of all reaction species during the ammonia decomposition on hcp Ru(0001), fcc Ru(111) and fcc Ir(111) and make a comparison with former data. We extended these results with microkinetic simulations, including batch reactor and temperature-programmed desorption simulations, hence, providing rates and selectivity information as a function of the catalysts' nature closing the gap between modeling and experiments.

5.1.1 Computational Details

DFT calculations. We employed the Vienna Ab-initio Simulation Package (VASP) to simulate the NH_3 decomposition reactions on Ru (hcp and fcc) and Ir metal catalyst.[44,45] The spin-polarized revised Perdew-Burke-Ernzerhof (rPBE) method of the generalized gradient approximation (GGA) was adopted to describe the exchange-correlation with a plane-wave kinetic cutoff energy of 500 eV.[46] Non-spherical contributions to atomic cores from the gradient corrections were represented by the projector augmented wave (PAW).[47–49] The zero-damping DFT-D3 method was used to describe long-range interactions.[50] The optimized convergence threshold of internal forces and electronic relaxation was set to 0.02 eV/Å and 10^{-5} eV, respectively. A 3×3×1 k-spacing Monkhorst-Pack grid sampled the Brillouin zone with a smearing broadening of 0.2 eV.

Table 5-1. The bulk lattice parameters of Ru(hcp), Ru(fcc) and Ir(fcc)

Surface	This work	Previous works	Experiments
Ru(hcp)	a=2.691 Å, c/a = 1.572	a = 2.754 Å, c/a = 1.587 [51]	a = 2.706 Å, c/a = 1.582 [52]
Ru(fcc)	3.792 Å	3.825 Å [53]	-
Ir(fcc)	3.842 Å	3.876 Å [54]	3.839 Å [55]

The optimized bulk lattice parameters are shown in Table 5-1. All surfaces were represented by a *p(4x4)* supercell slab model with five atomic layers, where the top

three layers were fully relaxed and the bottom two fixed at the optimized bulk lattice. We added 15 Å of vacuum perpendicular to the slab to avoid any spurious interaction with periodic images. Dipole correction perpendicular to the surface was applied upon the adsorption of any species. The molecular adsorption energies are defined by Eq 5-1, and the relative energies along the energy profiles are calculated by Eq 5-2.

$$\mathrm{E_{ads}} = \mathrm{E_{system}} - \mathrm{E_{surface}} - \mathrm{E}_{molecule} \qquad \text{Eq 5-1}$$

$$\Delta E = E_{system} + \frac{n}{2} \times E_{H_2} - E_{surf} - E_{NH_3} \qquad \text{Eq 5-2}$$

Where $\mathrm{E_{system}}$ is the total energy of the adsorbed system, $\mathrm{E_{surface}}$ denotes the energy of the clean surfaces, $\mathrm{E_{NH_3}}$ and E_{H_2} are the energy of the ammonia and the hydrogen isolated molecules. The half energy of a hydrogen molecule refers to the energy of one H atom, and n is the number of H dissociated from NH_3.

The reaction energy (E_r) is given by the energy difference of the final state (FS) and the initial state (IS) (Eq 5-3). When the E_r value is negative, it means an exothermic step. The transition states (TS) were determined using the climb-image nudged elastic band (ci-NEB) combined with the improved dimer method (IDM) and ensuring a unique imaginary frequency along the reaction coordinate.[56–58] We defined the forward and reverse activation barriers (E_a) as the energy difference between TS and IS and between TS and FS, respectively (Eq 5-4 and Eq 5-5).

$$\mathrm{E_r} = \mathrm{E^{FS}} - \mathrm{E^{IS}} \qquad \text{Eq 5-3}$$

$$\mathrm{E_a^{forward}} = \mathrm{E^{TS}} - \mathrm{E^{IS}} \qquad \text{Eq 5-4}$$

$$\mathrm{E_a^{reverse}} = \mathrm{E^{TS}} - \mathrm{E^{FS}} \qquad \text{Eq 5-5}$$

Microkinetic simulations. We constructed a kinetic model of the NH_3 decomposition reaction based on a microcanonical ensemble within the transition state theory (TST) framework, which employs the Eyring and Evans and Polanyi approximation to compute the reaction constants of all surface elementary reactions (Eq S24, Eq S26 and Eq S27 in supporting information (SI)).[59–61] Although the TST has weaknesses, it is widely used to provide useful information in the design of catalysts.[62,63] Some of the TST weaknesses are that it assumes (i) no quantum tunneling, (ii) the intermediates are long-lived to follow the Boltzmann distribution of energy, and (iii) all the species reaching the transition state evolve only to products. In

the used model, the lateral adsorbate-adsorbate interactions are assumed to be negligible, *i.e.* low coverages, and mass transfer and diffusions are not limiting the process kinetics. The partition functions to describe the thermodynamic properties as functions of the temperature are listed in the SI, Eq S5-1-Eq S5-12. We have used numerical methods to solve the set of differential equations describing the relationship between the species, pressure and coverages, and time (listed in SI).

5.1.2 Results and discussion

Surface species

We studied all the non-equivalent adsorptions and configurations of surface species on Ru(0001), Ru(111), and Ir(111) in order to derive the reaction mechanism. Table 5-2 summarizes the most favorable adsorption properties of NH_x (x=1-3), and atomic and molecular hydrogen and nitrogen. The adsorption modes are represented in Figure 5-1, Figure 5-2, and Figure 5-3, respectively, for Ru(0001), Ru(111), and Ir(111). The interaction of N lone pair of electrons with the d_{Z2} orbital of the metals dominates the NH_3 adsorption, which agrees with the NH_3 preferable adsorption site on top of the metal atom. The extra electron in the Ir valence band stabilizes the NH_2 on the top site while, on Ru, it falls to a bridge position. These adsorption trends are consistent with experimental findings using the scanning tunneling microscopy method.[22]

Generally, ammonia decomposition intermediates over Ru(0001) and Ru(111) present a very similar behavior, except that the adsorption of N_2 on Ru(111) is more favorable, attributed to the meta-stability of the fcc phase. Ir(111) has the strongest NH_3 adsorption compared with the Ru surfaces as it favors the electron back-donation with the adsorbed species. Along the dehydrogenation of ammonia, the coordination of N with metal atoms increases, i.e. the adsorption site changes from top to bridge to hollow, and the perpendicular distance between N atoms and the surface decreases. These findings indicate that the interaction of N atoms with surfaces is strengthened with each dehydrogenation.

Table 5-2. Adsorption energies of molecules (E_{ads}), relative energy (ΔE) of intermediates and average distances between the metal and nitrogen (d_{TM-N}) and between nitrogen and hydrogens (d_{N-H}) of NH_x (x=1-3) and atomic and molecular H_2 and N_2 on (a) Ru(0001), (b) Ru(111) and (c) Ir(111). (T: top; B: bridge; hcp: hcp hollow; fcc: fcc hollow).

Species	Favorable site			$E_{ads}/\Delta E$(eV)			$E_{ads}^{zpe}/\Delta E^{zpe}$(eV)			d_{N-H}(Å)			d_{TM-N}(Å)		
	a	b	c	a	b	c	a	b	c	a	b	c	a	b	c
NH_3	T	T	T	-0.98	-0.88	-1.19	-0.94	-0.84	-1.13	1.018	1.016	1.021	2.228	2.248	2.163
NH_2	B	B	T	-0.48	-0.30	-0.32	-0.61	-0.44	-0.43	1.015	1.012	1.005	2.134	2.128	2.118
NH	hcp	hcp	fcc	-0.46	-0.24	0.09	-0.76	-0.53	-0.19	1.011	1.006	0.975	2.017	2.015	2.031
N	hcp	hcp	fcc	-0.85	-0.84	0.11	-0.83	-0.82	0.11	-	-	-	1.930	1.937	1.977
H	fcc	fcc	fcc	-0.56	-0.41	-0.33	-0.53	-0.39	-0.34	-	-	-	-	-	-
N_2	T	T	T	-0.06	-0.55	-0.38	-0.01	-0.50	-0.31	-	-	-	1.971	1.982	1.927
H_2	T	T	T	-0.40	-0.35	-0.36	-0.35	-0.28	-0.32	-	-	-	-	-	-

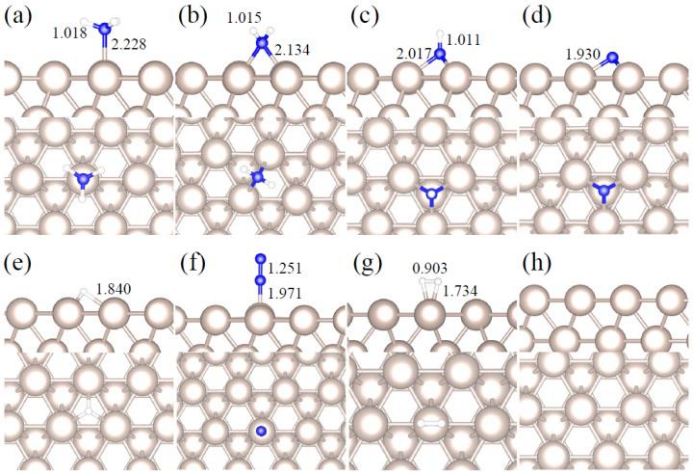

Figure 5-1. Side and top representation of the most favorable adsorption configurations on Ru(0001). (a) NH_3, (b) NH_2, (c) NH, (d) N, (e) H, (f) N_2, (g) H_2, (h) clean Ru(0001) surface. Insets are the average distances in Å. Blue, white, and khaki balls refer to nitrogen, hydrogen, and ruthenium atoms, respectively.

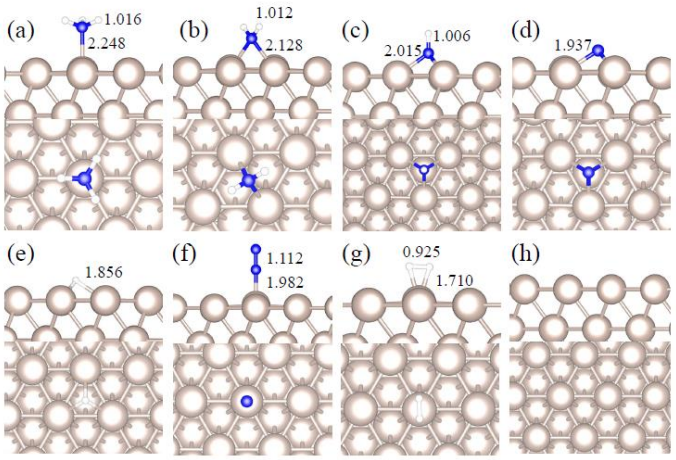

Figure 5-2. Side and top representation of the most favorable adsorption configurations on Ru(111). (a) NH_3, (b) NH_2, (c) NH, (d) N, (e) H, (f) N_2, (g) H_2, (h) clean Ru(111) surface. Insets are the average distances in Å. Blue, white, and khaki balls refer to nitrogen, hydrogen, and ruthenium atoms, respectively.

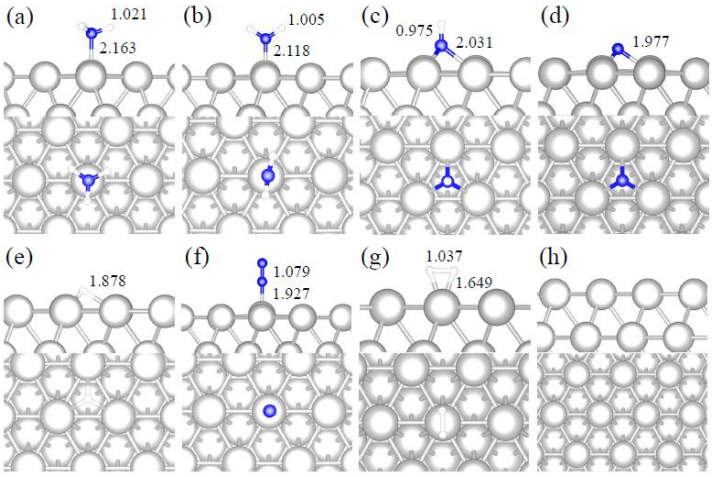

Figure 5-3. Side and top representation of the most favorable adsorption configurations on Ir(111). (a) NH_3, (b) NH_2, (c) NH, (d) N, (e) H, (f) N_2, (g) H_2, (h) clean Ir(111) surface. Insets are the average distances in Å. Blue, white, and light grey balls refer to nitrogen, hydrogen, and iridium atoms, respectively.

Reaction thermochemistry

We calculated the reaction energies (ΔG_r) (Figure 5-4) and the activation energies (ΔG_a) as a function of the temperature (Figure 5-5) for each reaction step in the ammonia dehydrogenation (R1, R3, and R5 inTable 5-3) and in the N_2 and H_2

formations (R7, R9 in Table 5-3). The NH_3 decomposition is thermodynamically favorable on Ru, but on Ir(111), it is limited by the dehydrogenation of NH_3 (R1) and NH (R5). In particular, R1 presents substantial activation energy, which aligns with the stability of the NH_3 molecule over the surface. The most endothermic processes on Ru surfaces are the formation of N_2 (R7) and H_2 (R9). Indeed, nitrogen recombination has been identified as the rate determining rate step in both, Ru(0001) and Ir(111).[64,65] As shown in Figure 5-5, the rise of temperature promoted the hydrogen recombination (R9) on Ru surfaces and the higher activation energy slows the dehydrogenation of ammonia. Interestingly, in Figure 5-5, the activation energy for hydrogen evolution (R9) on Ru(111) is practically half of that on Ru(0001) and only slightly higher than on Ir(111). Such energy difference explains the divergent results when comparing the H_2 formation rate, *i.e.* Ru loading beyond a certain amount decreases the catalytic activity since it reduces the Ru fcc phase.[66] Therefore, to improve the catalytic activity under low temperatures, tuning the morphology of the catalyst is crucial.

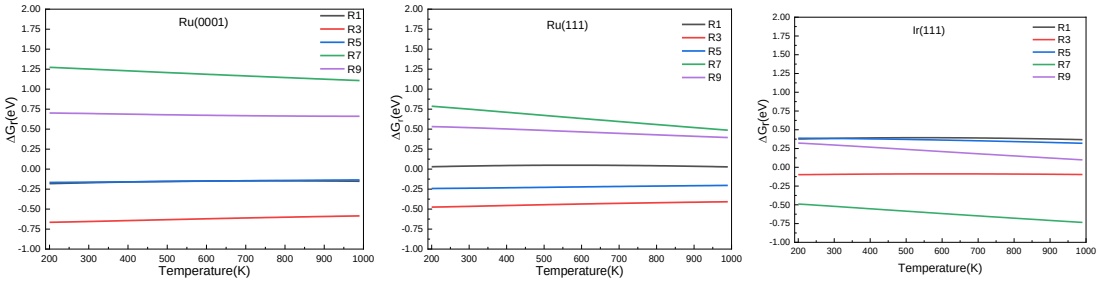

Figure 5-4. Free energy difference (ΔG_r) of the elementary steps in ammonia dehydrogenation (R1-R5) and N_2 and H_2 formations (R7 and R9) as a function of the temperature.

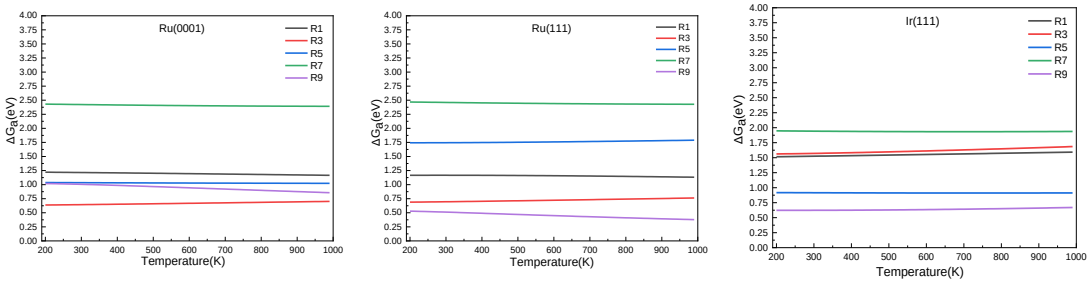

Figure 5-5. The activation energy (ΔG_a) of the elementary steps in ammonia dehydrogenation (R1-R5) and N_2 and H_2 formations (R7 and R9) as a function of the

temperature.

We have selected three different temperatures (i.e. 300, 600, and 900 K) and calculated the energetic profiles of the stoichiometric reaction ($NH_3 \rightarrow 0.5N_2 + 1.5H_2$), see appendix Figure S5-6 – Figure S5-8 in the SI where TS1, TS2, and TS3 are transition states of ammonia dehydrogenation processes, and TS4 and TS5 are transition states for the atomic recombination of nitrogen and hydrogen respectively.

Reaction constants

We have derived the rate law's pre-exponential factors and reaction constants for every N-H dissociative step and adsorbate recombination based on the reaction energy profiles, see Table 5-3. Fully aligned with the discussion above is that the formation of adsorbate N_2 has the smallest reaction constants indicating to be the rate-determining step.

Table 5-3. Elementary reactions and corresponding pre-exponential factors (ν) and reaction constants (k, in corresponding units) in the ammonia decomposition process over Ru(0001), Ru(111), and Ir(111) at 300K.

No	Reaction	Ru(0001)		Ru(111)		Ir(111)	
		ν	k	ν	k	ν	k
A1	$NH_3 + * \longrightarrow NH_3^*$	1.29×10^{8}	48.09	1.28×10^{8}	47.75	9.53×10^{7}	35.60
D1	$NH_3^* \longrightarrow NH_3 + *$	1.29×10^{8}	3.53×10^{-5}	1.28×10^{8}	1.79×10^{-3}	9.53×10^{7}	3.60×10^{-8}
R1	$NH_3^* + * \longrightarrow NH_2^* + H^*$	1.09×10^{13}	4.20×10^{-8}	5.37×10^{12}	1.36×10^{-7}	3.15×10^{12}	7.63×10^{-14}
R2	$NH_2^* + H^* \longrightarrow NH_3^* + *$	2.61×10^{13}	1.38×10^{-10}	1.12×10^{13}	1.24×10^{-6}	6.60×10^{12}	4.73×10^{-7}
R3	$NH_2^* + * \longrightarrow NH^* + H^*$	4.01×10^{12}	60.34	3.95×10^{12}	8.14	3.71×10^{12}	1.48×10^{-14}
R4	$NH^* + H^* \longrightarrow NH_2^* + *$	7.78×10^{12}	1.15×10^{-9}	7.51×10^{12}	2.31×10^{-7}	5.06×10^{12}	5.26×10^{-16}
R5	$NH^* + * \longrightarrow N^* + H^*$	7.13×10^{12}	2.97×10^{-5}	6.01×10^{12}	2.92×10^{-17}	6.93×10^{12}	2.86×10^{-3}
R6	$N^* + H^* \longrightarrow NH^* + *$	8.32×10^{12}	6.17×10^{-8}	7.19×10^{12}	3.42×10^{-21}	5.74×10^{12}	6.68×10^{3}
R7	$2N^* \longrightarrow N_2^* + *$	1.06×10^{13}	2.11×10^{-28}	1.08×10^{13}	5.03×10^{-29}	9.18×10^{12}	2.13×10^{-20}
R8	$N_2^* + * \longrightarrow 2N^*$	1.97×10^{12}	4.08×10^{-8}	5.48×10^{11}	9.95×10^{-18}	7.79×10^{11}	3.24×10^{-30}
D2	$N_2^* \longrightarrow N_2 + *$	1.29×10^{8}	1.24×10^{12}	1.28×10^{8}	410.62	9.52×10^{7}	1.25×10^{6}
A2	$N_2 + * \longrightarrow N_2^*$	1.29×10^{8}	1.26×10^{4}	1.28×10^{8}	1.25×10^{4}	9.52×10^{7}	9.34×10^{3}
R9	$2H^* \longrightarrow H_2^* + *$	1.44×10^{13}	1.86×10^{-4}	1.79×10^{13}	4.56×10^{4}	6.25×10^{12}	2.12×10^{2}
R10	$H_2^* + * \longrightarrow 2H^*$	4.99×10^{11}	6.21×10^{10}	8.54×10^{12}	1.12×10^{13}	8.14×10^{11}	2.65×10^{6}
D3	$H_2^* \longrightarrow H_2 + *$	1.29×10^{8}	7.04×10^{3}	1.28×10^{8}	4.84×10^{4}	9.54×10^{7}	3.86×10^{2}
A3	$H_2 + * \longrightarrow H_2^*$	1.29×10^{8}	7.29×10^{2}	1.28×10^{8}	7.23×10^{2}	9.54×10^{7}	5.39×10^{2}

Comparing the reaction constants for adsorbate N_2 formation (R7) and its dissociation (R8), we can conclude that, on Ru, the equilibrium is shifted towards the adsorbed atomic species; in contrast, it is shifted towards N_2, on Ir. This result highlights the ability of Ir catalysts to promote the N_2 desorption.

Temperature programmed desorption (TPD)

We investigated the individual desorption of N_2 and H_2 from the surfaces as a crucial step to complete the catalytic cycle. We found that the N_2 TPD spectra (Figure 5-6 left) on the two Ru surfaces are very similar. There is a ~10K shift to high temperature for nitrogen desorption on the Ru(111) compared with Ru(0001). Compared with the experimental curve, the simulated TPD has a slight shift to higher temperatures.[67] The reason for this deviation is that, although we considered the N coverage effect to be negligible beyond 1/9 ML, it actually weakens the N adsorption considerably.[68] This conclusion is derived from the agreement between the experiment and simulation at low coverage ($\theta = 0.15\,ML$). Another difference between the simulated and experimental N_2 TPD is the width of the signal, which can be related to the lack of uniform nanoparticles and the temperature rate during the experiments.

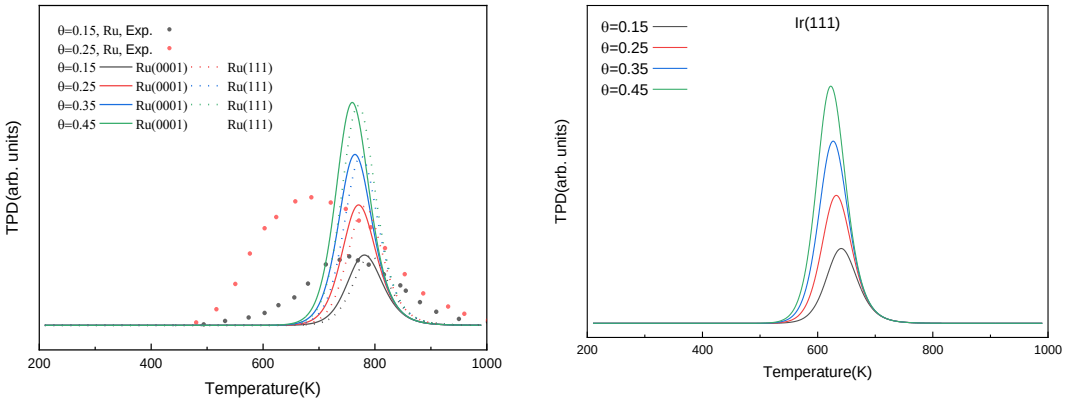

Figure 5-6. Simulated N_2 TPD spectra on Ru(0001) and Ru(111) (left) and on Ir(111) (right) at different initial coverages (θ in ML) with a heating rate of 1K/min. The experimental data was extracted from ref. 67.

The simulated H_2 TPD patterns of Ru and Ir(111) surfaces are plotted in Figure 5-7. The simulated data of Ru(0001) at 0.20 ML coverage fits the experimental research very well. While at an H_2 coverage of 0.45 ML, the experimental signal falls between the simulated patterns of hcp and fcc Ru surfaces, indicating the importance of nanoparticles' size and uniformity in the experiment. The match between simulation and experiments also implies a low effect of H coverage on the H adsorption energy. We can conclude that, although the ammonia dehydrogenation on Ir is not as favorable as on Ru, the more favorable desorption of products makes it a suitable catalyst.

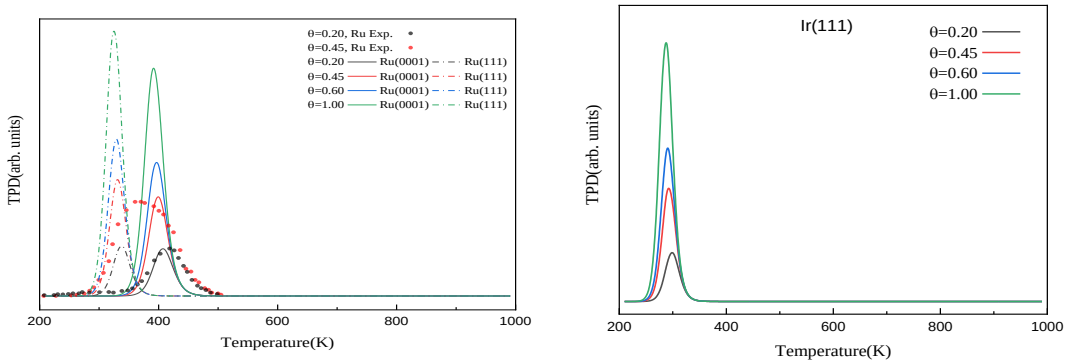

Figure 5-7. Simulated H_2 TPD spectra on Ru(0001) and Ru(111) (left) and Ir(111) (right) at different initial coverages (θ in ML) with the heating rate of 1K/min. The experimental data was extracted from ref. [69].

Batch reactor simulation

We have simulated the ratio between molecular species and active sites as a function of the temperature and time, as shown in Figure 5-8. At low temperatures, gas-phase NH_3 will adsorb on the surface and saturate the free sites. Then, as the temperature increases, the adsorbed NH_3 may react and desorb. The temperature range of the NH_3 desorption process on Ru is from 400 to 450 K, while it is between 500 and 700 K on Ir(111). The NH_3 desorption is observed in Figure 5-8 by the increase of molecular NH_3 before it decomposes. The NH_3 contents on Ru(0001) and Ru(111) reach the steady-state in ~100 s, but on Ir(111), it needs at least ~300 s, which is seen in Figure 5-8 for N_2 and H_2. The three surfaces generate molecular N_2 at a temperature of ~700 K. Ru(111) starts to produce H_2 at ~400 K, the lowest temperature among these three surfaces.

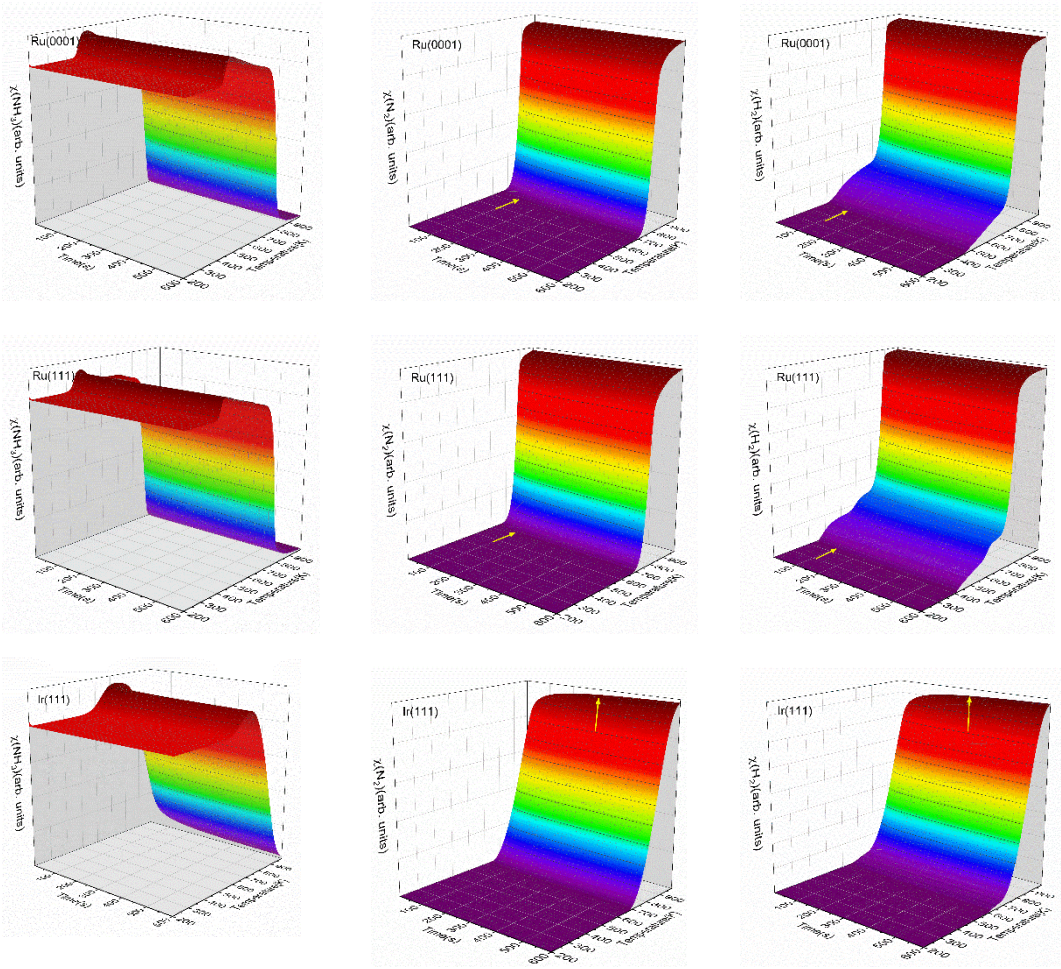

Figure 5-8. The relative concentration of molecular NH_3, N_2 and H_2 as functions of the temperature and time on (a) Ru(0001), (b) Ru(111), and (c) Ir(111) batch reactor simulations. The initial ratio of NH_3: surface sites is 5:1. The inset yellow arrows indicate the stabilization of N_2 and H_2.

Figure 5-9 shows the steady-state reaction details by depicting the NH_3, N_2, H_2 content at 600 s as functions of temperature for the three surfaces. Ru(0001) has similar catalytic behavior to Ru(111): after a relatively slow evolution, the H_2 production increases dramatically from 700 K and reaches a plateau at around 900 K. However, the H_2 production on Ru(111) take place at 400 K, while on Ru(0001), it is at 425 K. Our simulation results suggest that ammonia dissociate on Ir(111) at above 500 K. These results are consistent with the low- and high-temperature profiles for the decomposition of hydrazine (N_2H_4) on Ir(111), i.e. at temperatures below 500 K, the products of hydrazine decomposition are mainly NH_3 and N_2, however, NH_3, N_2, and

H_2 are observed above 500 K.[70,71] Ru is more favourable for H_2 evolution from ammonia than Ir according to the Fig. 5-9. When it comes to the H_2 generation curves, the hydrogen production on Ru at 400 K and increases dramatically from 700 K and reaches a plateau at around 900 K. While the hydrogen equilibrium concentration on Ir increase slowly with temperature at 600 K.

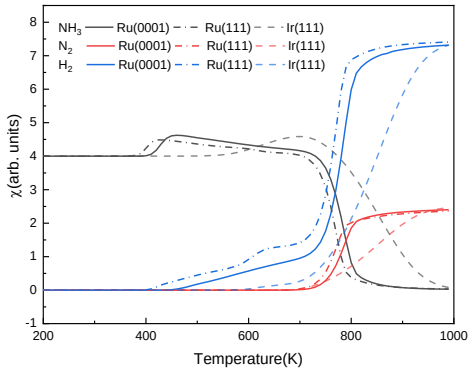

Figure 5-9. The steady-state ratio (χ) of NH_3, N_2, H_2 as functions of temperature on Ru(0001), Ru(111), and Ir(111) on batch reactor simulations. The initial simulated conditions are an NH_3 ratio of 5:1 with a free surface. The reaction time is 600 s.

We also made a comparison between experimental and simulated ammonia conversion on Ru catalysts, Figure 5-10.[66] Below 770 K, the results of Ru(111) fits the experimental data well, since, above that temperature, the existing fcc Ru moieties may reconstruct to hcp and sinter to larger structures.[72] Notice that Ru hcp fits better at high temperatures. However, the NH_3 conversion in the simulated process rises faster than the experimental one. This discrepancy between simulations and experiments may be due to the coverage effect of N, *i.e.* the NH_3 decomposition reaction becomes more favorable at high N coverages as discussed in the TPD section.

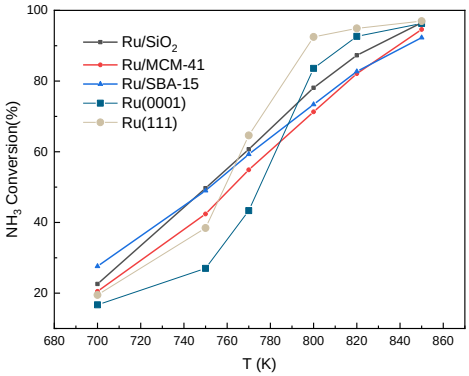

Figure 5-10. Ammonia conversion (in %) over supported Ru catalysts. Experimental trends were obtained from ref [66]. The initial simulated conditions are an NH_3:surface ratio of 5:1. The reaction time is 600 s.

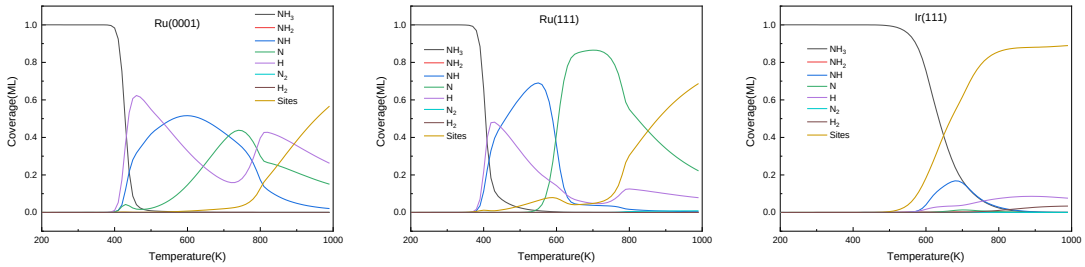

Figure 5-11. The steady-state of surface species distribution on Ru(0001), Ru(111), and Ir(111) surfaces at the temperature range of 200-1000 K at 600 s and the interpolation is 10 K.

The predominant species on the surfaces at steady-state (time is 600 s) within a temperature range of 200~1000 K (interpolation is 10 K) are plotted in Figure 5-11. Ru surfaces have a wider variety of surface species than Ir(111). As shown in Figure 5-11, NH_3, NH, N, and H are the main predominant species with high coverages on Ru surfaces during the NH_3 decomposition process. On Ru(0001), H is the dominant species at 430~535K, and at 700 K, atomic N accumulates on the surface and replaces NH as the main surface species. The notable species on Ru(111) during the reaction are NH and N at 445~600 K and 600~850 K respectively. Since Ru(111) has a lower ΔG_r for H_2 evolution (R9) than Ru(0001), H is the predominant species on Ru(111) at a narrow temperature range of 410~445 K. In contrast, the Ir(111) surface presents considerable content (>0.1 ML) of only NH_3 and NH as the dissociation of NH_3 start at 500 K; NH is the predominant species on the surface at the temperature range of 550~760 K with maximum coverage of 0.17 ML at 680K. Owing to the low ΔG_a of R7,

atomic N does not accumulates on the Ir(111) surface.

5.1.3 Conclusions

We carried out a mechanistic investigation of NH_3 decomposition on hcp Ru, fcc Ru, and fcc Ir using DFT-D3. The most favorable adsorption sites trend from NH_3 being on top, to bridge (NH_2), and to hollow sites (NH), with every dehydrogenation strengthening the N bonding to the surface. The energy profiles show that the rate-limiting step is the atomic nitrogen recombination on all the surfaces studied and, although the NH_3 dehydrogenation on Ir(111) is not as favorable as on Ru, the N_2 desorption indicates that it is a promising catalyst candidate. We derived the free energies of each gas phase and surface species between 200 and 1000 K by including entropic and specific heat contributions to the DFT energy. We implemented these free energies in a microkinetic model where the TPD experiment showed that both Ru surfaces, i.e. (0001) and (111), have similar desorption properties. The simulated TPD also proved to be useful in assessing the importance of N coverage on the model, i.e. the desorption shifts to lower temperatures with increasing N coverage. Batch reaction simulations described the reaction processes along the temperature and time and indicated that Ru(111) produces H_2 at a lower temperature than Ru(0001). On Ir(111) surface, the dehydrogenation starts at higher temperatures than on Ru, but the desorption of N_2 takes place at a lower temperature. The comparison between these results and experiments demonstrates that microkinetic simulations based on DFT results are a useful tool to investigate heterogeneous catalytic reactions and design novel catalysts.

5.2 NH_3 reforming on non-noble metals

Climate change has piqued the interest of the whole human community in recent years.[73,74] Many countries have pledged to achieve emission-free goals by the middle

of this century and have proposed tougher short-term commitments. To meet these goals, large-scale renewable energy and reduced fossil energy usage are mandatory, with hydrogen energy being a viable energy vector to connect renewable energies and the end-users.[75] In terms of hydrogen storage density, operating conditions, reversible cycle performance, and safety, no hydrogen storage technology can currently meet all the requirements for practical use.

Ammonia (NH_3) is a good carbon-free molecule for storing H_2 since it has high H_2 content (17.64 wt%) and decomposes into H_2 and N_2. NH_3 is liquid at room temperature and low pressure (~7.5 atm), and the cost of ammonia storage, based on the existing equipment and technologies, is around 1/30 of storing pure hydrogen.[76] Hence, research into low-temperature NH_3 catalytic decomposition is critical for the implementation of a clean H_2 energy system. Although Ru and Ir have high NH_3 decomposition activity, their high cost and restricted resources render them unsuitable for large-scale manufacturing.[77–80] Therefore, exploring the low-cost alternative transition-metal catalysts, such as Fe, Ni, and Co, is an important step for the NH_3 application as H_2 media.

To investigate the adsorption and dehydrogenation of NH_3 on hcp Co(0001), Kizilkaya *et al.* conducted experiments under ultrahigh vacuum (UHV) conditions and DFT simulations. The TPD spectra of NH_3 and H_2 showed that the adsorption capacity of the surface for NH_3 is not affected by the H_2 coverage.[81] Ma *et al.* used DFT calculations to explore the stepwise dehydrogenation of ammonia on clean and O-covered hcp Co surfaces and discovered that as the dehydrogenation progresses, the adsorption of intermediates becomes stronger, although NH dissociation is the rate-determining step.[82] Yeo *et al.* studied the reforming mechanism on bcc Fe(100) and found that the NH_3 decomposition reaction is affected by N coverage of the Fe surface and the recombination of nitrogen (N_2) has a significant energy barrier.[83] Hansgen *et al.* found that the nitrogen desorption peak is constant at ~630 K on Ni-Pt-Pt surface overall nitrogen coverages since surface reconstruction may be occurring.[84] Weiss *et al.* investigated the adsorption and decomposition of NH_3 on Fe(110) utilizing low-

energy electron diffraction (LEED) and thermal desorption measurements. They concluded that, above 400 K, the complete dissociation and desorption of H_2 takes place and the remaining adsorbed N-atoms recombine and desorb above 850 K. To investigate the mechanism of ammonia synthesis on Fe(111) surface, Qian *et al.* used quantum mechanics to predict reaction mechanisms and kinetics for NH_3 synthesis in an agreement with the experiment.[85] Duan *et al.* carried out a mechanistic study of ammonia decomposition on Ni(110) surface and found that the associative desorption of N has a reaction rate lower than NH_x dehydrogenation and is, therefore, the rate-determining step.[86] They also performed a theoretical investigation of NH_3 stepwise decomposition on the stepped Ni(211) and the Ni(111) surfaces and found that although step edge atoms can promote the first dehydrogenation of NH_3, the associative desorption of N is energetically frustrated on the stepped surface.[87]

Considering the variable structures of nano-scale particles, the reaction mechanism on hcp Co(0001), fcc Co(111), bcc Fe(110), fcc Fe(111), and fcc Ni(111) were investigated and made a comparison with the previous results on noble metals. We extended these results with microkinetic simulations, including batch reactor and temperature-programmed desorption simulations, hence, providing rates and selectivity information as a function of the catalysts' nature closing the gap between modeling and experiments.

5.2.1 Computational details

We employed the Vienna Ab-initio Simulation Package (VASP) to simulate the NH_3 decomposition reactions on non-noble transition metal catalysts.[88,89] The spin-polarized revised Perdew-Burke-Ernzerhof (rPBE) method of the generalized gradient approximation (GGA) was adopted to describe the exchange-correlation with a plane-wave kinetic cutoff energy of 500 eV.[46] Non-spherical contributions to atomic cores from the gradient corrections were represented by the projector augmented wave (PAW).[47–49] The zero-damping DFT-D3 method was used to describe long-range interactions.[50] The optimized convergence threshold of internal forces and electronic

relaxation was set to 0.02 eV/Å and 10^{-5} eV, respectively. A 3×3×1 k-spacing Monkhorst-Pack grid sampled the Brillouin zone with a smearing broadening of 0.2 eV.

Table 5-4. The bulk lattice parameters of Co(hcp), Co(fcc), Fe(bcc), Fe(fcc) and Ni(fcc)

Surface	This work	Reference
Co(hcp)	a=2.482 Å, c/a = 1.610	a = 2.507 Å, c/a = 1.623 [90]
Co(fcc)	3.495 Å	3.420 Å [91]
Fe(bcc)	2.870 Å	2.862 Å [92]
Fe(fcc)	3.622 Å	3.430 Å [91]
Ni(fcc)	3.486 Å	3.545 Å [93]

The optimized bulk lattice parameters are shown in Table 5-4. The metal surfaces were generated from the optimized bulk and represented by a *p(4x4)* supercell slab model with five atomic layers, where the top three layers were fully relaxed and the bottom two fixed at the optimized bulk lattice. We added 15 Å of vacuum perpendicular to the slab to avoid any spurious interaction with periodic images. Dipole correction perpendicular to the surface was applied upon the adsorption of any species. The molecular adsorption energies are defined by Eq 5-1, and the relative energies along the energy profiles are calculated by Eq 5-2.

$$\mathrm{E_{ads}} = \mathrm{E_{system}} - \mathrm{E_{surface}} - \mathrm{E}_{molecule} \qquad \text{Eq 5-1}$$

$$\Delta E = E_{system} + \frac{n}{2} \times E_{H_2} - E_{surf} - E_{NH_3} \qquad \text{Eq 5-2}$$

Where $\mathrm{E_{system}}$ is the total energy of the adsorbed system, $\mathrm{E_{surface}}$ denotes the energy of the clean surfaces, $\mathrm{E_{NH_3}}$ and E_{H_2} are the energy of the ammonia and the hydrogen isolated molecules. The half energy of a hydrogen molecule refers to the energy of one H atom, and n is the number of H dissociated from NH_3.

The reaction energy (E_r) is given by the energy difference of the final state (FS) and the initial state (IS) (Eq 5-3). When the E_r value is negative, it means an exothermic step. The transition states (TS) were determined using the climb-image nudged elastic band (ci-NEB) combined with the improved dimer method (IDM) and characterized with vibrational modes until obtained a unique imaginary frequency along with the reaction coordinate.[56–58] We defined the forward and reverse activation barriers (E_a) as the energy difference between TS and IS and between TS and FS, respectively (Eq 5-4 and Eq 5-5).

$$E_r = E^{FS} - E^{IS} \quad \text{Eq 5-3}$$

$$E_a^{forward} = E^{TS} - E^{IS} \quad \text{Eq 5-4}$$

$$E_a^{reverse} = E^{TS} - E^{FS} \quad \text{Eq 5-5}$$

5.2.2 Results and discussion

Surface species

To investigate the NH_3 reforming mechanism on the non-noble transition metals, *i.e.*, Co(0001), Co(111), Fe(110), Fe(111) and Ni(111), we studied all the non-equivalent adsorptions and configurations of surface species. Table 5-5 summarizes the most favorable adsorption properties of NH_x (x=1-3), and atomic and molecular hydrogen and nitrogen. The adsorption modes on surfaces are represented in Figure 5-12 - Figure 5-16, respectively. Similar to noble metals, the NH_3 preferable adsorption site is the top site of the metal atom because of the interaction between N lone pair of electrons with the surface metals' d_{Z2} orbital. Upon the first dehydrogenation, NH_2 falls to bridge sites on all transition metal surfaces. Hollow sites are preferable for the NH, N and H species. These adsorption trends are consistent with the former experimental and theoretical studies.[81–83,86,94,95]

Table 5-5. Adsorption energies (E_{ads}) and average distances between the metal and nitrogen (d_{TM-N}) and between nitrogen and hydrogens (d_{N-H}) of NH_x (x=1-3) and atomic and molecular H_2 and N_2 on the most favorable adsorption site. (T: top; B: bridge; hcp: hcp hollow; fcc: fcc hollow; bcc: bcc hollow, SB: short bridge; LB: long bridge).

Species		NH_3	NH_2	NH	N	H	N_2	H_2
Site	Co(0001)	T	B	hcp	hcp	fcc	T	-
	Co(111)	T	B	fcc	fcc	fcc	T	T
	Fe(110)	T	LB	bcc	bcc	bcc	T	T
	Fe(111)	T	B	fcc	fcc	hcp	T	T
	Ni(111)	T	B	fcc	fcc	fcc	T	T
$E_{ads}\ (eV)$	Co(0001)	-0.88	-0.35	-0.07	-0.33	-0.52	-0.47	+0.03
	Co(111)	-1.03	-0.48	-0.25	-0.11	-0.64	-0.53	-0.52
	Fe(110)	-0.73	-0.57	-0.74	-1.01	-0.66	-0.58	-0.43
	Fe(111)	-0.89	-0.55	-0.65	-0.97	-0.94	-0.58	-1.27
	Ni(111)	-0.9	-0.32	+0.02	-0.03	-0.51	-0.26	-0.30
	Co(0001)	-0.85	-0.50	-0.37	-0.31	-0.50	-0.43	+0.08

E_{ads}^{zpe} (eV)	Co(111)	-1.00	-0.62	-0.55	-0.09	-0.58	-0.48	-0.48
	Fe(110)	-0.71	-0.75	-1.05	-1.01	-0.64	-0.53	-0.42
	Fe(111)	-0.86	-0.71	-0.95	-0.97	-0.90	-0.57	-1.27
	Ni(111)	-0.87	-0.46	-0.27	-0.01	-0.48	-0.22	-0.25
d_{N-H} (Å)	Co(0001)	1.010	0.987	0.970	-	-	-	-
	Co(111)	1.022	0.992	0.972	-	-	-	-
	Fe(110)	1.017	1.030	1.010	-	-	-	-
	Fe(111)	1.022	0.995	0.971	-	-	-	-
	Ni(111)	1.007	1.024	0.975	-	-	-	-
d_{TM-N} (Å)	Co(0001)	2.098	1.979	1.847	1.740	-	1.830	-
	Co(111)	2.101	1.980	1.864	1.690	-	1.819	-
	Fe(110)	2.154	2.033	1.886	1.181	-	1.851	-
	Fe(111)	2.122	1.980	1.868	1.804	-	-	-
	Ni(111)	2.054	1.933	1.831	1.733	-	1.962	-

The N coordination with metal atoms increases along the dehydrogenation of ammonia, i.e. the adsorption site changes from top to bridge to hollow, and the perpendicular distance between N atoms and the surface decreases. These findings also indicate that the interaction of N atoms with surfaces is strengthened with each dehydrogenation.

In general, NH_3 reforming intermediates over fcc structures (Co(111), Fe(111), Ni(111)) behave similarly, except that the H adsorption on the Fe(111) hcp hollow is more favorable than fcc hollow. The strongest NH_3 adsorption seen on the Co(111) surface, including the ZPE correction, is -1.00 eV, very close to the -0.94 eV and -1.13 eV of Ru and Ir, respectively, suggesting that cobalt is potential to be an NH_3 decomposition catalyst.[96] Compared with noble metals (Ir and Ru), the interaction between intermediate species and the non-noble metal surfaces are weaker but the adsorption of N_2 and H_2 are stronger, implying that the NH_3 decomposition catalytic activity of noble metals may be thermodynamically driven and therefore more favorable.

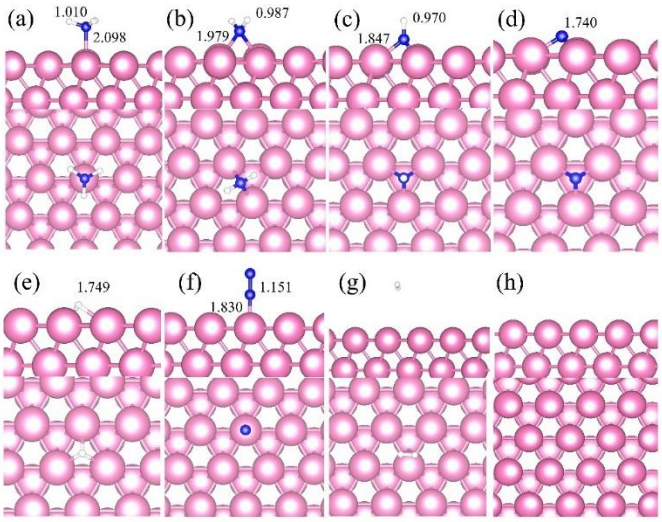

Figure 5-12. Side and top representation of the most favorable adsorption configurations on hcp Co(0001). (a) NH_3, (b) NH_2, (c) NH, (d) N, (e) H, (f) N_2, (g) H_2, (h) clean Co(0001) surface. Insets are the average distances in Å. Blue, white and pink balls refer to nitrogen, hydrogen and cobalt atoms, respectively.

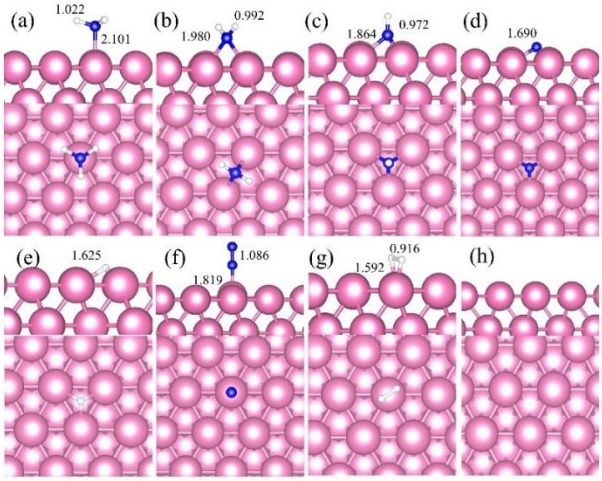

Figure 5-13. Side and top representation of the most favorable adsorption configurations on fcc Co(111). (a) NH_3, (b) NH_2, (c) NH, (d) N, (e) H, (f) N_2, (g) H_2, (h) clean Co(111) surface. Insets are the average distances in Å. Blue, white and pink balls refer to nitrogen, hydrogen and cobalt atoms, respectively.

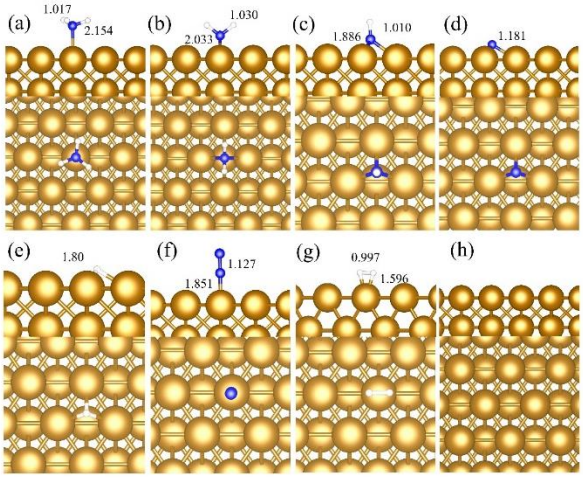

Figure 5-14. Side and top representation of the most favorable adsorption configurations on bcc Fe(110). (a) NH_3, (b) NH_2, (c) NH, (d) N, (e) H, (f) N_2, (g) H_2, (h) clean Fe(110) surface. Insets are the average distances in Å. Blue, white and bright yellow balls refer to nitrogen, hydrogen and cobalt atoms, respectively.

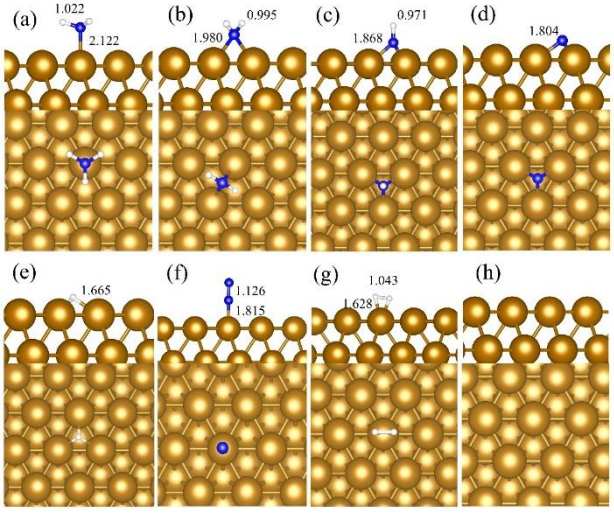

Figure 5-15. Side and top representation of the most favorable adsorption configurations on fcc Fe(111). (a) NH_3, (b) NH_2, (c) NH, (d) N, (e) H, (f) N_2, (g) H_2, (h) clean Fe(111) surface. Insets are the average distances in Å. Blue, white and bright yellow balls refer to nitrogen, hydrogen and cobalt atoms, respectively.

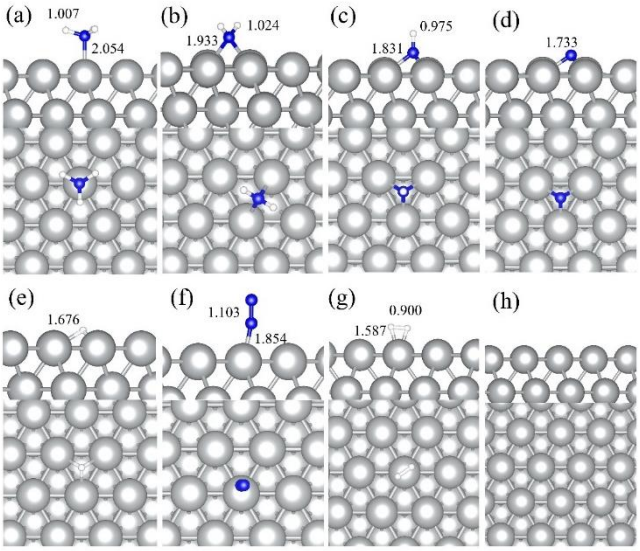

Figure 5-16. Side and top representation of the most favorable adsorption configurations on fcc Ni(111). (a) NH_3, (b) NH_2, (c) NH, (d) N, (e) H, (f) N_2, (g) H_2, (h) clean Ni(111) surface. Insets are the average distances in Å. Blue, white, and silver white balls refer to nitrogen, hydrogen, and cobalt atoms, respectively.

Reaction thermochemistry

The reaction free energies (ΔG_r) and the activation free energies (ΔG_a) as a function of the temperature for each reaction step in the ammonia reforming (R1, R3, and R5) and the N_2 and H_2 formations (R7, R9) were calculated to study the elementary steps in detail. On the investigated surfaces, the N recombination reaction (R9) is the rate-determining step, except on fcc Fe(111); NH dehydrogenation has the highest energy barrier of the reforming process on fcc Fe(111).

Compared with hcp cobalt, the NH_3 decomposition is thermodynamically less favorable on fcc cobalt in Figure 5-17, although with lower activation energies of NH_x dehydrogenation (R1, R3, R5) in Figure 5-18. The first step dehydrogenation of NH_3 on hcp Co and the nitrogen recombination on fcc Co become more favorable thermally and kinetically with the temperature. These differences demonstrate the sensitivity of ammonia decomposition to the crystal structure.[97] In Figure 5-19, the main endothermic elementary steps on bcc and fcc Fe are the recombination of N and H (R7 and R9). Note that, the recoupling of N (R7) on bcc Fe is endothermic and with a large energy barrier (Figure 5-20) suggesting bcc Fe is a good catalyst for NH_3

synthesis, in full agreement with the literature and the Haber–Bosch industrial catalyst.[98,99] However, when it comes to the fcc structure, although the barrier energy of R7 is lower than bcc Fe, the stepwise dehydrogenation limits the NH_3 decomposition. As shown in Figure 5-21, different from Co(111) and Fe(111), the H_2 formation (R9) is the most endothermic step on Ni(111) although it is still lower than in the other metals and becomes more favorable with temperature. The relatively low N recombination (R7) energy barrier makes fcc Ni a promising candidate for NH_3 decomposition under low temperatures. The reaction rate of N_2 formation improved with the temperature on Co(111), Co(0001) and Fe(111), showing that temperature control is an important way to tune the elementary rates. The thermochemistry analysis shows that: (1) Co and Ni are supposed to perform better than Fe at low temperatures; and (2) the catalysts' structure and morphology are crucial to control the catalytic activity.

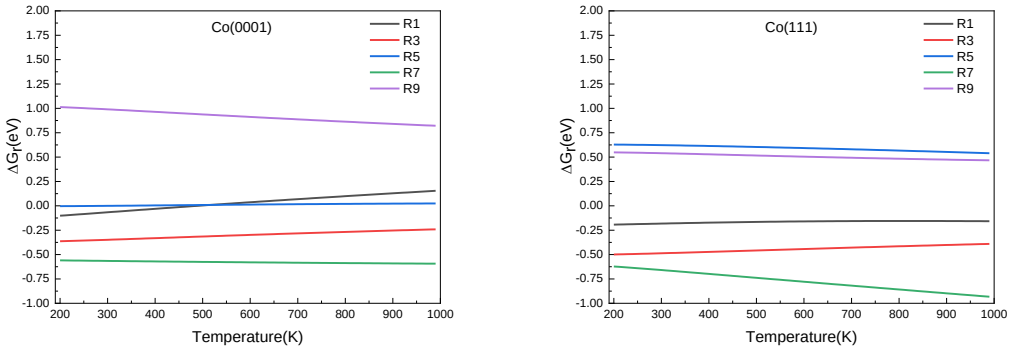

Figure 5-17. Reaction free energy (ΔG_r) of the elementary steps in ammonia dehydrogenation (R1-R5) and N_2 and H_2 formations (R7 and R9) on Co(0001) and Co(111) as a function of the temperature.

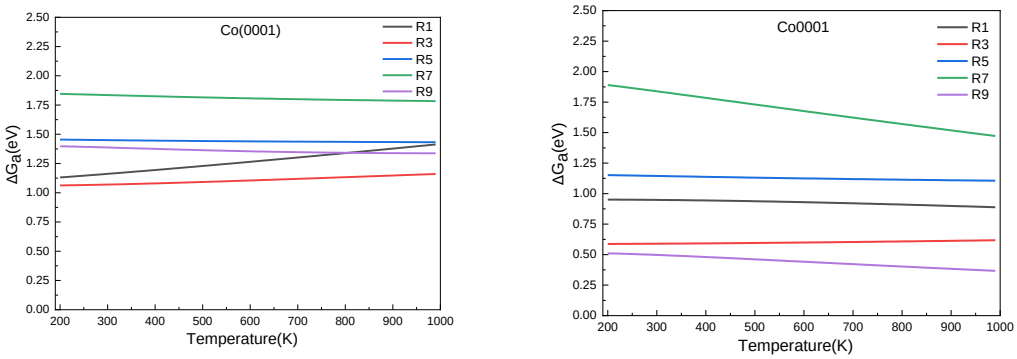

Figure 5-18. The activation free energy (ΔG_a) of the elementary steps in ammonia dehydrogenation (R1-R5) and N_2 and H_2 formations (R7 and R9) on Co(0001) and

Co(111) as a function of the temperature.

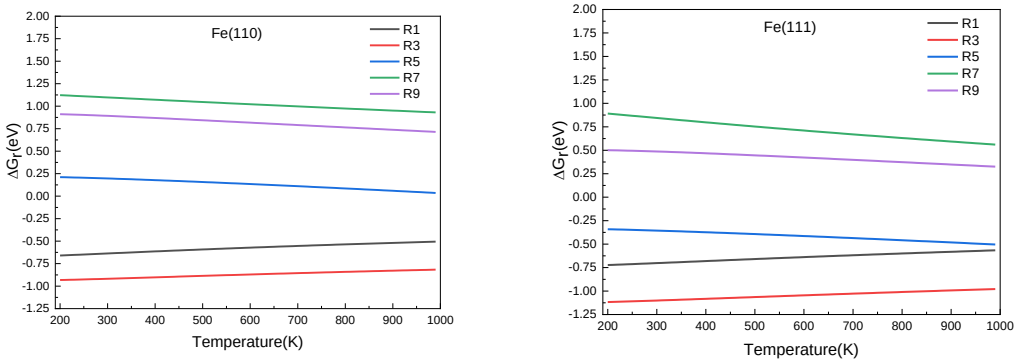

Figure 5-19. Reaction free energy (ΔG_r) of the elementary steps in ammonia dehydrogenation (R1-R5) and N_2 and H_2 formations (R7 and R9) on Fe(110) and Fe(111) as a function of the temperature.

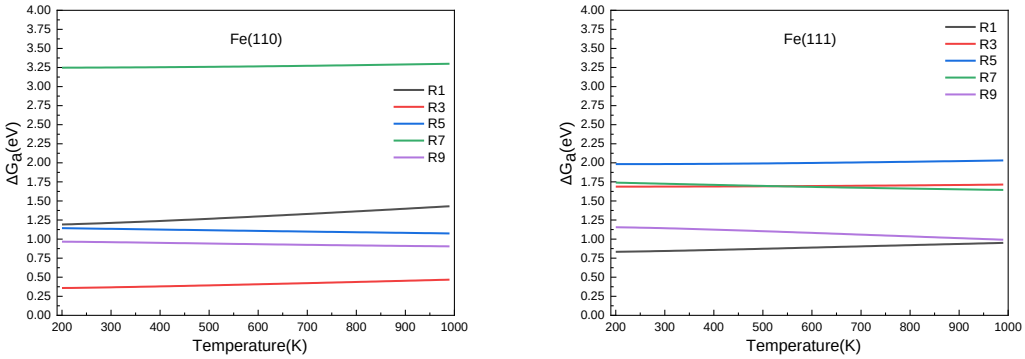

Figure 5-20. The activation free energy (ΔG_a) of the elementary steps in ammonia dehydrogenation (R1-R5) and N_2 and H_2 formations (R7 and R9) on Fe(110) and Fe(111) as a function of the temperature.

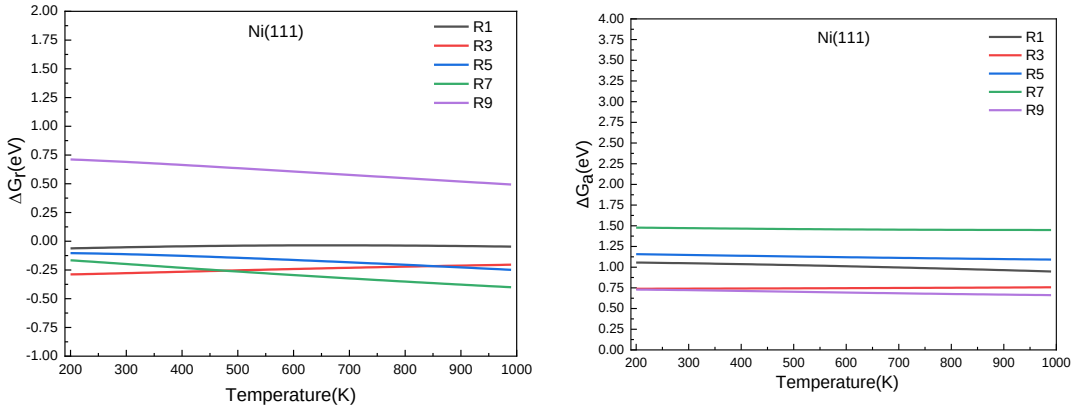

Figure 5-21. Reaction free energy (ΔG_r) and the activation free energy (ΔG_a) of the elementary steps in ammonia dehydrogenation (R1-R5) and N_2 and H_2 formations (R7 and R9) on Ni(111) as a function of the temperature.

Reaction constants

We have derived the rate law's pre-exponential factors and reaction constants for every dehydrogenation step and adsorbate recombination and desorption based on the reaction energy profiles. Table 5-6 summarizes these values, which are fully aligned with the discussion above. The formation of adsorbate N_2 has the smallest reaction constants indicating to be the rate-determining step. Comparing the reaction constants for adsorbate N_2 formation (R7) and its dissociation (R8), we can conclude that, on Fe, the equilibrium is shifted towards the adsorbed atomic species; in contrast, it is shifted towards molecular N on Co and Ni. This result highlights the ability of Co and Ni catalysts to promote the N_2 desorption, which is more suitable for NH_3 decomposition.

Table 5-6. Elementary reactions and corresponding pre-exponential factors (ν) and reaction constants (k, in is corresponding units) in the NH_3 reforming process over Co(0001), Co(111), Fe(110), Fe(111) and Ni(111) at 300K.

No.	Reaction	Co(0001)		Co(111)		Fe(110)		Fe(111)		Ni(111)	
		ν	k	ν	k	ν	k	ν	k	ν	k
A1	$NH_3 + * \longrightarrow NH_3^*$	1.42×10^{8}	8.03×10^{-1}	1.42×10^{8}	0.77	1.61×10^{8}	0.68	1.43×10^{8}	1.48	1.42×10^{8}	1.92
D1	$NH_3^* \longrightarrow NH_3 + *$	1.42×10^{8}	1.11×10^{-7}	1.42×10^{8}	4.43×10^{-8}	1.61×10^{8}	2.07×10^{-4}	1.43×10^{8}	1.83×10^{-6}	1.42×10^{8}	3.14×10^{-5}
R1	$NH_3^* + * \longrightarrow NH_2^* + H^*$	6.36×10^{9}	1.94×10^{-10}	1.01×10^{11}	1.18×10^{-5}	1.62×10^{10}	7.04×10^{-11}	9.96×10^{10}	6.63×10^{-4}	4.73×10^{11}	1.22×10^{-6}
R2	$NH_2^* + H^* \longrightarrow NH_3^* + *$	1.52×10^{11}	3.57×10^{-10}	2.36×10^{11}	2.39×10^{-8}	1.02×10^{11}	8.85×10^{-21}	4.66×10^{11}	4.94×10^{-15}	1.01×10^{12}	3.42×10^{-7}
R3	$NH_2^* + * \longrightarrow NH^* + H^*$	6.02×10^{10}	6.35×10^{-8}	7.74×10^{10}	9.70	3.79×10^{10}	2.54×10^{4}	1.70×10^{11}	7.35×10^{-18}	2.02×10^{11}	0.07
R4	$NH^* + H^* \longrightarrow NH_2^* + *$	1.64×10^{11}	2.42×10^{-13}	1.79×10^{11}	1.49×10^{-7}	9.89×10^{10}	2.49×10^{-11}	5.54×10^{11}	7.66×10^{-36}	4.35×10^{11}	3.4×10^{-6}
R5	$NH^* + * \longrightarrow N^* + H^*$	1.11×10^{11}	1.00×10^{-34}	1.46×10^{11}	8.57×10^{-9}	1.41×10^{11}	1.25×10^{-8}	1.81×10^{11}	8.49×10^{-23}	4.45×10^{11}	2.34×10^{-8}
R6	$N^* + H^* \longrightarrow NH^* + *$	1.34×10^{11}	1.20×10^{-34}	1.97×10^{11}	332.17	1.50×10^{11}	2.67×10^{-5}	1.92×10^{11}	9.53×10^{-29}	5.17×10^{11}	3.43×10^{-10}
R7	$2N^* \longrightarrow N_2^* + *$	2.62×10^{12}	2.98×10^{-27}	5.86×10^{14}	7.59×10^{-17}	4.93×10^{12}	1.24×10^{-42}	2.12×10^{13}	2.18×10^{-16}	9.62×10^{12}	1.83×10^{-13}
R8	$N_2^* + * \longrightarrow 2N^*$	1.49×10^{12}	5.41×10^{-37}	3.45×10^{13}	3.8×10^{-29}	6.35×10^{11}	4.35×10^{-25}	3.29×10^{11}	5.14×10^{-4}	8.33×10^{11}	7.39×10^{-17}
D2	$N_2^* \longrightarrow N_2 + *$	1.42×10^{8}	7.59×10^{2}	1.42×10^{8}	28.11	1.60×10^{8}	5.56	1.43×10^{8}	5.32×10^{-2}	1.41×10^{8}	1.66×10^{13}
A2	$N_2 + * \longrightarrow N_2^*$	1.42×10^{8}	2.10×10^{2}	1.42×10^{8}	202.00	1.60×10^{8}	177.6345	1.43×10^{8}	3.88×10^{2}	1.41×10^{8}	5.04×10^{2}
R9	$2H^* \longrightarrow H_2^* + *$	1.14×10^{13}	5.69×10^{-11}	1.36×10^{13}	5.96×10^{4}	9.08×10^{12}	6.92×10^{-4}	1.33×10^{13}	8.57×10^{-7}	9.32×10^{12}	6.88
R10	$H_2^* + * \longrightarrow 2H^*$	2.06×10^{12}	4.39×10^{5}	8.30×10^{12}	4.28×10^{13}	2.89×10^{12}	2.17×10^{11}	6.17×10^{12}	60.71	2.23×10^{12}	6.38×10^{11}
D3	$H_2^* \longrightarrow H_2 + *$	1.43×10^{8}	1.71×10^{8}	1.42×10^{8}	0.80	1.61×10^{8}	1.49	1.44×10^{8}	4.04×10^{-14}	1.42×10^{8}	1.99×10^{3}
A3	$H_2 + * \longrightarrow H_2^*$	1.43×10^{8}	12.20	1.42×10^{8}	11.68	1.61×10^{8}	10.29	1.44×10^{8}	22.47	1.42×10^{8}	29.16

Temperature programmed desorption (TPD)

The individual desorption of N_2 and H_2 from the surfaces is a vital process in the catalytic cycle as shown above. We found that the N_2 TPD spectra (Figure 5-22) on the two Co surfaces present a ~70K shift to high temperature for nitrogen desorption on the Co(0001) compared with Co(111), highlighting the importance of well-defined structure on catalytic activity. Furthermore, the N adsorption on Fe(110) is too strong to desorb successfully across the investigated temperatures. However, the desorption of molecular N_2 happens on fcc Fe at ~550K which is in good agreement with the previous experiment on fcc Fe (570 K).[100] Among all the investigated transition metal surfaces, Ni(111) has the lowest N_2 desorption temperature (~480 K).

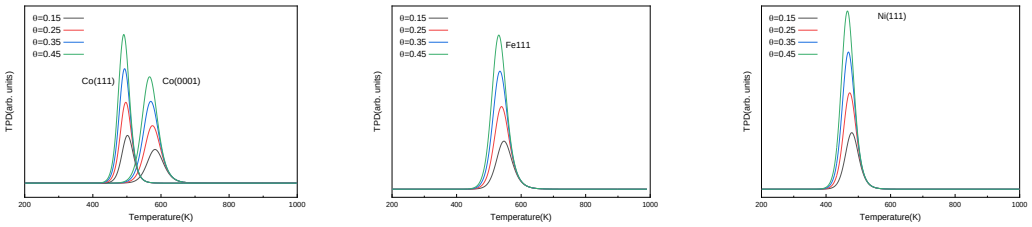

Figure 5-22. Simulated N_2 TPD spectra on Co, Fe, and Ni at different initial coverages (θ in ML) with a heating rate of 1K/min.

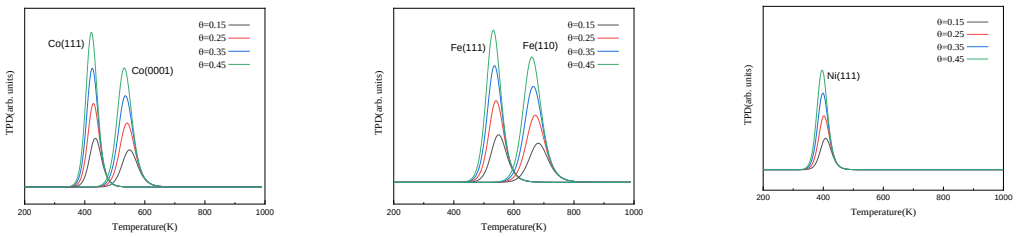

Figure 5-23. Simulated H_2 TPD spectra on Co, Fe and Ni at different initial coverages (θ in ML) with a heating rate of 1K/min.

The simulated H_2 TPD patterns of Co, Fe, and Ni surfaces are plotted in Figure 5-23. The experimental H_2 TPD patterns on cobalt surfaces show desorption peaks at ~ 350 K.[81] Compared with the experimental curve on the Co(0001) surface, the simulated TPD has a shift to higher temperatures by ~100 K.[101] Such small differences can be associated with the coverage effect as we considered to be negligible in the simulation. At high temperatures, Co/SiO_2 shows a curve at 600 K on the H_2 TPD pattern, which fits the simulation of Co(0001) very well.[102] Apart from this, the width difference of the TPD patterns between simulation and experiments can be assigned to the lack of uniform crystallinity and different facet in nanoparticles and the temperature rate of the experiments. The earliest H_2 desorption on Fe(110) happens at ~700 K, which is ~ 120 k higher than on Fe(111). Ni(111) also performs a low-temperature desorption property for H_2 desorption (~400 K), similarly to the experiment (332 K).[103] However, the fastest

H_2 desorption temperature of non-noble metals is generally hundreds of degrees higher than that of precious metals (Ru: 340 K - 410 K and Ir: 300 K).[79]

Batch reactor simulation

We have simulated a batch reactor where the ratio between molecular species and active sites on Co, Ni, and Fe varies as a function of temperature and time, as shown in Figure 5-24 and Figure 5-25.

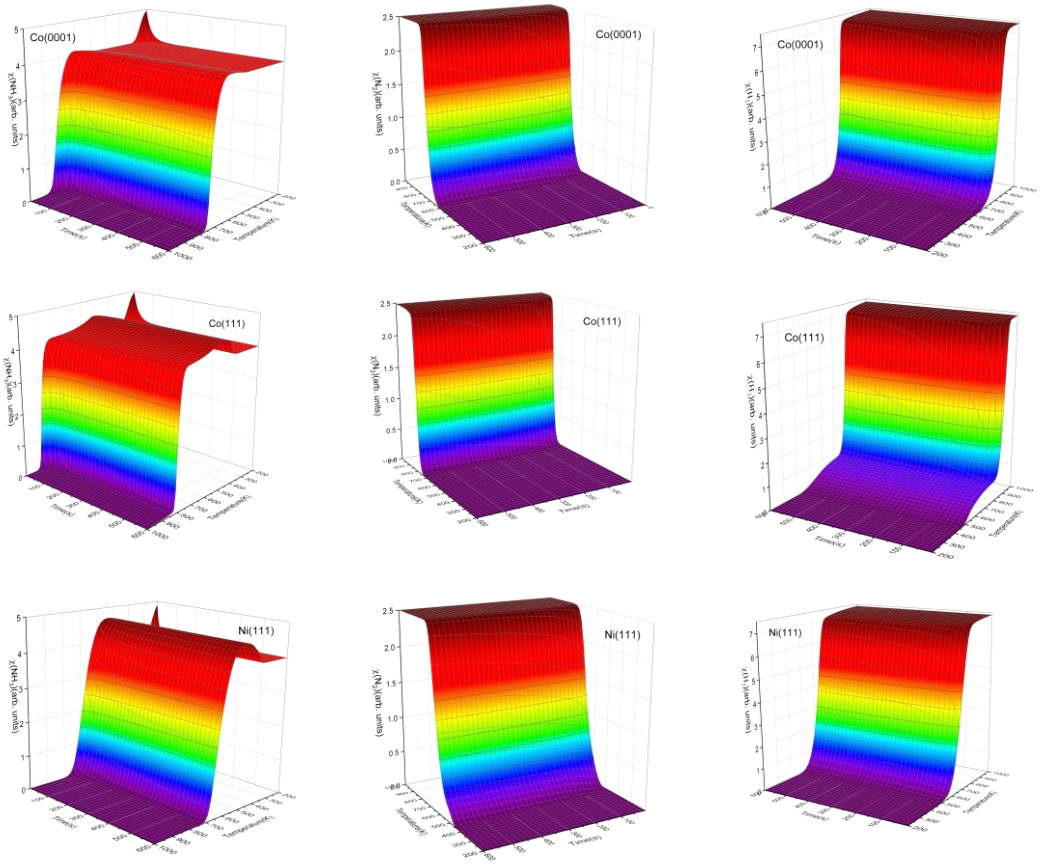

Figure 5-24. The relative concentration (χ) of molecular NH_3, N_2 and H_2 as functions of the temperature and time on (top) Co(0001), (middle) Co(111) and (bottom) Ni(111) batch reactor simulations. The initial ratio of NH_3: surface sites is 5:1 and the temperature increases 10 K every second.

At low temperatures, gas-phase NH_3 will adsorb on the surface and saturate the free adsorption sites. Since the adsorption reaction constants are small, the adsorption of NH_3 at low temperature (200~300 K) takes around 100 s to reach the steady-state, which is slower than on Ru and Ir.[79] With the rise of temperature, there is a competitive relationship between the NH_3 desorption and its dehydrogenation reaction. On Co(0001) surface, the decomposition reaction begins to dominate when the temperature reaches 425 K, while it is at 620 and 500 K on Co(111) and Ni(111), respectively. Before these temperatures, a slight increase of NH_3 gas is observed indicating preferential desorption. Once NH_3 starts reforming, its partial pressure drops,

and N_2 and H_2 molecular species appear depending on their relative adsorption energies. On Fe, the equilibrium is shifted towards molecular NH_3 showing prevalent desorption compared to dehydrogenation, which validates Fe as an NH_3 synthesis catalyst independently of its crystal structure. In Figure 5-25, the high equilibrium contents of NH_3 on Fe(110) and Fe(111) at investigated temperature demonstrate the excellent ammonia synthesis catalytic property of Fe. Furthermore, the H_2 production from NH_3 reforming is practically negligible concluding that Fe surfaces are not a favorable catalyst for the NH_3 decomposition.

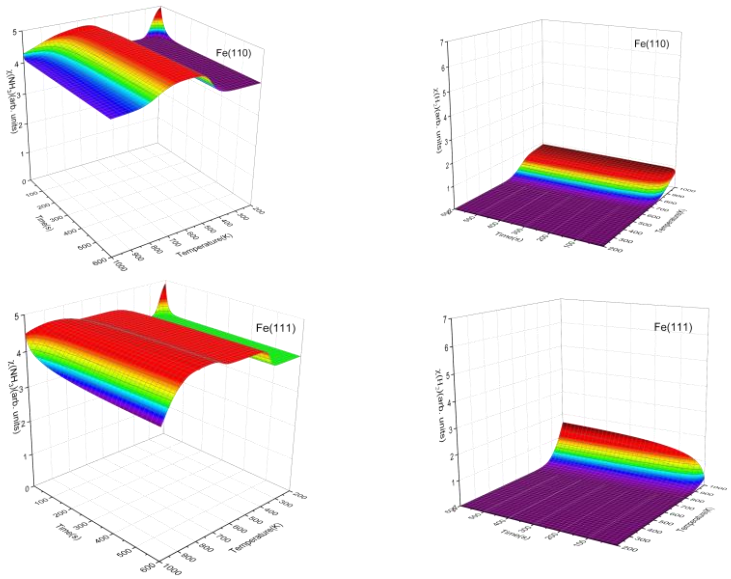

Figure 5-25. The relative concentration (χ) of molecular NH_3 and H_2 as functions of the temperature and time on (top) Fe(110) and (bottom) Fe(111) batch reactor simulations. The initial ratio of NH_3: surface sites is 5:1 and the temperature increase 10 K every second. The color from dark to bright of the surface stands for the values form low to high.

Figure 5-26 depicts the relative molecular concentrations at the steady-state as a function of temperature at 600 s. It clearly shows the catalytic behavior of Co(111) is different from Co(0001) due to the crystal structure causing the sensitivity to NH_3 reforming. The production of H_2 on Co starts at 450 K on the fcc structure, 150 K before that on the hcp. However, the process is slow and does not peak until 800 K, around 100 K after the production peak on the (0001) surface. Especially, Ni(111) has the lowest temperature for a fast H_2 production (~625 K). While the NH_3 decomposition happens on Fe(111) at the temperature is higher than 800 K, the simulations suggest that ammonia synthesis takes place preferentially between 500~700 K on Fe(110), which is also the operational temperature of iron catalyst in the NH_3 synthesis.

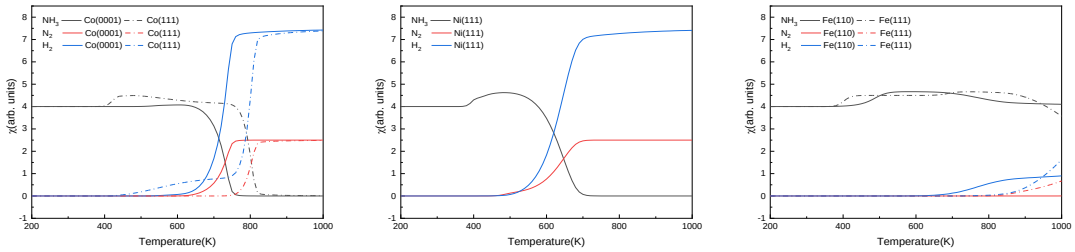

Figure 5-26. The steady-state ratio (χ) of NH_3, N_2, H_2 as functions of temperature on Co, Ni, and Fe in batch reactor simulations. The initial simulated conditions are an NH_3 ratio of 5:1 with a free surface. The reaction time is 600 s.

The predominant surface species on the Co and Ni at the steady-state (time is 600 s) within a temperature range of 200~1000 K are plotted in Figure 5-27. Adsorbate NH_3 on Co(0001) is the main surface species below 700 K as a result of the high energy barriers for dehydrogenation (> 1 eV). Contrarily, H, NH, and NH_3 are the main predominant species with high coverages on Co(111) during the decomposition process. H is the dominant species at 410~510 K, and at 510~810 K, adsorbate NH replaces H as the main surface species since NH accumulates due to its high dissociation energy barrier(R5). Under 600 K, Ni(111) has a broader diversity of surface species than cobalt demonstrating its catalytic activity for the NH_3 decomposition at low temperature. At 380~600 K, NH_3, NH, N, and H exist on Ni(111) simultaneously, and above 600K, the atomic H recombines to molecular H_2 leaving from the sites, which accumulates N atoms.

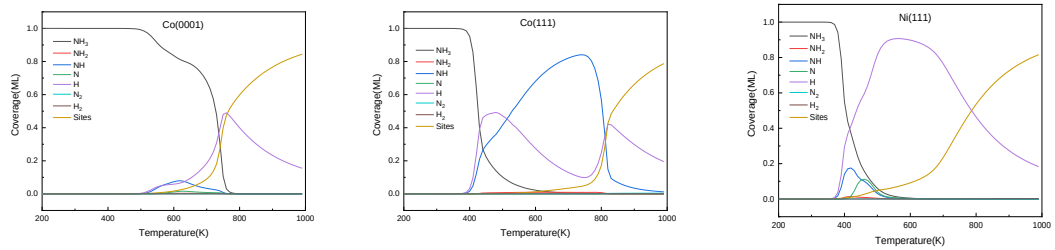

Figure 5-27. The steady-state of surface species distribution on Co(0001), Co(111), and Ni(111) surfaces at the temperature range of 200-1000 K at 600 s.

The surface species distribution of Fe(110) and Fe(111) in Figure 5-28 can also give detailed information for the ammonia synthesis. Considering the steady-state reaction details of the NH_3 content on Fe(110), the equilibrium NH_3 content keeps a high level with 100% surface sites' utilization > 600 K, which is in excellent agreement with the practical NH_3 synthesis operation temperature of 700~750 K.[98,104] The simulation results show that Fe(111) is supposed to perform better than Fe(110) on the NH_3 synthesis catalysis since the equilibrium NH_3 content stays high level at a wider range of temperature (400~800 K), which is also supported by former experiments.[105]

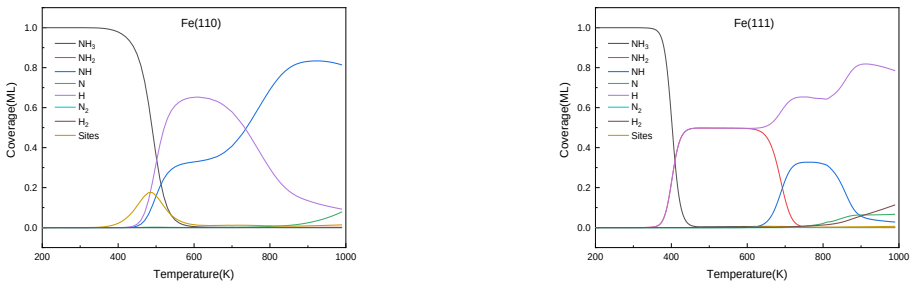

Figure 5-28. The steady-state of surface species distribution on Fe(110) and Fe(111) surfaces at the temperature range of 200-1000 K at 600 s.

5.2.3 Conclusion

The mechanisms of NH_3 decomposition on hcp and fcc Co, bcc and fcc Fe, and fcc Ni were investigated using the DFT-D3 method. The NH_3 adsorption over fcc structures is similar, i.e. the adsorption site changes from top to bridge to hollow with NH_3 reduction, and the perpendicular distance between N atoms and the surface decreases. Compared with noble metals (Ir and Ru), the combination of decomposition species with the non-noble metal surfaces is weaker but the adsorption of N_2 and H_2 are stronger, implying that the NH_3 decomposition catalytic activity of noble metals should be better. We derived the free energies of each gas phase and surface species between 200 and 1000 K by including entropic and specific heat contributions to the DFT energy. It shows that the recombination of atomic N on non-noble surfaces is the rate-determining step. We implemented these free energies in a microkinetic model where the TPD experiment showed that Co and Ni are more suitable to be low-cost candidates for the ammonia catalytic decomposition than Fe. Batch reaction simulations described the reaction processes along the temperature and time and indicated that although Co(111) has seen a broader H_2 production range, the temperature of the fastest H_2 production on Co(0001) is around 100 K lower than on Co(111). And Ni(111) has the lowest temperature of the fastest H_2 production (~625 K). The comparison between these results and experiments of NH_3 synthesis on iron explained the morphology effect of iron catalysts and supply a detailed understanding of its practical operation.

5.3 Reference

(1) Schüth, F.; Palkovits, R.; Schlögl, R.; Su, D. S. Ammonia as a Possible Element in an Energy Infrastructure: Catalysts for Ammonia Decomposition. *Energy Environ. Sci.* **2012**, *5* (4), 6278–6289. https://doi.org/10.1039/C2EE02865D.

(2) Valera-Medina, A.; Banares-Alcantara, R. *Techno-Economic Challenges of Green*

Ammonia as an Energy Vector; Academic Press, 2020.
(3) Lamb, K. E.; Dolan, M. D.; Kennedy, D. F. Ammonia for Hydrogen Storage; A Review of Catalytic Ammonia Decomposition and Hydrogen Separation and Purification. *International Journal of Hydrogen Energy* **2019**, *44* (7), 3580–3593.
(4) Mukherjee, S.; Devaguptapu, S. V.; Sviripa, A.; Lund, C. R.; Wu, G. Low-Temperature Ammonia Decomposition Catalysts for Hydrogen Generation. *Applied Catalysis B: Environmental* **2018**, *226*, 162–181.
(5) Nitrogen Statistics and Information https://www.usgs.gov/centers/nmic/nitrogen-statistics-and-information (accessed 2020 -08 -09).
(6) Hill, A. K.; Torrente-Murciano, L. Low Temperature H2 Production from Ammonia Using Ruthenium-Based Catalysts: Synergetic Effect of Promoter and Support. *Applied Catalysis B: Environmental* **2015**, *172*, 129–135.
(7) Duan, X.; Qian, G.; Zhou, X.; Sui, Z.; Chen, D.; Yuan, W. Tuning the Size and Shape of Fe Nanoparticles on Carbon Nanofibers for Catalytic Ammonia Decomposition. *Applied Catalysis B: Environmental* **2011**, *101* (3–4), 189–196.
(8) Lin, R.-J.; Li, F.-Y.; Chen, H.-L. Computational Investigation on Adsorption and Dissociation of the NH3 Molecule on the Fe (111) Surface. *The Journal of Physical Chemistry C* **2011**, *115* (2), 521–528.
(9) Yeo, S. C.; Han, S. S.; Lee, H. M. Mechanistic Investigation of the Catalytic Decomposition of Ammonia (NH3) on an Fe (100) Surface: A DFT Study. *The Journal of Physical Chemistry C* **2014**, *118* (10), 5309–5316.
(10) Nakamura, I.; Fujitani, T. Role of Metal Oxide Supports in NH3 Decomposition over Ni Catalysts. *Applied Catalysis A: General* **2016**, *524*, 45–49.
(11) Chellappa, A. S.; Fischer, C. M.; Thomson, W. J. Ammonia Decomposition Kinetics over Ni-Pt/Al2O3 for PEM Fuel Cell Applications. *Applied Catalysis A: General* **2002**, *227* (1–2), 231–240.
(12) Diawara, B.; Joubert, L.; Costa, D.; Marcus, P.; Adamo, C. Ammonia on Ni (1 1 1) Surface Studied by First Principles: Bonding, Multilayers Structure and Comparison with Experimental IR and XPS Data. *Surface science* **2009**, *603* (20), 3025–3034.
(13) Zhang, J.; Xu, H.; Li, W. Kinetic Study of NH3 Decomposition over Ni Nanoparticles: The Role of La Promoter, Structure Sensitivity and Compensation Effect. *Applied Catalysis A: General* **2005**, *296* (2), 257–267.
(14) Ji, J.; Duan, X.; Qian, G.; Zhou, X.; Tong, G.; Yuan, W. Towards an Efficient CoMo/γ-Al2O3 Catalyst Using Metal Amine Metallate as an Active Phase Precursor: Enhanced Hydrogen Production by Ammonia Decomposition. *international journal of hydrogen energy* **2014**, *39* (24), 12490–12498.
(15) Torrente-Murciano, L.; Hill, A. K.; Bell, T. E. Ammonia Decomposition over Cobalt/Carbon Catalysts—Effect of Carbon Support and Electron Donating Promoter on Activity. *Catalysis Today* **2017**, *286*, 131–140.
(16) Jiang, Z.; Qin, P.; Fang, T. Mechanism of Ammonia Decomposition on Clean and Oxygen-Covered Cu (1 1 1) Surface: A DFT Study. *Chemical Physics* **2014**, *445*, 59–67.
(17) Jiang, Z.; Qin, P.; Fang, T. Theoretical Study of NH3 Decomposition on Pd-Cu (1 1 1) and Cu-Pd (1 1 1) Surfaces: A Comparison with Clean Pd (1 1 1) and Cu (1 1 1). *Applied Surface Science* **2016**, *371*, 337–342.
(18) Löffler, D. G.; Schmidt, L. D. Kinetics of NH3 Decomposition on Polycrystalline Pt. *Journal of Catalysis* **1976**, *41* (3), 440–454.
(19) Wagner, M. L.; Schmidt, L. D. Adsorption and Decomposition of H2NCHO, D2NCHO, N2H4, and NH3 on Rh (111). *Surface science* **1991**, *257* (1–3), 113–128.
(20) Hellman, A.; Honkala, K.; Remediakis, I. N.; Logadottir, A.; Carlsson, A.; Dahl, S.; Christensen, C. H.; Nørskov, J. K. Ammonia Synthesis and Decomposition on a Ru-Based Catalyst Modeled by First-Principles. *Surface Science* **2009**, *603* (10–12), 1731–1739.
(21) Logadottir, A.; Nørskov, J. K. Ammonia Synthesis over a Ru (0001) Surface Studied by Density Functional Calculations. *Journal of Catalysis* **2003**, *220* (2), 273–279.
(22) Maier, S.; Stass, I.; Cerda, J. I.; Salmeron, M. Bonding of Ammonia and Its Dehydrogenated Fragments on Ru (0001). *The Journal of Physical Chemistry C* **2012**,

116 (48), 25395–25400.
(23) Li, L.; Zhu, Z. H.; Yan, Z. F.; Lu, G. Q.; Rintoul, L. Catalytic Ammonia Decomposition over Ru/Carbon Catalysts: The Importance of the Structure of Carbon Support. *Applied Catalysis A: General* **2007**, *320*, 166–172.
(24) Mortensen, H.; Diekhöner, L.; Baurichter, A.; Jensen, E.; Luntz, A. C. Dynamics of Ammonia Decomposition on Ru (0001). *The Journal of Chemical Physics* **2000**, *113* (16), 6882–6887.
(25) Deshmukh, S. R.; Mhadeshwar, A. B.; Vlachos, D. G. Microreactor Modeling for Hydrogen Production from Ammonia Decomposition on Ruthenium. *Industrial & Engineering Chemistry Research* **2004**, *43* (12), 2986–2999.
(26) Yin, S.-F.; Xu, B.-Q.; Ng, C.-F.; Au, C.-T. Nano Ru/CNTs: A Highly Active and Stable Catalyst for the Generation of COx-Free Hydrogen in Ammonia Decomposition. *Applied Catalysis B: Environmental* **2004**, *48* (4), 237–241.
(27) Dahl, S.; Sehested, J.; Jacobsen, C. J. H.; Törnqvist, E.; Chorkendorff, I. Surface Science Based Microkinetic Analysis of Ammonia Synthesis over Ruthenium Catalysts. *Journal of Catalysis* **2000**, *192* (2), 391–399.
(28) Huang, W.; Cheng, C.; Feng, E. Adsorption and Decomposition of NH3 on Ir (111): A Density Functional Theory Study. *Surface science* **2013**, *616*, 29–35.
(29) Santra, A. K.; Min, B. K.; Yi, C. W.; Luo, K.; Choudhary, T. V.; Goodman, D. W. Decomposition of NH3 on Ir (100): A Temperature Programmed Desorption Study. *The Journal of Physical Chemistry B* **2002**, *106* (2), 340–344.
(30) Xiao, X.-Z.; Cao, Y.-L.; Cai, Y.-Y. Decomposition of NH3 on Ir (110): A First-Principle Study. *Surface science* **2011**, *605* (7–8), 802–807.
(31) Huang, W.; Lai, W.; Xie, D. First-Principles Study of Decomposition of NH3 on Ir (1 0 0). *Surface science* **2008**, *602* (6), 1288–1294.
(32) García-García, F. R.; Guerrero-Ruiz, A.; Rodríguez-Ramos, I.; Goguet, A.; Shekhtman, S. O.; Hardacre, C. TAP Studies of Ammonia Decomposition over Ru and Ir Catalysts. *Physical Chemistry Chemical Physics* **2011**, *13* (28), 12892–12899.
(33) Boisen, A.; Dahl, S.; Nørskov, J. K.; Christensen, C. H. Why the Optimal Ammonia Synthesis Catalyst Is Not the Optimal Ammonia Decomposition Catalyst. *Journal of Catalysis* **2005**, *230* (2), 309–312.
(34) Egawa, C.; Nishida, T.; Naito, S.; Tamaru, K. Ammonia Decomposition on (1 1 10) and (0 0 1) Surfaces of Ruthenium. *Journal of the Chemical Society, Faraday Transactions 1: Physical Chemistry in Condensed Phases* **1984**, *80* (6), 1595–1604.
(35) Mortensen, H.; Diekhöner, L.; Baurichter, A.; Jensen, E.; Luntz, A. C. Dynamics of Ammonia Decomposition on Ru (0001). *The Journal of Chemical Physics* **2000**, *113* (16), 6882–6887.
(36) Schulz-Ekloff, G.; Hoppe, R. Electron Diffraction Determination of an Orientation-Relationship for Iridium-on-η-Alumina. *Catalysis letters* **1990**, *6* (3–6), 383–387.
(37) Papapolymerou, G.; Bontozoglou, V. Decomposition of NH3 on Pd and Ir Comparison with Pt and Rh. *Journal of Molecular Catalysis A: Chemical* **1997**, *120* (1–3), 165–171.
(38) Constales, D.; Yablonsky, G. S.; Galvita, V.; Marin, G. B. Thermodynamic Time-Invariances: Theory of TAP Pulse-Response Experiments. *Chemical engineering science* **2011**, *66* (20), 4683–4689.
(39) Gleaves, J. T.; Yablonsky, G.; Zheng, X.; Fushimi, R.; Mills, P. L. Temporal Analysis of Products (TAP)—Recent Advances in Technology for Kinetic Analysis of Multi-Component Catalysts. *Journal of Molecular Catalysis A: Chemical* **2010**, *315* (2), 108–134.
(40) Nwalor, J. U.; Goodwin, J. G. Isotopic Tracing Study of K Promotion of NH 3 Synthesis on Ru. *Topics in Catalysis* **1994**, *1* (3–4), 285–293.
(41) Nwalor, J. U.; Goodwin Jr, J. G.; Biloen, P. Steady-State Isotopic Transient-Kinetic Analysis of Iron-Catalyzed Ammonia Synthesis. *Journal of Catalysis* **1989**, *117* (1), 121–134.
(42) Efstathiou, A. M.; Verykios, X. E. Transient Methods in Heterogeneous Catalysis: Experimental Features and Application to Study Mechanistic Aspects of the CH4/O2 (OCM), NH3/O2 and NO/He Reactions. *Applied Catalysis A: General* **1997**, *151* (1),

109–166.
(43) Fu, W.; Chen, W.; Qian, G.; Chen, D.; Yuan, W.; Zhou, X.; Duan, X. Kinetics-Assisted Discrimination of Active Sites in Ru Catalyzed Hydrolytic Dehydrogenation of Ammonia Borane. *Reaction Chemistry & Engineering* **2019**, *4* (2), 316–322.
(44) Bucko, T.; Hafner, J.; Lebegue, S.; Angyán, J. G. Improved Description of the Structure of Molecular and Layered Crystals: Ab Initio DFT Calculations with van Der Waals Corrections. *The Journal of Physical Chemistry A* **2010**, *114* (43), 11814–11824.
(45) Kresse, G.; Furthmüller, J. Efficiency of Ab-Initio Total Energy Calculations for Metals and Semiconductors Using a Plane-Wave Basis Set. *Computational materials science* **1996**, *6* (1), 15–50.
(46) Hammer, B.; Hansen, L. B.; Nørskov, J. K. Improved Adsorption Energetics within Density-Functional Theory Using Revised Perdew-Burke-Ernzerhof Functionals. *Physical review B* **1999**, *59* (11), 7413.
(47) Perdew, J. P.; Burke, K.; Ernzerhof, M. Generalized Gradient Approximation Made Simple. *Physical review letters* **1996**, *77* (18), 3865.
(48) Kresse, G.; Joubert, D. From Ultrasoft Pseudopotentials to the Projector Augmented-Wave Method. *Physical review b* **1999**, *59* (3), 1758.
(49) Blöchl, P. E.; Jepsen, O.; Andersen, O. K. Improved Tetrahedron Method for Brillouin-Zone Integrations. *Physical Review B* **1994**, *49* (23), 16223.
(50) Grimme, S.; Ehrlich, S.; Goerigk, L. Effect of the Damping Function in Dispersion Corrected Density Functional Theory. *Journal of computational chemistry* **2011**, *32* (7), 1456–1465.
(51) Stampfl, C.; Scheffler, M. Theoretical Study of O Adlayers on Ru (0001). *Physical Review B* **1996**, *54* (4), 2868.
(52) Arblaster, J. W. Crystallographic Properties of Ruthenium. *Platinum Metals Review* **2013**, *57* (2), 127–136.
(53) Persson, K. Materials Data on Ru by Materials Project, 2020. https://doi.org/10.17188/1309980.
(54) Persson, K. Materials Data on Ir by Materials Project, 2020. https://doi.org/10.17188/1186086.
(55) Arblaster, J. W. Crystallographic Properties of Iridium. *Platinum Metals Review* **2010**, *54* (2), 93–102.
(56) Sheppard, D.; Xiao, P.; Chemelewski, W.; Johnson, D. D.; Henkelman, G. A Generalized Solid-State Nudged Elastic Band Method. *The Journal of chemical physics* **2012**, *136* (7), 074103.
(57) Ghasemi, A.; Xiao, P.; Gao, W. Nudged Elastic Band Method for Solid-Solid Transition under Finite Deformation. *The Journal of Chemical Physics* **2019**, *151* (5), 054110.
(58) Xiao, P.; Sheppard, D.; Rogal, J.; Henkelman, G. Solid-State Dimer Method for Calculating Solid-Solid Phase Transitions. *The Journal of Chemical Physics* **2014**, *140* (17), 174104.
(59) Evans, M. G.; Polanyi, M. Some Applications of the Transition State Method to the Calculation of Reaction Velocities, Especially in Solution. *Transactions of the Faraday Society* **1935**, *31*, 875–894.
(60) Eyring, H. The Activated Complex and the Absolute Rate of Chemical Reactions. *Chemical Reviews* **1935**, *17* (1), 65–77.
(61) Eyring, H. The Activated Complex in Chemical Reactions. *The Journal of Chemical Physics* **1935**, *3* (2), 107–115.
(62) Laidler, K. J.; King, M. C. Development of Transition-State Theory. *The Journal of physical chemistry* **1983**, *87* (15), 2657–2664.
(63) Tafreshi, S. S.; Roldan, A.; De Leeuw, N. H. Micro-Kinetic Simulations of the Catalytic Decomposition of Hydrazine on the Cu (111) Surface. *Faraday Discussions* **2017**, *197*, 41–57.
(64) Maier, S.; Stass, I.; Cerda, J. I.; Salmeron, M. Bonding of Ammonia and Its Dehydrogenated Fragments on Ru (0001). *The Journal of Physical Chemistry C* **2012**, *116* (48), 25395–25400.
(65) Huang, W.; Cheng, C.; Feng, E. Adsorption and Decomposition of NH3 on Ir(111): A

Density Functional Theory Study. *Surface Science* **2013**, *616*, 29–35. https://doi.org/10.1016/j.susc.2013.06.001.
(66) Li, X.-K.; Ji, W.-J.; Zhao, J.; Wang, S.-J.; Au, C.-T. Ammonia Decomposition over Ru and Ni Catalysts Supported on Fumed SiO2, MCM-41, and SBA-15. *Journal of Catalysis* **2005**, *236* (2), 181–189.
(67) Dahl, S.; Törnqvist, E.; Chorkendorff, I. Dissociative Adsorption of N2 on Ru (0001): A Surface Reaction Totally Dominated by Steps. *Journal of Catalysis* **2000**, *192* (2), 381–390.
(68) Diekhöner, L.; Mortensen, H.; Baurichter, A.; Luntz, A. C. Coverage Dependence of Activation Barriers: Nitrogen on Ru (0001). *Journal of Vacuum Science & Technology A: Vacuum, Surfaces, and Films* **2000**, *18* (4), 1509–1513.
(69) Yates Jr, J. T.; Peden, C. H. F.; Houston, J. E.; Goodman, D. W. Subsurface Penetration of Chemisorbed Hydrogen Isotopes into the Ru (0001) Crystal Surface. *Surface Science* **1985**, *160* (1), 37–45.
(70) Cho, S. J.; Lee, J.; Lee, Y. S.; Kim, D. P. Characterization of Iridium Catalyst for Decomposition of Hydrazine Hydrate for Hydrogen Generation. *Catalysis letters* **2006**, *109* (3–4), 181–186.
(71) Lu, X.; Francis, S.; Motta, D.; Dimitratos, N.; Roldan, A. Mechanistic Study of Hydrazine Decomposition on Ir (111). *Physical Chemistry Chemical Physics* **2020**, *22* (7), 3883–3896.
(72) Kusada, K. Discovery of the Face-Centered Cubic Ruthenium Nanoparticles: Facile Size-Controlled Synthesis Using the Chemical Reduction Method. In *Creation of New Metal Nanoparticles and Their Hydrogen-Storage and Catalytic Properties*; Springer, 2014; pp 59–67.
(73) Abe, J. O.; Popoola, A. P. I.; Ajenifuja, E.; Popoola, O. M. Hydrogen Energy, Economy and Storage: Review and Recommendation. *International journal of hydrogen energy* **2019**, *44* (29), 15072–15086.
(74) Parra, D.; Valverde, L.; Pino, F. J.; Patel, M. K. A Review on the Role, Cost and Value of Hydrogen Energy Systems for Deep Decarbonisation. *Renewable and Sustainable Energy Reviews* **2019**, *101*, 279–294.
(75) Filippov, S. P.; Yaroslavtsev, A. B. Hydrogen Energy: Development Prospects and Materials. *Russ. Chem. Rev.* **2021**, *90* (6), 627. https://doi.org/10.1070/RCR5014.
(76) Kojima, Y. A Green Ammonia Economy. In *10th annual NH 10th annual NH3 fuel conference*; 2013.
(77) Weststrate, C. J.; Bakker, J. W.; Gluhoi, A. C.; Ludwig, W.; Nieuwenhuys, B. E. Ammonia Oxidation on Ir (1 1 1): Why Ir Is More Selective to N2 than Pt. *Catalysis Today* **2010**, *154* (1–2), 46–52.
(78) Sayas, S.; Morlanés, N.; Katikaneni, S. P.; Harale, A.; Solami, B.; Gascon, J. High Pressure Ammonia Decomposition on Ru–K/CaO Catalysts. *Catalysis Science & Technology* **2020**, *10* (15), 5027–5035.
(79) Lu, X.; Zhang, J.; Chen, W.-K.; Roldan, A. Kinetic and Mechanistic Analysis of NH 3 Decomposition on Ru (0001), Ru (111) and Ir (111) Surfaces. *Nanoscale Advances* **2021**, *3* (6), 1624–1632.
(80) He, C.; Wang, H.; Huai, L.; Liu, J. Mechanism of Ammonia Decomposition and Oxidation on Ir (100): A First-Principles Study. *The Journal of Physical Chemistry C* **2012**, *116* (45), 24035–24045.
(81) Kizilkaya, A. C.; Niemantsverdriet, J. W.; Weststrate, C. J. Ammonia Adsorption and Decomposition on Co (0001) in Relation to Fischer–Tropsch Synthesis. *The Journal of Physical Chemistry C* **2016**, *120* (7), 3834–3845.
(82) Ma, F. F.; Ma, S. H.; Jiao, Z. Y.; Dai, X. Q. Stepwise Dehydrogenation of Ammonia on Fcc-Co Surfaces: A DFT Study. *Applied Surface Science* **2017**, *405*, 71–78. https://doi.org/10.1016/j.apsusc.2017.02.015.
(83) Yeo, S. C.; Han, S. S.; Lee, H. M. Mechanistic Investigation of the Catalytic Decomposition of Ammonia (NH3) on an Fe(100) Surface: A DFT Study. *J. Phys. Chem. C* **2014**, *118* (10), 5309–5316. https://doi.org/10.1021/jp410947d.
(84) Hansgen, D. A.; Vlachos, D. G.; Chen, J. G. Using First Principles to Predict Bimetallic Catalysts for the Ammonia Decomposition Reaction. *Nature Chem* **2010**, *2* (6), 484–

489. https://doi.org/10.1038/nchem.626.
(85) Qian, J.; An, Q.; Fortunelli, A.; Nielsen, R. J.; Goddard, W. A. Reaction Mechanism and Kinetics for Ammonia Synthesis on the Fe(111) Surface. *J. Am. Chem. Soc.* **2018**, *140* (20), 6288–6297. https://doi.org/10.1021/jacs.7b13409.
(86) Duan, X.; Qian, G.; Fan, C.; Zhu, Y.; Zhou, X.; Chen, D.; Yuan, W. First-Principles Calculations of Ammonia Decomposition on Ni (110) Surface. *Surface science* **2012**, *606* (3–4), 549–553.
(87) Duan, X.; Qian, G.; Liu, Y.; Ji, J.; Zhou, X.; Chen, D.; Yuan, W. Structure Sensitivity of Ammonia Decomposition over Ni Catalysts: A Computational and Experimental Study. *Fuel Processing Technology* **2013**, *108*, 112–117. https://doi.org/10.1016/j.fuproc.2012.05.030.
(88) Kresse, G.; Furthmüller, J. Efficiency of Ab-Initio Total Energy Calculations for Metals and Semiconductors Using a Plane-Wave Basis Set. *Computational materials science* **1996**, *6* (1), 15–50.
(89) Bucko, T.; Hafner, J.; Lebegue, S.; Angyán, J. G. Improved Description of the Structure of Molecular and Layered Crystals: Ab Initio DFT Calculations with van Der Waals Corrections. *The Journal of Physical Chemistry A* **2010**, *114* (43), 11814–11824.
(90) Taylor, A.; Floyd, R. W. Precision Measurements of Lattice Parameters of Non-Cubic Crystals. *Acta Crystallographica* **1950**, *3* (4), 285–289.
(91) Häglund, J.; Guillermet, A. F.; Grimvall, G.; Körling, M. Theory of Bonding in Transition-Metal Carbides and Nitrides. *Physical Review B* **1993**, *48* (16), 11685.
(92) Woodward, P. M.; Suard, E.; Karen, P. Structural Tuning of Charge, Orbital, and Spin Ordering in Double-Cell Perovskite Series between NdBaFe2O5 and HoBaFe2O5. *Journal of the American Chemical Society* **2003**, *125* (29), 8889–8899.
(93) Jørgensen, J.-E.; Filinchuk, Y.; Dmitriev, V. Tilting of Semi-Rigid GaF6 Octahedra in GaF3 at High Pressures. *Powder Diffraction* **2017**, *32* (S1), S69–S73.
(94) Lin, R.-J.; Li, F.-Y.; Chen, H.-L. Computational Investigation on Adsorption and Dissociation of the NH3 Molecule on the Fe (111) Surface. *The Journal of Physical Chemistry C* **2011**, *115* (2), 521–528.
(95) Ji, J.; Duan, X.; Gong, X.; Qian, G.; Zhou, X.; Chen, D.; Yuan, W. Promotional Effect of Carbon on Fe Catalysts for Ammonia Decomposition: A Density Functional Theory Study. *Industrial & Engineering Chemistry Research* **2013**, *52* (48), 17151–17155.
(96) Lara-García, H. A.; Mendoza-Nieto, J. A.; Pfeiffer, H.; Torrente-Murciano, L. COx-Free Hydrogen Production from Ammonia on Novel Cobalt Catalysts Supported on 1D Titanate Nanotubes. *International Journal of Hydrogen Energy* **2019**, *44* (57), 30062–30074.
(97) Raróg-Pilecka, W.; Miśkiewicz, E.; Matyszek, M.; Kaszkur, Z.; Kępiński, L.; Kowalczyk, Z. Carbon-Supported Cobalt Catalyst for Ammonia Synthesis: Effect of Preparation Procedure. *Journal of Catalysis* **2006**, *237* (1), 207–210. https://doi.org/10.1016/j.jcat.2005.10.029.
(98) Liu, H. *Ammonia Synthesis Catalysts: Innovation and Practice*; World Scientific, 2013.
(99) Jennings, J. R. *Catalytic Ammonia Synthesis: Fundamentals and Practice*; Springer Science & Business Media, 1991.
(100) Alstrup, I.; Chorkendorff, I.; Ullmann, S. The Interaction of Nitrogen with the (111) Surface of Iron at Low and at Elevated Pressures. *Journal of Catalysis* **1997**, *168* (2), 217–234. https://doi.org/10.1006/jcat.1997.1652.
(101) (Kees-Jan) Weststrate, C. J.; Garcia Rodriguez, D.; Sharma, D.; (Hans) Niemantsverdriet, J. W. Structure-Dependent Adsorption and Desorption of Hydrogen on FCC and HCP Cobalt Surfaces. *Journal of Catalysis* **2021**. https://doi.org/10.1016/j.jcat.2021.12.016.
(102) Barbier, A.; Tuel, A.; Arcon, I.; Kodre, A.; Martin, G. A. Characterization and Catalytic Behavior of Co/SiO2 Catalysts: Influence of Dispersion in the Fischer–Tropsch Reaction. *Journal of catalysis* **2001**, *200* (1), 106–116.
(103) Low-Temperature Hydrodesulfurization of Thiophene on Ni/Pt(111) Bimetallic Surfaces with Monolayer Ni Coverage | Elsevier Enhanced Reader https://reader.elsevier.com/reader/sd/pii/S0021951701934530?token=DF65B69A6A

6622DA14819B8D5518BB10F4C65CA4B3F8787F8428C4A225C983187D44DD70EB82BC7B7C1D662964A3AF2A&originRegion=eu-west-1&originCreation=20211220102931 (accessed 2021 -12 -20). https://doi.org/10.1006/jcat.2001.3453.

(104) Grabke, H. J. Conclusions on the Mechanism of Ammonia-Synthesis from the Kinetics of Nitrogenation and Denitrogenation of Iron. *Zeitschrift für Physikalische Chemie* **1976**, *100* (3–6), 185–200.

(105) Bowker, M. Modelling of Ammonia Synthesis Kinetics. *Catalysis today* **1992**, *12* (2–3), 153–163.

Chapter 6 Ammonia Reforming on Single-Atom Catalysts

6.1 Introduction

Hydrogen is a valued energy vector able to replace fossil fuels and promote the transition toward a net-zero society.[1,2] Ammonia (NH_3) is a potential H_2 medium with high hydrogen density (17.64 wt%), low storage pressure (~7.5 atm at 300 K) and long-term storage stability, which can be produced from many different types of energy sources, including renewables, fossil fuels and surplus power.[3] The NH_3 reforming process allows for a steady H_2 supply on fuel cells since no carbon monoxide is generated.[4] However, the high cost of efficient NH_3 reforming catalysts (Ru, Ir) hinders their large-scale application. This could be mitigated by using single-atom catalysts (SACs).[5] SACs are catalysts with the highest level of atom efficiency, i.e., each atom participates in independent catalytic reactions.

Lately, although SACs have attracted much attention on nitrogen reduction reaction (NRR), which is similar to the NH_3 reforming, the related literature is still scarce.[6,7] Up to date, only SACs containing Ru, Au, and Pt noble-transition metals have been utilized on SACs for the NRR.[8–10] Wang and co-workers found that Au SACs supported on g-C3N4 have a lower energy barrier for the N_2 adsorption step than the Au(211) surface, resulting in a better NRR electrocatalytic activity and selectivity.[11] Despite Au/C_2N_4 has an 11.1% faradaic efficiency (FE) and 1305 $\mu g * h^{-1} * mg_{Au}^{-1}$ NH_4^+ yield rate. Ru-based SACs presents better electro-catalytic efficiency (29.6 % FE) for the same reaction.[12] Tao *et al.* reported Ru SACs supported on N-doped carbon to fix nitrogen at room temperature and pressure, which greatly promoted the electroreduction of aqueous N_2 selectively to NH_3 compared with Ru nanoparticles by hindering hydrogen evolution reaction.[12] A DFT investigation of Ru SAC for NRR found that the Ru atom is anchored in the carbon materials with strong cohesive energy on which NRR limiting potentials are similar on different carbon materials (C_2N, T-C_3N_4, and γ-graphene).[13] As a non-noble metal, Fe is the active site of the Haber process catalyst and the biological nitrogenase.[14] Therefore, Fe-based SACs are also potential candidates for high-performance NRR catalysis. Li and co-workers modeled the highly spin-polarized FeN_3 center and found it to be an active site for efficient NRR because it promoted N_2 adsorption and activated the N-N triple bond.[15] Furthermore, Sc, V, and

Mn atoms embedded in the graphene's lattice also lead to a high-spin polarization structure for N_2 activation.[15] Lü *et al.* reported a Fe single-atom catalyst for ambient electrochemical NH_3 synthesis and a theoretical investigation revealed the catalytic activation of N_2 on FeN_4.[16] Sardroodi *et al.* employed DFT calculations to investigate the stability and electronic structures of Co SACs supported on defective N-doped graphene. They found high catalytic performance at the low-temperature electrochemical reduction of N_2 owing to Co SACs stronger adsorption energy and electron transfer.[17] Zhang *et al.* demonstrated Mo SACs with high-performance NRR and revealed its mechanism following the Mars–van Krevelen mechanism.[18] Liu *et al.* found that Sc and Y atoms with a large atomic radius make these atoms to be anchored at large-sized carbon defects through six coordination bonds with nitrogen and carbon and exhibit catalytic activities towards NRR at room temperature.[19]

Although the development of effective SACs NRR is currently a hotspot, the main investigations remain largely behind the research on nanoparticle catalysts. Due to the complexity and difficulty to observe experimentally the SACs structure and reaction intermediates, it is hard to determine the effective sites and reaction mechanisms. For this reason, we have performed a density functional theory (DFT) investigation on carbon-supported SACs with seven transition metals (Fe, Co, Ni, Ir, Ru, Rh and Zn) and simulated all the elementary steps for NH_3 reforming reaction. Furthermore, microkinetic simulations and temperature-programmed desorption (TPD) simulations were carried out to provide reaction information of batch reactor and desorption properties, respectively.

6.2 Computational details

We employed the Vienna Ab-initio Simulation Package (VASP) to model the NH_3 reforming reactions on single-metal catalysts (Fe, Co, Ni, Ir, Ru, Rh and Zn) anchored on a nitrogen-doped graphene matrix.[20,21] The spin-polarized revised Perdew-Burke-Ernzerhof (rPBE) method of the generalized gradient approximation (GGA) was adopted to describe the exchange-correlation with a plane-wave kinetic cutoff energy of 500 eV.[22] Non-spherical contributions to atomic cores from the gradient corrections were represented by the projector augmented wave (PAW).[23–25] The zero-damping DFT-D3 method was used to describe long-range interactions.[26] The optimized convergence threshold of internal forces and electronic relaxation were set to 0.02 eV/Å and 10^{-5} eV, respectively. A 3×3×1 k-spacing Monkhorst-Pack grid sampled the Brillouin zone with a smearing broadening of 0.2 eV.[27]

The binding energy (E_b) defined in Equation 9 evaluates the strength of single atom incorporation on the carbon and nitrogen-doped carbon matrix:

$$E_b = E_{SAC} - E_g - E_m \quad \text{Equation 9}$$

Where E_{SAC}, E_g and E_m represent the energies of the single-atom catalyst, the modified N-doped graphene, and the metal atom within the metal bulk in its most stable crystal structure, respectively.

The optimized metal bulk lattice parameters are shown in Table S6-1. SACs' surfaces were represented by a *p(6x6)* supercell slab model with a single atomic layer thickness. We added 15 Å of vacuum perpendicular to the slab to avoid any spurious interaction with periodic images. Dipole correction perpendicular to the surface was applied upon the adsorption of any species.

The molecular adsorption energies were defined by Equation 10, and the relative energies along the energy profiles are calculated by Equation 11.

$$\mathrm{E_{ads}} = \mathrm{E_{system}} - \mathrm{E_{surface}} - \mathrm{E}_{molecule} \quad \text{Equation 10}$$

$$\Delta E = E_{system} + \frac{n}{2} * E_{H_2} - E_{surf} - E_{NH_3} \quad \text{Equation 11}$$

Where $\mathrm{E_{system}}$ is the total energy of the adsorbed system, $\mathrm{E_{surface}}$ denotes the energy of the clean surfaces, $\mathrm{E_{NH_3}}$ and E_{H_2} are the energy of the ammonia and the hydrogen isolated molecules. The half energy of a hydrogen molecule refers to the energy of one H atom, and n is the number of H dissociated from NH_3.

The reaction energy (E_r) was given by the energy difference of the final state (FS) and the initial state (IS) (Equation 12). When the E_r value is negative, it means an exothermic step. The transition states (TS) were determined using the climb-image nudged elastic band (ci-NEB) combined with the improved dimer method (IDM) and ensuring a unique imaginary frequency along the reaction coordinate.[28–30] We defined the forward and reverse activation barriers (E_a) as the energy difference between TS and IS and between TS and FS, respectively (Equation 13 and Equation 14).

$$\mathrm{E_r} = \mathrm{E^{FS}} - \mathrm{E^{IS}} \quad \text{Equation 12}$$

$$\mathrm{E_a^{forward}} = \mathrm{E^{TS}} - \mathrm{E^{IS}} \quad \text{Equation 13}$$

$$\mathrm{E_a^{reverse}} = \mathrm{E^{TS}} - \mathrm{E^{FS}} \quad \text{Equation 14}$$

6.3 Results and discussion

6.3.1 Anchoring sites

We established clean and nitrogen-modified graphene (g-N_3 and g-N_4) and single- and double-carbon vacancy in graphene.[31] The carbon vacant sites are known to anchor single metal atoms to saturate the dangling bond.[32–34] Figure 6-1 represents schematically the different structures according to the anchoring site. The surfaces properties of SACs with different transition metals are summarized in Table 6-1.

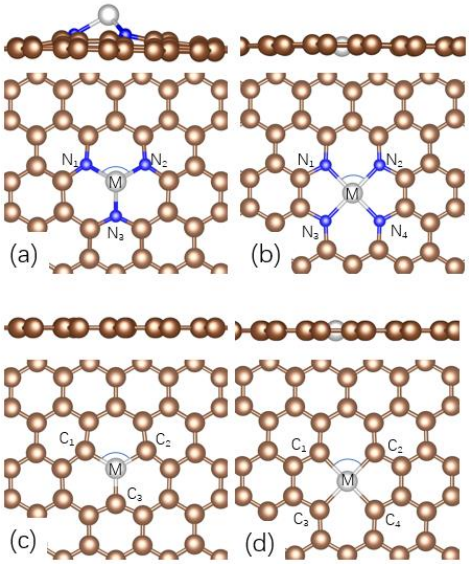

Figure 6-1. Schematic representations of SACs anchoring sites: (a) MN_3, (b) MN_4, (c) MC_3 and (d) MC_4. The khaki, blue and silver sphere represent carbon, nitrogen and metal atoms, respectively.

The binding energy of a transition metal atom within the nitrogen-modified graphene is lower than in the non-doped defective carbon matrix. Indeed, the positive value of Eb indicates the thermodynamic driving force for the atoms to coalescence into a metallic bulk, which agrees with the previous investigation.[32–34] Therefore, the nitrogen modification of the graphene is an important strategy to synthesize robust SACs supported on carbon materials.[35,36] In general, due to the protrusion on MN_3, the M-N bond is elongated and becomes longer than the M-C bond. The binding energy in Table 6-1 shows that the 4-coordinated structures are easier to form than the 3-coordinated structures thermodynamically. Moreover, Fe, Co and Ni have a stronger affinity with nitrogen (more negative binding energy) than the noble metals (Ir, Ru and Rh), so they are easier to form a single-atom structure on the N-modified surface.

Table 6-1. Geometric structure parameters and binding energies of SACs. MX (X= N, C) is the bond length between metal atoms and nitrogen or carbon. NMN and CMC represent the angle between the MX bonds. E_b, q, p and mag represent the binding energy, difference of electron density, the difference of spin density and magnetism, respectively.

	Item	Fe	Co	Ni	Ir	Ru	Rh	Zn
MN_3	MN(Å)	1.891	1.857	1.874	2.054	1.931	2.055	2.028
	N_1MN_2(°)	94.8	96.8	95.1	82.0	90.9	81.4	83.9
	E_b(eV)	0.51	-0.17	0.27	3.3	2.22	2.06	-0.14
	q(e^-)	-1.06	-0.93	-0.97	-0.75	-1.12	-0.72	-0.79
	p(e^-)	3.28	2.17	1.31	1.08	0.00	1.21	0.64
	mag(μ_B)	3.35	2.34	1.50	2.23	0.00	1.75	0.69
MC_3	MC(Å)	1.675	1.667	1.693	1.769	1.754	1.751	1.775
	C_1MC_2(°)	120.0	120.0	118.1	120.0	120.0	119.9	115.4
	E_b(eV)	0.90	0.77	1.20	3.08	3.38	2.49	2.97
MN_4	MN(Å)	1.898	1.88	1.885	1.957	1.954	1.946	1.967
	N_1MN_2(°)	88.6	88.2	88.3	89.9	89.0	89.3	88.2
	E_b(eV)	-2.47	-2.6	-3.14	-0.65	0.07	-1.25	-2.26
	q(e^-)	-1.20	-1.07	-1.05	-1.15	-1.36	-0.95	-1.28
	p(e^-)	2.01	0.87	0.00	0.42	1.67	0.05	0.00
	mag(μ_B)	1.60	0.94	0.00	1.00	0.00	0.40	0.00
MC_4	MC(Å)	1.917	1.894	1.874	1.887	1.858	1.865	1.939
	N_1MN_2(°)	87.4	88.0	87.9	83.0	81.9	82.1	87.6
	E_b(eV)	-0.48	-0.3	-0.94	0.59	1.05	0.34	-0.78

6.3.2 Surface species

To investigate the reaction mechanism on SACs, we investigated all the non-equivalent NH_x(x=0-3) and H adsorptions modes on the N-doped graphene SACs, *i.e.*, with three and four nitrogens respectively, MN_3 and MN_4 (M= Fe, Co, Ni, Ir, Ru, Rh and Zn). The most favorable adsorption site of reacting species is on top of the single transition metal atom, which partially occupation of its hybridized sd orbitals favors electron transfer and back donation with the N lone electrons pair.[37] Table 6-2 summarizes the adsorption properties of NH_x (x=1-3), and atomic and molecular hydrogen and nitrogen. The adsorbed structures are schematically represented in appendix Figure S6-1 to Figure S6-14.

Table 6-2. ZPE corrected adsorption energies (E_{ads}) and the relative energies (ΔE) respect to isolating MN_x(x=3,4) of adsorbates and reaction intermediates, respectively, and distances between the metal and nitrogen (d_{MN}).

	NH_3		NH_2		NH		N		H		N_2	H_2
Species	$E_{ads}(eV$	$d_{MN}(\text{Å})$	$\Delta E(eV)$	$d_{MN}(\text{Å})$	$\Delta E(eV)$	$d_{MN}(\text{Å})$	$\Delta E(eV)$	$d_{MN}(\text{Å})$	$\Delta E(eV)$	$d_{MH}(\text{Å})$	$E_{ads}(eV$	$E_{ads}(eV$
FeN_3	-1.02	2.135	-0.75	1.813	0.43	1.632	1.09	1.516	0.06	1.555	-0.75	-0.46
FeN_4	-0.61	2.285	0.47	1.849	1.89	1.715	1.92	1.580	0.30	1.493	-0.14	-0.11
CoN_3	-0.44	2.073	-0.18	1.827	1.19	1.682	1.41	1.566	-0.14	1.547	-0.13	-0.35
CoN_4	-0.57	2.193	0.96	1.919	2.45	1.823	3.17	1.718	0.31	1.444	-0.11	0.00
NiN_3	-0.84	2.197	-0.74	1.823	0.96	1.664	1.97	1.603	0.02	1.526	-0.79	-0.41
NiN_4	0.05	2.997	0.87	2.039	2.05	1.858	2.33	1.772	-0.26	1.499	-0.10	-0.03
IrN_3	-1.28	2.154	-1.33	1.909	-0.89	1.741	-1.06	1.660	-0.85	1.635	-0.46	0.09
IrN_4	-0.74	2.285	0.63	1.849	3.52	1.715	5.36	1.580	0.47	1.493	-0.12	-0.11
RuN_3	-1.19	2.256	-0.94	1.929	-0.13	1.740	-0.99	1.619	-0.52	1.650	-1.28	-0.78
RuN_4	-0.20	2.071	0.55	1.931	2.38	1.794	2.89	1.643	-0.39	1.580	-0.12	-0.09
RhN_3	-1.11	2.193	-0.85	1.921	-0.10	1.743	-0.09	1.630	-0.62	1.590	-1.18	-0.71
RhN_4	-0.13	2.404	1.84	2.042	4.22	1.930	4.92	1.800	1.45	1.531	-0.13	-0.10
ZnN_3	-0.17	2.061	-0.94	1.877	-0.12	1.886	-1.00	1.890	-0.52	1.517	-0.14	-0.09
ZnN_4	-1.07	2.171	-0.41	1.930	0.47	1.904	-0.25	1.895	-0.80	1.560	-0.18	-1.18

It also indicates that MN_3 performs better catalytic performance than MN_4, therefore the adsorption behaviors on MN_3 were investigated deeply in the following sections. Favorable adsorption of NH_3 molecules on the surface is the basis for a subsequent dehydrogenation reaction, namely weak NH_3 adsorption is not favorable to the dehydrogenation reaction. Noticeably, the interactions between intermediates (NH_x, x=0, 1, 2) and the MN_3 non-noble metals' SACs structures are not as favorable as with the 3N-coordinated noble metals (Ir, Ru, Rh) and Zn. Likewise, instead of a highly exothermic N_2 and H_2 adsorption on RuN_3 and RhN_3, weak and moderate adsorption energies of products, such as on IrN_3 and ZnN_3, make the SAC a potential candidate for ammonia reforming.

We also calculated the d-orbital projected density of state (PDOS) of the SACs surface to investigate the structure-activity relationship, which is shown in Figure S6-15. The metal atoms in MN_3 transfer fewer electrons to the graphene surface than MN_4, which has a higher electronic density. Generally, after hybridization, there are more states near the Fermi energy in d orbitals of MN_3 metal atom than MN_4, explaining the stronger interaction between NH_3 dangling bond and MN_3 surfaces.

6.3.3 Reaction thermochemistry

The differences of Gibbs free energy (ΔG_r) and activation energy (ΔG_a) of each elementary surface reaction were determined to extract accurate insights on the NH_3 reforming reaction.[38] The NH_3 reforming upon the Mars-van Krevelen mechanism is hardly realized with an extremely high N_2 recombination barrier energy (>3 eV). Therefore, based on the surface species analysis, the thermochemical details of NH_3 stepwise dehydrogenation (R1: $\mathrm{NH_3^* + * \longrightarrow NH_2^* + H^*}$; R3: $\mathrm{NH_2^* + * \longrightarrow NH^* + H^*}$; R5: $\mathrm{NH^* + * \longrightarrow N^* + H^*}$) and the N_2 and H_2 formations (R7: $\mathrm{2N^* \longrightarrow N_2^* + *}$; R9: $\mathrm{2H^* \longrightarrow H_2^* + *}$) on 3N-coordinated noble metals and Zn single-atom sites were represented in Figure 6-2, and other the non-noble metals SACs were represented in Figure S6-16. The transition states (TS1-TS5) on SACs were shown in the schematic diagram of Figure S6-17.

The recombination reaction of N is the rate-determining step of the ammonia reforming reaction on IrN_3 with the highest barrier energy of ~2 eV and it is also an endothermic process, which will hinder the continuous generation of N_2. While the barrier energies of the stepwise dehydrogenation reactions on the IrN_3 are ~1.00 eV and the H_2 recombination is thermodynamically unfavorable at high temperatures, indicating that the ammonia dehydrogenation can occur in mild conditions. Similar to IrN_3, N_2 recombination is also the rate-determining step on RuN_3, however, the dehydrogenation steps are not as favorable as on IrN_3 with the barrier energy of ~1.50 eV. Ammonia reforming on RhN_3 is thermodynamically favorable with moderate ΔG_r but the energy barrier of NH dehydrogenation (R5) is high (~1.50 eV). The recombination reaction of N_2 on the RhN_3 has a negative ΔG_r (~ -1.25 eV), indicating that the desorption of N on RhN_3 can happen spontaneously at mild temperatures. On the RhN_3, the stepwise dehydrogenation reactions control the overall reaction rate, and the temperatures have little effect on barrier energy. The energy barriers of the ammonia dehydrogenation reactions on the ZnN_3 are too high (> 2 eV) and increase with the temperature, indicating that it is not suitable as an ammonia reforming catalyst.

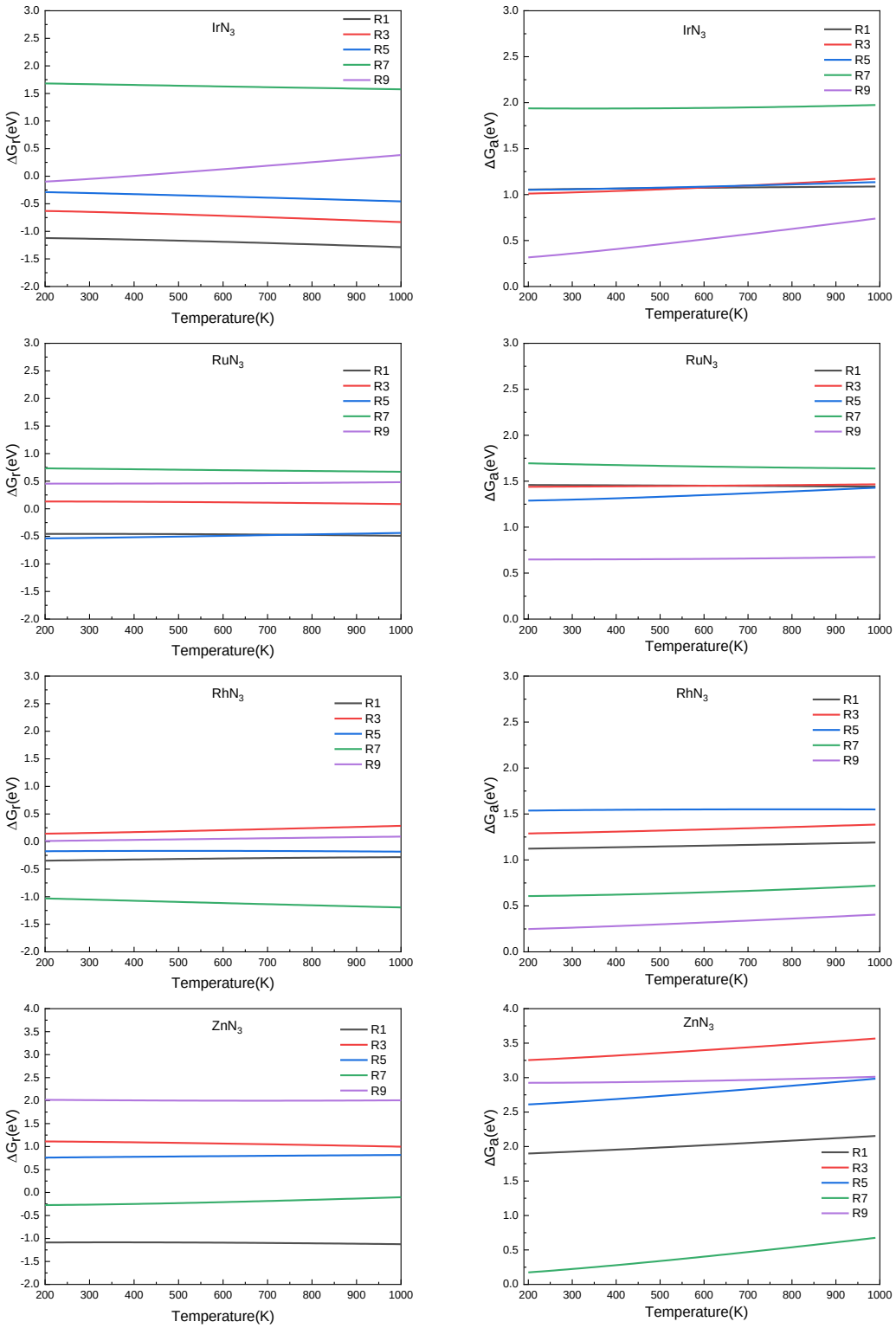

Figure 6-2. Free energy difference (ΔG_r) and activation energy (ΔG_a) of each elementary step in ammonia dehydrogenation (R1, R3, R5) and N_2 and H_2 formations (R7 and R9) on IrN_3, RuN_3, RhN_3 and ZnN_3 as a function of the temperature.

6.3.4 Reaction constants

We have derived the rate law's pre-exponential factors and reaction constants for every N-H dissociative step and associative recombination based on the reaction energy profiles, see Table 6-3. Fully aligned with the discussion above, the N_2 formation on IrN_3 and RuN_3 has the smallest reaction constants indicating to be the rate-determining step. This is not the case with RhN_3 SAC where the dehydrogenation of NH species limits the overall reaction rate. Comparing the reaction constants for NH_x(x=1-3) dehydrogenation (R1, R3, R5) and formation (R2, R4, R6), it concludes that the equilibrium is shifted towards the dehydrogenation of NH_x (x=1-3) on these three SACs, *i.e.*, IrN_3, RuN_3 and RhN_3, indicating to be potential NH_3 reforming catalysts.

Table 6-3. Elementary reactions in the ammonia reforming process corresponding pre-exponential factors (ν) and reaction constants (k, in its corresponding units) over IrN_3, RuN_3 and RhN_3 SACs at 300K.

No.	Reaction	IrN_3		RuN_3		RhN_3	
		ν	k	ν	k	ν	k
A1	$NH_3 + * \longrightarrow NH_3^*$	8.97×10^{8}	2.24×10^{2}	9.38×10^{8}	3.50×10^{2}	9.37×10^{8}	2.18×10^{2}
D1	$NH_3^* \longrightarrow NH_3 + *$	8.97×10^{8}	1.96×10^{-9}	9.38×10^{8}	3.26×10^{-7}	9.37×10^{8}	9.84×10^{-8}
R1	$NH_3^* + * \longrightarrow NH_2^* + H^*$	2.61×10^{12}	4.02×10^{-6}	7.28×10^{12}	2.43×10^{-12}	2.30×10^{12}	2.41×10^{-7}
R2	$NH_2^* + H^* \longrightarrow NH_3^* + *$	1.11×10^{12}	1.51×10^{-25}	6.08×10^{12}	4.52×10^{-20}	5.50×10^{12}	1.31×10^{-12}
R3	$NH_2^* + * \longrightarrow NH^* + H^*$	1.62×10^{12}	1.04×10^{-5}	4.49×10^{12}	2.75×10^{-12}	1.62×10^{12}	2.62×10^{-10}
R4	$NH^* + H^* \longrightarrow NH_2^* + *$	5.48×10^{11}	4.71×10^{-17}	4.36×10^{12}	4.13×10^{-10}	4.50×10^{12}	3.04×10^{-8}
R5	$NH^* + * \longrightarrow N^* + H^*$	2.50×10^{12}	4.28×10^{-6}	3.07×10^{12}	4.54×10^{-10}	2.12×10^{12}	2.67×10^{-14}
R6	$N^* + H^* \longrightarrow NH^* + *$	7.06×10^{11}	8.67×10^{-12}	5.64×10^{12}	1.12×10^{-18}	3.60×10^{12}	5.82×10^{-17}
R7	$2N^* \longrightarrow N_2^* + *$	6.22×10^{12}	1.83×10^{-20}	1.78×10^{13}	8.92×10^{-16}	3.28×10^{12}	1.62×10^{2}
R8	$N_2^* + * \longrightarrow 2N^*$	1.41×10^{12}	4.44×10^{7}	7.91×10^{12}	5.96×10^{-4}	3.32×10^{11}	3.48×10^{-17}
D2	$N_2^* \longrightarrow N_2 + *$	8.93×10^{8}	5.89×10^{5}	9.33×10^{8}	2.34×10^{-8}	9.32×10^{8}	1.10×10^{-8}
A2	$N_2 + * \longrightarrow N_2^*$	8.93×10^{8}	5.85×10^{4}	9.33×10^{8}	9.15×10^{4}	9.32×10^{8}	5.69×10^{4}
R9	$2H^* \longrightarrow H_2^* + *$	1.85×10^{11}	1.73×10^{5}	5.35×10^{12}	66.90	2.04×10^{12}	7.76×10^{7}
R10	$H_2^* + * \longrightarrow 2H^*$	6.92×10^{12}	9.40×10^{5}	6.30×10^{12}	3.60×10^{9}	4.70×10^{12}	3.89×10^{8}
D3	$H_2^* \longrightarrow H_2 + *$	9.03×10^{8}	2.93×10^{11}	9.45×10^{8}	2.40×10^{2}	9.44×10^{8}	2.57×10^{-2}
A3	$H_2 + * \longrightarrow H_2^*$	9.03×10^{8}	3.41×10^{3}	9.45×10^{8}	5.34×10^{3}	9.44×10^{8}	3.32×10^{3}

6.3.5 Microkinetic

Temperature programmed desorption (TPD)

The individual desorption of N_2 and H_2 from the SACs sites is a crucial step to complete the catalytic cycle. We found that there is a significant difference between the TPD spectra (Figure 6-3) on three SACs sites. Compared with the Ir(111) structure where the H_2 desorption takes place at ~300 K, there is no H_2 desorption spectrum on IrN_3 SACs at 200-1000 K. While the N_2 desorption curve is similar to the one on Ir(111) (500~700 K).

Compared with hcp Ru(0001) surface, the desorption curve of N_2 and H_2 on Ru SACs shifted to the lower temperature region to be ~150 K and ~25 K.[38,39] These results prove how effective are SACs to improve the desorption performance. The desorption temperature of H_2 and N_2 on the RhN_3 surface is close at 300-400 K, indicating that the desorption of the product could take place almost at ambient temperature although it is not the rate-determining step on ammonia reforming, which is also consistent with the previous discussion.

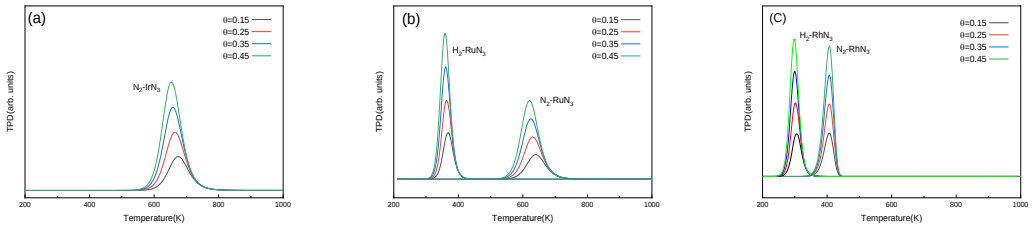

Figure 6-3. Simulated N_2 and H_2 TPD spectra on (a) IrN_3, (b) RuN_3, and (c) RhN_3 at different initial coverages (θ in ML) with the heating rate of 1K/min.

Batch reactor simulation

We have simulated the ratio between molecular species and active sites as a function of the temperature and the reaction time. Figure 6-4 shows the relative concentration (χ) of NH_3, N_2, H_2 as functions of temperature on batch reactor simulations for IrN_3 and RhN_3, with the initial ratio of 5:1 NH_3: surface. At low temperatures, gas-phase NH_3 will adsorb on the surface and saturate the free sites which are similar to the behaviors of pure metals. The gas contents on RhN_3 reach the

steady-state in ~100 s, but on IrN_3, it needs at least ~200 s, which is seen in Figure 6-4. The IrN_3 and RhN_3 generate molecular N_2 at a temperature of 700K and 650 K, respectively. And the two surfaces have similar H_2 production at ~500 K.

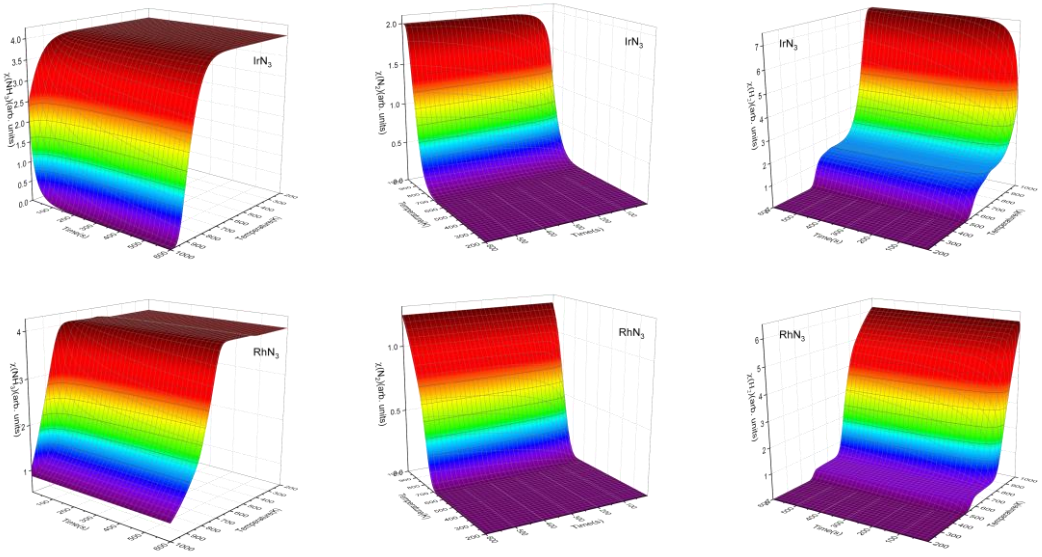

Figure 6-4. The relative concentration (χ) of molecular NH_3, N_2 and H_2 as functions of the temperature and time on IrN_3 and RhN_3 batch reactor simulations. The initial ratio of NH_3: surface sites is 5:1 and the temperature increase 10 K every second. The yellow arrows point out the equilibrium time.

The steady-state ratio (χ) of NH_3, N_2, H_2 as functions of temperature on the three surfaces is shown in Figure 6-5. Although the generated H_2 appears in the gas phase at 520 K, RuN_3 does not generate N_2 in the range of temperature tested and, therefore, the catalytic cycle is not completed. Our research suggests that the catalytic temperature range of nitrogen reduction reaction on RuN_3 is > 500 K, which is in agreement with the NH_3 synthesis experiment on the Ru SACs.[40]

The catalytic behavior of IrN_3 is similar to that of RhN_3: the content of H_2 in the gas phase starts to rise at a low temperature (~425 K), and then quickly reaches a plateau at around 500 K. Individually, the χ of H_2 on IrN_3 (~1.5) is higher than on RhN_3, indicating stronger H_2 generation on IrN_3 at low temperatures. When the temperature rises to 750 K and 700 K, the H_2 generation on IrN_3 and RhN_3 increases rapidly. Among these three SACs, NH_3 can only completely decompose on IrN_3 at ~1000 K. So far, there are no reports on the catalytic synthesis or reforming of ammonia on IrN_3 and

RhN_3. Through our theoretical investigation, these two SACs are determined to be good candidates for NH_3 synthesis reforming.

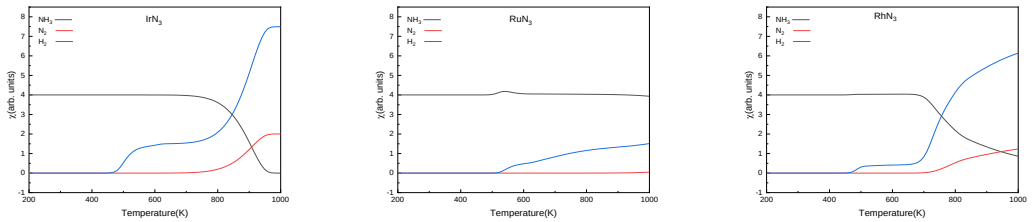

Figure 6-5. The steady-state ratio (χ) of molecular NH_3, N_2, H_2 as functions of temperature upon NH_3 reforming catalyzed by IrN_3, RuN_3 and RhN_3 on batch reactor simulations. The initial simulated conditions are an NH_3 ratio of 5:1 of NH_3 with the free surface. The reaction time is 600 s.

The predominant species on the surfaces after 600 s of reaction within a temperature range of 200~1000 K are plotted in Figure 6-6. At low temperatures (<450 K), the adsorbed NH_3 molecule accommodates on the three surfaces. At 500 K, NH_2 becomes the dominant species on the IrN_3 surface, but it is quickly replaced by N as the temperature rises. The strong adsorption of N hinders the reactivity of the site. When temperatures reach 800 K, N recombines and evolves as N_2 allowing the site to proceed. The dominant species on RuN_3 during the reaction are NH_2 and N at 460~520 K and 520~1000 K respectively, due to the high energy barrier of the N recombination (R7). The RhN_3 surface presents a considerable amount (>0.1 ML) of NH_3, NH_2 and N_2 as the dissociation of NH_3 start at 425 K; NH_2 is the predominant species on the surface at the temperature range of 500~720 K with maximum coverage of 0.9 ML at 680K; after, it is molecular N_2 taking most of the active sites, due to its favorable adsorption on RhN_3.

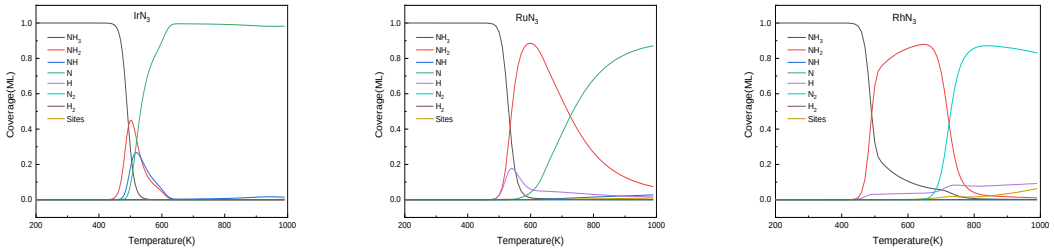

Figure 6-6. Surface species distribution upon NH_3 desorption on IrN_3, RuN_3 and RhN_3 surface at the temperature range of 200-1000 K at 600 s.

6.4 Conclusion

The single transition metal atoms supported on clean and nitrogen-modified graphene were simulated as MN_3, MN_4, MC_3 and MC_4 (M= Fe, Co, Ni, Ir, Ru, Rh and Zn). The results show that nitrogen-modified graphene has a stronger combination with metal atoms than vacancy graphene, hence, providing high resistance to metal sintering and leaching. We investigated the NH_3 reforming reaction mechanism on SACs supported on N-modified graphene. The most favorable adsorption site of species is on top of the metal atom. The relative adsorption energies suggested that MN_3 structures are more active than MN_4. The process catalyzed by noble metals (Ir, Ru, Rh) is more favorable than non-noble metal SACs.

The free energies of molecules and adsorbed species were calculated between 200 and 1000 K. The thermochemical analysis concluded that IrN_3, RuN_3 and RhN_3 are the potential catalysts for the NH_3 reforming and that the recombination reaction of N is generally the rate-determining step of the ammonia reforming, but not on the RhN_3, where the stepwise dehydrogenation reactions of ammonia control the overall reaction rate. We implemented the free energies in microkinetic models to simulate the temperature programmed desorption and batch reactors. The TPR simulations showed that compared with Ru, the N_2 desorption on Ru SACs shifted to the low-temperature region. Batch reaction simulations explored the catalytic performance and mechanism of SACs on NH_3 reforming and supply a detailed understanding of its practical operation for the experiment.

6.5 Reference

(1) Pareek, A.; Dom, R.; Gupta, J.; Chandran, J.; Adepu, V.; Borse, P. H. Insights into Renewable Hydrogen Energy: Recent Advances and Prospects. *Materials Science for Energy Technologies* **2020**, *3*, 319–327.

https://doi.org/10.1016/j.mset.2019.12.002.

(2) Lara-García, H. A.; Mendoza-Nieto, J. A.; Pfeiffer, H.; Torrente-Murciano, L. COx-Free Hydrogen Production from Ammonia on Novel Cobalt Catalysts Supported on 1D Titanate Nanotubes. *International Journal of Hydrogen Energy* **2019**, *44* (57), 30062–30074.

(3) Aziz, M.; Wijayanta, A. T.; Nandiyanto, A. B. D. Ammonia as Effective Hydrogen Storage: A Review on Production, Storage and Utilization. *Energies* **2020**, *13* (12), 3062.

(4) Chiuta, S.; Everson, R. C.; Neomagus, H. W.; Van der Gryp, P.; Bessarabov, D. G. Reactor Technology Options for Distributed Hydrogen Generation via Ammonia Decomposition: A Review. *International journal of hydrogen energy* **2013**, *38* (35), 14968–14991.

(5) Qiu, Y.; Peng, X.; Lü, F.; Mi, Y.; Zhuo, L.; Ren, J.; Liu, X.; Luo, J. Single-Atom Catalysts for the Electrocatalytic Reduction of Nitrogen to Ammonia under Ambient Conditions. *Chemistry – An Asian Journal* **2019**, *14* (16), 2770–2779. https://doi.org/10.1002/asia.201900793.

(6) Kyriakou, G.; Boucher, M. B.; Jewell, A. D.; Lewis, E. A.; Lawton, T. J.; Baber, A. E.; Tierney, H. L.; Flytzani-Stephanopoulos, M.; Sykes, E. C. H. Isolated Metal Atom Geometries as a Strategy for Selective Heterogeneous Hydrogenations. *Science* **2012**, *335* (6073), 1209–1212.

(7) Han, L.; Liu, X.; Chen, J.; Lin, R.; Liu, H.; Lü, F.; Bak, S.; Liang, Z.; Zhao, S.; Stavitski, E.; Luo, J.; Adzic, R. R.; Xin, H. L. Atomically Dispersed Molybdenum Catalysts for Efficient Ambient Nitrogen Fixation. *Angewandte Chemie International Edition* **2019**, *58* (8), 2321–2325. https://doi.org/10.1002/anie.201811728.

(8) Yao, Y.; Zhu, S.; Wang, H.; Li, H.; Shao, M. A Spectroscopic Study on the Nitrogen Electrochemical Reduction Reaction on Gold and Platinum Surfaces. *J. Am. Chem. Soc.* **2018**, *140* (4), 1496–1501. https://doi.org/10.1021/jacs.7b12101.

(9) Geng, Z.; Liu, Y.; Kong, X.; Li, P.; Li, K.; Liu, Z.; Du, J.; Shu, M.; Si, R.; Zeng, J. Achieving a Record-High Yield Rate of 120.9 for N2 Electrochemical Reduction over Ru Single-Atom Catalysts. *Advanced Materials* **2018**, *30* (40), 1803498. https://doi.org/10.1002/adma.201803498.

(10) Qin, Q.; Heil, T.; Antonietti, M.; Oschatz, M. Single-Site Gold Catalysts on Hierarchical N-Doped Porous Noble Carbon for Enhanced Electrochemical Reduction of Nitrogen. *Small Methods* **2018**, *2* (12), 1800202.

(11) Wang, X.; Wang, W.; Qiao, M.; Wu, G.; Chen, W.; Yuan, T.; Xu, Q.; Chen, M.; Zhang, Y.; Wang, X. Atomically Dispersed Au1 Catalyst towards Efficient Electrochemical Synthesis of Ammonia. *Science bulletin* **2018**, *63* (19), 1246–1253.

(12) Tao, H.; Choi, C.; Ding, L.-X.; Jiang, Z.; Han, Z.; Jia, M.; Fan, Q.; Gao, Y.; Wang, H.; Robertson, A. W.; Hong, S.; Jung, Y.; Liu, S.; Sun, Z. Nitrogen Fixation by Ru Single-Atom Electrocatalytic Reduction. *Chem* **2019**, *5* (1), 204–214. https://doi.org/10.1016/j.chempr.2018.10.007.

(13) Cao, Y.; Gao, Y.; Zhou, H.; Chen, X.; Hu, H.; Deng, S.; Zhong, X.; Zhuang, G.; Wang, J. Highly Efficient Ammonia Synthesis Electrocatalyst: Single Ru Atom on Naturally Nanoporous Carbon Materials. *Advanced Theory and Simulations* **2018**, *1* (5),

1800018. https://doi.org/10.1002/adts.201800018.
(14) Foster, S. L.; Bakovic, S. I. P.; Duda, R. D.; Maheshwari, S.; Milton, R. D.; Minteer, S. D.; Janik, M. J.; Renner, J. N.; Greenlee, L. F. Catalysts for Nitrogen Reduction to Ammonia. *Nature Catalysis* **2018**, *1* (7), 490–500.
(15) Li, X.-F.; Li, Q.-K.; Cheng, J.; Liu, L.; Yan, Q.; Wu, Y.; Zhang, X.-H.; Wang, Z.-Y.; Qiu, Q.; Luo, Y. Conversion of Dinitrogen to Ammonia by FeN3-Embedded Graphene. *J. Am. Chem. Soc.* **2016**, *138* (28), 8706–8709. https://doi.org/10.1021/jacs.6b04778.
(16) Lü, F.; Zhao, S.; Guo, R.; He, J.; Peng, X.; Bao, H.; Fu, J.; Han, L.; Qi, G.; Luo, J.; Tang, X.; Liu, X. Nitrogen-Coordinated Single Fe Sites for Efficient Electrocatalytic N2 Fixation in Neutral Media. *Nano Energy* **2019**, *61*, 420–427. https://doi.org/10.1016/j.nanoen.2019.04.092.
(17) Saeidi, N.; Esrafili, M. D.; Sardroodi, J. J. Electrochemical Reduction of N2 to NH3 Using a Co-Atom Stabilized on Defective N-Doped Graphene: A Computational Study. *ChemistrySelect* **2019**, *4* (42), 12216–12226.
(18) Zhang, L.; Ji, X.; Ren, X.; Luo, Y.; Shi, X.; Asiri, A. M.; Zheng, B.; Sun, X. Efficient Electrochemical N2 Reduction to NH3 on MoN Nanosheets Array under Ambient Conditions. *ACS Sustainable Chem. Eng.* **2018**, *6* (8), 9550–9554. https://doi.org/10.1021/acssuschemeng.8b01438.
(19) Liu, J.; Kong, X.; Zheng, L.; Guo, X.; Liu, X.; Shui, J. Rare Earth Single-Atom Catalysts for Nitrogen and Carbon Dioxide Reduction. *ACS Nano* **2020**, *14* (1), 1093–1101. https://doi.org/10.1021/acsnano.9b08835.
(20) Kresse, G.; Furthmüller, J. Efficiency of Ab-Initio Total Energy Calculations for Metals and Semiconductors Using a Plane-Wave Basis Set. *Computational materials science* **1996**, *6* (1), 15–50.
(21) Bucko, T.; Hafner, J.; Lebegue, S.; Angyán, J. G. Improved Description of the Structure of Molecular and Layered Crystals: Ab Initio DFT Calculations with van Der Waals Corrections. *The Journal of Physical Chemistry A* **2010**, *114* (43), 11814–11824.
(22) Hammer, B.; Hansen, L. B.; Nørskov, J. K. Improved Adsorption Energetics within Density-Functional Theory Using Revised Perdew-Burke-Ernzerhof Functionals. *Physical review B* **1999**, *59* (11), 7413.
(23) Perdew, J. P.; Burke, K.; Ernzerhof, M. Generalized Gradient Approximation Made Simple. *Physical review letters* **1996**, *77* (18), 3865.
(24) Kresse, G.; Joubert, D. From Ultrasoft Pseudopotentials to the Projector Augmented-Wave Method. *Physical review b* **1999**, *59* (3), 1758.
(25) Blöchl, P. E.; Jepsen, O.; Andersen, O. K. Improved Tetrahedron Method for Brillouin-Zone Integrations. *Physical Review B* **1994**, *49* (23), 16223.
(26) Grimme, S.; Ehrlich, S.; Goerigk, L. Effect of the Damping Function in Dispersion Corrected Density Functional Theory. *Journal of computational chemistry* **2011**, *32* (7), 1456–1465.
(27) Monkhorst, H. J.; Pack, J. D. Special Points for Brillouin-Zone Integrations. *Phys. Rev. B* **1976**, *13* (12), 5188–5192. https://doi.org/10.1103/PhysRevB.13.5188.
(28) Sheppard, D.; Xiao, P.; Chemelewski, W.; Johnson, D. D.; Henkelman, G. A Generalized Solid-State Nudged Elastic Band Method. *The Journal of chemical*

physics **2012**, *136* (7), 074103.
(29) Ghasemi, A.; Xiao, P.; Gao, W. Nudged Elastic Band Method for Solid-Solid Transition under Finite Deformation. *The Journal of Chemical Physics* **2019**, *151* (5), 054110.
(30) Xiao, P.; Sheppard, D.; Rogal, J.; Henkelman, G. Solid-State Dimer Method for Calculating Solid-Solid Phase Transitions. *The Journal of Chemical Physics* **2014**, *140* (17), 174104.
(31) Lu, X.; Roldan, A. Are Carbon-Based Materials Good Supports for the Catalytic Reforming of Ammonia? *The Journal of Physical Chemistry C* **2021**, *125* (29), 15950–15958.
(32) Gawande, M. B.; Fornasiero, P.; Zbořil, R. Carbon-Based Single-Atom Catalysts for Advanced Applications. *ACS Catalysis* **2020**, *10* (3), 2231–2259.
(33) Peng, Y.; Lu, B.; Chen, S. Carbon-Supported Single Atom Catalysts for Electrochemical Energy Conversion and Storage. *Advanced Materials* **2018**, *30* (48), 1801995.
(34) Rivera-Cárcamo, C.; Serp, P. Single Atom Catalysts on Carbon-Based Materials. *ChemCatChem* **2018**, *10* (22), 5058–5091.
(35) Fei, H.; Dong, J.; Feng, Y.; Allen, C. S.; Wan, C.; Volosskiy, B.; Li, M.; Zhao, Z.; Wang, Y.; Sun, H. General Synthesis and Definitive Structural Identification of MN 4 C 4 Single-Atom Catalysts with Tunable Electrocatalytic Activities. *Nature Catalysis* **2018**, *1* (1), 63–72.
(36) Zitolo, A.; Ranjbar-Sahraie, N.; Mineva, T.; Li, J.; Jia, Q.; Stamatin, S.; Harrington, G. F.; Lyth, S. M.; Krtil, P.; Mukerjee, S.; Fonda, E.; Jaouen, F. Identification of Catalytic Sites in Cobalt-Nitrogen-Carbon Materials for the Oxygen Reduction Reaction. *Nat Commun* **2017**, *8* (1), 957. https://doi.org/10.1038/s41467-017-01100-7.
(37) Long, J.; Fu, X.; Xiao, J. The Rational Design of Single-Atom Catalysts for Electrochemical Ammonia Synthesis via a Descriptor-Based Approach. *Journal of Materials Chemistry A* **2020**, *8* (33), 17078–17088.
(38) Lu, X.; Zhang, J.; Chen, W.-K.; Roldan, A. Kinetic and Mechanistic Analysis of NH 3 Decomposition on Ru (0001), Ru (111) and Ir (111) Surfaces. *Nanoscale Advances* **2021**, *3* (6), 1624–1632.
(39) Li, X.-K.; Ji, W.-J.; Zhao, J.; Wang, S.-J.; Au, C.-T. Ammonia Decomposition over Ru and Ni Catalysts Supported on Fumed SiO2, MCM-41, and SBA-15. *Journal of Catalysis* **2005**, *236* (2), 181–189.
(40) Qiu, J.-Z.; Hu, J.; Lan, J.; Wang, L.-F.; Fu, G.; Xiao, R.; Ge, B.; Jiang, J. Pure Siliceous Zeolite-Supported Ru Single-Atom Active Sites for Ammonia Synthesis. *Chemistry of Materials* **2019**, *31* (22), 9413–9421.

Chapter 7 Concluding Remarks and Future Research

7.1 Concluding Remarks

The effective nitrogen-based fuels' reforming needs high-performance and affordable catalysts, and they are critical for the clean and efficient utilization of fuels. This work mainly presents theoretical studies of transition metals, defective and doped graphene, and single-atom catalysts in terms of their electronic structures and catalytic performances. A research method based on the DFT to the mechanisms of ammonia reforming on defective and doped carbon materials, transition metals and SACs is developed, which can promote the novel catalytsts design. Especially the SACs, it is scarce report about the catalytic activity of ammonia reforming yet.

Combining computational and experimental techniques, the adsorption process of hydrazine and products of its decomposition on Ir(111) and IrO_2 surfaces were investigated. The results indicated that the strong molecular adsorptions on IrO_2 block the catalytic site and the electron density and density of states (DOS) of the hydrazine adsorbate system explained the N-N bond scission by the molecular orbital theory. Intermediate adsorptions were followed by the analysis of three catalytic mechanisms (intramolecular reaction between hydrazine, the intramolecular reaction between NH_2, and NH_2 assisted dehydrogenation). It is challenging to produce hydrogen ad-atoms by N-H bond breaking and perform recombination of hydrogen molecules at moderate temperatures because of the high activation barriers and reaction energies. Therefore, it can be understood from the calculations that at ambient conditions, the main products are NH_3 and N_2, as supported by experimental work, and that controlling the antibonding molecular orbital (π^*) occupation may lead to a more selective decomposition towards molecular hydrogen.

The catalytic activity of carbon materials was investigated by analyzing the NH_3 reforming mechanism on pristine and a series of point defects graphene (C-vacancy

and dopants). Vacancies (SV and DV) and doped (PN, PO, and GO) structures were identified to be potential catalysts by comparing the thermodynamic reaction pathways. The reforming rate-determining steps were found to be first dehydrogenation and the N and H recombination. These results imply that C-catalysts may be able to accelerate and tune the graphite catalytic activity, e.g., for high-efficient electrocatalysts. Batch reaction simulations indicated that although SV and GO can dehydrogenate NH_3, these sites will be poisoned respectively by N and H adatoms' strong interactions. A charge transfer of 0.37 e^- from the N-H bond to the SV triggered the NH_3 activation. The study demonstrated that the carbon-based materials are long-term inert supports for the catalytic NH_3 reforming even in the presence of defects.

Mechanistic investigations of NH_3 reforming on noble metals (hcp Ru, fcc Ru, and fcc Ir) and non-noble metals (hcp and fcc Co, bcc and fcc Fe and fcc Ni) were carried out using DFT-D3. Compared with noble metals (Ir and Ru), the combination of decomposition species with the non-noble metal surfaces is weaker but the adsorption of N_2 and H_2 are stronger, implying that the NH_3 decomposition catalytic activity of noble metals should be better. The simulated TPD also proved to be useful in assessing the importance of N coverage on the model, i.e. the desorption shifts to lower temperatures with increasing N's coverage. Moreover, TPD experiment showed that Co and Ni are more suitable to be low-cost candidates for the ammonia catalytic decomposition than Fe. Batch reaction simulations described the reaction processes along the temperature and time and indicated that Ru(111) produces H_2 at a lower temperature than Ru(0001). On Ir(111) surface, the dehydrogenation starts at higher temperatures than on Ru, but the desorption of N_2 takes place at a lower temperature. For non-noble metals, although Co(111) has seen a broader H_2 production range, the temperature of the fastest H_2 production on Co(0001) is around 100 K lower than on Co(111). And Ni(111) has the lowest temperature of the fastest H_2 production (~625 K). The comparison between these results and experiments demonstrates that microkinetic simulations based on DFT results are a useful tool to investigate heterogeneous catalytic reactions and design novel catalysts.

The single transition metal atoms supported on clean and nitrogen-modified graphene were simulated as MN_3, MN_4, MC_3 and MC_4 (M= Fe, Co, Ni, Ir, Ru, Rh and Zn). The results show that nitrogen-modified graphene has a stronger combination with metal atoms than vacancy graphene, hence, providing high resistance to metal sintering and leaching. We investigated the NH_3 reforming reaction mechanism on SACs supported on N-modified graphene. The most favorable adsorption site of species is on top of the metal atom. The relative adsorption energies suggested that MN_3 structures are more active than MN_4. The process catalyzed by noble metals (Ir, Ru, Rh) is more favorable than non-noble metal SACs. The free energies of molecules and adsorbed species were calculated between 200 and 1000 K. The thermochemical analysis concluded that IrN_3, RuN_3 and RhN_3 are potential catalyst for the NH_3 reforming, and that the recombination reaction of N is generally the rate-determining step of the ammonia reforming, but not on the RhN_3, where the stepwise dehydrogenation reactions of ammonia control the overall reaction rate. We implemented the free energies in microkinetic models to simulate the temperature programmed desorption and batch reactors. The TPS simulations showed that compared with Ru, the N_2 desorption on Ru SACs shifted to the low-temperature region. Batch reaction simulations explored the catalytic performance and mechanism of SACs on NH_3 reforming and supply a detailed understanding of its practical operation for the experiment.

This work aims at improving the understanding of the structure and catalytic behaviors of these materials and exploring their applications in hydrogen energy, which contributes to the construction of a net-zero global society.

7.2 Future Research

Like all scientific studies, this study has limitations and needs future work to improve it. In the investigation about NH_3 reforming, only intramolecular decomposition pathway was considered by transition state theory without the diffusion processes. However, the intermolecular reaction pathway may result in by-products and high

diffusion energy barriers may also affect the microkinetic simulation, moreover, the transition state theory also has its own fundamental flaw. In addition, the adsorption energies of intermediates are significantly affected by the coverage rate according to the TPD research. Therefore, to construct more accurate microkinetic model, it is important to consider the intermolecular reaction pathway, diffusion effect, and coverage effect in the future work. Meanwhile, the theoretical study of alloy materials and the exploration of general descriptor for the SACs are meaningful to the development of novel NH_3 reforming catalysts.

Appendix

Appendix A: Chapter 3 Supporting Information

Content:

1. Bulk structure of Ir(111)
2. Adsorption structures on IrO_2
3. The density of states (DOS) and projected density of state (PDOS) of hydrazine
4. Electron distribution of gas-phase and adsorbate hydrazine
5. Vibration modes of transition states
6. Vibration modes of ammonia and hydrazine
7. Reference

1. Bulk structure of Ir(111)

We have created a perfect Ir (111) surface, which is the close-packed plane of the fcc structure and is the most stable iridium surface (Figure S3-1). The Iridium atoms in the surface model are arranged in a hexagonal lattice with a separation of 0.701 Å between nearest-neighbor atoms, and there are four main adsorption positions: top, fcc site, hcp site, and bridge.

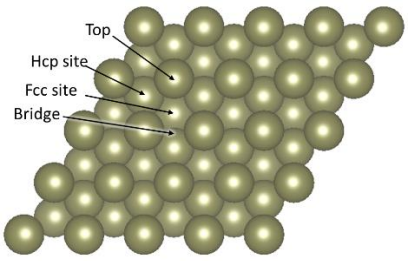

Figure S3-1. The simulation perfect Ir(111) surface

Gauche is the most stable structure among the three dominant conformations of hydrazine (gauche, trans, and eclipsed). As shown in Figure S3-2, the optimized bond length of N-N and N-H in the hydrazine is 1.450 Å and 1.020 Å, respectively. A similar

structure is used in many pieces of research.[1-4]

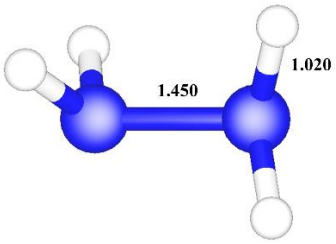

Figure S3-2. The optimized structure of hydrazine

2. Species adsorption on IrO_2

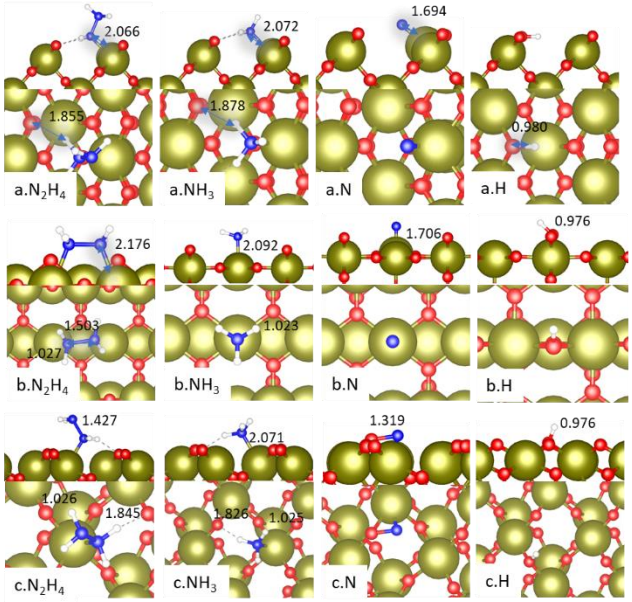

	IrO_2(101)	IrO_2(110)	IrO_2(100)	IrO_2(001)	IrO_2(111)
γ_{hkl} (J/m^2)	1.46	1.82	2.34	2.74	2.83
N_2H_4	-2.35	-3.24	-2.81	-	-
NH_3	-2.02	-2.46	-2.69	-	-
N	-3.16	-3.65	-3.92	-	-
H	-3.13	-3.57	-3.46	-	-

Figure S3- 3. Surface energies of the most stable IrO_2 terminations and schematic representation of the most favorable adsorption geometries.

3. The density of states (DOS) and projected density of state (PDOS) of hydrazine

The density of states (DOS) is defined by the equation:

$$DOS(E)dE = \ number\ of\ levels\ between\ E\ and\ E + dE$$

The band structure of the surface determines the DOS curve's shape. Notably, the

integral of DOS up to the Fermi level is the total *number* of occupied molecule orbitals. When this number is timed by two, it is the number of valence electrons. Hence, the DOS patterns also plot the distribution of electrons in energy.[5]

The decomposition of the gauche N_2H_4 DOS is shown in Figure S3-4, which can help us to trace down the bonding in the chemisorbed N_2H_4 system. It can be seen that 2p orbital of nitrogen and 1s orbital of hydrogen form the bonding orbital π_1 and π_2, while the antibonding orbital π^* was mainly contributed by the 2p orbital of nitrogen atoms. When the antibonding orbital π^* was been partly filled, the overlap of nitrogen 2p orbitals decreased, and π bond between the nitrogen was weakened.

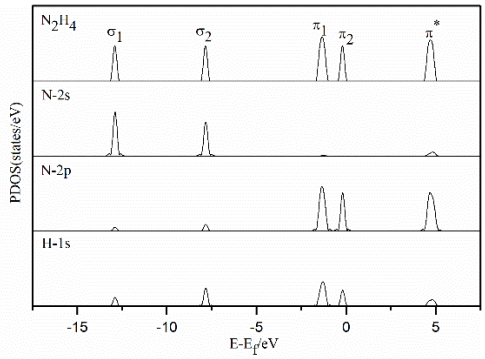

Figure S3-4. Projected density of states of the orbital of N and H in the hydrazine

4. Electron distribution of gas-phase and adsorbate hydrazine

The Bader charge analysis is employed to characterize the electron distribution of gas-phase and adsorbate hydrazine. Table S3-1 shows the details of the total valence electron in gas and adsorbed hydrazine. It suggests that 0.6 electrons transfer from the hydrazine molecule to the surface, which is mainly contributed by the hydrogen in the molecule.

Table S3-1. The number of electrons in the gas phase and adsorbate N_2H_4

Atom	Gas-phase N_2H_4	Adsorbate N_2H_4
N1	5.81	5.76
N2	5.79	5.78
H1	0.59	0.47
H2	0.60	0.44
H3	0.59	0.47
H4	0.59	0.45
sum	13.97	13.37

5. Vibration modes of transition states

We have obtained the vibrational modes of every imaginary frequency, which is along the reaction direction, Table S3-2. Nearly all imaginary vibrations of dehydrogenation are N-H stretching except NNH*, which is due to N-H bending, and for the N-N split pathway, the imaginary vibrations are along with N-N stretching.

Table S3-2. The imaginary frequency and vibrational mode of transition states in the decomposition of N_2H_4

Reaction	Imaginary frequency(cm^{-1})	Vibrational mode
N_2H_4*↔N_2H_3*+H*	956.9	N-H stretching
N_2H_3*↔NNH_2*+H*	482.8	N-H stretching
N_2H_3*↔HNNH*+H*	1126.8	N-H stretching
HNNH*↔ NNH* + H*	1115.8	N-H stretching
NNH_2*↔NNH* + H*	386.1	N-H stretching
NNH*↔ N_2* + H*	910.2	N-H bending
N_2H_4*↔2NH_2*	154.3	N-N stretching
N_2H_3*↔NH_2*+NH*	356.9	N -N stretching
NNH_2*↔NH_2* + N*	398.7	N -N stretching
NHNH*↔ 2NH*	549.7	N -N stretching
NNH*↔ NH* + N*	571.9	N -N stretching
N_2H_4* + NH_2* ↔ N_2H_3* + NH_3*	335.8	N-H stretching
N_2H_3* + NH_2* ↔ HNNH* + NH_3*	268.3	N-H stretching
HNNH* + NH_2* ↔ NNH* + NH_3*	322.9	N-H stretching
N_2H_3* + NH_2* ↔ NNH_2* +NH_3*	252.5	N-H stretching
NNH_2* + NH_2* ↔ NNH* +NH_3*	654.9	N-H stretching
NNH* + NH_2* ↔ N_2* + NH_3*	1291.0	N-H stretching
NH_3* ↔ NH_2* + H*	1229.5	N-H stretching
NH_2* ↔ NH* + H*	1274.3	N-H stretching
NH* ↔ N* + H*	1154.5	N-H stretching
2NH_2* ↔ NH* + NH_3*	124.1	N-H stretching
NH* + NH_2* ↔ N* + NH_3*	213.9	N-H stretching
2N* ↔ N_2*	568.3	N-N stretching
2H* ↔ H_2*	271.1	H-H stretching

6. Vibration modes of ammonia and hydrazine

Figure S3-5 and Figure S3-6 show 12 vibration modes of hydrazine, six vibration modes of ammonia, and corresponding vibrational frequencies. Our calculation results are in line with experimental research.[6-10]

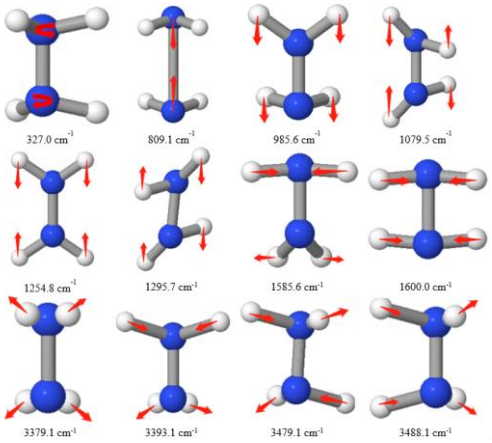

Figure S3-5. Vibrational mode and frequency of the isolate hydrazine molecule

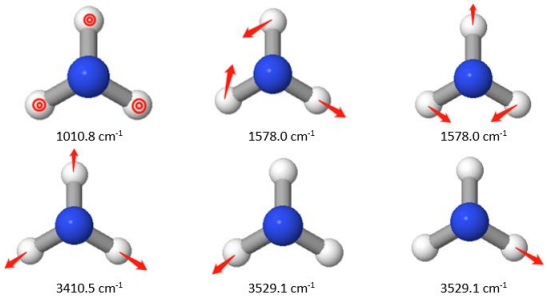

Figure S3-6. Vibrational mode and frequency of the isolate ammonia molecule

Reference

1. Agusta, M. K.; Kasai, H., First principles investigations of hydrazine adsorption conformations on Ni(111) surface. *Surface Science* **2012,** *606* (7-8), 766-771.
2. Deng, Z.; Lu, X.; Wen, Z.; Wei, S.; Liu, Y.; Fu, D.; Zhao, L.; Guo, W., Mechanistic insight into the hydrazine decomposition on Rh(111): effect of reaction intermediate on catalytic activity. *Phys Chem Chem Phys* **2013,** *15* (38), 16172-82.
3. Tafreshi, S. S.; Roldan, A.; Dzade, N. Y.; de Leeuw, N. H., Adsorption of hydrazine on the perfect and defective copper (111) surface: a dispersion-corrected DFT study. *Surface Science* **2014,** *622*, 1-8.
4. Zhang, P.-X.; Wang, Y.-G.; Huang, Y.-Q.; Zhang, T.; Wu, G.-S.; Li, J., Density functional theory investigations on the catalytic mechanisms of hydrazine decompositions on Ir(111). *Catalysis Today* **2011,** *165* (1), 80-88.
5. Hoffmann, R., A chemical and theoretical way to look at bonding on surfaces. *Reviews of modern Physics* **1988,** *60* (3), 601.

6. Shimanouchi, T., Tables of molecular vibrational frequencies. Consolidated volume II. *Journal of physical and chemical reference data* **1977,** *6* (3), 993-1102.
7. Koops, T.; Visser, T.; Smit, W., Measurement and interpretation of the absolute infrared intensities of NH3 and ND3. *Journal of Molecular Structure* **1983,** *96* (3-4), 203-218.
8. Yamaguchi, A.; Ichishima, I.; Shimanouchi, T.; Mizushima, S.-I., Far infra-red spectrum of hydrazine. *Spectrochimica Acta* **1960,** *16* (11-12), 1471-1485.
9. Durig, J.; Griffin, M.; Macnamee, R., Raman spectra of gases. XV: Hydrazine and hydrazine - d4. *Journal of Raman Spectroscopy* **1975,** *3* (2 - 3), 133-141.
10. Gurvich, L. V.; Veyts, I.; Alcock, C. B., *Thermodynamic Properties of Individual Substances: Elements O, H (D, T), F, Cl, Br, I, He, Ne, Ar, Kr, Xe, Rn, S, N, P and their compounds. pt. 1. Methods and computation. pt. 2. Tables*. Hemisphere: 1989; Vol. 1.

Appendix B: Chapter 4 Supporting Information

1. Adsorption structures

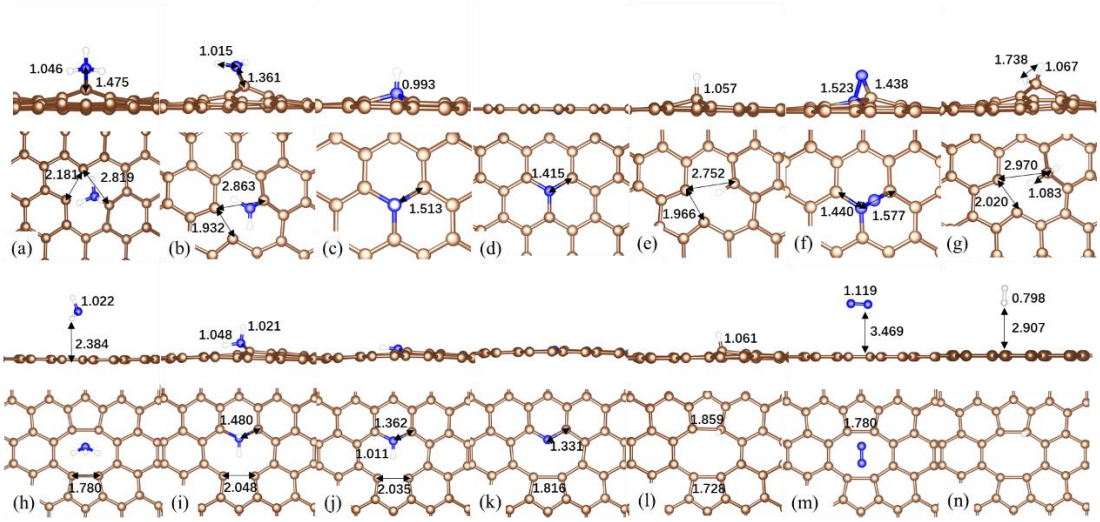

Figure S4-1. NH_x(x=1-3), N, H, N_2 and H_2 species on SV and DV. (a-g and h-n are surface species on SV and DV respectively. The unit of length is Å. Blue spheres represent N atoms, white is hydrogen and C is the khaki sphere.

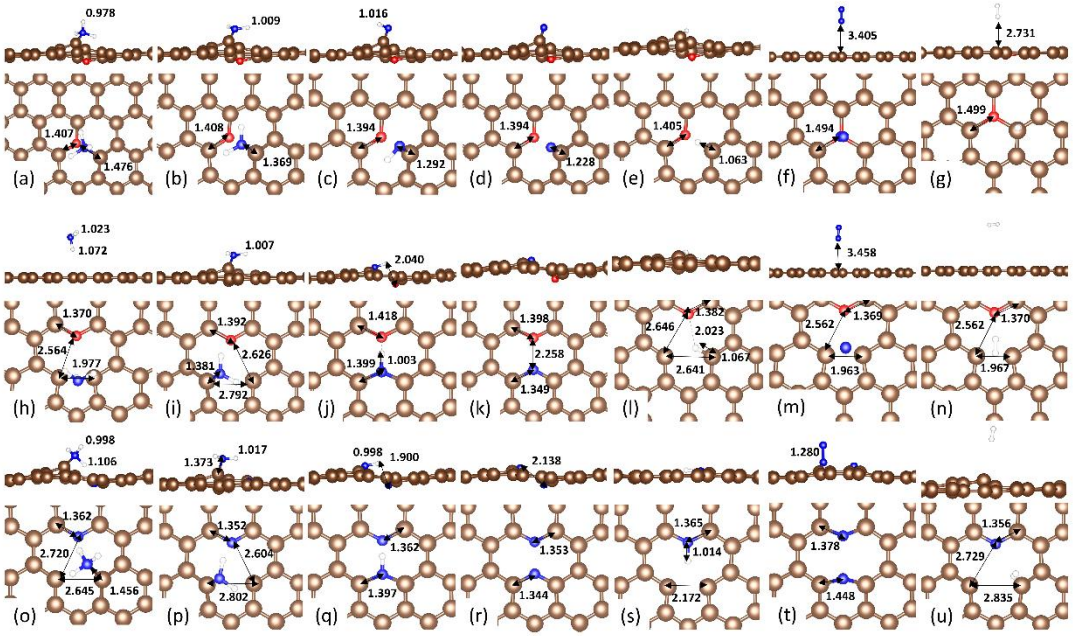

Figure S4-2. NH_x(x=1-3), N, H, N_2, and H_2 species on GO, PO, and PN. (a-g, h-n, and o-u are surface species on GO, PO, and PN respectively. The unit of length is Å. Blue spheres represent N atoms, white is hydrogen and C is the khaki sphere.

2. Charge distribution

The pz orbital (-3~3 eV) partial charge distribution of surfaces (Figure S4-3) is employed to describe the formation of π system. The overlap of pz orbital on the surface means the formation of π system. The introduction of vacancy and dopant create bumps or interrupts of pz orbital charge distribtution and damage the stability of π system.

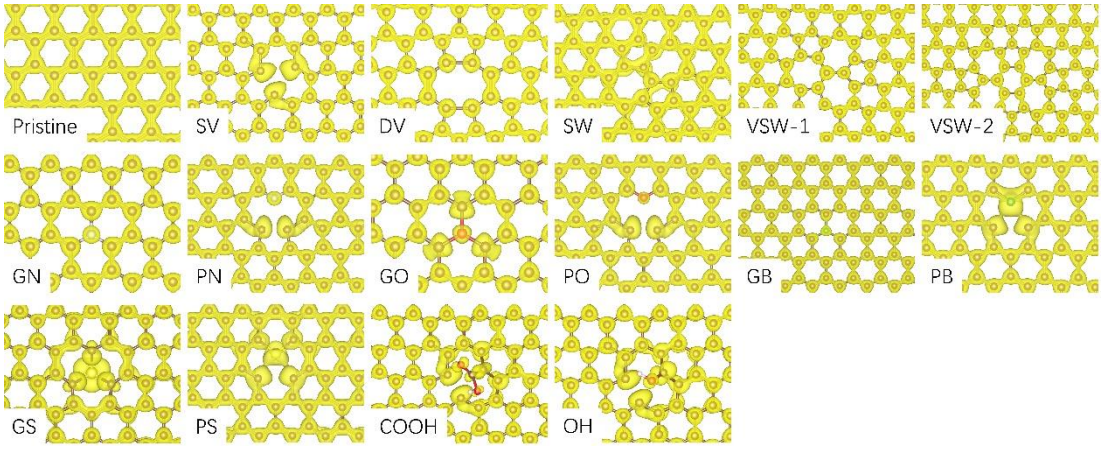

Figure S4-3. The pz orbital (-3~3 eV) partial charge distribution of surfaces.

3. Thermodynamic calculation

Calculation of thermodynamic properties and quantities (entropy, enthalpy, and free energy, etc.) under a series temperature is the first step to constructing a kinetic model. We programmed python and matlab scripts to achieve the calculation of thermodynamic properties and quantities, as the flow diagram *Figure S4-4* below, furthermore, the calculations at high temperature were extrapolated from the optimized data at 0K. In the scripts, the temperature and time step of the numerical integration is 10K and 1s, respectively.

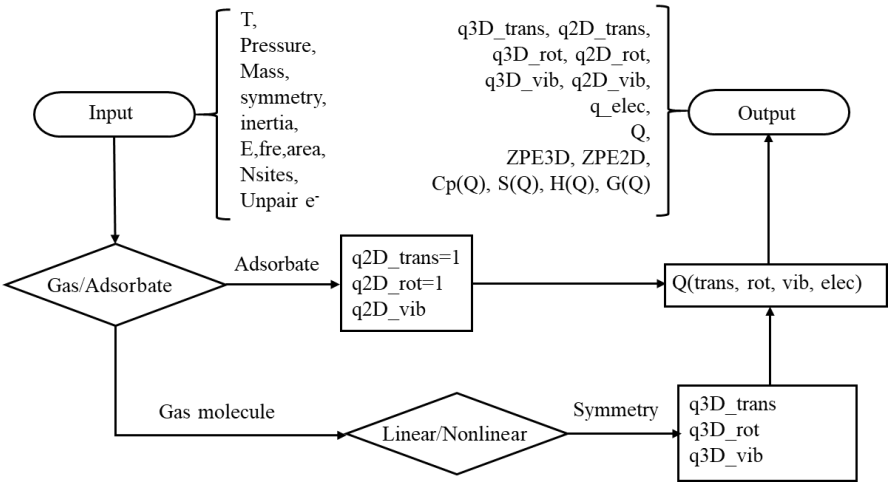

Figure S4-4. The flow diagram of thermodynamic calculation

To improve the accuracy of the energy, the zero-point energies (*ZPE*) are used to correct the static DFT electronic energy. *ZPE* refers to the vibrational energies that exist even at 0 K and is calculated as Eq S4-1 where v_i accounts for the vibrational modes of the species.

$$ZPE = \sum_{i}^{n} \frac{1}{2} h v_i \qquad \text{Eq S4-1}$$

The temperature effect on adsorption energy (E_{ads}), reaction energy (E_r), activation energy (E_a) is taken into account to obtain more accurate results. The global partition function, Q, is used to depict the energy as a function of temperature for the intermediates on the surface or in the gas phase, and the basic thermodynamic characters such as entropy (S), specific heat at constant pressure (C_p) and enthalpy (H) can be derived by Q as the following equations:

$$S = klnQ + kT\left(\frac{\partial lnQ}{\partial T}\right)_V \qquad \text{Eq S4-2}$$

$$C_p = T\left(\frac{\partial S}{\partial T}\right)_P \qquad \text{Eq S4-3}$$

$$H = E_{DFT} + E_{(S=0,T=0,ZPE)} + \int_0^T C_p \, \partial T \qquad \text{Eq S4-4}$$

$$G = H - TS \qquad \text{Eq S4-5}$$

Where k is Boltzmann constant, T is the temperature. The global partition function is calculated as Eq S4-6.

$$Q = q_{translational} \times q_{rotational} \times q_{vibrational} \times q_{electronic} \times q_{nuclear} \quad \text{Eq S4-6}$$

Translational, rotational, vibrational, electronic and nuclear contributions are considered. Normally, the electronic systems are in a single electronic state, and the nuclear partition functions are unity, i.e. $q_{electronic}$, $q_{nuclear}$ equal constant 1. The vibrational partition function of a system is obtained via Eq S4-7,

$$q_{vib} = \prod_{i=1}^{N} \frac{1}{1 - e^{-hv_i/k_BT}} \quad \text{Eq S4-7}$$

Where i is a specific vibrational mode and N is the number of vibrations. The vibrational partition function in the gas phase, q_{vib}^{gas}, is also calculated using the equation above for $3N_i$-6 and $3N_i$-5 vibrational degrees of freedom of a non-linear and linear molecule in the gas phase, respectively, where N_i is the number of atoms in the molecule. The 2D-translational partition function for a free molecule is derived by the Eq S4-8.

$$q_{translation}^{2D}(A,T) = \left(\frac{2\pi m k_B T}{h^2}\right) A_{cat} \quad \text{Eq S4-8}$$

Where A_{cat} is the average area of one active site on a catalyst.

The 3D-translational partition function for a molecule is calculated by the Eq S4-9, where $V_{(P,T)}$ is derived by $V_{(P,T)} = k_B T/p$, p is the pressure of the gas phase.

$$q_{trans}^{3D} = V_{(P,T)} \times \frac{(2\pi m k_B T)^{3/2}}{h^3} \quad \text{Eq S4-9}$$

The Rotational partition function for a free molecule is calculated using Eq S4-10 and Eq S4-11, depending on its symmetry and linear type.

$$q_{rot}^{linear} = \frac{\pi^{1/2}}{\sigma h}(I_{ZZ})^{1/2}(8\pi^2 k_B T)^{1/2} \quad \text{Eq S4-10}$$

$$q_{rot}^{nonlinear} = \frac{1}{\sigma}\left(\frac{8\pi^2 k_B T}{h^2}\right)^{3/2} \sqrt{\pi I_a I_b I_c} \quad \text{Eq S4-11}$$

Where σ is the symmetry factor and *I* is the moment of inertia defined as *Eq S4-12*,

$$I = \sum_i m_i r_i^2 \quad \text{Eq S4-12}$$

Where the sum is over the atoms in the molecule, m_i is the mass of atom and r_i is its distance from the rotation axis.

The thermodynamic properties in our system were calculated according to the above equations. To evaluate the accuracy of our method, a comparison between calculated and standard thermodynamic properties of NH_3, N_2, H_2 was carried out. The reference properties are from the NIST database and Thermochemical Data of Pure Substances. contains the data we used in the thermodynamic calculations, including the gas pressure, the electronic energy, the moment of inertia and vibration frequency from VASP calculation and the mass and symmetry of molecules.

Species	Energy(eV)	Vibration(cm^{-1})	Mass(kg)	Pressure(Pa)	Symmetry(σ)	Inertia($kg*m^2$)
H_2	-7.047	4360.85	3.35×10^{-27}	101325	2	2.35×10^{-48}
N_2	-17.0944	2006.95	4.65×10^{-26}	101325	2	7.82×10^{-47}
NH_3	-20.0541	3504.75,3503.83, 3372.67,1633.87, 1633.20,1035.29	2.83×10^{-26}	101325	3	3.51×10^{-140}

Figure S4-5, Figure S4-6 and Figure S4-7 show both the calculated and reference thermodynamic data between 300-1000K. According to the Gibbs energy calculated, the delta Gibbs energy of ammonia synthesis reaction was given. The delta Gibbs energy of calculation is corrected by experimental formation enthalpy of ammonia and pure gas, which is -45.94 kJ mol^{-1} and 0 kJ mol^{-1}. Since the absolute values of the delta Gibbs energy are small at 400 and 500K, the errors turned a little bit. Generally, our method based on VASP optimized results to calculate thermodynamic properties was proved accurately.

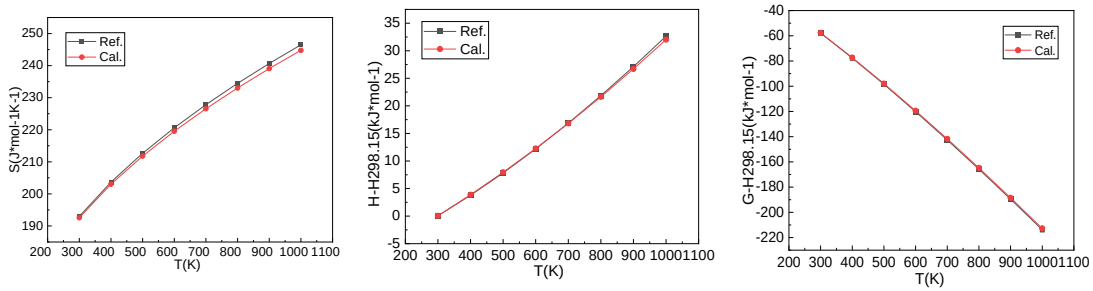

Figure S4-5. Calculated thermodynamic properties of gas phase NH_3 compared with reference data from 300-1000 K

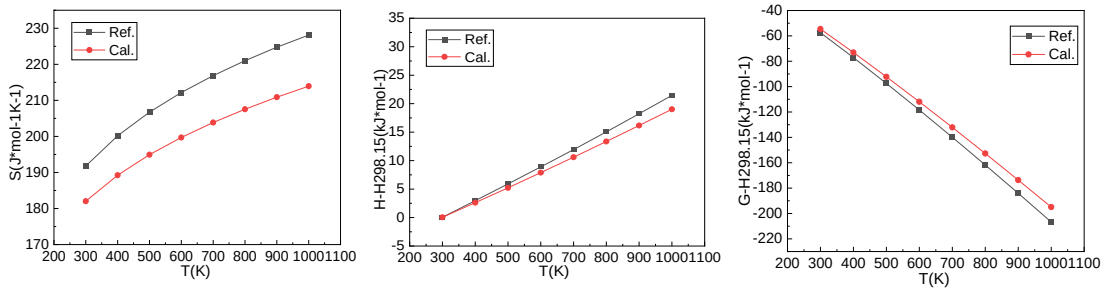

Figure S4-6. Calculated thermodynamic properties of gas phase N_2 compared with reference data from 300-1000 K

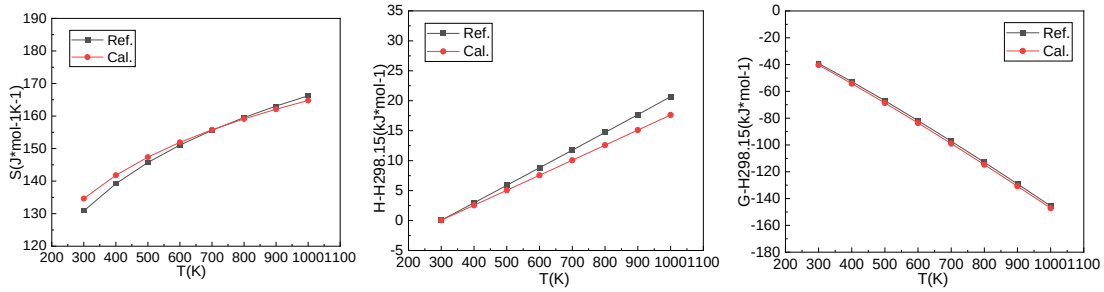

Figure S4-7. Calculated thermodynamic properties of gas phase H_2 compared with

reference data from 300-1000 K

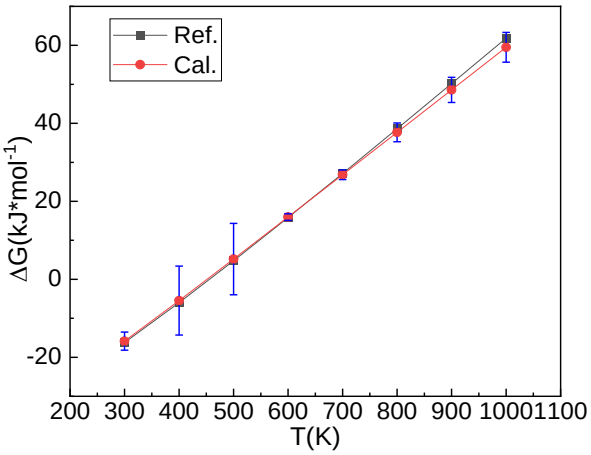

Figure S4-8. The delta Gibbs energy of ammonia synthesis reaction with error bar. The error was calculated by $(G_{cal} - G_{reference})/G_{reference} * 100$.

4. Equilibrium constant and Reaction rate constant calculations

A script reading the partition functions, thermodynamic properties was implemented to calculate the equilibrium constant and reaction rate constant of all elementary steps. Figure S4-9 shows the process of the script. In the scripts, the temperature and time step of the numerical integration is 10K and 1s, respectively.

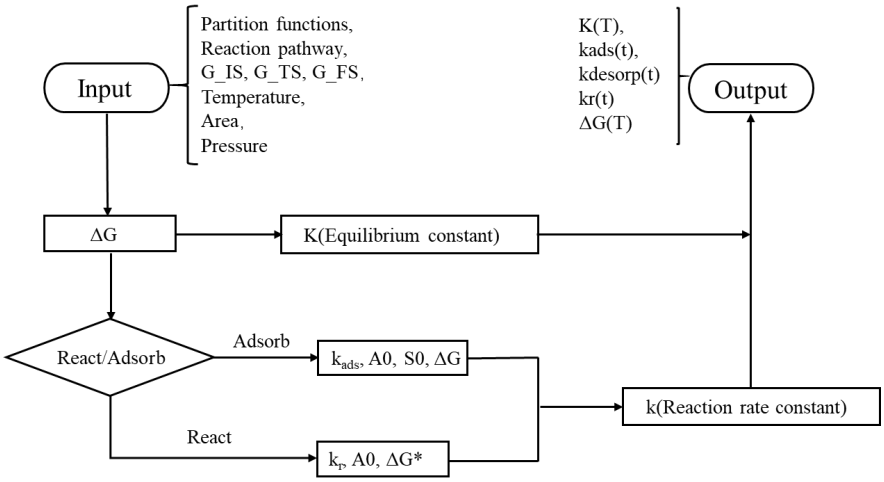

Figure S4-9. The flow diagram of reaction rate constant and equilibrium constant calculation

The barrier energy of adsorption and desorption processes are calculated by Eq S4-13, Eq S4-14 and Eq S4-15:

$$E_a^{ads} = E_{ts} - E_{gas} - E_{surf} \quad \text{Eq S4-13}$$

$$E_a^{des} = E_{ts} - E_{ads} \quad \text{Eq S4-14}$$

$$E_{ts} = E_{gas} + E_{surf} + \left(ZPE_{2D}^{gas} - ZPE_{3D}^{gas}\right) \quad \text{Eq S4-15}$$

The adsorption energy is calculated by Eq S4-16:

$$E_r = E_{gas} + E_{surf} - E_{ads} \quad \text{Eq S4-16}$$

The classical Hertz-Knudsen equation was employed to estimate the rate of

adsorption, as following Eq S4-17 to Eq S4-18.

$$Q_{reactants} = \left(q_{trans2D}^{ads} \times Q_{notrans3D}^{gas}\right)^{(stoichio_{ads})} \times Q_{surf}^{(stoichio_{surf})} \quad \text{Eq S4-17}$$

$$Q_{ts} = \left(q_{vib2D}^{ads}\right)^{(stoichio_{ads})} \times Q_{surf}^{(stoichio_{surf})} \quad \text{Eq S4-18}$$

$$Q_{reactants} = \left(Q_{3D}^{ads}\right)^{stoichio_{ads}} \quad \text{Eq S4-19}$$

$$Sticky_{ads} = \frac{Q_{ts}}{Q_{reactants}} \times e^{-\frac{E_a^{ads}}{k_B T}} \quad \text{Eq S4-20}$$

$$Sticky_{des} = \frac{Q_{ts}}{Q_{products}} \times e^{-\frac{E_a^{ads}}{k_B T}} \quad \text{Eq S4-21}$$

$$A_0 = areaS \times \frac{1}{(2\pi Mass \times k_B T)^{0.5}} \quad \text{Eq S4-22}$$

$$k_{ads/des} = A_0 \times Sticky_{ads/des} \quad \text{Eq S4-23}$$

Where A_0 is the pre-exponential factor. The sticking coefficient, *Sticky*, is a measure of the fraction of incident molecules which adsorb upon the surface and is calculated via Eq S4-20 and Eq S4-21.

As for the surface reactions in the heterogeneous catalytic system, which is considered in our research, the rate constant (k) of each surface elementary step is commonly computed using the transition state theory (TST) approximation of Eyring and Evans and Polanyi, as follows:

$$k_r = A_0 e^{-\frac{\Delta G^*}{k_B T}} = \frac{k_B T}{h} \frac{q_{TS}}{q_{IS}} e^{-\frac{\Delta G^*}{k_B T}} \quad \text{Eq S4-24}$$

Where h is the Planck constant, k_B is the Boltzmann constant, T is the temperature, A_0 is the pre-exponential factor, ΔG* is the reaction activation energy, and q_{TS} and q_{IS} are the partition functions of reactants and transition states respectively. The translations and rotations of the adsorbed species are frustrated on the surface and therefore we considered only vibrational modes.

We have considered an active site as a hexagonal site where the reactants and products in every elementary step occupy only one site on the surface. Consequently, the coverage of free sites, $\theta_*(t)$, is defined by:

$$\theta_*(t) = 1 - \sum_i^n \theta_i(t) \quad \text{Eq S4-25}$$

Where the $\theta_i(t)$ represents the coverage of the intermediates present in the reaction system.

The adsorption and first dehydrogenation of NH_3 are highly exothermic and the desorbed hydrogen and nitrogen molecules are assumed to leave from the surface immediately, therefore, the dissociated adsorption model is applied in the adsorption and desorption process of molecules. All the elementary steps in the ammonia decomposition and their rate equations are listed below.

Table S4-3. Elementary steps in the ammonia decomposition

No	Reaction	Rate equation
A1	$NH_3 + * \longrightarrow NH_3^*$	$r_{a1} = k_{a1} Y_{NH_3}(t)\theta_*(t)$
D1	$NH_3^* \longrightarrow NH_3 + *$	$r_{d1} = k_{d1}\theta_{NH_3}(t)$
R1	$NH_3^* + * \longrightarrow NH_2^* + H^*$	$r_{r1} = k_{r1}\theta_{NH_3}(t)\theta_*(t)$
R2	$NH_2^* + H^* \longrightarrow NH_3^* + *$	$r_{r2} = k_{r2}\theta_{NH_2}(t)\theta_H(t)$
R3	$NH_2^* + * \longrightarrow NH^* + H^*$	$r_{r3} = k_{r3}\theta_{NH_2}(t)\theta_*(t)$
R4	$NH^* + H^* \longrightarrow NH_2^* + *$	$r_{r4} = k_{r4}\theta_{NH}(t)\theta_H(t)$
R5	$NH^* + * \longrightarrow N^* + H^*$	$r_{r5} = k_{r5}\theta_{NH}(t)\theta_*(t)$
R6	$N^* + H^* \longrightarrow NH^* + *$	$r_{r6} = k_{r6}\theta_N(t)\theta_H(t)$
R7	$2N^* \longrightarrow N_2^* + *$	$r_{r7} = k_{r7}\theta_N^2(t)$
R8	$N_2^* + * \longrightarrow 2N^*$	$r_{r8} = k_{r8}\theta_{N_2}(t)\theta_*(t)$
D2	$N_2^* \longrightarrow N_2 + *$	$r_{d2} = k_{d2}\theta_{N_2}(t)$
A2	$N_2 + * \longrightarrow N_2^*$	$r_{a2} = k_{a2} Y_{N_2}(t)\theta_*(t)$
R9	$2H^* \longrightarrow H_2^* + *$	$r_{r9} = k_{r9}\theta_H^2(t)$
R10	$H_2^* + * \longrightarrow 2H^*$	$r_{r10} = k_{r10}\theta_{H_2}(t)\theta_*(t)$
D3	$H_2^* \longrightarrow H_2 + *$	$r_{d3} = k_{d3}\theta_{H_2}(t)$
A3	$H_2 + * \longrightarrow H_2^*$	$r_{a3} = k_{a3} Y_{H_2}(t)\theta_*(t)$

Where $Y_{molecule}(t)$ is the time-dependent ratio of the molecule and free sites.

Differential equations in the TPD simulation of hydrogen and nitrogen

Temperature programmed reaction model start from pre-adsorbed NH_3, the temperature increases at a different rate from 200 to 1000 K while any gas was extracted to avoid the re-adsorption of gases. It is applied to examine the adsorption properties of N_2 and H_2 over different surfaces in our research.

Differential equations in the reactor simulation

A batch reactor model under a variety of conditions is employed to investigate the catalytic properties when the metallic surface is in contact with a given pressure of NH_3.

The initial parameter is input into the program by the command: Y_{NH3}, Y_{N2}, Y_{H2}, θ_{NH_3}, θ_{N_2}, θ_{H_2}, θ_{NH_2}, θ_{NH}, θ_N, θ_H, θ_* = [a,0,0,0,0,0,0,1]

Table S4-4. The reaction rate of ammonia decomposition on SV and DV. * refers the active sites on the surfaces. (k in s^{-1} are kinetic rate constants of the reaction under 300 K and A in s^{-1} is the pre-exponential factor)

No	SV		DV	
	A	k	A	k
A1	9.94×10^{8}	1.52×10^{2}	1.00×10^{9}	3.74×10^{2}
D1	2.78×10^{-16}	2.76×10^{-7}	1.00×10^{9}	1.64×10^{6}
R1	1.73×10^{12}	3.44×10^{12}	7.97×10^{10}	3.64×10^{-53}

R2	5.33×10^{12}	8.32×10^{-28}	8.93×10^{12}	1.98×10^{-52}
R3	1.64×10^{12}	1.96	1.03×10^{13}	2.12×10^{14}
R4	8.06×10^{12}	5.64×10^{-77}	1.11×10^{13}	1.5×10^{-12}
R5	4.36×10^{12}	1.76×10^{-2}	8.52×10^{12}	2.9×10^{3}
R6	1.01×10^{13}	5.99×10^{-67}	9.07×10^{12}	1.97×10^{19}
R7	7.89×10^{13}	5.50×10^{-69}	2.25×10^{12}	2.79×10^{-37}
R8	7.36×10^{13}	1.33×10^{-50}	1.01×10^{9}	8.87×10^{-53}
D3	9.88×10^{8}	7.21×10^{-23}	9.95×10^{8}	1.06×10^{5}
A3	9.88×10^{8}	3.97×10^{4}	9.95×10^{8}	9.75×10^{4}
R9	1.59×10^{13}	1.52×10^{-25}	6.54×10^{12}	2.19×10^{-11}
R10	1.67×10^{13}	4.30×10^{-18}	1.82×10^{11}	3.62×10^{-28}
D2	1.00×10^{9}	2.80×10^{-26}	1.01×10^{9}	5.29×10^{7}
A2	1.00×10^{9}	2.32×10^{3}	1.01×10^{9}	5.70×10^{3}

Table S4-5. The reaction rate of ammonia decomposition on GO, PO and PN. * refers the active sites on the surfaces. (k in s^{-1} are kinetic rate of the reaction under 300 K and A in s^{-1} is the pre-exponential factor)

No	GO		PO		PN	
	A	k	A	k	A	k
A1	6.46×10^{8}	2.41×10^{2}	6.57×10^{8}	2.45×10^{2}	6.59×10^{8}	2.46×10^{2}
D1	6.46×10^{8}	6.96×10^{12}	6.57×10^{8}	$9.36E\times10^{5}$	6.59×10^{8}	6.61×10^{6}
R1	5.11×10^{12}	4.74×10^{-11}	1.79×10^{11}	4.65×10^{-43}	6.81×10^{11}	5.53×10^{-35}
R2	8.13×10^{12}	2.93×10^{-48}	5.82×10^{12}	7.23×10^{-45}	9.84×10^{12}	9.21×10^{-50}
R3	2.12×10^{12}	1.29×10^{-6}	1.36×10^{12}	3.30×10^{6}	6.11×10^{12}	1.32×10^{8}
R4	2.29×10^{12}	1.84×10^{-22}	2.93×10^{12}	8.91×10^{-40}	1.52×10^{13}	1.30×10^{-37}
R5	6.88×10^{12}	5.66×10^{-29}	5.88×10^{12}	7.51×10^{-15}	1.45×10^{13}	1.28×10^{-34}
R6	1.61×10^{12}	1.33×10^{-22}	2.52×10^{12}	6.86×10^{-13}	1.48×10^{13}	2.95×10^{-41}
R7	1.49×10^{13}	1.52×10^{-8}	4.00×10^{13}	2.49×10^{-22}	3.69×10^{13}	1.47×10^{-10}
R8	2.35×10^{10}	1.48×10^{-20}	1.35×10^{10}	2.75×10^{-39}	1.59×10^{13}	4.37×10^{-9}
D3	6.58×10^{8}	1.35×10^{7}	6.70×10^{8}	2.46×10^{6}	6.72×10^{8}	1.94×10^{9}
A3	6.58×10^{8}	3.72×10^{3}	6.70×10^{8}	3.78×10^{3}	6.72×10^{8}	3.79×10^{3}
R9	7.55×10^{12}	2.22×10^{-56}	7.95×10^{12}	6.10×10^{-70}	1.77×10^{13}	5.99×10^{-71}
R10	2.57×10^{11}	2.17×10^{-31}	7.89×10^{10}	7.13×10^{-32}	5.84×10^{12}	1.03×10^{-33}
D2	6.37×10^{8}	5.15×10^{8}	6.48×10^{8}	2.52×10^{9}	6.50×10^{8}	7.33×10^{21}
A2	6.37×10^{8}	6.25×10^{4}	6.48×10^{8}	6.35×10^{4}	6.50×10^{8}	6.37×10^{-4}

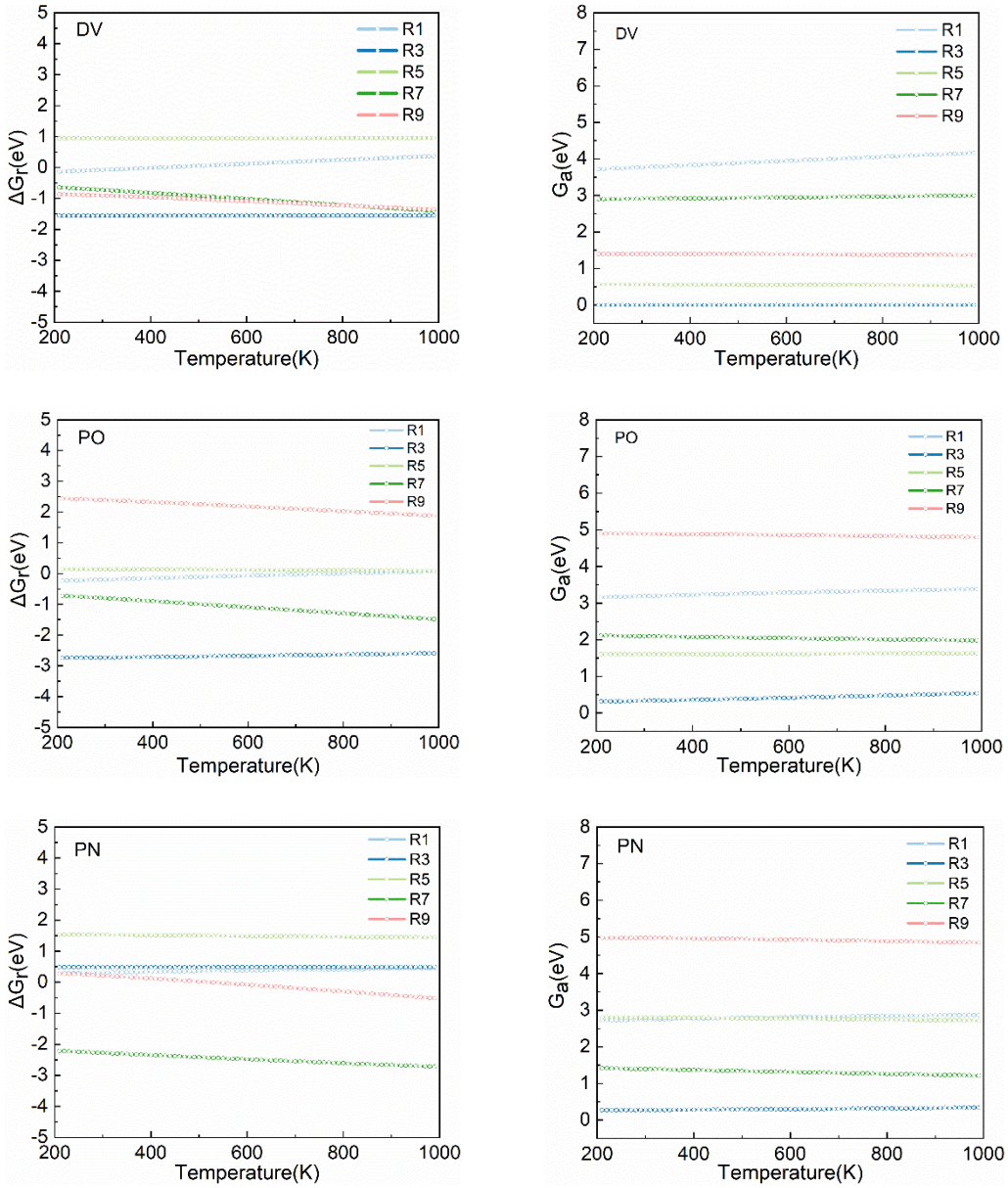

Figure S4-10. Free reaction (ΔG_r) and barrier (G_a) energies of the elementary steps in the ammonia dehydrogenation (R1, R3, R5) and molecular N_2 and H_2 formations (R7 and R9) on SV, DV, PO, GO, and PN as a function of the temperature.

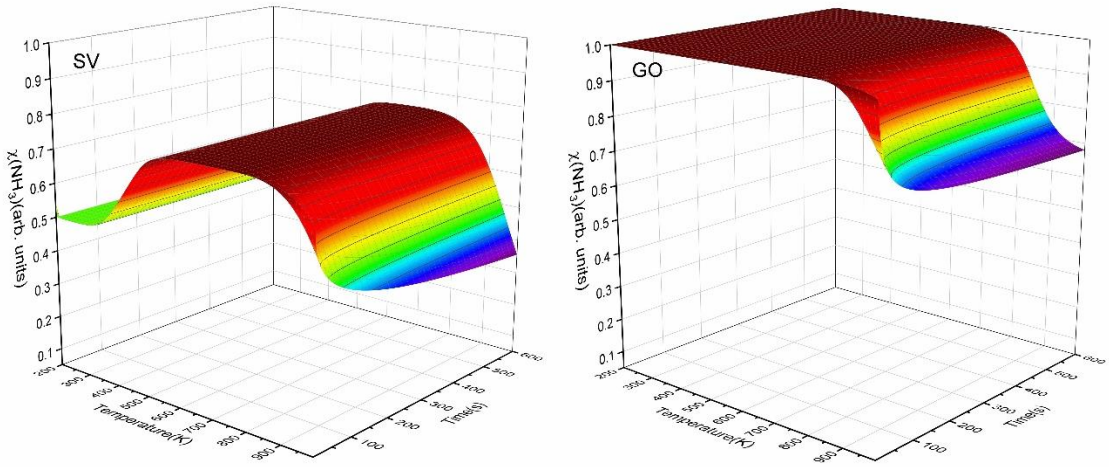

Figure S4-11. The relative concentration of molecular NH_3 as functions of the temperature and time on SV and GO batch reactor simulations. The initial ratio of NH_3: surface sites is 1:1. The color from dark to bright of the surface stands for the value form low to high.

Appendix C: Chapter 5 Supporting Information

Supporting Information

Ⅰ. Thermodynamic calculation

Calculation of thermodynamic properties (entropy, enthalpy and free energy) under a series temperature is the first step to construct a kinetic model. We programmed python scripts to achieve the calculation of partition functions and thermodynamic properties, as the flow diagram *Figure S4-4* below, furthermore, the properties at high temperature were extrapolated from the optimized data at 0K. In the scripts, the temperature and time step of the numerical integration is 10K and 1s, respectively.

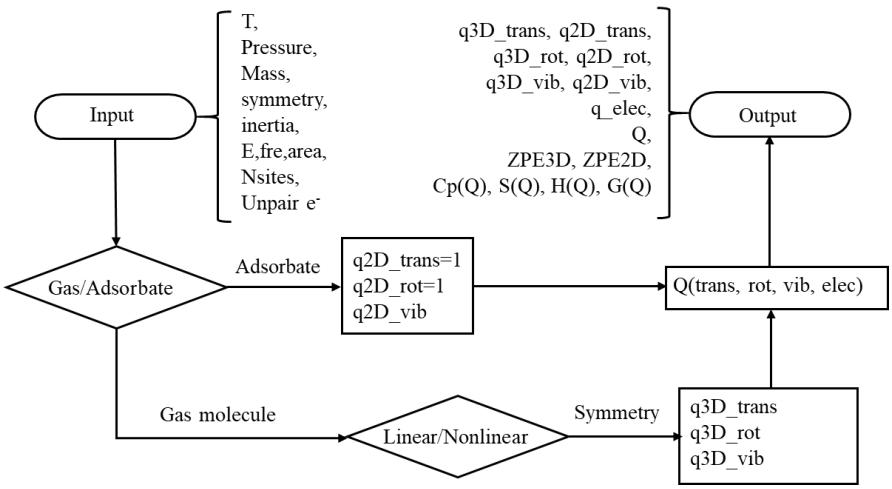

Figure S5-5. The flow diagram of thermodynamic calculation

To improve the accuracy of the energy, the zero-point energies (ZPE) are used to correct the static DFT electronic energy. ZPE refers to the vibrational energies that exist even at 0 K and is calculated as *Eq S4-1* where υ_i accounts for the vibrational modes of the species.

$$\mathrm{ZPE} = \sum_{i}^{n} \frac{1}{2} h\upsilon_i \qquad \text{Eq S5-26}$$

The temperature effect on adsorption energy (E_{ads}), reaction energy (E_r), activation energy (E_a) is taken into account to obtain more accurate results. The global partition function, Q, is used to depict the energy as a function of temperature for the intermediates on the surface or in the gas phase, and the basic thermodynamic characters such as entropy (S), specific heat at constant pressure (C_p) and enthalpy (H) can be derived by Q as the following equations:

$$S = klnQ + kT\left(\frac{\partial \ln Q}{\partial T}\right)_V \qquad \text{Eq S5-27}$$

$$C_p = T\left(\frac{\partial S}{\partial T}\right)_P \qquad \text{Eq S5-28}$$

$$H = E_{DFT} + E_{(S=0,T=0,ZPE)} + \int_0^T C_p\, \partial T \qquad \text{Eq S5-29}$$

$$G = H - TS \qquad \text{Eq S5-30}$$

Where k is Boltzmann constant, T is the temperature. The global partition function is calculated as *Eq S4-6*.

$$Q = q_{translational} \times q_{rotational} \times q_{vibrational} \times q_{electronic} \times q_{nuclear} \qquad \text{Eq S5-31}$$

Translational, rotational, vibrational, electronic and nuclear contributions are considered. Normally, the electronic systems are in a single electronic state, and the nuclear partition functions are unity, i.e. $q_{electronic}$, $q_{nuclear}$ equal constant 1. The vibrational partition function of a system is obtained via *Eq S4-7*,

$$q_{vib} = \prod_{i=1}^{N} \frac{1}{1 - e^{-hv_i/k_B T}} \quad \text{Eq S5-32}$$

Where i is a specific vibrational mode and N is the number of vibrations. The vibrational partition function in the gas phase, q_{vib}^{gas}, is also calculated using the equation above for $3N_i$-6 and $3N_i$-5 vibrational degrees of freedom of a non-linear and linear molecule in the gas phase, respectively, where N_i is the number of atoms in the molecule. The 2D-translational partition function for a free molecule is derived by the Eq S4-8.

$$q_{translation}^{2D}(A,T) = \left(\frac{2\pi m k_B T}{h^2}\right) A_{cat} \quad \text{Eq S5-33}$$

Where A_{cat} is the average area of one active site on a catalyst.

The 3D-translational partition function for a molecule is calculated by the Eq S4-9, where $V_{(P,T)}$ is derived by $V_{(P,T)} = k_B T/p$, p is the pressure of the gas phase.

$$q_{trans}^{3D} = V_{(P,T)} \times \frac{(2\pi m k_B T)^{3/2}}{h^3} \quad \text{Eq S5-34}$$

The Rotational partition function for a free molecule is calculated using Eq S4-10 and Eq S4-11, depending on its symmetry and linear type.

$$q_{rot}^{linear} = \frac{\pi^{1/2}}{\sigma h}(I_{ZZ})^{1/2}(8\pi^2 k_B T)^{1/2} \quad \text{Eq S5-35}$$

$$q_{rot}^{nonlinear} = \frac{1}{\sigma}\left(\frac{8\pi^2 k_B T}{h^2}\right)^{3/2} \sqrt{\pi I_a I_b I_c} \quad \text{Eq S5-36}$$

Where σ is the symmetry factor and I is the moment of inertia defined as *Eq S4-12*,

$$I = \sum_i m_i r_i^2 \quad \text{Eq S5-37}$$

Where the sum is over the atoms in the molecule, m_i is the mass of atom and r_i is its distance from the rotation axis.

The thermodynamic properties in our system were calculated according to the above equations. To evaluate the accuracy of our method, a comparison between calculated and standard thermodynamic properties of NH_3, N_2, H_2 was carried out. The reference properties are from the NIST database and Thermochemical Data of Pure Substances.

Table S5-6 Optimized gas molecule information

Species	Energy(eV)	Vibration(cm^{-1})	Mass(kg)	Pressure(Pa)	Symmetry	Inertia($kg*m^2$)
H_2	-7.047	4360.85	3.35×10^{-27}	101325	2	2.35×10^{-48}
N_2	-17.0944	2006.95	4.65×10^{-26}	101325	2	7.82×10^{-47}
NH_3	-20.0541	3504.75,3503.83, 3372.67,1633.87, 1633.20,1035.29	2.83×10^{-26}	101325	3	3.51×10^{-140}

Figures below show both the calculated and reference thermodynamic data between 300-1000K. According to the Gibbs energy calculated, the delta Gibbs energy of ammonia synthesis reaction was given. The delta Gibbs energy of calculation is corrected by experimental formation enthalpy of ammonia and pure gas, which is -45.94 kJ mol^{-1} and 0 kJ mol^{-1}. Since the absolute values of the delta Gibbs energy are small at 400 and 500K, the errors turned a little bit. Generally, our method based on VASP optimized results to calculate thermodynamic properties was proved accurately.

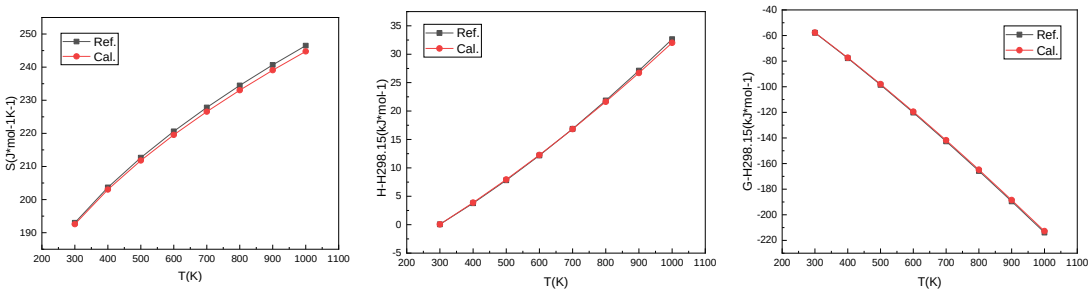

Figure S5-6. Calculated thermodynamic properties of gas phase NH_3 compared with reference data from 300-1000K

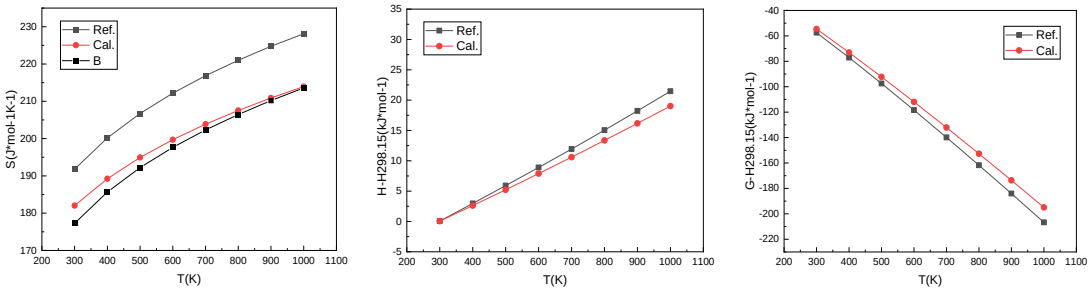

Figure S5-7. Calculated thermodynamic properties of gas phase N_2 compared with reference data from 300-1000K

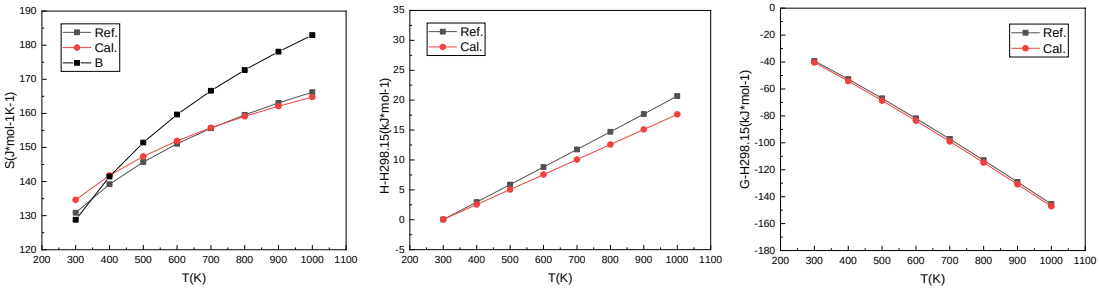

Figure S5-8. Calculated thermodynamic properties of gas phase H_2 compared with reference data from 300-1000K

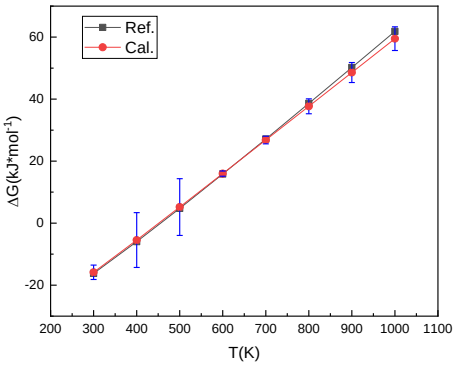

Figure S5-9. The delta Gibbs energy of ammonia synthesis reaction with error bar. The error was calculated by $(G_{cal} - G_{reference})/G_{reference} * 100$.

Ⅱ. Reaction thermochemistry

The recombination of dissociated N to nitrogen molecule on the surface (R7) needs to overcome a barrier (E_{a4}) of 2.40-2.62 eV at the temperature explored, which is supposed to be the rate-determining step. R5 and R9 carry out the NH dehydrogenation and the H re-coupling have close barrier energy at 300K, which are 1.03 eV and 1.01 eV respectively. Furthermore, only the N and H atoms recombination (R7 and R9) are endothermic elementary steps needing energy of 1.25 eV and 0.69 eV under 300K. With the rise of temperature from 300K to 900K, the dehydrogenation energy barrier (E_{a1}) of R1 decrease from 1.22 eV to 1.17 eV, indicating that high temperature is favourable to the first step dehydrogenation. Conversely, the energy barrier (E_{a2}) of R3 up from 0.64 eV to 0.69 eV with the rise of temperature. As the energy barrier to form NH by NH_2 (R3) dehydrogenation is relatively small. The lifetime of NH_2 is very short and detect it experimentally will be extremely challenging on Ru(0001).

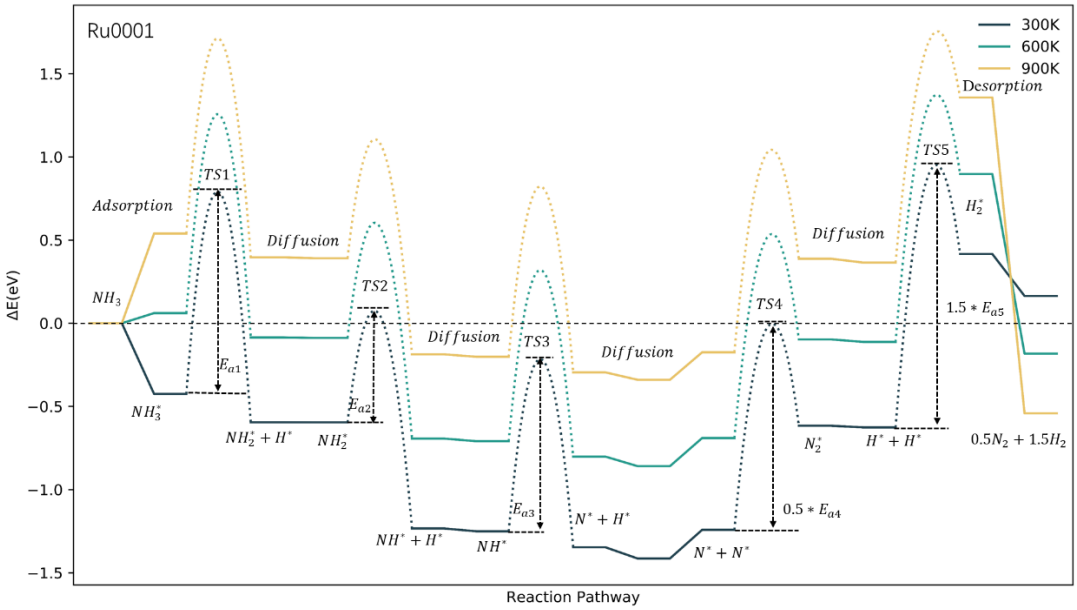

Figure S5-10. Energy profile of ammonia decomposition on Ru(0001) under 300K, 600K and 900K

Figure S5-11 depicts the energy profile of ammonia decomposition on Ru(111) at 300K, 600K and 900K. It suggests that the N_2 formation, R7, is the rate-determining step under the studied temperature proceeding barrier energy (E_{a4}) of 2.46 to 2.43 eV. The third dehydrogenation step (R5) to form N and H atoms, has the second-highest barrier energy (E_{a3} =1.74eV) at 300K, and with the temperature increasing to 900K, it rises to 1.78 eV. The dehydrogenation of NH_3 has the third-highest barrier energy under 300 K which is 1.17 eV and decrease with the temperature. Comparing with Ru(0001), R5 on Ru(111) has higher barrier energy for generating N^* and H^*, but the H_2 molecule generation (R9) becomes easier by overcoming barrier energy of 0.51 eV to 0.39 eV under 300 to 900 K. The shrinkage of barrier energy suggests that high temperature is favourable for the hydrogen generation thermodynamically. E_{a2}(0.70 eV) for R3 is close with E_{a5} for R9 under 300 K, while it will increase to 0.75 eV when temperature up to 900K.

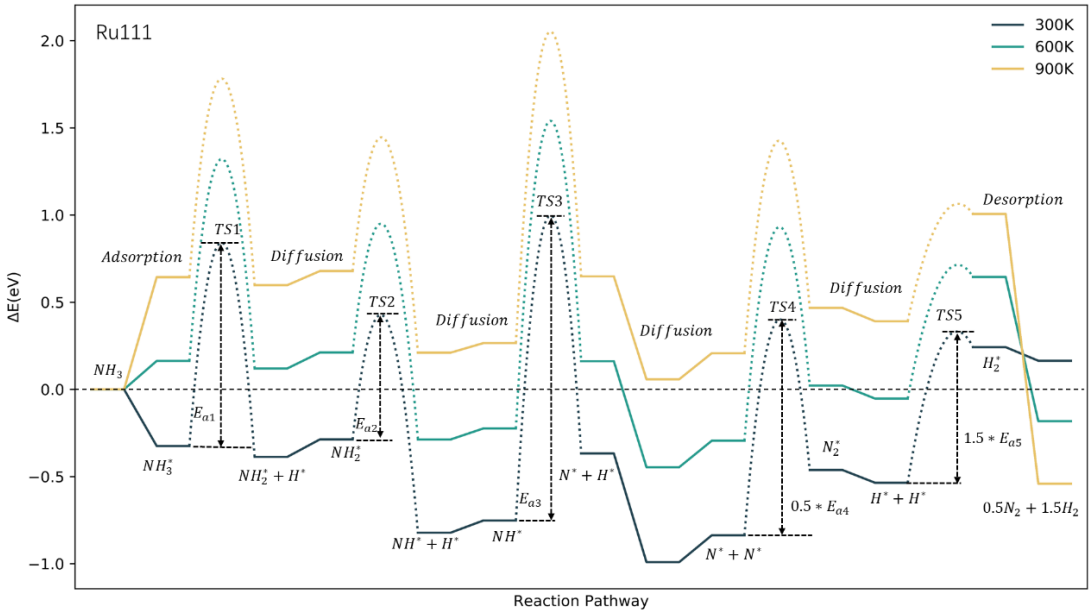

Figure S5-11. Energy profile of ammonia decomposition on Ru(111) under 300K, 600K and 900K

Figure S5-12 shows the energy profile of ammonia decomposition on Ir(111) at 300K, 600K and 900K. It suggests that nitrogen recombination, R7, is the rate-determining step as well, with barrier energy (E_{a4}) of 1.94 eV at studied temperature, which is close to previous research (1.75 eV for Ir(110)).[284] The first (R1) and second (R3) dehydrogenation of NH_3 needs to overcome similar barriers of around 1.55 eV at 300 K, which are increasing with the temperature. The last dehydrogenation step, R5, yields N^* and H^* by surpassing a 0.91 eV barrier at 300-900K, which is a moderate elementary step. The recombination of H^*, R9, is impaired by the rise of temperature since the barrier energy (E_{a5}) rise from 0.62 eV at 300 K to 0.66 eV at 900K.

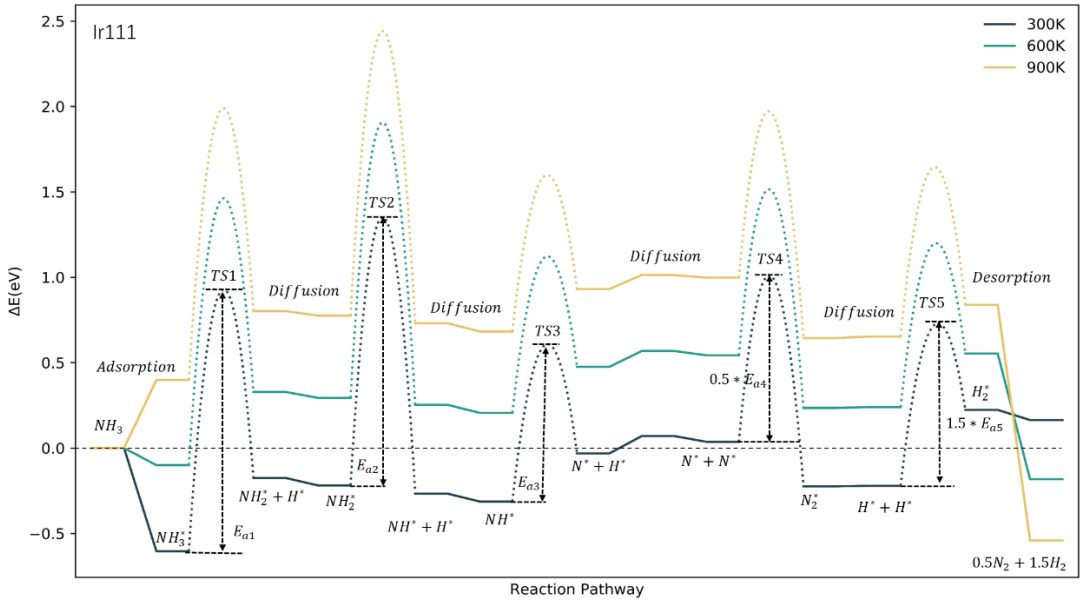

Figure S5-12. Energy profile of ammonia decomposition on Ir(111) under 300K, 600K and 900K

Ⅱ. Equilibrium constant and Reaction rate constant calculations

A script reading the partition functions, thermodynamic properties was implemented to calculate the equilibrium constant and reaction rate constant of all elementary steps. *Figure S4-9* shows the process of the script. In the scripts, the temperature and time step of the numerical integration is 10K and 1s, respectively.

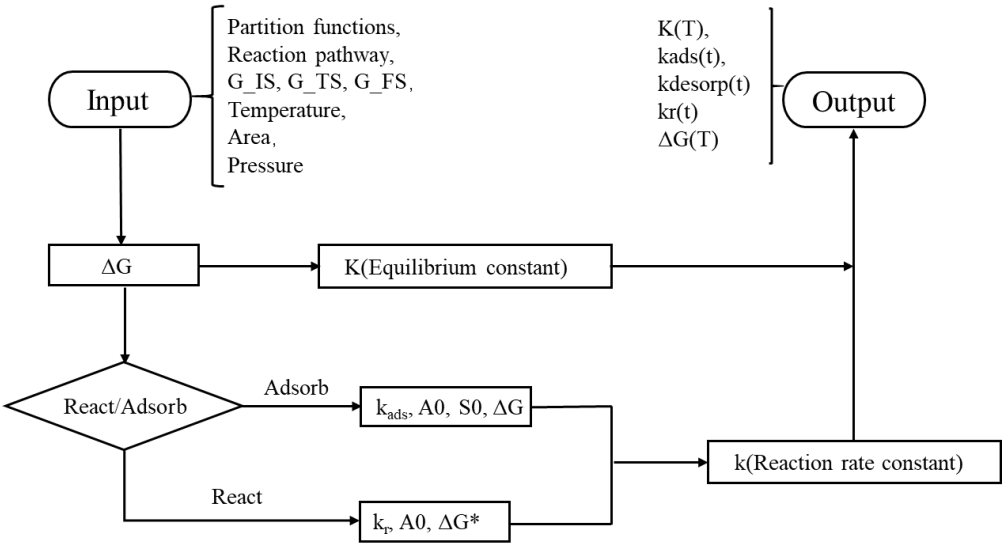

Figure S5-13. The flow diagram of reaction rate constant and equilibrium constant calculation

The barrier energy of adsorption and desorption processes are calculated by Eq S4-13, Eq S4-14 and Eq S4-15:

$$\mathrm{E_a^{ads}} = \mathrm{E_{ts}} - \mathrm{E_{gas}} - E_{surf} \qquad \text{Eq S5-38}$$

$$\mathrm{E_a^{des}} = \mathrm{E_{ts}} - \mathrm{E_{ads}} \quad \text{Eq S5-39}$$

$$\mathrm{E_{ts}} = \mathrm{E_{gas}} + E_{surf} + \left(ZPE_{2D}^{gas} - ZPE_{3D}^{gas}\right) \quad \textit{Eq S5-40}$$

The adsorption energy is calculated by Eq S4-16:

$$\mathrm{E_r} = \mathrm{E_{gas}} + E_{surf} - \mathrm{E_{ads}} \quad \textit{Eq S5-41}$$

The classical Hertz-Knudsen equation was employed to estimate the rate of adsorption, as following Eq S4-17 to Eq S4-18.

$$\mathrm{Q_{reactants}} = \left(\mathrm{q_{trans2D}^{ads}} \times \mathrm{Q_{notrans3D}^{gas}}\right)^{(\mathrm{stoichio_{ads}})} \times \mathrm{Q_{surf}^{(stoichio_{surf})}} \quad \textit{Eq S5-42}$$

$$\mathrm{Q_{ts}} = \left(\mathrm{q_{vib2D}^{ads}}\right)^{(\mathrm{stoichio_{ads}})} \times \mathrm{Q_{surf}^{(stoichio_{surf})}} \quad \textit{Eq S5-43}$$

$$\mathrm{Q_{reactants}} = \left(\mathrm{Q_{3D}^{ads}}\right)^{\mathrm{stoichio_{ads}}} \quad \textit{Eq S5-44}$$

$$\mathrm{Sticky_{ads}} = \frac{\mathrm{Q_{ts}}}{\mathrm{Q_{reactants}}} \times \mathrm{e}^{-\frac{\mathrm{E_a^{ads}}}{\mathrm{k_B T}}} \quad \textit{Eq S5-45}$$

$$\mathrm{Sticky_{des}} = \frac{\mathrm{Q_{ts}}}{\mathrm{Q_{products}}} \times \mathrm{e}^{-\frac{\mathrm{E_a^{ads}}}{\mathrm{k_B T}}} \quad \textit{Eq S5-46}$$

$$\mathrm{A_0} = \mathrm{areaS} \times \frac{1}{(2\pi \mathrm{Mass} \times \mathrm{k_B T})^{0.5}} \quad \textit{Eq S5-47}$$

$$\mathrm{k_{ads/des}} = \mathrm{A_0} \times \mathrm{Sticky_{ads/des}} \quad \textit{Eq S5-48}$$

Where $\mathrm{A_0}$ is the pre-exponential factor. The sticking coefficient, Sticky, is a measure of the fraction of incident molecules which adsorb upon the surface and is calculated via *Eq S4-20* and *Eq S4-21*.

As for the ***surface reactions*** in the heterogeneous catalytic system, which is considered in our research, the constant rate (k) of each surface elementary step is commonly computed using the transition state theory (TST) approximation of Eyring and Evans and Polanyi, as follows:

$$\mathrm{k_r} = \mathrm{A_0 e}^{-\frac{\Delta \mathrm{G}^*}{\mathrm{k_B T}}} = \frac{\mathrm{k_B T}}{\mathrm{h}} \frac{\mathrm{q_{TS}}}{\mathrm{q_{IS}}} \mathrm{e}^{-\frac{\Delta \mathrm{G}^*}{\mathrm{k_B T}}} \quad \text{Eq S5-49}$$

Where h is the Plank constant, kB is the Boltzmann constant, T is the temperature, A_0 is the pre-exponential factor, ΔG* is the reaction activation energy, and $\mathrm{q_{TS}}$ and $\mathrm{q_{IS}}$ are the partition functions of reactants and transition states respectively. The translations and rotations of the adsorbed species are frustrated on the surface and therefore we considered only vibrational modes.

We have considered an active site as a hexagonal site where the reactants and products in every elementary step occupy only one site on the surface. Consequently, the coverage of free sites, $\theta_*(t)$, is defined by:

$$\theta_*(t) = 1 - \sum_i^n \theta_i(t) \quad \text{Eq S5-50}$$

Where the $\theta_i(t)$ represents the coverage of the intermediates present in the reaction system.

Ⅲ. The reaction and rate equations

The adsorption and first dehydrogenation of NH_3 are highly exothermic and the desorbed hydrogen and nitrogen molecules are assumed to leave from the surface immediately, therefore, the dissociated adsorption model is applied in the adsorption and desorption process of molecules. All the elementary steps in the ammonia decomposition and their rate equations are listed below.

Table S5-7. Elementary steps in the ammonia decomposition

No	Reaction	Rate equation
A1	$\mathrm{NH_3} + * \longrightarrow \mathrm{NH_3^*}$	$\mathrm{r_{a1}} = \mathrm{k_{a1}} Y_{\mathrm{NH_3}}(\mathrm{t})\theta_*(\mathrm{t})$
D1	$\mathrm{NH_3^*} \longrightarrow \mathrm{NH_3} + *$	$r_{d1} = k_{d1}\theta_{NH_3}(t)$
R1	$\mathrm{NH_3^*} + * \longrightarrow \mathrm{NH_2^*} + \mathrm{H^*}$	$r_{r1} = k_{r1}\theta_{NH_3}(t)\theta_*(\mathrm{t})$
R2	$\mathrm{NH_2^*} + \mathrm{H^*} \longrightarrow \mathrm{NH_3^*} + *$	$r_{\mathrm{r2}} = k_{\mathrm{r2}}\theta_{NH_2}(t)\theta_{\mathrm{H}}(t)$
R3	$\mathrm{NH_2^*} + * \longrightarrow \mathrm{NH^*} + \mathrm{H^*}$	$r_{\mathrm{r3}} = k_{\mathrm{r3}}\theta_{NH_2}(t)\theta_*(\mathrm{t})$
R4	$\mathrm{NH^*} + \mathrm{H^*} \longrightarrow \mathrm{NH_2^*} + *$	$r_{\mathrm{r4}} = k_{\mathrm{r4}}\theta_{\mathrm{NH}}(t)\theta_H(t)$
R5	$\mathrm{NH^*} + * \longrightarrow \mathrm{N^*} + \mathrm{H^*}$	$r_{\mathrm{r5}} = k_{\mathrm{r5}}\theta_{NH}(t)\theta_*(\mathrm{t})$
R6	$\mathrm{N^*} + \mathrm{H^*} \longrightarrow \mathrm{NH^*} + *$	$r_{r6} = k_{r6}\theta_N(t)\theta_H(t)$
R7	$2\mathrm{N^*} \longrightarrow N_2^* + *$	$r_{r7} = k_{r7}\theta_N^2(t)$
R8	$N_2^* + * \longrightarrow 2\mathrm{N^*}$	$r_{r8} = k_{r8}\theta_{N_2}(t)\theta_*(\mathrm{t})$
D2	$N_2^* \longrightarrow N_2 + *$	$r_{d2} = k_{d2}\theta_{N_2}(t)$
A2	$N_2 + * \longrightarrow N_2^*$	$\mathrm{r_{a2}} = \mathrm{k_{a2}} Y_{\mathrm{N_2}}(\mathrm{t})\theta_*(\mathrm{t})$
R9	$2\mathrm{H^*} \longrightarrow H_2^* + *$	$r_{r9} = k_{r9}\theta_H^2(t)$
R10	$H_2^* + * \longrightarrow 2\mathrm{H^*}$	$r_{r10} = k_{r10}\theta_{H_2}(t)\theta_*(\mathrm{t})$
D3	$H_2^* \longrightarrow \mathrm{H_2} + *$	$r_{d3} = k_{d3}\theta_{H_2}(t)$
A3	$\mathrm{H_2} + * \longrightarrow H_2^*$	$\mathrm{r_{a3}} = \mathrm{k_{a3}} Y_{H_2}(\mathrm{t})\theta_*(\mathrm{t})$

Where $Y_{molecule}(t)$ is the time-dependent ratio of the molecule and free sites.

Ⅳ. Differential equations in the TPD simulation of hydrogen and nitrogen

Temperature programmed reaction model start from pre-adsorbed NH_3, the temperature increases at a different rate from 200 to 1000 K while any gas was extracted to avoid the re-adsorption of gases. It is applied to examine the adsorption properties of N_2 and H_2 over different surfaces in our research. The initial parameter is input into the program by the command: YN_2, YH_2, θ_N, θ_H, θ_* = [0, 0, a, b, 1]

V. Differential equations in the reactor simulation

A batch reactor model under a variety of conditions is employed to investigate the catalytic properties when the metallic surface is in contact with a given pressure of NH_3. The initial parameter is input into the program by the command: Y_{NH3}, Y_{N2}, Y_{H2}, θ_{NH_3}, θ_{N_2}, θ_{H_2}, θ_{NH_2},θ_{NH},θ_N,θ_H,θ_* = [a,0,0,0,0,0,0,1]

VI. Reference

(1) Chorkendorff, I.; Niemantsverdriet, J. W. *Concepts of Modern Catalysis and Kinetics*; John Wiley & Sons, 2017.

(2) Chase Jr, M. W.; Tables, N.-J. T. Data Reported in NIST Standard Reference

Database 69, June 2005 Release: NIST Chemistry WebBook. *J. Phys. Chem. Ref. Data, Monograph* **1998**, *9*, 1–1951.
(3) Ihsan, B. Thermochemical Data of Pure Substances. *and* **1995**, *934*, 587.

Appendix D: Chapter 6 Supporting Information

Supporting Information: Kinetic and Mechanistic Analysis of NH_3 Reforming on Single-Atom Catalysts

Table S6-1. The bulk lattice parameters of Co(hcp), Co(fcc), Fe(bcc), Fe(fcc) and Ni(fcc)

Surface	This work	Reference
Co(hcp)	a=2.482 Å, c/a = 1.610	a = 2.507 Å, c/a = 1.623 [337]
Co(fcc)	3.495 Å	3.420 Å [338]
Fe(bcc)	2.870 Å	2.862 Å [339]
Fe(fcc)	3.622 Å	3.430 Å [338]
Ni(fcc)	3.486 Å	3.545 Å [340]
Ru(hcp)	a=2.691 Å, c/a = 1.572	a = 2.754 Å, c/a = 1.587 [305]
Ru(fcc)	3.792 Å	3.825 Å [307]
Ir(fcc)	3.842 Å	3.876 Å [308]

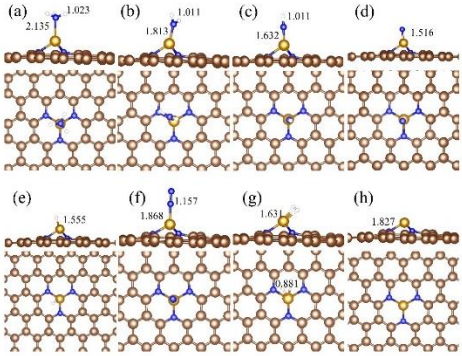

Figure S6-1. The structural representation of intermediate adsorption on FeN_3. (a) NH_3, (b) NH_2, (c) NH, (d) N, (e) H, (f) N_2, (g) H_2, (h) FeN_3.

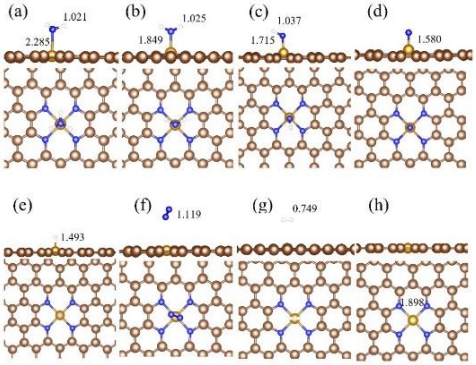

Figure S6-2. The structural representation of intermediate adsorption on FeN_4. (a) NH_3, (b) NH_2, (c) NH, (d) N, (e) H, (f) N_2, (g) H_2, (h) FeN_4.

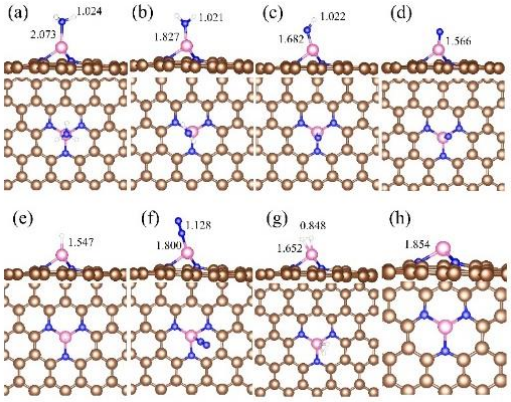

Figure S6-3.The structural representation of intermediate adsorption on CoN_3. (a) NH_3, (b) NH_2, (c) NH, (d) N, (e) H, (f) N_2, (g) H_2, (h) CoN_3.

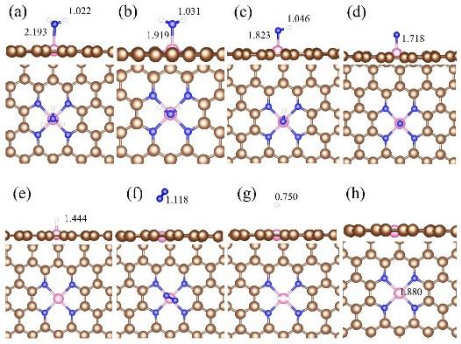

Figure S6-4. The structural representation of intermediate adsorption on CoN_4. (a) NH_3, (b) NH_2, (c) NH, (d) N, (e) H, (f) N_2, (g) H_2, (h) CoN_4.

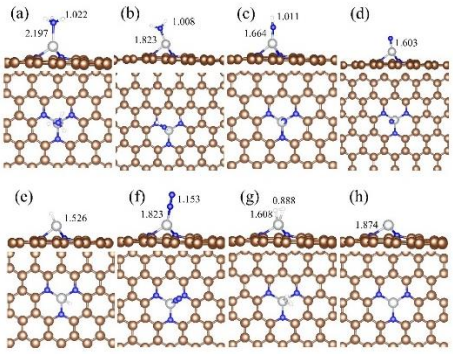

Figure S6-5. The structural representation of intermediate adsorption on NiN_3. (a) NH_3, (b) NH_2, (c) NH, (d) N, (e) H, (f) N_2, (g) H_2, (h) NiN_3.

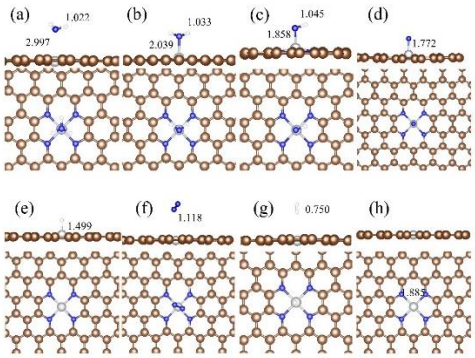

Figure S6-6. The structural representation of intermediate adsorption on NiN_4. (a) NH_3, (b) NH_2, (c) NH, (d) N, (e) H, (f) N_2, (g) H_2, (h) NiN_4.

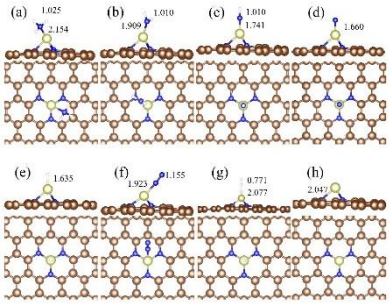

Figure S6-7. The structural representation of intermediate adsorption on IrN_3. (a) NH_3, (b) NH_2, (c) NH, (d) N, (e) H, (f) N_2, (g) H_2, (h) IrN_3.

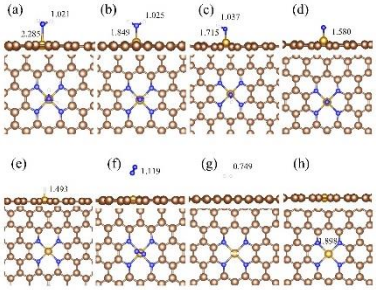

Figure S6-8. The structural representation of intermediate adsorption on IrN_4. (a) NH_3, (b) NH_2, (c) NH, (d) N, (e) H, (f) N_2, (g) H_2, (h) IrN_4.

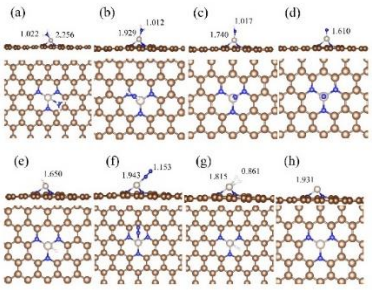

Figure S6-9. The structural representation of intermediate adsorption on RuN_3. (a) NH_3, (b) NH_2, (c) NH, (d) N, (e) H, (f) N_2, (g) H_2, (h) RuN_3.

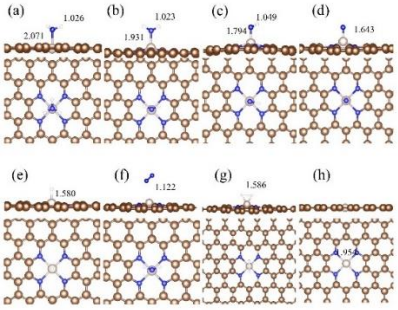

Figure S6-10. The structural representation of intermediate adsorption on RuN_4. (a) NH_3, (b) NH_2, (c) NH, (d) N, (e) H, (f) N_2, (g) H_2, (h) RuN_4.

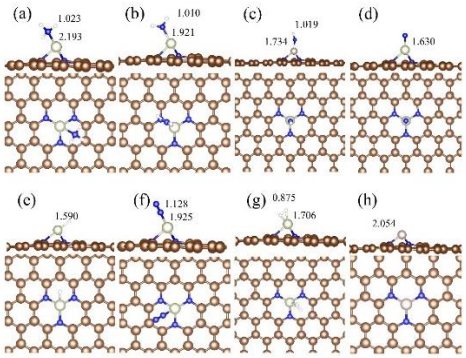

Figure S6-11. The structural representation of intermediate adsorption on RhN_3. (a) NH_3, (b) NH_2, (c) NH, (d) N, (e) H, (f) N_2, (g) H_2, (h) RhN_3.

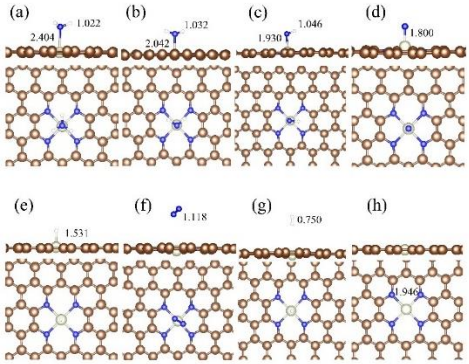

Figure S6-12. The structural representation of intermediate adsorption on RhN_4. (a) NH_3, (b) NH_2, (c) NH, (d) N, (e) H, (f) N_2, (g) H_2, (h) RhN_4.

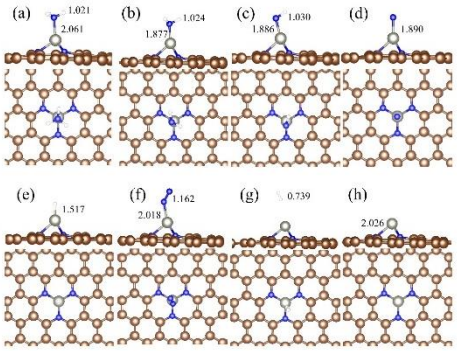

Figure S6-13.The structural representation of intermediate adsorption on ZnN_3. (a) NH_3, (b) NH_2, (c) NH, (d) N, (e) H, (f) N_2, (g) H_2, (h) ZnN_3.

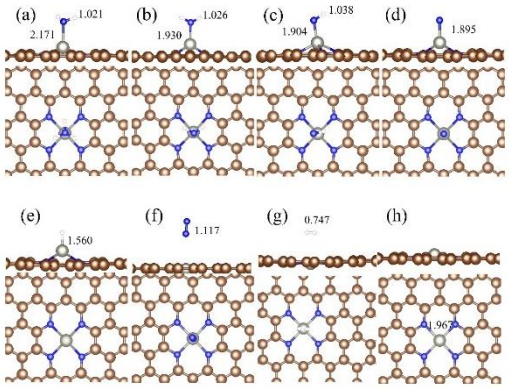

Figure S6-14. The structural representation of intermediate adsorption on ZnN_4. (a) NH_3, (b) NH_2, (c) NH, (d) N, (e) H, (f) N_2, (g) H_2, (h) ZnN_4.

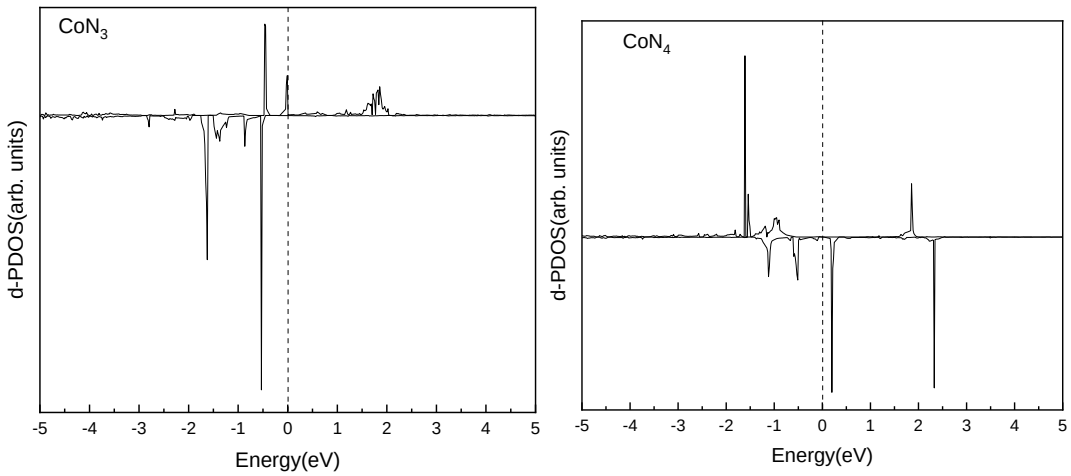

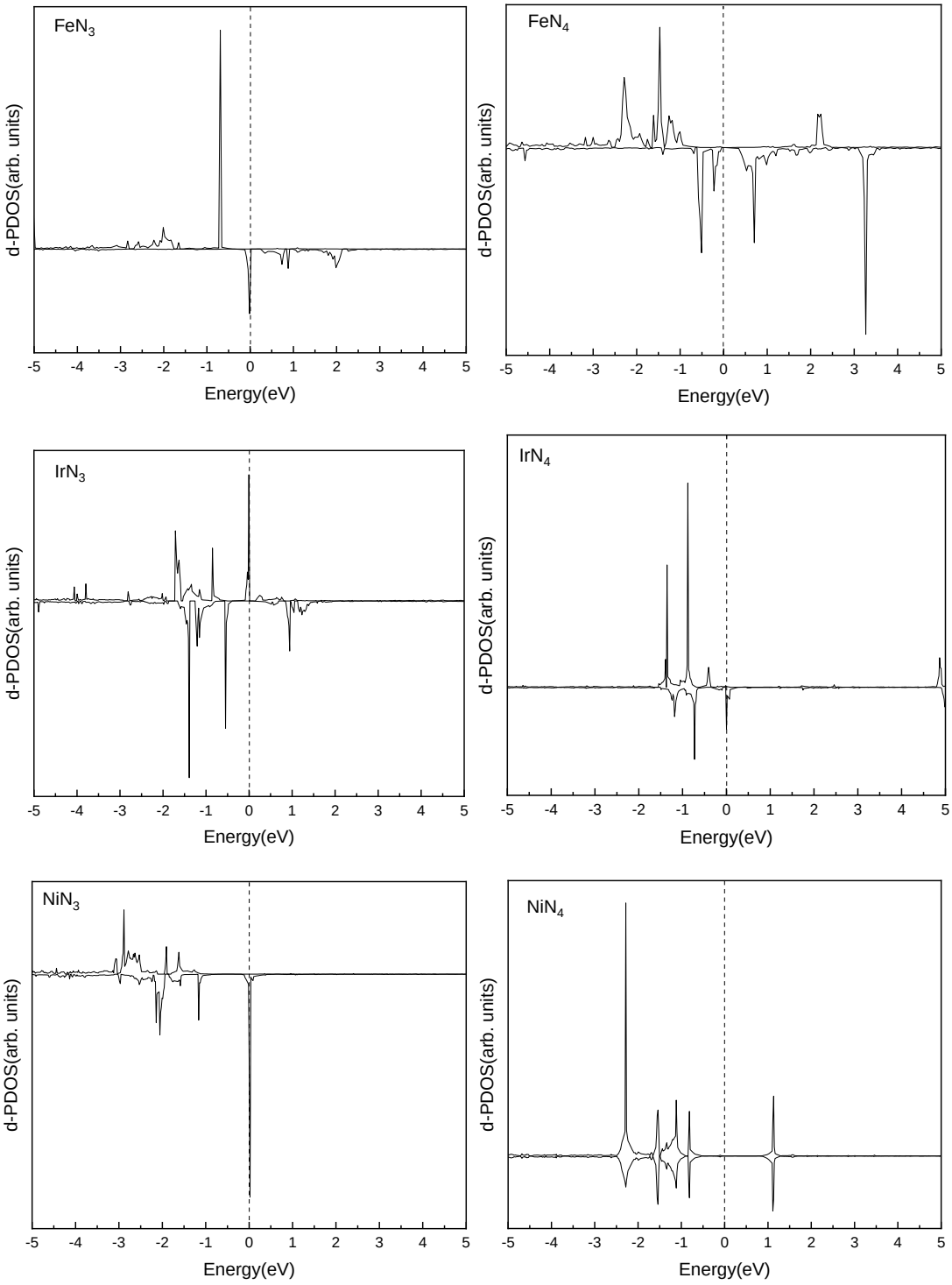
FeN3
FeN4
IrN3
IrN4
NiN3
NiN4
d-PDOS(arb. units)
Energy(eV)
-5 -4 -3 -2 -1 0 1 2 3 4 5

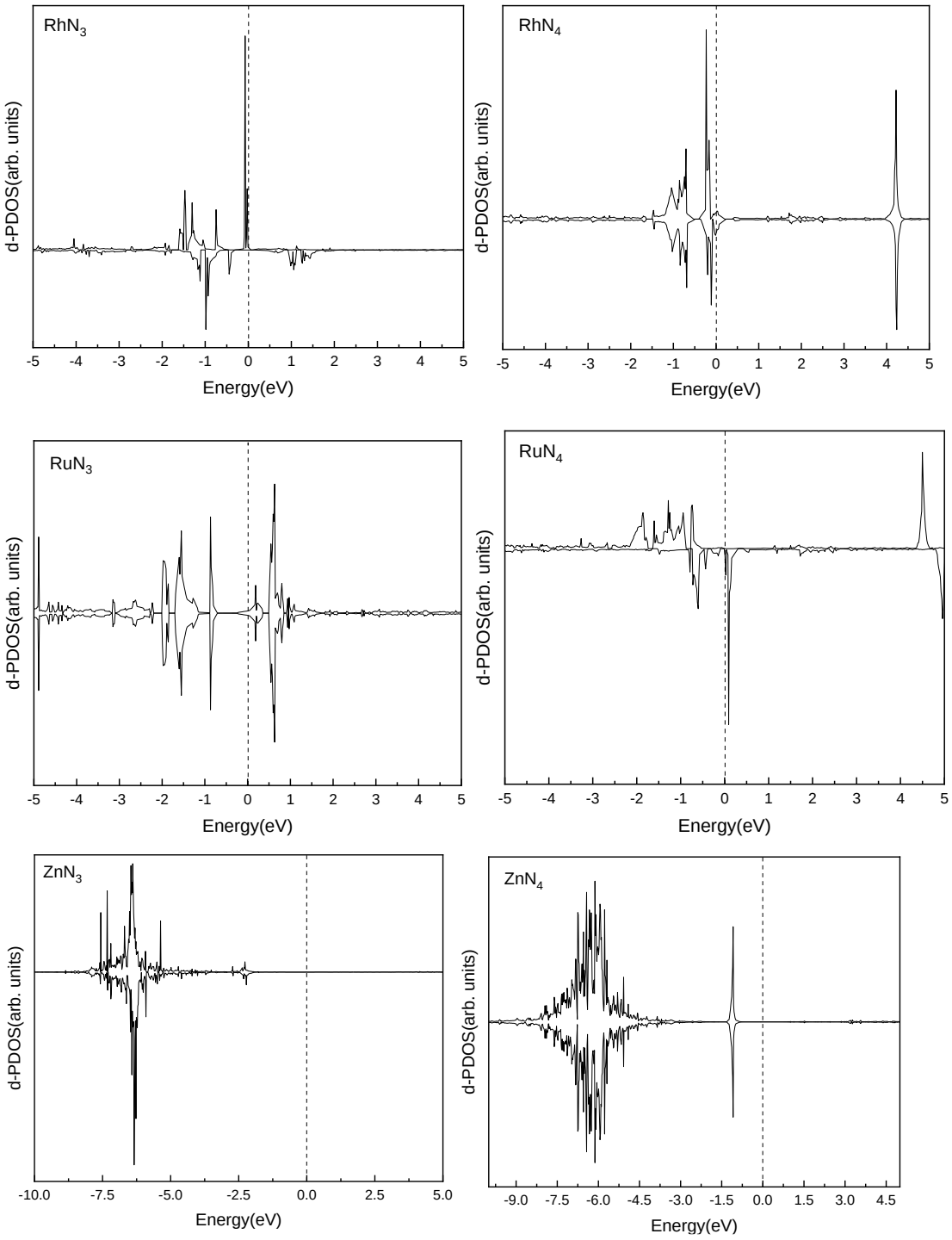

Figure S6-15. The d orbital PDOS of metals (Co, Fe, Ir, Ni, Rh, Ru and Zn) in SACs.

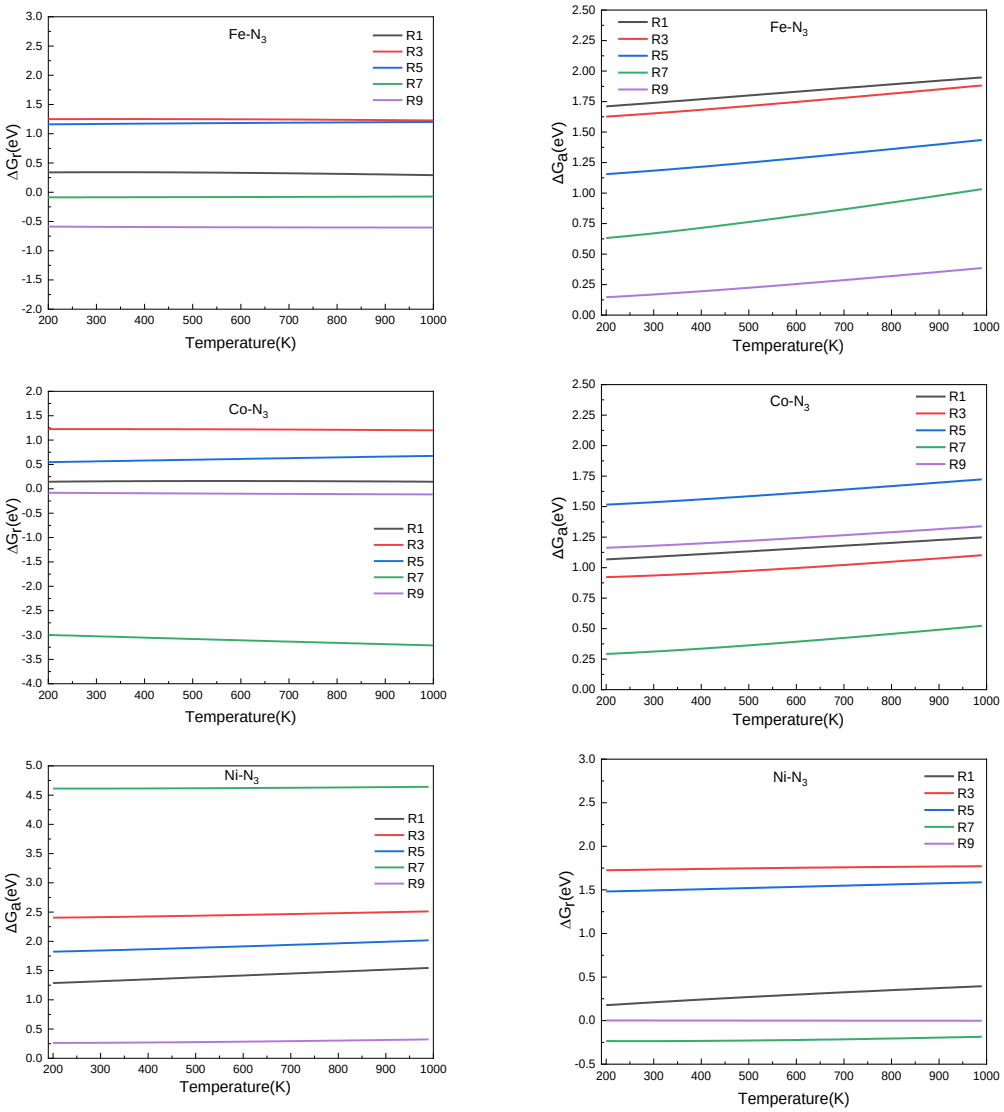

Figure S6-16. Free energy difference (ΔG_r) and activation energy (ΔG_a) of the elementary steps in ammonia dehydrogenation (R1, R3, R5) and N_2 and H_2 formations (R7 and R9) on FeN_3, CoN_3, and NiN_3 as a function of the temperature.

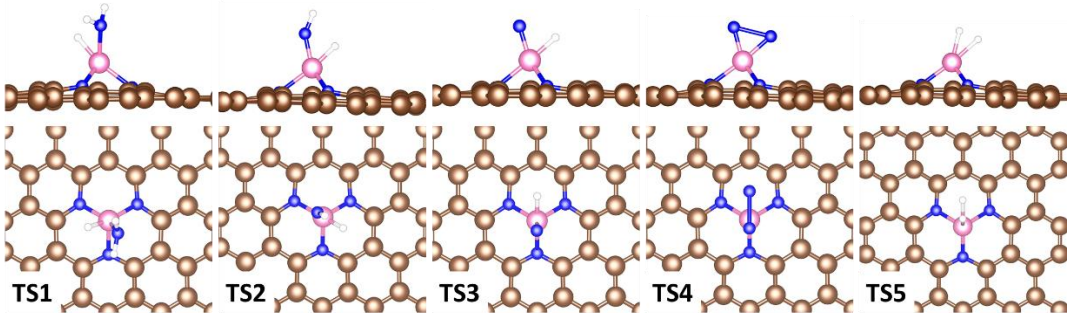

Figure S6-17. Schematic diagram of the NH_3 reforming reaction transition states on SACs.